Titre: Title:	Flow Induced Orientation in Carbon Nanotube Suspension: Modeling and Experiments
Auteur: Author:	Giovanniantonio Natale
Date:	2015
Type:	Mémoire ou thèse / Dissertation or Thesis
Référence: Citation:	Natale, G. (2015). Flow Induced Orientation in Carbon Nanotube Suspension: Modeling and Experiments [Thèse de doctorat, École Polytechnique de Montréal]. PolyPublie. https://publications.polymtl.ca/1810/

UNIVERSITÉ DE MONTRÉAL

FLOW INDUCED ORIENTATION IN CARBON NANOTUBE SUSPENSIONS: MODELING AND EXPERIMENTS

GIOVANNIANTONIO NATALE

DÉPARTEMENT DE GÉNIE CHIMIQUE

ÉCOLE POLYTECHNIQUE DE MONTRÉAL

THÈSE PRÉSENTÉE EN VUE DE L'OBTENTION

DU DIPLÔME DE PHILOSOPHIAE DOCTOR

(GÉNIE CHIMIQUE)

AOÛT 2015

UNIVERSITÉ DE MONTRÉAL

ÉCOLE POLYTECHNIQUE DE MONTRÉAL

Cette thèse intitulée:

FLOW INDUCED ORIENTATION IN CARBON NANOTUBE SUSPENSIONS: MODELING AND EXPERIMENTS

présentée par : NATALE Giovanniantonio

en vue de l'obtention du diplôme de : Philosophiae Doctor

a été dûment acceptée par le jury d'examen constitué de :

M. DUBOIS Charles, Ph. D., président

Mme HEUZEY Marie-Claude, Ph. D., membre et directrice de recherche

M. CARREAU Pierre, Ph. D., membre et codirecteur de recherche

M. FÉREC Julien, Ph. D., membre et codirecteur de recherche

M. GRMELA Miroslav, Doctorat, membre

M. CHINESTA Francisco José, Ph. D., membre externe

DEDICATION

Alla mia nonna…

To my grandmother…

ACKNOWLEDGEMENTS

First and foremost, I would like to express all my gratitude to my research director, Professor Marie-Claude Heuzey and to my research co-directors, Professors Pierre Carreau and Julien Férec. During these past years, their support and guidance has been integral throughout my thesis project.

I would like to thank Professor Gilles Ausias for its help in the modeling aspects of this project and for his constructive comments on the articles. Thank you to Professors Jan Vermant and Paula Moldenaers for providing access to their rheo-optical setup at KU Leuven and, in particular, Dr. Naveen Krishna Reddy for his help with the rheo-optical measurements.

I would like to thank Professor Daniel Therriault for providing me access to the composite laboratory in the Mechanical Engineering Department of École Polytechnique and Professor Michael Buschmann, Dr. Vincent Darras and Dr. Nicolas Tran-Khanh of the Biomedical Engineering Department for their help with the Confocal microscopy.

Mostly, I would like to thank Professors Fabio Cicoira and Clara Santato for letting me participate in their research.

I would also like to thank Université de Bretagne-Sud for the mobility scholarship and the Society of Rheology for the conference travel grant.

My gratitude is also directed to all the members of the CREPEC group of the École Polytechnique de Montréal and especially, the rheology group. Thank you to Melina Hadmine for training me at the beginning of my Ph.D. and to my friends and colleagues Gilles Lenfant and Marie Matet for having shared long hours in the lab with me and turned those hours into fond memories.

Thank you to Franco, Filippo, Luca, Matteo and the other Italian researchers here at École Polytechnique de Montréal. Our coffee breaks made me miss Italy a little less.

I would like to thank my parents and my brothers who support me in so many ways even if we are far. Finally, I would like to thank my partner, Madeleine, for her love and support during these years and for her ability to make me smile even in the most difficult moments.

RÉSUMÉ

De par leurs propriétés uniques, les nanotubes de carbone (NTCs) sont très prometteurs pour la prochaine génération de matériaux. Les applications sont multiples et variées et touchent des domaines comme l'électronique organique, le renforcement de composites en plastiques conducteurs, les alliages et même de nouveaux types de capteurs biologiques. En dépit de ces promesses et potentialités, les composites et les suspensions de nanotubes de carbone sont par nature difficiles à traiter. La formulation de procédés efficaces pour obtenir des résultats à la hauteur des espérances souhaitées ne font que commencer. Le succès des NTCs, dans toutes les applications possibles, dépend de leur compréhension fondamentale et de la capacité à contrôler l'évolution de leur microstructure lors de leur mise en œuvre.

Lors d'un écoulement, les NTCs dispersés dans une matrice polymère s'orientent et interagissent induisant des corrélations spatiales et orientationnelles. Les agglomérats peuvent également se briser si les forces hydrodynamiques sont suffisantes ce qui augmente la probabilité de contact entre les différents nanotubes et améliore leur interactions avec la matrice ainsi que la fluidité du matériau composite. Au repos, la microstructure d'une suspension de NTCs ne cesse de changer à cause du mouvement brownien et des forces attractives de van der Waals; les nanotubes de carbone diffusent dans la phase liquide et tendent à former un réseau.

Pour analyser un système aussi complexe, une résine époxy de faible viscosité a été utilisée comme matrice pour disperser les nanotubes de carbone à parois multiples (NTCPMs). Les polymères newtoniens sont particulièrement utiles car ils peuvent conférer une relativement large contrainte de cisaillement permettant de briser les agglomérats de NTCs facilitant ainsi leur dispersion. Le comportement newtonien, lui, permet de ne pas masquer les propriétés viscoélastiques de l'ensemble du système.

Du régime de concentration dilué vers un régime plus concentré, les suspensions de NTCs ont été étudiées rhéologiquement afin d'obtenir des informations sur l'orientation et le transport des nanotubes de carbone individuels ainsi que sur les propriétés viscoélastiques du réseau formé par ces particules cylindriques. La rhéologie a été utilisée pour comprendre l'évolution de la microstructure sous écoulement ainsi que dans des conditions statiques. Les effets de l'histoire de

l'écoulement, de la vitesse de cisaillement, du temps de repos et de la direction de cisaillement ont été étudiés.

Pour corréler la microstructure avec les données rhéologiques, deux voies ont été choisies. La première voie comprenait une analyse rhéo-optique. Le dichroïsme des suspensions a été étudié pour les suspensions appartenant aux régimes dilués et semi-dilués. Des informations directes sur la dispersion, l'évolution de l'orientation lors de l'écoulement et les effets dus au mouvement brownien ont ainsi été obtenus. La seconde voie consistait à développer de nouveaux modèles rhéologiques afin de corréler les informations à l'échelle de la microstructure avec l'évolution du tenseur de contrainte ou de l'indice de réfraction de la suspension.

Dans le régime dilué, les nanotubes ont été modélisés comme des particules flexibles. Un modèle modifié à deux tiges a été utilisé ce qui permet d'obtenir des conformations d'équilibre non-alignées. Dans les régimes plus concentrés, la dynamique du système est contrôlée par des interactions de type tige-tige. Les nanotubes ont été modélisés comme des bâtonnets rigides sans inertie et l'état d'orientation du système est influencé par des interactions via des forces de lubrification non-linéaires, des forces hydrodynamiques et par le mouvement brownien. La comparaison des résultats expérimentaux avec les prédictions des modèles proposés permet de quantifier les mécanismes fondamentaux derrière l'évolution de la microstructure des suspensions de NTCs. Afin de mieux différencier la rhéologie des suspensions de NTCs, les prédictions du modèle ont également été confrontées aux données expérimentales pour une suspension de particules microscopiques: des fibres de verre dans le polybutène [Sepehr et al. (2004b)]. Dans le cas des micro-particules, les prédictions du modèle ont confirmé que la réponse rhéologique du système est contrôlée par des effets d'orientation tandis que les interactions entre particules sont dominantes dans le cas des suspensions de NTCs.

Ainsi, ce travail explore les liens entre la rhéologie des suspensions de nanotubes de carbone et l'évolution de leur microstructure en suspension. Ceci est la première étape vers la conception de nouveaux systèmes de traitement afin d'exploiter complètement les propriétés uniques des nanotubes de carbone.

ABSTRACT

Due to their unique properties, carbon nanotubes (CNTs) hold remarkable promise for the next generation of materials, with potential applications in organic electronics, reinforced and electrically conducting plastic composites, new alloys, and even new types of biological sensors and devices. Despite these promises and potentialities, carbon nanotube composites and suspensions are inherently difficult to process, and efficient processing schemes are only just starting to be formulated. The success of CNTs, in all potential applications, depends on the understanding and ability to control the microstructure evolution during processing.

During flow, CNTs dispersed in a polymeric matrix orient and interact, inducing spatial and orientation correlations. Agglomerates can also break if the hydrodynamic forces are sufficient, increasing the probability of contact between different nanotubes and improving the interactions with the matrix and the flowability of the composite. At rest, the microstructure of the CNT suspension keeps changing due to Brownian motion and van der Waals attractive forces, and the CNTs diffuse in the suspending fluid and eventually form a network of particles.

To analyze such a complex system, a low viscosity epoxy was used as the matrix to disperse the multiwall carbon nanotubes (MWCNTs). Nearly Newtonian polymers are particularly useful because they can impart significant shear stress to break the CNT agglomerates and facilitate their dispersion, while their Newtonian behavior does not mask the viscoelastic properties of the overall system.

From dilute to concentrated regimes, CNT suspensions were rheologically probed to obtain information ranging from the orientation and transport of individual carbon nanotubes to the viscoelastic properties of dense and isotropic network of rods. Rheology was used to understand the microstructure evolution under flow and in static conditions. The effects of flow history, shearing velocity, rest time and shearing direction were studied.

To correlate the microstructure with the rheological data, two different routes were undertaken. The first route involved rheo-optical analysis. Dichroism was investigated for suspensions belonging to the dilute and semi-dilute regimes. Direct information on dispersion, orientation evolution during flow and Brownian motion were obtained. The second route consisted in

developing new rheological models in order to correlate micro-scale information to the evolution of the related stress tensor or refractive index tensor.

In the dilute regime, the nanotubes were modeled as flexible particles. A modified two-rod model was used, allowing non-straight equilibrium conformations. In more concentrated regimes, the dynamic of the system is controlled by rod-rod interactions. The nanotubes were modeled as inertialess rigid rods and the system orientation state is influenced by interactions via non-linear lubrication forces, hydrodynamic forces and Brownian motion. The comparison of the experimental results with the models predictions allowed to quantify the fundamental mechanisms behind the microstructure evolution of CNT suspensions. To further differentiate the rheology of CNT suspensions, the model predictions were also confronted with the experimental data for a microsize particle suspension: glass fiber-filled polybutene [Sepehr *et al.* (2004b)]. In the case of the micro-size particles, the model predictions confirmed that the rheological response of the system was controlled by orientation effects while interactions were dominant in the case of CNT suspensions.

Hence, this work explores the connections between the bulk rheology of carbon nanotube suspensions and their microstructural evolution. This is the first step towards the design of new processing schemes in order to completely exploit carbon nanotube unique properties.

TABLE OF CONTENTS

LIST OF TABLES

LIST OF FIGURES

LIST OF SYMBOLS AND ABBREVIATIONS

$\mathbf{a}_2$	Second order orientation tensor
$\dot{\mathbf{a}}_2$	Time evolution of $\mathbf{a}_2$
$\mathbf{a}_4$	Fourth order orientation tensor
$\mathbf{a}_6$	Sixth order orientation tensor
$a_E, a_W, a_N, a_S, a_M, a_P$	Coefficients of the discretization for finite volume method
AF	Anisotropy factor
AFM	Atomic force microscope
$\mathbf{B}$	Dimensionless conformation tensor of a macromolecule
$\mathbf{b}_2, \mathbf{b}_2^{(m)}$	Second order interaction tensor
$\mathbf{b}_4, \mathbf{b}_4^{(m)}$	Fourth order interaction tensor
$\mathbf{c}$	Conformation tensor of macromolecule
C_I	Interaction coefficient
CC	Couette cell
CP	Cone and plate
CNT	Carbon nanotube
D	Rod diameter
D_r	Coefficient of rotational diffusion
$d\mathbf{f}_I$	Differential interaction force
$d\mathbf{T}_I$	Differential interaction torque
E_Y	Young modulus
EPO	Epoxy

$\mathbf{f}_I$	Interaction force
F_z	Normal force
f	Trace of $\mathbf{b}_2^{(m)}$
G’	Storage modulus
G”	Loss modulus
GF	Glass fiber
I_{DC}	Continuous intensity in dichroism
J_m	Bessel function of the mth order
k	Geometrical adimensional factor
k_B	Boltzmann constant
L	Rod length
L_i	Length of the connector i
m	Power-law index
MWCNT	Multi-walled carbon nanotube
n	Rod number density
$\mathbf{n}$	Refractive index
$\mathbf{n}$’	Real part of the refractive index
$\Delta\mathbf{n}$’	Birefringence
N_1	First normal stress difference
N_2	Second normal stress difference
$\mathbf{n}$”	Complex part of the refractive index
P	Hydrostatic pressure
P_C	Contact probability

Pe	Peclet number
PMMA	Poly methyl methacrylate
$\mathbf{p}$	Unit vector parallel to the principal axis of the rod
$\mathbf{p}^{\alpha}$	Orientation vector of the rod α
$\mathbf{p}^{\beta}$	Orientation vector of the rod β
$\dot{\mathbf{p}}$	Time evolution of $\mathbf{p}$
$\dot{\mathbf{p}}^{\alpha}$	Time evolution of the rod α
$\dot{\mathbf{p}}^{\beta}$	Time evolution of the rod β
$\dot{\mathbf{p}}_J$	Time evolution of $\mathbf{p}$ (Jeffery equation)
p_1, p_2, p_3	Cartesian components of $\mathbf{p}$
PB	Polybutene
$\mathbf{q}$	Scattering vector
q	Dimensionless interaction coefficient
R	External radius of the disk in parallel plate geometry
$\mathbf{r}_C^{\alpha}$	Center of mass of the rod α
$\mathbf{r}_C^{\beta}$	Center of mass of the rod β
r	- Radial position
	- Rod aspect ratio
S_B	Boltzmann dissipative contribution
S_{eff}	Effective stiffness
S_L	Lifshitz contribution
S_O	Osanger contribution

s^{α}	Curvilinear coordinate on the rod α
s^{β}	Curvilinear coordinate on the rod β
SEM	Scanning electron microscopy
$\mathbf{T}$	Torque
$\mathbf{T}_I$	Interaction torque
T_r	Period of rotation of a spheroid
T	Absolute temperature
t	Time
TEM	Transmission electron microscopy
$\mathbf{v}$	Velocity vector
$\mathbf{v}^{\infty}$	Velocity vector of the fluid
X_A	Parallel friction coefficient to translation
X_C	Parallel friction coefficient to rotation
Y_A	Perpendicular friction coefficient to translation
Y_C	Perpendicular friction coefficient to rotation
Y_H	Friction coefficient

Greek alphabet

β	Lagrange multiplier
γ_R	Strain evaluated at R
$\dot{\boldsymbol{\gamma}}$	Rate of deformation tensor

$\dot{\gamma}$	Shear rate
$\dot{\gamma}_R$	Shear rate evaluated at R
$\lvert\dot{\gamma}\rvert$	Scalar measure of the rate of deformation tensor
$\Delta\theta$	Numerical step in the θ direction
$\Delta\varphi$	Numerical step in the φ direction
ΔA	Elementary surface
$\Delta\dot{\mathbf{r}}$	Rod relative velocity at the contact point
$\boldsymbol{\delta}$	Identity tensor
δ	Phase angle
$\boldsymbol{\varepsilon}$	Permutation tensor
η	Shear viscosity
η_0	Matrix viscosity
η_r	Relative viscosity
η^*	Complex viscosity
η'	Real part of the complex viscosity
θ	Euler azimuthal angle
$\dot{\theta}$	Velocity in the θ direction
$\boldsymbol{\kappa}^\dagger$	Velocity gradient tensor
$\boldsymbol{\Lambda}$	Mobility tensor
Λ_0	Mobility constant
λ	- Rod form factor - Wavelength

$\mu_1, \mu_2, \mu_3, \mu_4$	Material constants
$\boldsymbol{\sigma}$	Stress tensor
$\boldsymbol{\tau}$	Deviatoric part of the stress tensor
ϕ	Volume fraction
φ	Euler polar angle
$\dot{\varphi}$	Velocity in the φ direction
ψ	Orientation distribution function
$\psi_{\mathbf{p}^\alpha}$	Orientation distribution for the test rod $\mathbf{p}^\alpha$
$\psi_{\mathbf{p}^\beta}$	Orientation distribution for the test rod $\mathbf{p}^\beta$
$\boldsymbol{\Omega}^\infty$	Angular fluid velocity
$\boldsymbol{\omega}$	Antisymmetric part of the velocity gradient
$\boldsymbol{\varpi}^\alpha$	Angular velocity vector of the rod α

LIST OF APPENDICES

CHAPTER 1

1.1 Introduction

Due to their remarkable physical properties, carbon nanotubes (CNTs) are foreseen as the building blocks for the next generation of materials. Many potential applications have been proposed including conductive and high-performance composites, electrochemical devices, hydrogen storage media, chemical sensors, etc. [Baughman *et al.* (2002)].

Despite such potentialities, complications arise in the processability of CNT suspensions and research on issues such as dispersion, orientation and chemical modifications is currently pursued.

CNTs orientation distribution is affected during processing [Jin *et al.* (1998), Rahatekar *et al.* (2009)] and it influences various material properties like bulk rheology [Du *et al.* (2004), Hobbie (2010)], mechanical properties [Thostenson and Chou (2002)], electrical percolation [Du *et al.* (2005)] and thermal conductivity [Zhou *et al.* (2004b), Wang *et al.* (2008)]. Robust methods to quantify and predict the orientation state of CNT systems and to understand the effect of flow on particle orientation are of great interest both academically and industrially [Zhou *et al.* (2004a), Pujari *et al.* (2009a), Pujari *et al.* (2011)].

Furthermore, CNT suspensions present a complex rheological response due to the combination of the CNT high aspect ratios and their colloidal character. Strong shear-thinning behaviour and apparent yield stress are reported in steady simple shear flow [Hobbie (2010)]. When increasing the particle concentration a network is developed, characterized by a well-defined storage modulus and the system behaves like a soft gel [Hough *et al.* (2004), Hobbie and Fry (2007), Khalkhal *et al.* (2011)]. During rest, Brownian motion leads the system to a more isotropic state corresponding to a structural build-up in terms of rheological properties [Khalkhal and Carreau (2012)].

This thesis focuses on the orientation behaviour of CNT suspensions and on their rheological response. Rheological and rheo-optical methods are used to probe experimentally the microstructure evolution of these suspensions. Moreover, two microstructural models are proposed. The first describes the dynamics of dilute suspensions. A detailed description of the individual particle conformation is used and its connection with average microstructural properties is derived. In the second approach, a microstructural model accounting for rod-rod interactions is

derived in order to explain the shear-thinning behaviour and the transient rheology of CNT suspensions.

This manuscript is composed of 8 chapters. A review of the current literature is presented in Chapter 2. The research objectives and a summary of the articles are reported in Chapter 3. Chapter 4 focuses on the rheo-optical study and on the modified two-rod model. The presentation of the rigid-rod model accounting for rod-rod interactions and the comparison of its predictions with rheological data at steady state is reported in Chapter 5, while transient shear flows are examined in Chapter 6. Finally, a general discussion and the final conclusions are contained in Chapter 7 and 8, respectively.

CHAPTER 2 LITERATURE REVIEW

This literature review focuses on the rheology of carbon nanotube suspensions and it is divided in two main sections. The first section describes the rheology of CNT suspensions and in particular, defines the connection between CNT physical properties and their rheological response in suspensions. The second part reports some of the mathematical descriptions available in the literature to model the behaviour of suspension of rod-like particles. We focus on continuum modelling approaches because they are at the base of the models developed in this work. Direct simulations are not analysed here.

2.1 Carbon nanotubes: experimental characterization

Carbon nanotubes (CNTs) come in two varieties, single-wall (SWCNT) or multi-wall (MWCNT). The multi-wall carbon nanotubes were the first to be discovered and they consist of concentric cylinders placed around a common central hollow area with a constant separation between layers similar to the graphite interlayer spacing (~0.34 nm). Each individual cylinder has different helicity with diameter ranging from 2 to 50 nm and length of several microns. Only in 1993, it was found that the addition of metals as cobalt to the graphite electrodes in the arc evaporation method resulted in tubes with a single wall [Iijima and Ichihashi (1993)]. A single wall nanotube is close to an ideal fullerene fiber and consists of a single cylinder extending from end to end with a narrow distribution in diameter range (1 - 2 nm). SWCNTs are usually stronger and they present smaller diameters (of the order of few nanometers) than MWCNTs (with diameters of usually 10-200 nanometers). CNT aspect ratios (length to diameter ratio) range between 30 and 1000.

CNTs have incredible mechanical properties with Young's modulus as high as 1.2 TPa and tensile strength of 50-200 GPa [Qian *et al.* (2002)] which make them the strongest material on earth. Table 2.1 reports a comparison between of physical properties of different carbon materials. It is clear that CNTs offer advantages in terms of thermal and electrical conductivities with respect to the other carbon materials. Thanks to these properties, a wide range of applications are possible like conductive plastics, energy storage materials, catalyst support, air and water filtration, sensing devices and so on [Thostenson *et al.* (2001), Ma *et al.* (2010)].

Table 2.1: Physical properties of different carbon materials [Ma *et al.* (2010)].

Property	Graphite	Diamond	Fullerene	SWCNT	MWCNT
Specific gravity (g/cm^3)	1.9–2.3	3.5	1.7	0.8	1.8
Electrical conductivity (S/cm)	$4 \cdot 10^3{}_p$, 3.3_c	10^{-2}-10^{-15}	10^{-5}	10^2-10^6	10^3-10^5
Thermal conductivity (W/(m K))	298_p, 2.2_c	$(0.9\text{-}2.3) \cdot 10^3$	0.4	$6 \cdot 10^3$	$2 \cdot 10^3$
Thermal expansion coefficient (K^{-1})	$-10^{-6}{}_p$, $2.9 \cdot 10^{-5}{}_c$	$(1\text{-}3) \cdot 10^{-6}$	$6.2 \cdot 10^{-5}$	Negligible	Negligible
Thermal stability in air (°C)	$(4.5\text{-}6.5) \cdot 10^2$	$<6 \cdot 10^2$	$\sim 6 \cdot 10^2$	$>6 \cdot 10^2$	$>6 \cdot 10^2$

p: in-plane; c: carbon-axis

The rheological properties of CNT/polymer suspensions play a crucial role in processing and manufacturing of composites. However, CNT suspensions rheology is a complex subject since these slender colloidal particles present rheological features between those of rigid rod suspensions and semi-flexible polymers. The rheological behavior of CNT suspensions is a function of concentration, aspect ratio, dispersion and orientation state [Fan and Advani (2007)]. These different aspects are examined in the following sections.

2.1.1 Dispersion of CNTs

In order to achieve the full potential of CNTs as reinforcements, it is necessary to obtain a good degree of dispersion. The entangled CNTs agglomerates produced by synthesis must be broken down to disperse CNTs homogeneously in the polymer matrix [Song and Youn (2005)]. Due to their large aspect ratios and strong van der Waals interactions, the dispersion of CNTs into

polymers is a very challenging task and has been the main bottleneck to the industrial employment of CNTs.

These difficulties can be easily understood by comparing ideal dispersions of micro and nano scale fillers in a polymer matrix at the same volume fraction (0.1 vol.%) as shown in Figure 2.1.

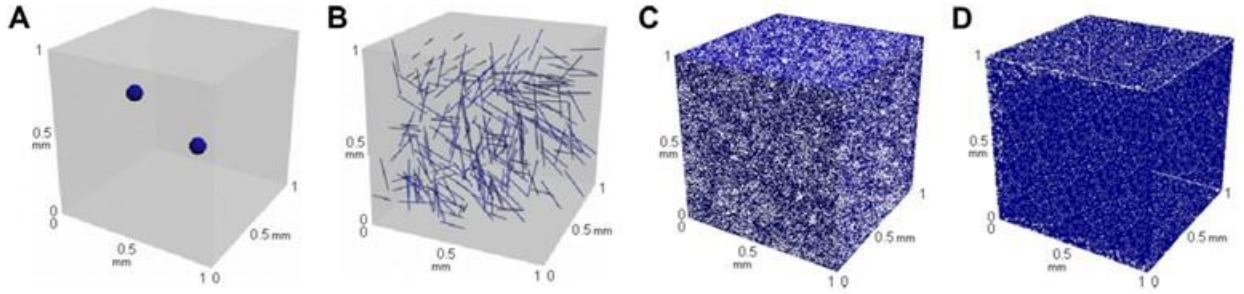

Figure 2.1 Distribution of micro and nano scale fillers of the same 0.1 vol.% in a reference volume of 1 mm^3 (A: Al_2O_3 particle; B: carbon fiber; C: GNP; D: CNT) [Ma *et al.* (2010)].

In the case of the micro size fillers (cases A and B in Figure 2.1), particles can be easily distinguished. For nanoparticles like graphene nanoplatelets (GNPs) and CNTs (cases C and D in Figure 2.1), the microstructure is completely different. A complex network is formed in the medium where individual nanoparticles cannot be isolated. Interactions between particles are frequent and in the case of poor interfacial properties with the polymer counterpart, re-aggregation phenomena may occur. This simple observation sheds some lights on the difficulties related to nano filler dispersion in composites.

Several techniques have been employed to disperse CNTs in polymeric matrices such as twin screw extrusion [Prashantha *et al.* (2009)], micro-compounding [Abdel-Goad and Pötschke (2005)], melt mixing in internal mixer [Abbasi *et al.* (2009a)], three roll milling [Khalkhal *et al.* (2011)], sonication etc. The method chosen depends on the viscosity of the matrix and on the operating conditions. The idea behind all these techniques is to take advantage of high shear and elongational stresses to break down the CNT agglomerates. At the lab scale, the three roll mill machines has been successful in achieving fine dispersions with thermoset polymers, however this tool is not yet applicable to thermoplastic polymers [Schulz *et al.* (2011), Khalkhal *et al.* (2011), Olowojoba *et al.* (2013)].

As an alternative to direct mixing, the use of solvents can improve the quality of dispersion since solvents reduce the viscosity of the medium and facilitate the diffusion of particles. However, after mixing, the solvent needs to be removed, which is time consuming and non-environmentally friendly. In addition, the separation process of the solvent becomes more difficult with increasing filler content and some residual trace of solvent can remain in solution. This could affect the rheological properties of the suspension [Khalkhal (2012)].

Another possibility to improve the CNT dispersion is to modify chemically or physically the nature of carbon nanotube surface [Lee *et al.* (2007)]. This route will not be analyzed in detail here since it was not investigated in this work. However, a concise presentation of most common approaches is reported since its great importance in manufacturing nano-composites.

Chemical functionalization of CNTs is a mean to improve the affinity between CNTs and the polymer matrix. The attachment of functional entities on the CNT sidewalls is associated with a change of hybridization from sp^2 to sp^3 and a loss of π-conjugation on the graphene layer. This structural change can be obtained with the use of molecules with high chemical activity, such as fluorine [Mickelson *et al.* (1998)]. The C-F bonds in the fluorinated CNT can be replaced by amino, alkyl and hydroxyl groups [Touhara *et al.* (2002), Stevens *et al.* (2003)]. In addition to fluorination of CNTs, similar methods, including cycloaddition [Tagmatarchis and Prato (2004)], chlorination, bromination [Unger *et al.* (2002)], hydrogenation [Kim *et al.* (2002)] and others, have also been employed in the recent years. Attachment of oxygen containing functional groups (carboxyl, carbonyl, hydroxyl groups, etc.) on the surface of CNTs could be achieved by applying several oxidative processes such as strong acids (HNO_3, H_2SO_4) or a mixture of them [Esumi *et al.* (1996), Lee *et al.* (2007)], ozone [Sham and Kim (2006)] or reactive plasma [Wang *et al.* (2009), Ávila-Orta *et al.* (2009)]. It is well known that carboxylic and hydroxyl groups can be used as precursors for successive modifications specific to the nature of the bulk polymer chosen.

However, functionalization has large drawbacks since modification of CNT surface morphologies causes defect formations which have detrimental consequences on the CNT mechanical and transport properties. In extreme cases, functionalization can break down the tubes and, hence, decrease their length (and aspect ratio).

Therefore, physical compatibilization is an interesting alternative to tune interfacial properties of nanotubes. Small-molecule surfactants that naturally form rod-like micelles in aqueous solutions [Wenseleers *et al.* (2004)] or wrapping polymers such as DNA [Badaire *et al.* (2005)] have been used to disperse CNTs, but their effectiveness decreases markedly with increasing nanotube concentration. In addition, surfactants generally reduce the electrical conductivity of the network by several order of magnitude [Hobbie (2010)].

Different dispersion states lead to different rheological and mechanical behaviors. Du *et al.* (2004) examined the effect of dispersion of single-walled carbon nanotubes (SWCNTs) in poly(methyl methacrylate) (PMMA). They produced three SWCNT/PMMA suspensions of different dispersions quality at the same concentration. They found that nanotubes dispersion impacts the viscoelastic properties of the resulting nanocomposites. The best dispersed samples presented higher values of the storage modulus, *G*', and a plateau at low frequencies in small amplitude oscillatory shear, SAOS, which suggests the formation of a network.

Huang *et al.* (2006) worked with MWCNTs in polydimethylsiloxane (PDMS). The samples were dispersed using an Ika Labortechnik mixer with rotation speed of the paddle of 1000 rpm and temperature of ~30 °C. The main objective of their work was to develop an alternative rheological method to monitor the dispersion state. First, they studied the effect of mixing time on the reproducibility of rheological data. The rheological measurements presented an erratic behavior for short mixing times but after a certain period of mixing, called the "characteristic or critical time", these erratic values turned to a plateau value as shown for the real part of the complex viscosity in Figure 2.2. The characteristic time increased with CNT loading but overall, such change in viscosity with mixing time occurred for all the mixtures investigated.

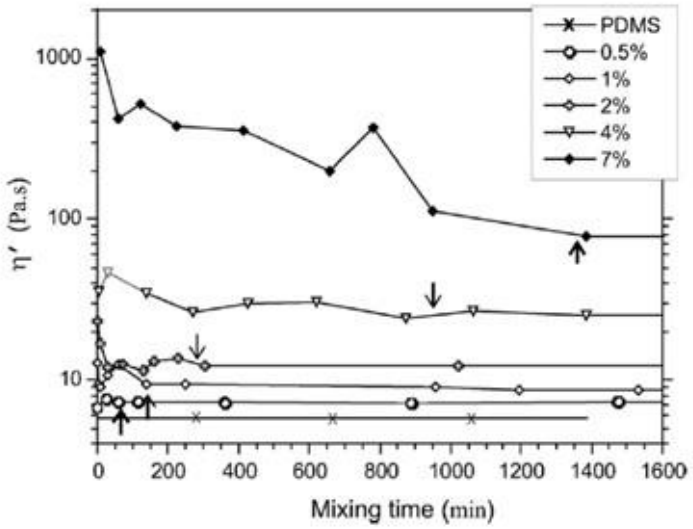

Figure 2.2 Real part of the complex viscosity, η', at 50 Hz, against time of mixing, for a range of different weight fractions of nanotubes. The arrows mark the critical time for each concentration [Huang *et al.* (2006)**]**.

Huang *et al.* (2006) suggested that the reason behind the large discrepancies in the rheological percolation threshold reported in the literature might arise from two distinct possibilities. First, when the suspension is mixed for longer time than its characteristic time, one may reach or exceed the percolation threshold by forming a well dispersed and homogenous network of nanotubes. Hence, the rheological response would become that of an elastic solid. Second, mechanical (rheological) percolation could take place when individual aggregates, or tube clusters at mixing time lower than the characteristic time, come into contact and form chains of aggregates through the medium. This second type of aggregate-mediated jamming may be responsible for much higher threshold concentrations.

An empirical method suggested to quantify nanotube dispersion is the evolution of the peak of the loss factor, tan(δ), with increasing mixing time as shown in Figure 2.3 for samples of 7 wt % CNT in PDMS.

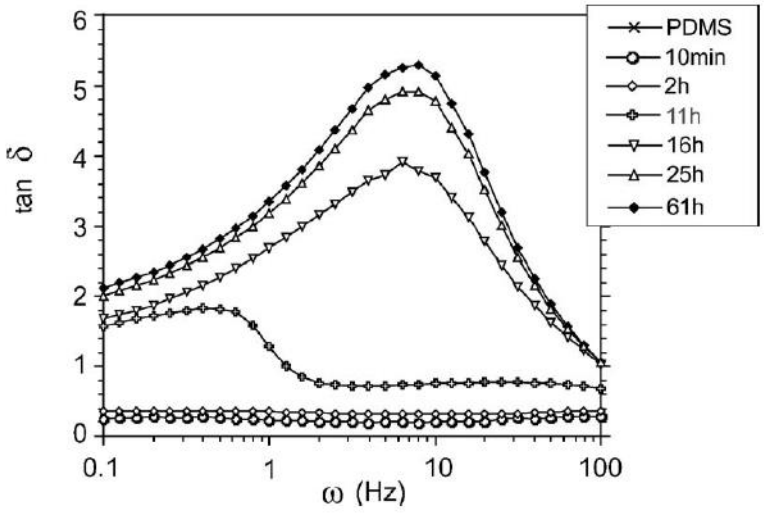

Figure 2.3 Data for tan (δ) against frequency for 7 wt % CNT-PDMS samples mixed for different times (tested immediately after mixing) [Huang *et al.* (2006)**]**.

This type of behavior was also confirmed for a suspension of 4 wt % CNTs. Huang et al. (2006) findings demonstrated that rheological measurements can be used as probe for the dispersion state. However, the authors did not show direct or indirect observations of their systems microstructure after such long mixing time (for a 7 wt % CNT suspension, the required mixing time is of about 23h). Furthermore, the characterization of the nanotubes dispersion is also a difficult process due the length scale involved in nano composites. The most common techniques used are: optical and confocal microscopy, scanning electron microscopy (SEM) and transmission electron microscopy (TEM). A superficial evaluation of the dispersion can be performed by optical microscopy. The quality of the dispersion can be qualitatively studied by uniformity of light intensity when viewed in transmission mode, where heterogeneities in nanotubes density are apparent at size scales greater than ~10 μm [Du *et al.* (2004)]. Dispersion at a finer length scale can be probed by imaging fracture surfaces of nanocomposites using SEM or on ultramicrotomed surfaces with TEM. However, these techniques require samples in the solid state.

2.1.2 Rheology of CNT suspensions

The rheology of CNT suspensions is of fundamental importance for the design and optimization of any processing scheme. CNT suspensions present a complex rheological behavior due to their quasi unidimensional structure, their colloidal character and the attractive van der Waals forces acting

on the rods. In addition, the high aspect ratio of these particles, when coupled with inter-particle attraction and Brownian motion, often favors the formation of rigid-rod networks or gels at remarkably low concentrations [Hough *et al.* (2004), Hobbie (2010)].

The rheological response of colloidal rod like particles in suspensions is strongly dependent on the regime of the concentration probed. Three concentration regimes have been defined in the literature for rod-like particles: dilute, semi-dilute and concentrated regime [Doi and Edwards (1986)].

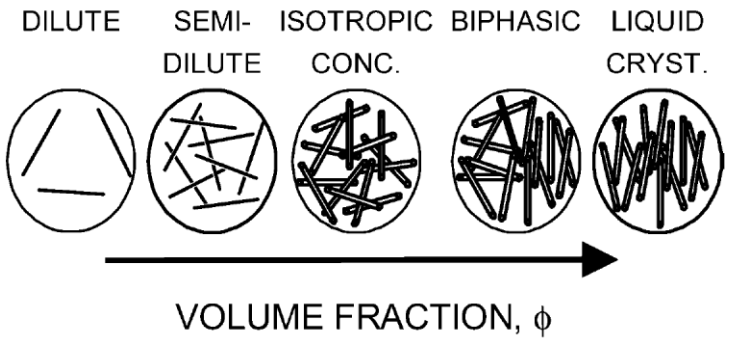

Figure 2.4 Phase behavior of a suspension of Brownian rigid rods [Doi and Edwards (1986)].

The dilute regime is defined by the constraint: $nL^3 \leq 1$ where *n* is the number density of the particles and *L* is the length of the rod. This ensures that the individual rods are able to rotate freely. The semi-dilute regime is limited between $nL^3 >> 1$ and $nL^2D \leq 1$ and the shear viscosity varies as a quadratic function of the concentration. These constrains imply that rods can overlap. Since the volume fraction is still sufficiently low, the static properties are not influenced by the excluded volume interaction being of the order of L^2D, but the dynamical ones are. At concentration higher than $nL^2D > 1$ multiple particle interactions are more frequent and terms which depends on powers of the volume fraction higher than 2 become more and more important. For Brownian rod-like particles interacting only with excluded volume effects, there will be a critical concentration at which the system will spontaneously form first a biphasic phase, where there will be coexistence of domains with an isotropic and aligned orientation state and, then, a complete nematic phase (liquid crystal) (Figure 2.4).

The effect of nanotube concentration can be clearly observed in small angle oscillatory shear (SAOS). Because of attractive forces and Brownian motion, the increase of concentration brings

the establishment of a CNT network through the system, accompanied with a transition from liquid to solid like behavior [Du *et al.* (2004), Pötschke *et al.* (2004), Abdel-Goad and Pötschke (2005), Fan and Advani (2007)]. This can be appreciated by analyzing the moduli and/or complex viscosity versus frequency. In particular, the appearance of a plateau at low frequencies of the storage modulus is a noticeable sign of the liquid to solid-like transition as shown in Figure 2.5.

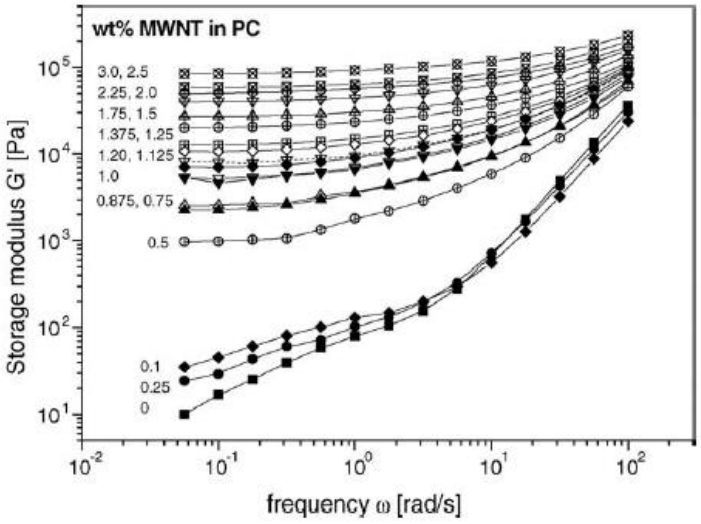

Figure 2.5 Storage modulus, G', of PC and PC/MWCNT composites as a function of frequency [Abdel-Goad and Pötschke (2005)**]**.

The onset of the solid like behavior has been explained as the concentration at which the size of polymer chains is larger than the separation between the nanotubes [Du *et al.* (2004)] or as the concentration when the polymer chain entangles with the CNTs to create a network [Pötschke *et al.* (2004)].

Abbasi *et al.* (2009a) reported similar results for MWCNTs and polycarbonate systems. The low frequency values of complex viscosity (Figure 2.6) significantly increase with the addition of MWCNTs indicating that the long polymer chain relaxation in the nanocomposites is effectively restrained by the presence of the nanotubes. Shear-thinning behavior also appears progressively.

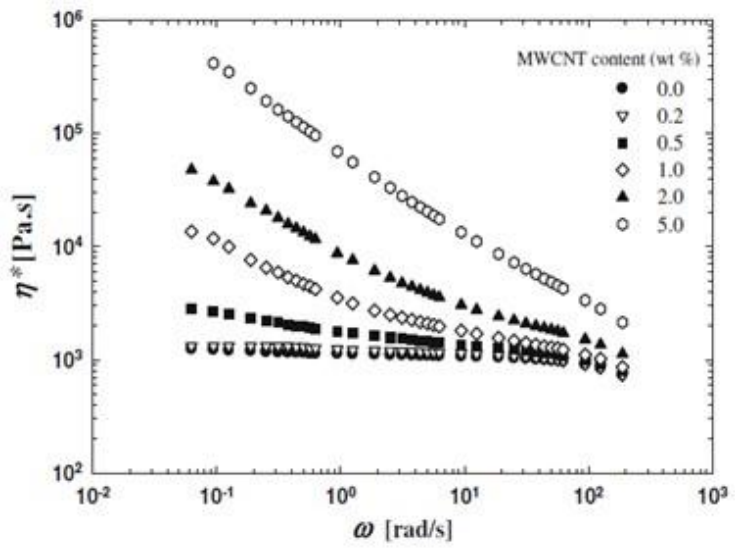

Figure 2.6 Complex viscosity of polycarbonate/MWCNTs as a function of frequency at 230 °C [Abbasi *et al.* (2009a)**]**.

The dependence of *G*' on ω at low frequencies becomes very weak as the concentration of MWCNTs increases (as showed in Figure 2.7). Increasing the filler content, nanotube-nanotube interactions become dominant and the percolated network restrains the long range motion of the polymer chains. At high frequencies the effect of the nanotubes on the rheological behavior is relatively weak. This behavior suggests that CNTs do not significantly affect the short-range dynamics of the polymer chains [Du *et al.* (2004)]. Similar rheological behavior have been observed by many authors: Du *et al.* (2004), Meincke *et al.* (2004), Fan and Advani (2007), Lee *et al.* (2007), etc.

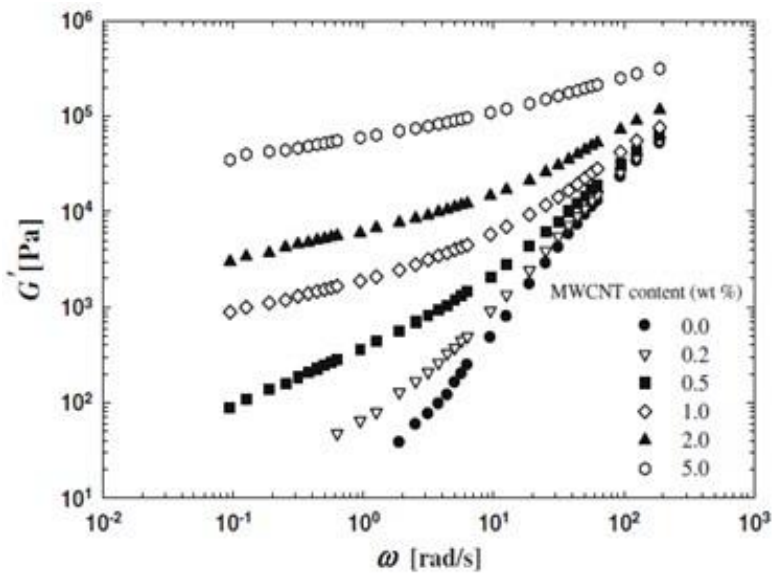

Figure 2.7 Storage moduli of polycarbonate/MWCNT as a function of frequency at 230 °C [Abbasi *et al.* (2009a)**]**.

The presence of a network can also be verified by electrical/thermal conductivity analysis and a comparison with the rheological data could help understanding the effects on the microstructure. Generally, polymers are really good insulators but the presence of a conductive filler such as CNTs can modify the conductivity of the system by different orders of magnitude. Du et al. (2004) compared the effect of SWCNT loading in poly (methyl methacrylate) (PMMA) on the rheological and electrical properties as reported in Figure 2.8.

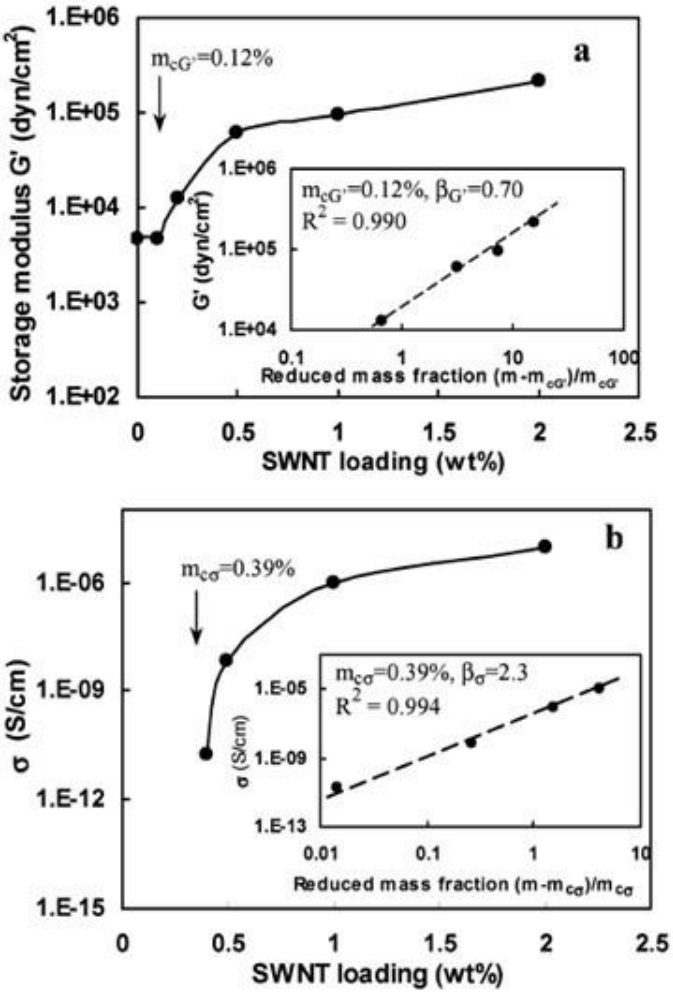

Figure 2.8 (a) Storage modulus, G', of SWCNT/PMMA nanocomposites as a function of the nanotube loading at a fixed frequency of 0.5 rad/s. Insert: a log-log plot of *G*' vs reduced mass fraction. (b) Electrical conductivity, σ, of SWCNT/PMMA nanocomposites as a function of the nanotube loading. Insert: a log-log plot of electrical conductivity vs reduced mass fraction. Note that β_σ is significantly larger than β_G, due to the larger magnitude of the change in $\boldsymbol{\sigma}$ at the threshold [Du *et al.* (2004)**]**.

Figure 2.8 (a) shows that G' increases drastically between 0.1 and 0.2 wt% loading, indicating a sudden change in the material structure, typical of a percolated system. Similar changes can be observed in the electrical conductivity. However, the sharp change appears only at larger loading values ~0.4 wt% (Figure 2.8 (b)). Different tube-tube distances are required for rheological and

electrical percolation. In this particular system, assuming valid the electron hopping mechanism, the rod-rod distances required to create a conductive path in the medium are ~5 nm. To have rheological percolation, the nanotube network needs to restrain polymer motion and this requires that the rod-rod distances are at least comparable to the diameters of random coils of polymer chains, which in this case are equal to ~18 nm. Thus, higher nanotubes content is needed to reach the electrical conductivity threshold due to the shorter distances required [Du *et al.* (2004)].

Because of their high aspect ratio, CNTs should be the ideal candidates for the formation of a lyotropic nematic liquid crystal. Unfortunately, this entropically driven phase is really hard to achieve because of the polydispersity in particle aspect ratios and of attractive interactions that have the effect of widening the biphasic regime. Lyotropic liquid crystalline formation was reported for SWCNTs dispersed in superacids [Davis *et al.* (2003)], stabilized with DNA [Badaire *et al.* (2005)] or dispersed in conjugated polymers [Lee *et al.* (2009), Allen *et al.* (2013)]. Figure 2.9 shows an example of a liquid crystalline phase of SWCNT in a conjugated polymer obtained by Allen *et al.* (2013).

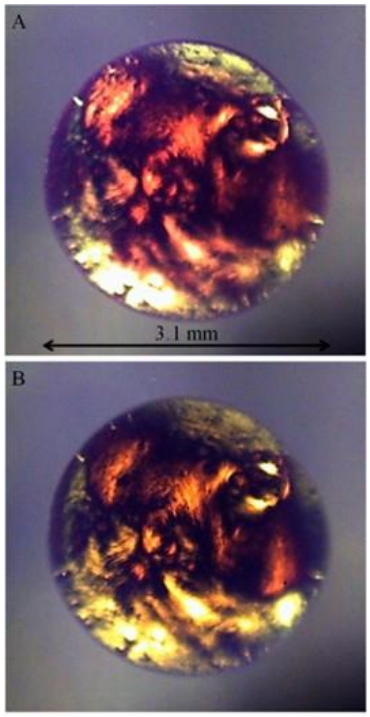

Figure 2.9 Evaporation of a drop of SWCNT/poly (3-hexylthiophene) (1:1) in 1, 2-dichlorobenzene placed between crossed polarizers. The change in light intensity represent the different aligned domains. (A) Before and (B) after evaporation [Allen *et al.* (2013)].

Such liquid crystal state could improve the processing of concentrated CNT suspensions, owing to the mutual spontaneous alignment and the reduced shear viscosity of the nematic phase [Davis *et al.* (2003)]. However, for the reasons cited above, a dense and isotropic network seems to be the most common high-concentration scenario [Hobbie (2010)].

Recently, Khalkhal and Carreau (2012) studied the non-linear rheological response of MWCNTs in a Newtonian epoxy matrix. By applying a constant shear rate to a CNT suspension, the shear stress present a clear overshoot at very low strains [Pujari *et al.* (2011)].

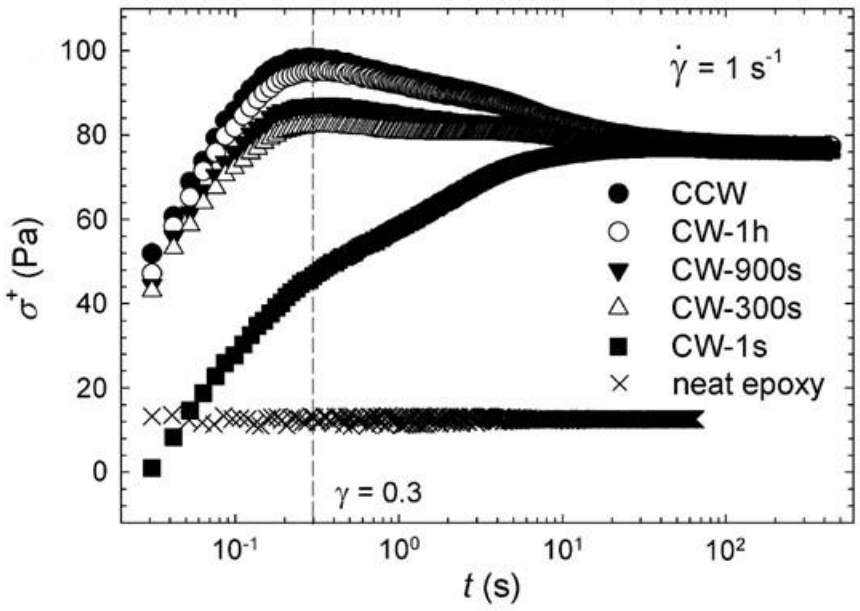

Figure 2.10 Transient stress data of a 2wt% MWCNT/epoxy suspension at shear rate of 1 s^{-1} [Khalkhal and Carreau (2012)].

By applying two consecutive stress growths, the overshoot in the shear stress disappears if no rest time is allowed between the two tests. If a certain rest time is allowed between two consecutive stress growths, the overshoot reappears again and its intensity is proportional to the duration of the rest time [Khalkhal and Carreau (2012)]. During rest, the system keeps evolving thanks to Brownian motion which helps to reform the network. This can be clearly observed by analyzing the storage modulus after a shearing step. *G*' decreases by increasing the shear rate until a critical shear rate is reached, however during rest, the network in the system is slowly restored.

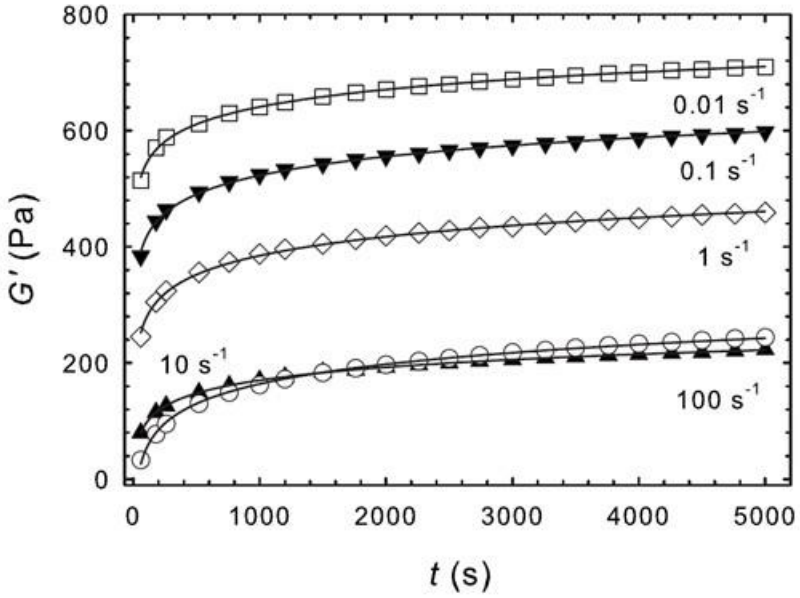

Figure 2.11 Development of *G*' at 1 rad/s for a 2 wt% MWCNT/epoxy suspension after cessation of shear flow for different shear rates [Khalkhal *et al.* (2011)].

This behavior was also reported for nano-clays platelets by Mobuchon *et al.* (2009a). However, the full understanding of this structure build-up is not clear. Pujari *et al.* (2011) studied the microstructure evolution of concentrated MWCNT suspensions with small and wide angle x-ray scattering (SAXS and WAXS). Their rods were essentially non Brownian. During rest they monitored the x-ray scattering and calculated the anisotropy factor (AF) relative to the scattering patterns. The anisotropy factor is defined as

$$AF = \sqrt{\left(\langle q_i q_i \rangle - \langle q_j q_j \rangle\right)^2 + 4\langle q_i q_j \rangle^2} \qquad (2.1)$$

where **q** is the scattering vector. The *AF* quantifies the degree of anisotropy in the 2D scattering patterns. They observed a fast change of *AF* at short time scale which was not possible to correlate with the low diffusion coefficient of their systems (Figure 2.12). Hence, they hypothesized that a portion of the shear-induced orientation was lost due to an elastic deformation of the rods within highly entangled clusters. Upon flow cessation the elastic energy stored during flow was released causing the fast change in *AF*. In more dilute samples, they did not observe such behavior and, hence, they attributed it to the presence of elastic clusters in concentrated systems [Pujari *et al.*

(2009a)]. This implies that the flexibility of these rods plays an important role in their suspension dynamics [Switzer III and Klingenberg (2003)].

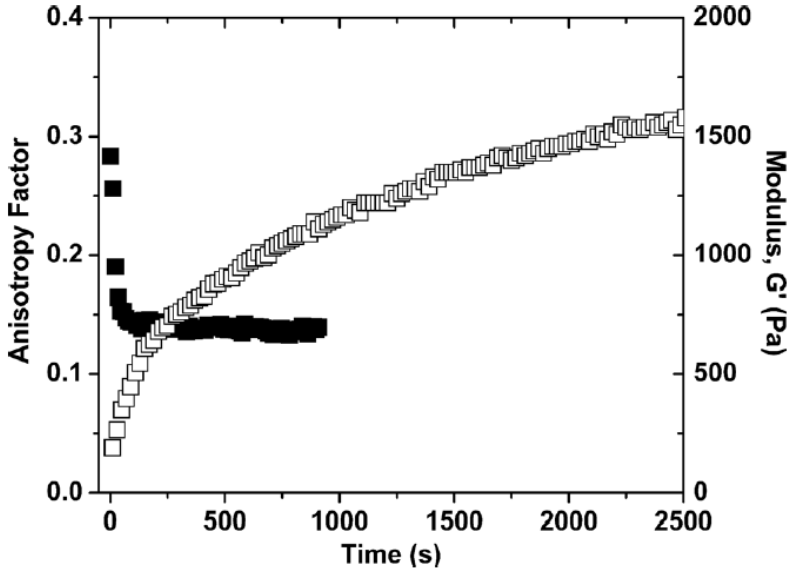

Figure 2.12 Anisotropy factor (filled symbols) and storage modulus (empty symbols) for a 2 wt% MWCNT suspension measured following flow cessation of steady shear at 200 s^{-1} [Pujari *et al.* (2011)]

In addition, Pujari *et al.* (2009a) and Pujari *et al.* (2011) reported progressive alignment of the rods in the flow direction by increasing the shear flow intensity. This shear-induced alignment was previously reported in the innovative work of Fry *et al.* (2006) where they probed the microstructure with a modulation polarization technique. Single- and multi-walled CNTs were analyzed in dilute and semi dilute regimes. Birefringence ($\Delta n'$) and dichroism ($\Delta n''$), respectively the real and complex parts of the refractive index tensor, were analyzed.

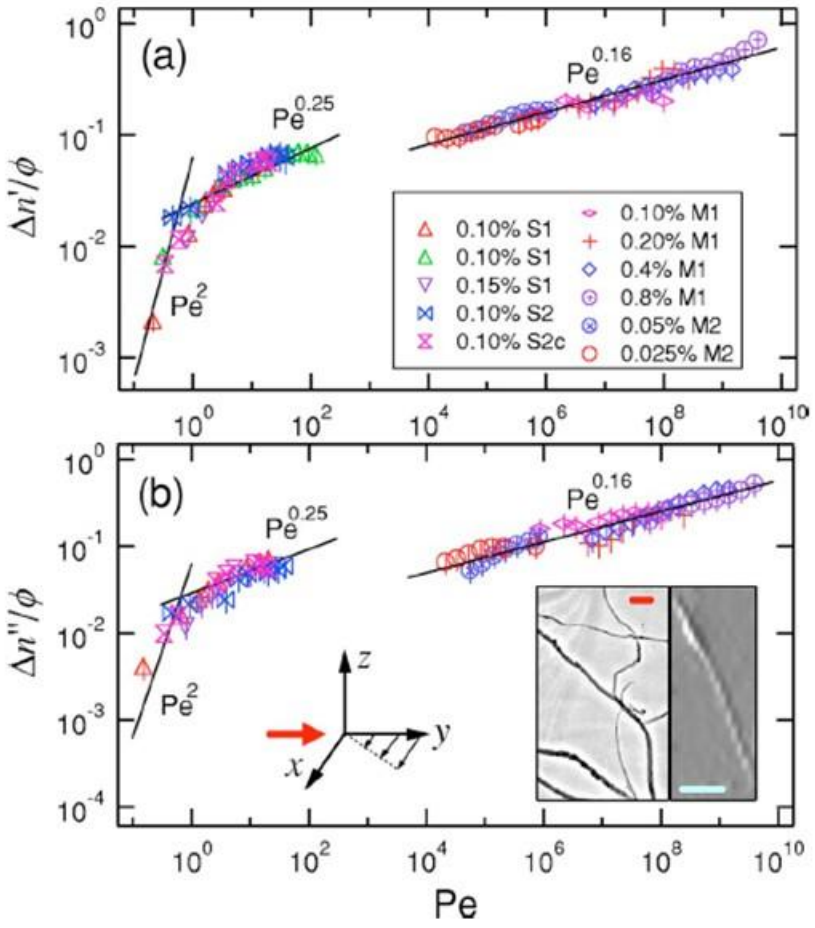

Figure 2.13 Scaled birefringence (a) and dichroism (b) as a function of Peclet number. The solid lines represent power-law fits as indicated. The left inset show a TEM of MWCNT (scale bar of 250 nm). The right inset is an AFM image of SWCNT (scale bar of 150 nm) [Fry *et al.* (2006)].

They found that the overall degree of alignment was proportional to Pe^2 in the range of small Pe for dilute suspensions and in semi-dilute suspensions for Pe<200 it scaled as $Pe^{0.25}$ as shown in Figure 2.13. These findings are in good agreement with the Doi and Edwards (1986) theory for rigid rods. In the limit of infinite Pe (Pe between 10^5 and 10^{10}), the scaled birefringence and dichroism increased as $Pe^{0.16}$. This response is weaker compared with the exponent (0.25) found at lower Pe, suggesting that rod deformation might influence the orientation behavior of these suspensions.

2.1.3 Flow induced microstructure

Flow can create anisotropic organization of suspending particles if interactions between particles are comparable to hydrodynamic forces [Vermant and Solomon (2005)]. When external shear stresses are applied to the suspension, mechanical entanglements and flow-induced clustering can be observed [Hobbie and Fry (2007), Rahatekar *et al.* (2006b)]. In the case of CNT suspensions, different types of microstructures have been reported as function of the shear stress by Hobbie and Fry (2006). When a certain stress is applied to a network structure, the network is gradually destroyed and fragmented into clusters (or flocs) that then flow as microscopic bodies. Increasing the shear stress or shear rate, the size of these aggregates decreases and, eventually, the scale of an individual nanotube is approached. This breakup can be quantitatively appreciated by analyzing the shear-thinning effect in steady state viscosity and a critical stress for homogenization, σ_c, can be defined as the shear stress corresponding to the state when clusters are visually absent from the suspension at the microscopic scale. Before reaching the critical stress, Hobbie and Fry (2006) found that the suspension passed through a series of states with different morphologies. The phase diagram is showed in Figure 2.14, the onset of full dispersion corresponds to the vertical line $\sigma/\sigma_c = 1$: on the left extreme, there is an isotropic elastic network (*I*) while on the right extreme there is a fully dispersed flow aligned (*N*) state. From the left side, one finds a fragmented network, vorticity banding, and isolated aggregates denoted in the sequence defined by increasing shear rate or shear stress, while to the right of the onset of full dispersion, the suspension consists entirely of flow-aligned individual nanotubes.

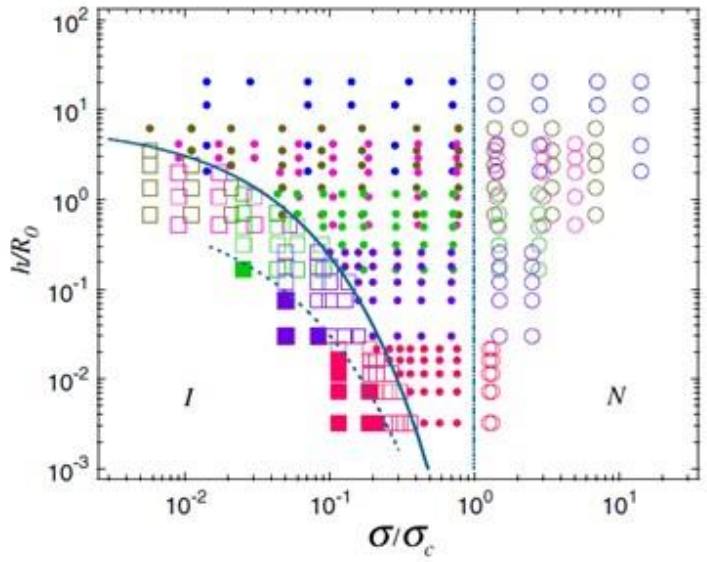

Figure 2.14 Scaled "phase diagram" describing the evolution from a solid-like disordered network (*I*) to a flowing nematic (*N*) for MWCNTs suspended in a low molecular weight polymer solvent, where concentration increases from top to bottom. Open circles are (para)nematic, closed circles are isolated aggregates, open squares are vorticity bands, and closed squares are cavitated networks. The vertical dashed line marks the stability limit. Colors denote MWNT mass concentration; blue (0.025%), brown (0.1%), pink (0.4%), green (0.85%), purple (1.7%), and magenta (3%). The parameter *h* denotes gap and R_0 represents the mean aggregate size in the limit of large gap and weak shear [Hobbie and Fry (2006)].

Rheo-optical studies can be used to understand better the formation mechanism of these flow-induced states, as reported by Ma *et al.* (2007). They studied MWCNTs in an epoxy matrix using a strain-controlled rheometer with 50 mm parallel plates and a gap size of 130 μm. While the suspensions were sheared, optical micrographs were taken to study the microstructures (Figure 2.15).

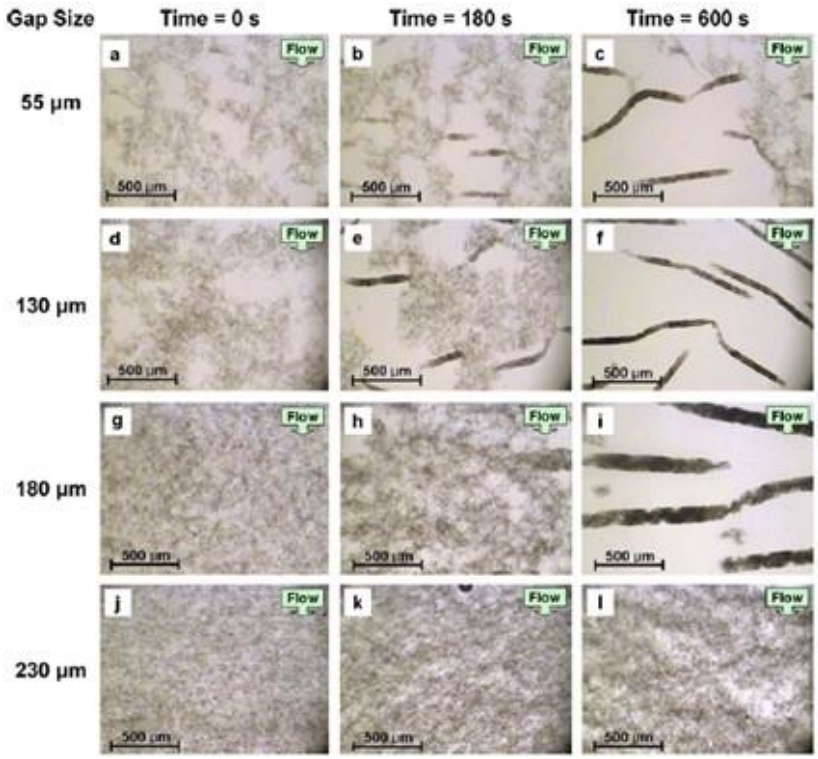

Figure 2.15 The effect of time and gap size on the formation of helical bands (HBs). The shear rate for all conditions was fixed at 0.5 s^{-1}. Direction of flow is vertical as indicated [Ma *et al.* (2007)].

With the application of shear, collisions occurred between CNTs and diffuse aggregate structures were interlocked to progressively form helical bands (HBs) aligned perpendicularly to the direction of flow as shown in the time evolution series of Figure 2.15 a, b and c. The gap size at which the shear is applied influences both the formation kinetics and the final diameter of the HBs. Applying shear rate of 0.5 s^{-1} , HBs were formed within a shear time of 600 s, for gaps lower than 180 μm. However at a gap of 230 μm, no clear HB structure was created. Thus, the confining effect of the gap plays an important role in the formation of such anisotropic structures. Hence, the presence of HBs may be derived from a mechanical and geometrical mechanism rather than being of rheological origin as proposed by Lin-Gibson *et al.* (2004). Ma *et al.* (2007) also observed that at high shear rate, the HBs, formed in the vorticity direction, broke up in a less clearly defined state that was aligned predominantly in the shear direction. The breakup of HBs in separated aggregates and the consequent alignment came with a certain shear thinning behavior of the suspension. However, during the change in microstructure from isotropic aggregates to HBs, no effects on the

shear stress measurements were registered. From a rheological perspective, the formation of HBs is accompanied with negative normal stress differences which have a relevant importance in processes such as extrusion, where the problematic of die swelling could be potentially minimized. The nematic state (right side of the phase diagram in Figure 2.14) is due to the alignment effect of the shear flow and it is named paranematic [Hobbie (2010)].

Different indirect techniques, commonly used with polymers, have been adopted to characterize the CNT orientation state. Jin *et al.* (1998) determined orientation and the degree of alignment by x-ray diffraction, Bhattacharyya *et al.* (2003) applied Raman spectroscopy and Hobbie *et al.* (2003) used polarized optical measurements of CNT orientation in sheared MWCNT/water suspensions. Direct measurements imply the use of SEM and/or TEM to characterize the alignment of the CNTs in the composite. This type of approach was used by Fan and Advani (2005) for a suspension of multi walled carbon nanotubes and vinyl ester resin. The suspension was subjected to shear flow in a micro channel, a nano-channel and across a micro cylinder and the microstructure was analyzed by TEM to observe CNT positions directly inside a composite sample. Second order orientation tensors were used to quantify the orientation state of the nanotubes at a selected location. The degree of MWCNTs alignment increased with shear rate and it was found much higher in the nano-channel than in the micro channel.

2.2 Continuum modeling of rod-like suspensions

Many studies on modeling of the rheological behavior of rod-like particle suspensions are available in the literature. A good starting point is to consider a single rigid rod immersed in a Newtonian fluid. In spherical coordinates, the orientation of a rigid rod can be described by a unit vector oriented along the symmetry axis of the particle, as shown in Figure 2.16.

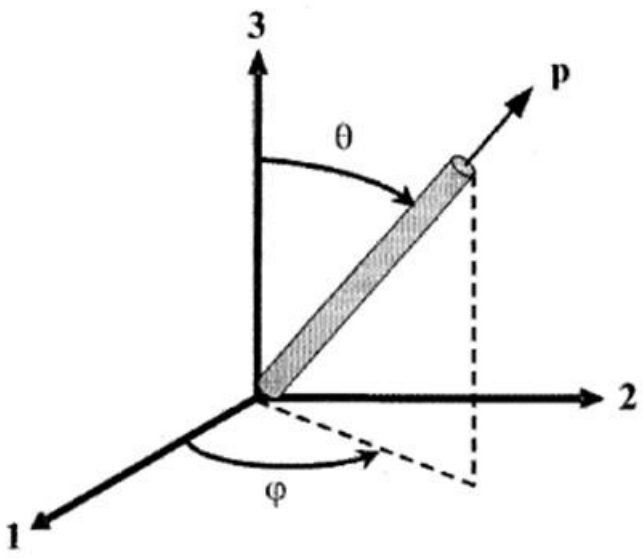

Figure 2.16 Orientation of a rigid rod described by the unit vector **p** in the principal direction of the symmetry axis of the rod.

The Cartesian components (p_1, p_2, p_3) of the unit vector **p** can be written as

$$\begin{aligned} p_1 &= \sin(\theta)\cos(\varphi) \\ p_2 &= \sin(\theta)\sin(\varphi) \\ p_3 &= \cos(\theta) \end{aligned} \tag{2.2}$$

2.2.1 Jeffery model

Jeffery (1922) solved the velocity field around a single rigid ellipsoidal particle immersed in a Newtonian fluid with negligible inertia. As boundary conditions, the no-slip condition at the particle surface and unperturbed flow field far away from the particle were used. In absence of external couples, the time evolution of the unit vector is

$$\frac{D\mathbf{p}}{Dt} = \dot{\mathbf{p}}_J = -\frac{1}{2}\boldsymbol{\omega}\cdot\mathbf{p} + \frac{\lambda}{2}\left(\dot{\boldsymbol{\gamma}}\cdot\mathbf{p} - \dot{\boldsymbol{\gamma}} : \mathbf{ppp}\right) \tag{2.3}$$

where $\boldsymbol{\omega} = \boldsymbol{\kappa} - \boldsymbol{\kappa}^{\dagger}$ and $\dot{\boldsymbol{\gamma}} = \boldsymbol{\kappa} + \boldsymbol{\kappa}^{\dagger}$ are, respectively, the vorticity and rate of deformation tensors with $\boldsymbol{\kappa}^{\dagger}$ the gradient of the velocity. λ is the form factor of the particle and is defined as

$$\lambda = \frac{r^2 - 1}{r^2 + 1} \tag{2.4}$$

with *r* being the particle aspect ratio. This equation implies that an ellipsoidal particle continuously tumbles under the effect of shear flow. Its period of rotation, T_r, is a function of the aspect ratio and of the shear rate, $\dot{\gamma}$, applied: $T_r = 2\pi\dot{\gamma}^{-1}\left(r + r^{-1}\right)$. For a rod of infinite aspect ratio, the period of rotation tends to infinity since the rod, during its rotation, will spend an infinite time aligned in the flow direction [Dinh and Armstrong (1984)].

2.2.2 Folgar and Tucker model

Increasing the concentration of the rods in the system, interactions between particles influence their dynamics. To account for these effects, Folgar and Tucker (1984) introduced a phenomenological diffusion factor in the Jeffery equation

$$\frac{D\mathbf{p}}{Dt} = \dot{\mathbf{p}} = -\frac{1}{2}\boldsymbol{\omega}\cdot\mathbf{p} + \frac{\lambda}{2}\left(\dot{\boldsymbol{\gamma}}\cdot\mathbf{p} - \dot{\boldsymbol{\gamma}} : \mathbf{ppp}\right) - C_I\left|\dot{\gamma}\right|\frac{\partial}{\partial\mathbf{p}}\ln\psi \tag{2.5}$$

where ψ is the rod orientation distribution function and C_I is a coefficient which controls the intensity of the perturbation of the rotary velocity due to particle interactions. $\partial/\partial\mathbf{p}$ is the vector operator producing a gradient on the surface of the unit sphere

$$\frac{\partial}{\partial\mathbf{p}} = \boldsymbol{\delta}_\theta\frac{\partial}{\partial\theta} + \boldsymbol{\delta}_\varphi\frac{1}{\sin(\theta)}\frac{\partial}{\partial\varphi} \tag{2.6}$$

where $\boldsymbol{\delta}_\theta$ and $\boldsymbol{\delta}_\varphi$ are unit vectors in spherical coordinates in θ and φ directions, respectively. The quantity $C_I\left|\dot{\gamma}\right|$ plays a similar role to the diffusivity, D_r, in rotary Brownian motion and the effect of introducing the phenomenological coefficient is equivalent to reduce the orientational anisotropy in the system. Much discussion can be found in the literature regarding the functionalities of the parameter C_I. Bay (1991) proposed this empiric expression

$$C_I = A\exp\left(-Br\phi\right) \tag{2.7}$$

where ϕ is the volume fraction and *A* and *B* are two numerical constants. The functionalities were obtained by fitting experimental data from injection molding with the components of the second order moment of the orientation distribution, $\mathbf{a}_2$. In particular, Bay (1991) found *A*=0.0184 and *B*=0.7148. Ranganathan and Advani (1991) suggested that the interaction coefficient C_I should be inversely proportional to the inter particle spacing. Later, Phan-Thien *et al.* (2002), by minimizing the error between direct simulations and continuum theory, proposed the following expression

$$C_I = A\left[1-\exp\left(-Br\phi\right)\right] \tag{2.8}$$

with *A*=0.03 and *B*=0.224. Furthermore, other authors proposed that the diffusion coefficient that simulates the effect of rod interactions should be anisotropic and hence, tensorial in nature. For example, Koch (1995) proposed an empirical expression for the orientational diffusion resulting from hydrodynamic rod-rod interactions in shear flow which involved fourth and sixth order moments of the orientation distribution. The anisotropic contribution to the diffusion was resulting from the sixth order orientation tensor. However, the use of these high order tensors makes this description cumbersome.

2.2.3 Orientation distribution

To close Eq. 2.5, the knowledge of the evolution of the orientation distribution is required. In the case of an homogeneous system, the rod orientation distribution can be regarded as a convected scalar and its evolution is equivalent to a continuity equation defined on the surface of the unit sphere [Bird *et al.* (1987)]

$$\frac{D\psi}{Dt} = -\frac{\partial}{\partial \mathbf{p}}\cdot\left(\dot{\mathbf{p}}\,\psi\right) \tag{2.9}$$

Once, the evolution of the unit vector **p** is known, the last equation gives the evolution of the orientation distribution. The orientation distribution needs to satisfy certain physical conditions. First, the orientation distribution has the following symmetry

$$\psi(\theta,\varphi) = \psi(\pi-\theta,\varphi+\pi) \tag{2.10}$$

implying that a rod oriented at any angle (θ,φ) is indistinguishable from a rod oriented at any angle $(\pi-\theta,\varphi+\pi)$. Thus, ψ must be periodic. Second, the orientation distribution needs to be normalized since every fiber has some orientation

$$\int_{\theta=0}^{\pi}\int_{\phi=0}^{2\pi}\psi(\theta,\varphi)\sin(\theta)d\theta d\varphi = \int\psi(\mathbf{p})d\mathbf{p} = 1 \tag{2.11}$$

Since the solution of Eq. 2.9 is expensive, a more concise description of the orientation state of the system can be defined by considering the moments of the full distribution. The second and fourth order tensors are respectively defined as

$$\begin{aligned}\mathbf{a}_2 &= \int \mathbf{pp}\,\psi(\mathbf{p})d\mathbf{p}\\ \mathbf{a}_4 &= \int \mathbf{pppp}\,\psi(\mathbf{p})d\mathbf{p}\end{aligned} \tag{2.12}$$

All the odd order moments are null since the orientation distribution is an even function. From the normalization condition, we have

$$\begin{aligned}tr(\mathbf{a}_2) &= a_{ii} = 1\\ a_{ijkk} &= a_{ij}\end{aligned} \tag{2.13}$$

Furthermore, the two orientation tensors have the following symmetries

$$\begin{aligned}a_{ij} &= a_{ji}\\ a_{ijkl} &= a_{jikl} = a_{kijl} = a_{lijk} = a_{klij} = \ldots\end{aligned} \tag{2.14}$$

Owing to Eqs. 2.13 and 2.14, the number of components needed to fully determine $\mathbf{a}_2$ and $\mathbf{a}_4$ is 5 and 15, respectively. Hence, many authors have derived the time evolution of the second order tensor $\mathbf{a}_2$ overcoming the need of the solution of the full Fokker-Planck equation. However, this strategy has two major drawbacks. The first is that there is a loss of information passing from the orientation distribution to the second order orientation tensor, and second, the time evolution of

any even moment of the orientation distribution involves higher order moments. This implies the need of what are known in the literature as “closure approximations”. In practice, the $\mathbf{a}_4$ orientation tensor is rewritten as a function of $\mathbf{a}_2$ causing inevitable errors and numerical artifacts. In this work, we circumvent the need of closure approximations since we solve the full Fokker-Planck equation. However, the interested reader is directed to the following studies: Advani and Tucker (1990), Cintra and Tucker (1995), Chung and Kwon (2001), Férec *et al.* (2014).

2.2.4 Dhont and Briels model

Following Doi and Edwards (1978b) and Kuzuu and Doi (1983), Dhont and Briels (2003b) derived a set of equations to describe the dynamics of long thin rods. The hydrodynamic interactions were neglected and the equilibrium pair correlation function was assumed to be valid during shear flow. The rods interacted with the excluded volume potential causing an extra torque on the rod which on average resulted in

$$\mathbf{T}(\mathbf{p},t) = -\left(2nDL^2 k_B T\right)\hat{R}\int |\mathbf{p}\times\mathbf{p}'|\psi(\mathbf{p}',t)\,d\mathbf{p}' \tag{2.15}$$

where the operator $\hat{R}$ is defined as $\mathbf{p}\times\dfrac{\partial}{\partial\mathbf{p}}$, k_B is the Boltzmann constant and T is the temperature.

The closed equation of motion in shear flow resulted in

$$\frac{D\psi}{Dt} = D_r\hat{R}\cdot\left[\hat{R}\psi + \left(2nDL^2\right)\hat{R}\int |\mathbf{p}\times\mathbf{p}'|\psi(\mathbf{p}',t)\,d\mathbf{p}'\right] - \hat{R}\cdot\left(\mathbf{p}\times\boldsymbol{\kappa}^{\dagger}\cdot\mathbf{p}\,\psi\right) \tag{2.16}$$

They also derived the macroscopic equivalent developing a new closure approximation for the fourth order tensor. Starting from the divergence of the stress tensor, its deviatoric part was calculated as

$$\boldsymbol{\sigma} = \eta_0\dot{\boldsymbol{\gamma}} + 3nk_BT\left[\mathbf{a}_2 - \frac{1}{3}\boldsymbol{\delta} + r\phi\left(\mathbf{a}_4 : \mathbf{a}_2 - \mathbf{a}_2\cdot\mathbf{a}_2\right) + \frac{1}{6D_r}\left(\mathbf{a}_4 : \dot{\boldsymbol{\gamma}} - \frac{1}{3}\mathbf{a}_2 : \dot{\boldsymbol{\gamma}}\boldsymbol{\delta}\right)\right] \tag{2.17}$$

where η_0 is the matrix viscosity.

The zero-shear viscosity was found to be a linear function of the volume fraction up to the isotropic-nematic transition and their theory predicted the phase transition between isotropic, paranematic and nematic regimes. Furthermore, no tumbling at low shear rates and wagging at intermediate shear rates was found under steady shear flow with their approach since the interaction parameter was always larger than the critical value of 9.2. Also, no changes in sign of the normal stresses as function of shear rate were encountered. The accuracy of these theory predictions is reduced by neglecting the effect of hydrodynamic interactions, which could account for up to 20 % of the total stress of the dilute suspension.

2.2.5 Aggregation/Orientation model

Based on the original ideas of Vaccaro and Marrucci (2000) to describe the dynamics of associating polymers, Ma *et al.* (2008) proposed a model to describe the aggregation/disaggregation dynamics in CNT suspensions. This model was named "the aggregation/orientation model" or AO model since the orientation distribution was assumed to be dependent on the orientation, **p**, and on the population coordinate *n*

$$\frac{D\psi(\mathbf{p},n)}{Dt} = \left.\frac{D\psi(\mathbf{p},n)}{Dt}\right|_{Orientation} + \left.\frac{D\psi(\mathbf{p},n)}{Dt}\right|_{Aggregation} \tag{2.18}$$

The orientation part is equivalent to substituting Eq. 2.5 in Eq. 2.9. However, the diffusion coefficient is assumed to be a linear function of *n*: $D_r(n) = D_r^{\max} n$, where $D_r^{\max}$ is an adjustable parameter. For the aggregation part, they obtained

$$\left.\frac{D\psi(\mathbf{p},n)}{Dt}\right|_{Aggregation} = v_c \int_{f=0}^{f=n} \psi(\mathbf{p},f)\,df + v_d \int_{f=n}^{f=1} \psi(\mathbf{p},f)\,df - \left[v_c(1-n) + v_d n\right]\psi(\mathbf{p},n) \tag{2.19}$$

where v_c and v_d are the aggregation and disaggregation velocity, respectively. In simple shear flow, v_c and v_d are defined as

$$\nu_c = \begin{cases} \nu_c^{\max}\left(\dfrac{\dot{\gamma}_{\max}-\dot{\gamma}}{\dot{\gamma}_{\max}}\right) & \text{if } \dot{\gamma} \le \dot{\gamma}_{\max} \\ 0 & \text{if } \dot{\gamma} > \dot{\gamma}_{\max} \end{cases} \tag{2.20}$$

and

$$\nu_d = \begin{cases} \nu_d^{\max}\left(\dfrac{\dot{\gamma}}{\dot{\gamma}_{\max}}\right) & \text{if } \dot{\gamma} \le \dot{\gamma}_{\max} \\ \nu_d^{\max} & \text{if } \dot{\gamma} > \dot{\gamma}_{\max} \end{cases} \tag{2.21}$$

where $\nu_c^{\max}$, $\nu_d^{\max}$ and $\dot{\gamma}_{\max}$ are adjustable parameters.

The stress contribution due to the presence of CNTs was obtained as

$$\boldsymbol{\tau} = 2\eta_0 \int_0^1 N_P(n)\left[\mathbf{a}_4(n) : \dot{\boldsymbol{\gamma}}\right] dn \tag{2.22}$$

where $N_P(n) = N_P^{\max} n$. $N_P^{\max}$ is an adjustable parameter.

The major success of this model is the introduction of a shear rate dependent microstructure and the ability to predict shear thinning. However, for each concentration different values of the adjustable parameters were used. Furthermore, it is a purely viscous model and particle-particle interactions are not accounted for.

2.2.6 Rigid and flexible clusters

Chinesta (2013) proposed an interesting description to model the behavior of rigid clusters in a suspension. In 2D, he calculated the rotary evolution of a cluster as

$$\begin{aligned} \dot{\mathbf{p}} &= \varpi \times \mathbf{p} \\ \varpi &= \boldsymbol{\varepsilon} : \left(\mathbf{a}_2 \cdot \boldsymbol{\kappa}\right) \end{aligned} \tag{2.23}$$

where ε is the Levi-Civita symbol. Hence, the rotary velocity of a rigid cluster is a function only of the second moment of the orientation distribution. The evolution of $\mathbf{a}_2$ for a suspension of rigid clusters was express as

$$\mathbf{a}_2 = \frac{1}{2}\left(\boldsymbol{\omega} + \mathbf{F}\right)\cdot\mathbf{a}_2 - \frac{1}{2}\mathbf{a}_2\cdot\left(\boldsymbol{\omega} + \mathbf{F}\right) \tag{2.24}$$

where,

$$\mathbf{F} = \begin{pmatrix} 0 & -f \\ f & 0 \end{pmatrix} \tag{2.25}$$
$$f = -\dot{\gamma}_{12} - 2\cdot\dot{\gamma}_{11}\cdot a_{12} + 2\cdot\dot{\gamma}_{12}\cdot a_{11}$$

Since the evolution of the cluster rotary velocity is a function only of $\mathbf{a}_2$, Chinesta (2013) suggested that the microstructure description for a homogeneous suspension of rigid cluster should be based on a distribution function $\psi(\mathbf{a}_2, t)$. Hence, the conformation variable is not anymore the simple orientation vector but directly the second order tensor, $\mathbf{a}_2$.

Also, this approach was generalized to deformable clusters by defining an equivalent traceless gradient as

$$\mathbf{G} = \frac{\mu\mathbf{W} + \xi\boldsymbol{\kappa}^{\dagger}}{\mu + \xi} \tag{2.26}$$

where $\mathbf{W} = \mathbf{F} + \boldsymbol{\omega}$ and μ and ξ are two weighting parameters. This equivalent gradient varies between the velocity gradient that a single rod would feel and the one of a rigid cluster simulating in this way the change in shape of the cluster during flow. However, no kinetic evolution of the ratio between μ/ξ was suggested. The evolution of the rotary velocity of the deformable cluster was obtained simply as

$$\dot{\mathbf{p}}_C = \mathbf{G}\cdot\mathbf{p} - \mathbf{G}:\mathbf{ppp} \tag{2.27}$$

where the subscript C stands for cluster.

Later, a fading memory term was added in the evolution of the second order tensor to represent the elasticity of the clusters and their tendency to return to more isotropic state once the flow is stopped [Abisset-Chavanne *et al.* (2013)].

The stress contribution due to the clusters was evaluated as

$$\boldsymbol{\tau}_C = \tilde{N}_P \int \left(\dot{\boldsymbol{\gamma}} \cdot \mathbf{a}_2 + \mathbf{a}_2 \cdot \dot{\boldsymbol{\gamma}} - \mathbf{F} \cdot \mathbf{a}_2 + \mathbf{a}_2 \cdot \mathbf{F} \right) \psi \left(\mathbf{a}_2, t \right) d\mathbf{a}_2 \tag{2.28}$$

where $\tilde{N}_P$ is an adjustable parameter. However, a direct comparison of this interesting approach with experimental results has not yet been completed. Furthermore, the presence of clusters is always accompanied experimentally with a microstructure where concentration gradients are present, requiring a description where spatial dynamics needs to be included. In addition, cluster-cluster and cluster-rod interactions are yet to be included in this mathematical approach.

2.2.7 Férec model

As mentioned above, the importance of the particle interactions grows strongly with the rod concentration in the system. Many authors worked on the problem on how to include this effect on the suspension dynamics. Sandstrom (1993) and Sandstrom and Tucker (1993) presented a theory for concentrated fiber suspensions with interactions between the rods. Later, Djalili-Moghaddam and Toll (2005) introduced in the total stress tensor a contribution due to the interaction forces acting on the rods. Recently, Férec *et al.* (2009) derived a continuum equivalent of Djalili-Moghaddam and Toll (2005) model without neglecting any term in the relative velocity of the rods at the interaction point. The average rotary velocity of the rod was found accounting for the effects of linear lubricated interactions as

$$\dot{\mathbf{p}}^{\alpha} = \dot{\mathbf{p}}_J^{\alpha} - \phi \tilde{M} \int \left| \mathbf{p}^{\alpha} \times \mathbf{p}^{\beta} \right| \left(\frac{1}{2} \dot{\boldsymbol{\gamma}} \cdot \mathbf{p}^{\alpha} - \frac{1}{2} \dot{\boldsymbol{\gamma}} : \mathbf{p}^{\alpha} \mathbf{p}^{\alpha} \mathbf{p}^{\alpha} + q \left| \dot{\gamma} \right| \frac{\partial \ln \psi_{\mathbf{p}^{\alpha}}}{\partial \mathbf{p}^{\alpha}} \right) \psi_{\mathbf{p}^{\beta}} d\mathbf{p}^{\beta} \tag{2.29}$$

where the superscript α and β stands for test rod and interacting neighboring rods, respectively. $\dot{\mathbf{p}}_J^{\alpha}$ is defined in Equation 2.3 with λ=1 (long and thin rods) while $\tilde{M}$ is a dimensionless scalar.

They also derived the evolution of the second order orientation tensor using a quadratic closure approximation. This closure approximation was later refined in Férec *et al.* (2014).

The deviatoric part of the stress tensor was derived starting from the Kramer's expression as

$$\boldsymbol{\sigma} = \eta_0 \dot{\boldsymbol{\gamma}} + \eta_0 \phi \frac{r^2}{6\pi} X_A \dot{\boldsymbol{\gamma}} : \mathbf{a}_4 + \eta_0 \phi^2 \frac{4r^2}{3\pi^2} k \dot{\boldsymbol{\gamma}} : \mathbf{b}_4 \tag{2.30}$$

where X_A is the parallel drag coefficient of the rods and *k* is an adjustable parameter controlling the intensity of the interactions. $\mathbf{b}_4$ is the fourth order interaction tensor defined as

$$\mathbf{b}_4 = \iint \left|\mathbf{p}^\alpha \times \mathbf{p}^\beta\right| \mathbf{p}^\alpha \mathbf{p}^\alpha \mathbf{p}^\alpha \mathbf{p}^\alpha \psi_{\mathbf{p}^\alpha} \psi_{\mathbf{p}^\beta} d\mathbf{p}^\alpha d\mathbf{p}^\beta \tag{2.31}$$

The last term on the right of Eq. 2.30 represents the rod-rod interaction contribution to the stress tensor. The model predictions were compared with the rheological response of glass fibers dispersed in a Newtonian matrix. The model was able to predict the overall transient rheology of the system (shear viscosity and normal stresses) and also, the effect of the concentration on the shear viscosity.

2.2.8 Rod flexibility

Strautins and Latz (2007) described a long and thin rod as made of three beads and two connectors as illustrated in Figure 2.17.

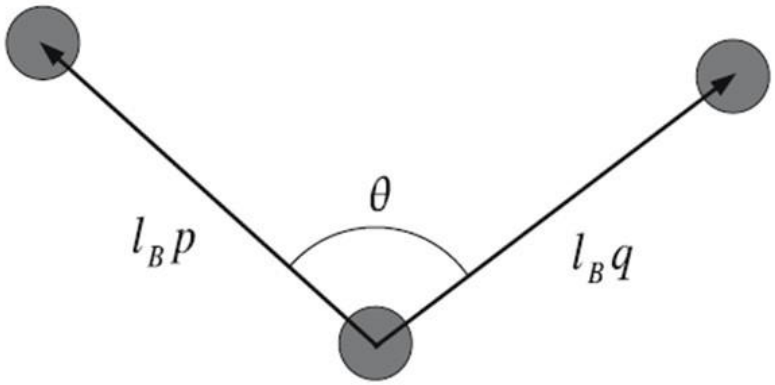

Figure 2.17 Schematic of the flexible rod.

The unit orientation vector **p** and **q** are defined as

$$\begin{aligned}\mathbf{p} &= \left(\mathbf{R}_1 - \mathbf{R}_0\right)/l_B \\ \mathbf{q} &= \left(\mathbf{R}_2 - \mathbf{R}_0\right)/l_B\end{aligned} \tag{2.32}$$

They point from the central bead located at $\mathbf{R}_0$, with respect to a fix reference system to the other two beads located respectively at $\mathbf{R}_1$ and $\mathbf{R}_2$. l_B is the length of the connectors. To model the flexibility, a bending potential is assumed to act on the connectors and is defined as

$$U = \tilde{k}\left(\mathbf{p}\cdot\mathbf{q}+1\right) \tag{2.33}$$

This bending potential has an equilibrium conformation of a straight rod.

Strautins and Latz (2007) derived the rotary velocity of the two connectors as

$$\begin{aligned}\dot{\mathbf{p}} &= \left[\mathbf{p}\times\left(\boldsymbol{\kappa}^{\dagger}\cdot\mathbf{p}+\frac{l_B}{2}\boldsymbol{\mu}:\mathbf{pp}\right)-b\mathbf{p}\times\mathbf{q}\right]\times\mathbf{p} \\ \dot{\mathbf{q}} &= \left[\mathbf{q}\times\left(\boldsymbol{\kappa}^{\dagger}\cdot\mathbf{q}+\frac{l_B}{2}\boldsymbol{\mu}:\mathbf{qq}\right)-b\mathbf{q}\times\mathbf{p}\right]\times\mathbf{q}\end{aligned} \tag{2.34}$$

where $\boldsymbol{\mu} = \dfrac{\partial^2 v_i}{\partial x_j \partial x_k}$ is the second order velocity gradient and $b = \dfrac{2\tilde{k}}{\varsigma l_B^2}$ is rod bending stiffness with ς the drag coefficient for a bead. The evolution of the orientation distribution for this two rod particle is written as

$$\frac{D\psi(\mathbf{p},\mathbf{q},t)}{Dt} = -\frac{\partial}{\partial\mathbf{p}}\cdot\left(\dot{\mathbf{p}}\psi\right)-\frac{\partial}{\partial\mathbf{q}}\cdot\left(\dot{\mathbf{q}}\psi\right)+D_r\left(\frac{\partial^2}{\partial\mathbf{p}^2}+\frac{\partial^2}{\partial\mathbf{q}^2}\right)\psi \tag{2.35}$$

Only the convective part of this equation was considered in their work. Due to the number of conformation variables involved in Eq. 2.35, the second order moments evolution was derived and solved for a simple channel flow, where the second gradient of the velocity field is non-zero.

Later, Ortman *et al.* (2012) introduced a diffusive contribution to the dynamics of these flexible rods to simulate the effect of interactions, as previously done by Folgar and Tucker (1984). They also derived a quadratic closure approximation for the second order orientation tensors. With the introduction of the diffusive contribution, the bending potential contributes to the dynamics of the system also in simple shear flow, where the second order gradient of the velocity is zero.

2.2.9 Thermodynamic approach

Based on thermodynamics arguments, Grmela (1986) and Grmela and Carreau (1987) derived an alternative method to describe the orientation evolution of a suspension of rigid rods. The evolution of the second order tensor was written as

$$\dot{\mathbf{a}}_2 = -\frac{1}{2}\left(\boldsymbol{\omega}\cdot\mathbf{a}_2 - \mathbf{a}_2\cdot\boldsymbol{\omega}\right) + \frac{1}{2}\left(\dot{\boldsymbol{\gamma}}\cdot\mathbf{a}_2 - \mathbf{a}_2\cdot\dot{\boldsymbol{\gamma}}\right) - \boldsymbol{\Lambda}\cdot\mathbf{a}_2\cdot\frac{\delta G}{\delta \mathbf{a}_2} \tag{2.36}$$

where $\delta/\delta\mathbf{a}_2$ is the Volterra derivative, $\boldsymbol{\Lambda}$ is a mobility tensor and G is the Gibbs free energy of the system. The derivative appearing in the third term on the right of Eq. 2.36 is defined for axisymmetric particles as

$$\frac{\delta G}{\delta \mathbf{a}_2} = \frac{k_B T}{2}\left[\beta\boldsymbol{\delta} - S_B\mathbf{a}_2^{-1} - L^2 S_L\mathbf{a}_2^{-1}\cdot\mathbf{a}_2^{-1} + 2\frac{S_0}{L^2}\left(\boldsymbol{\delta} - \frac{\mathbf{a}_2}{L^2}\right)\right] \tag{2.37}$$

β is a Langragian multiplier in order to keep constant the trace of $\mathbf{a}_2$ during deformation to respect the inextensibility of the rods. S_B and S_L are factors controlling, respectively, the Boltzmann dissipative contribution and the Lifshitz contribution which characterizes the semi-flexibility of the rods. Finally, S_0 is the Osanger factor to take into account the topologic interactions due to the excluded volume potential. An isotropic expression for the mobility tensor was derived by Ghosh *et al.* (1995) and its expression is the following

$$\boldsymbol{\Lambda} = \Lambda_0 \frac{\left(1 - \frac{n^2}{n_0^2}\right)}{\left[1 - a\ tr\left(\frac{\mathbf{a}_2 \cdot \mathbf{a}_2}{L^4}\right)\right]^2} \boldsymbol{\delta} \tag{2.38}$$

where Λ_0 is mobility constant and n_0 is the maximal concentration of rods. Finally, the parameter *a* controls the effect of fiber orientation. More recently, extensions of this approach to model nanoparticle suspensions in a FENE-P medium [Eslami *et al.* (2007)] or in a reptating medium [Eslami and Grmela (2008), Eslami *et al.* (2009)] have been proposed. In the case of nanoclay platelets composites, the model was found to give satisfactory predictions in transient shear flows while at steady state, it under predicted the viscosity values at low shear rates [Eslami *et al.* (2009)]. In SAOS, the model captures the fundamental behavior of the storage modulus, showing a plateau at low frequency. However, the agreement was only qualitative and the storage modulus presents a non-terminal behavior even at extremely low concentrations of lamellae [Eslami and Grmela (2008), Eslami *et al.* (2010)].

2.2.10 Constitutive equation

A constitutive equation is an expression that relates the stress tensor with the shear rate or the deformation applied to the material [Carreau *et al.* (1997)]. This equation is of fundamental importance to model manufacturing processes. In the case of rod suspensions, Batchelor (1971), Hinch and Leal (1972), Hinch and Leal (1973) and Lipscomb *et al.* (1988) developed a general equation for the deviatoric part of the stress tensor

$$\boldsymbol{\sigma} = \eta_0 \dot{\boldsymbol{\gamma}} + \eta_0 \phi \left[\mu_1 \dot{\boldsymbol{\gamma}} + \mu_2 \mathbf{a}_4 : \dot{\boldsymbol{\gamma}} + \mu_3 \left(\dot{\boldsymbol{\gamma}} \cdot \mathbf{a}_2 + \mathbf{a}_2 \cdot \dot{\boldsymbol{\gamma}} \right) + 2\mu_4 D_r \mathbf{a}_2 \right] \tag{2.39}$$

where the coefficients μ_1, μ_2, μ_3 and μ_4 are material constants. In the case of particles with high aspect ratio, $\mu_1 = \mu_3 = 0$ according to the slender body theory [Batchelor (1970)], while μ_4 controls the effects of Brownian motion being zero for non-Brownian rods. Many authors have worked on the determination of the material constants and the principal results are in Table 2.2 where only the non-zero constants are reported for clarity.

Table 2.2 Summary of material constants for the constitutive equation 2.39

Authors	**Material constants**	**Concentration regime**
Batchelor (1970)	$\mu_2 = \mu_2^{dilute} = \frac{8r^2}{3\ln(2r)}\left(\frac{\ln(2r)+0.64}{\ln(2r)-1.5}+\frac{1.659}{\ln^2(2r)}\right)$	Dilute
Mackaplow and Shaqfeh (1996)	$\mu_2 = \mu_2^{dilute} + \frac{C_1\phi r^4}{\ln^3(2r)}$; C_1=1.399 for aligned rods; C_1=1.508 for random rods	Dilute (two bodies interactions)
Hinch and Leal (1972)	$\mu_1 = 2$; $\mu_2 = \frac{r^2}{2\left[\ln(2r)-1.5\right]}$; $\mu_3 = \frac{6\ln(2r)-11}{r^2}$	Semi-dilute
Shaqfeh and Fredrickson (1990)	$\mu_2 = \frac{16r^2}{3\left(\ln(1/\phi)+\ln\ln(1/\phi)+C_2\right)}$; C_2=0.1585 for aligned rods; C_2=-0.6634 for random rods	Semi-dilute
Lipscomb *et al.* (1988)	$\mu_1 = 2$; $\mu_2 = \frac{r^2}{2\ln(r)}$;	Semi-dilute
Dinh and Armstrong (1984)	$\mu_2 = \frac{r^2}{3\ln(2h/D)}$; $h = h_{ali} = \frac{D}{2}\sqrt{\frac{\pi}{\phi}}$ for aligned rods; $h = h_{iso} = \frac{\pi D}{4r\phi}$ for random rods	Semi-concentrated
Chung and kwong 2002	$\mu_2 = \frac{r^2}{3\ln(2h/D)}$; $h = \left(1-f^*\right)h_{iso} + f^* h_{ali}$; $f^* = 1 - 27\det(\mathbf{a}_2)$	Semi-concentrated

2.2.11 Numerical methods

Combining Eqs. 2.5 and 2.9, and substituting $C_I|\dot{\gamma}|$ with D_r, we obtain the following time evolution of the orientation distribution:

$$\frac{D\psi}{Dt} = -\frac{\partial}{\partial \mathbf{p}} \cdot \left(\dot{\mathbf{p}}_J \psi\right) + D_r \frac{\partial^2}{\partial \mathbf{p}^2} \psi \tag{2.40}$$

where $\dot{\mathbf{p}}_J$ is defined in Eq. 2.3. Eq. 2.40 is known as Fokker-Planck equation and different numerical techniques are available to solve it. Advani and Tucker (1990) used a finite difference technique implicit in time and a central difference formula for the derivatives in θ and φ. They used $\psi(\theta = 0, \varphi) = \psi(\theta = \pi, \varphi) = 0$ as boundary condition, implying that the probability of finding a rod oriented in $(\theta = 0, \varphi)$ and $(\theta = \pi, \varphi)$ was null. This condition is physically not always true and it causes the loss of global conservation of the numerical method. Consequently, the distribution function needed to be normalized at each time step which can be the source of inaccuracies. Strand *et al.* (1987) used a spherical harmonic expansion of the orientation distribution applying the Galerkin method. This technique has been very successful for nematic liquids where the Fokker-Planck equation presents an extra term due to the excluded volume potential [Larson (1990), Larson and Ottinger (1991), Faraoni *et al.* (1999)]. However, the solutions were possible only for Peclet, $\mathrm{Pe} = \dot{\gamma}/D_r$, lower than 60 [Strand *et al.* (1987)].

Bay (1991) applied a finite volume method that did not need a re-normalization step, thanks to periodic boundary conditions. The integration scheme was explicit and centered difference formulas were used. Solutions were obtained only for $\mathrm{Pe} \leq 10^2$ since for higher Peclet, the numerical method required reduction in time step size and hence, very long CPU times. Han and Im (1999) obtained reliable solution until Pe of about 10^3 applying a finite element method using triangular mesh. Recently, Férec *et al.* (2008) extended the work of Bay (1991) writing a finite volume method where different time and spatial schemes could be tested. They found that a power law scheme was able to give correct solutions up to Pe ~ 10^5. We will focus now on the description of the numerical technique used by Férec *et al.* (2008) since it will be employed in the rest of the present work.

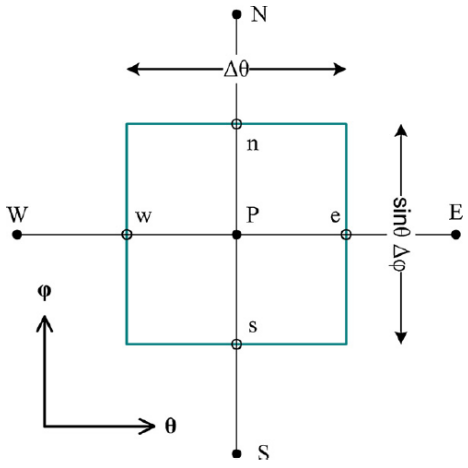

Figure 2.18 Control volume of the spatial discretization used to calculate the fluxes balance. The faces are labelled as e, w, n and s standing for east, west, north and south, respectively [Férec *et al.* (2008)].

The surface of the unit sphere is discretized with cells of areas $\Delta A = \sin(\theta)\Delta\theta\Delta\varphi$ as illustrated in Figure 2.18. Because of Eq. 2.10, the mesh of only one half of the sphere is required and number of nodes in θ and φ directions are the same. By integrating in space and time Eq. 2.40 we obtain

$$\int_t^{t+\Delta t}\int_A \frac{D\psi}{Dt}\,dA dt = -\int_t^{t+\Delta t}\int_A \frac{\partial}{\partial \mathbf{p}}\cdot\left(\dot{\mathbf{p}}_J\psi\right)dA dt + D_r\int_t^{t+\Delta t}\int_A \frac{\partial^2}{\partial \mathbf{p}^2}\psi\, dA dt \tag{2.41}$$

By making use of the Gauss theorem, we obtain

$$\int_t^{t+\Delta t}\int_A \frac{D\psi}{Dt}\,dA dt = -\int_t^{t+\Delta t}\int_\Gamma \psi\dot{\mathbf{p}}_J\cdot\mathbf{n}\,d\Gamma dt + D_r\int_t^{t+\Delta t}\int_\Gamma \frac{\partial}{\partial \mathbf{p}}\psi\cdot\mathbf{n}\,d\Gamma dt \tag{2.42}$$

where Γ is the contour of the cell of area ΔA and $\mathbf{n}$ is the normal vector to the contour.

After some algebra, the general form of the discretized Fokker-Planck equation 2.40 is

$$\begin{aligned}&\left(a_M+\alpha a_P\right)\psi_P^{t+\Delta t}-\alpha a_E\psi_E^{t+\Delta t}-\alpha a_W\psi_W^{t+\Delta t}-\alpha a_N\psi_N^{t+\Delta t}-\alpha a_S\psi_S^{t+\Delta t}=\\&\left[a_M-\left(1-\alpha\right)a_P\right]\psi_P^{\tau}+\left(1-\alpha\right)a_E\psi_E^{t}+\left(1-\alpha\right)a_W\psi_W^{t}+\left(1-\alpha\right)a_N\psi_N^{t}+\left(1-\alpha\right)a_S\psi_S^{t}\end{aligned} \tag{2.43}$$

Regarding the time differencing scheme, the explicit scheme is obtained for $\alpha = 0$. The Crank-Nicholson scheme is recovered for $\alpha = 0.5$ and for $\alpha = 1$, the scheme is fully implicit. The different expression for the coefficients a_E, a_W, a_N, a_S, a_M and a_P are reported for the different spatial discretizations in Appendix A. As previously done by Bay (1991), periodic boundary conditions were used and the initial orientation was assumed to be isotropic $(\psi = 1/4\pi)$.

At each time step, the following linear system is solved

$$\begin{bmatrix} (a_M + \alpha a_P) & -\alpha a_E & -\alpha a_W & -\alpha a_N & -\alpha a_S \\ 0 & 0 & 0 & 0 & 0 \\ 0 & 0 & 0 & 0 & 0 \\ 0 & 0 & 0 & 0 & 0 \\ 0 & 0 & 0 & 0 & 0 \end{bmatrix} \begin{Bmatrix} \psi_P^{t+\Delta t} \\ \psi_E^{t+\Delta t} \\ \psi_W^{t+\Delta t} \\ \psi_N^{t+\Delta t} \\ \psi_S^{t+\Delta t} \end{Bmatrix} = \begin{Bmatrix} (a_M - (1-\alpha)a_P)\psi_P^t + (1-\alpha)a_E\psi_E^t + (1-\alpha)a_W\psi_W^t \\ \qquad + (1-\alpha)a_N\psi_N^t + (1-\alpha)a_S\psi_S^t \\ 0 \\ 0 \\ 0 \\ 0 \end{Bmatrix} \tag{2.44}$$

The linear system $[K]\{\psi\} = \{F\}$ is solved with an LU (lower-upper) factorization method optimized in MATLAB©. The coefficient matrix, *K*, is stored as sparse since it contains a large number of zero elements. It is expressed as the product of two triangular matrices, one of them a permutation of a lower triangular matrix, *L*, and the other an upper triangular matrix, *U*. A row permutation matrix *P* is also stored. To find the solution of the linear system, we first pivot both sides by multiplying by the pivot matrix [*P*]

$$[P][K]\{\psi\} = [P]\{F\} = \{Q\} \tag{2.45}$$

By substituting L and U, we have

$$[L][U]\{\psi\} = \{Q\} \tag{2.46}$$

Then, the solution is found by solving two back substitution problems

$$\begin{aligned}[L]\{\xi\} &= \{Q\} \\ [U]\{\psi\} &= \{\xi\}\end{aligned} \tag{2.47}$$

In order, to reduce the memory used, we store the pivot matrix as a vector.

Recently, a new numerical method called proper generalized decomposition (PGD) has been proposed to solve multi-dimentional Fokker-Planck equations [Ammar *et al.* (2006), Ammar *et al.* (2007)]. This non-incremental method is based on the assumption that it is always possible to decompose the distribution function involved in the microstructural description as a product of finite number of functions of different independent variables. However, no results are available yet for the application of this technique to distribution functions in strongly non-linear problems.

2.3 Summary

Because of their high aspect ratio, conductive properties and exceptional mechanical properties, carbon nanotube suspensions have attracted the interest of the scientific community for the past 25 years. The rheology of carbon nanotube suspensions has been fairly investigated; however, due to its complexity and the variety of dispersion states obtained by the different researchers, misleading results are reported in the literature. A simple example is the variety of percolation values reported. Aspects like viscoelasticity at low carbon nanotube concentrations, flow-induced alignment and non-linear response in the concentrated regime are yet not completely characterized and understood. Furthermore, in poorly dispersed systems, the aggregation/disaggregation process has yet to be quantified and the dynamics of aggregated structure (and more complex structures like helical bands in confined flows) are still experimentally not characterized. Also, only few articles can be found on the employment of CNTs in viscoelastic matrices and on the rheological behavior of CNT suspensions in elongational flow.

Modeling CNT suspensions and the derivation of an appropriate constitutive law could help to design and optimize processing schemes with the added benefit of reducing the required experimental testing in terms of time and material needed. However, a general equation appropriate to different regime of concentrations is still missing in the literature.

CHAPTER 3 RESEARCH OBJECTIVES AND SUMMARY OF THE ARTICLES

3.1 Objectives

The main objective of this research is to correlate the microstructure evolution of MWCNT suspensions during shear flow and at rest with their macroscopic rheological response. In particular, the role of the phenomenological mechanisms in determining the state of the system is analyzed. Hence, the following specific objectives were undertaken:

1) To characterize the orientation dynamics of MWCNT suspensions during simple shear flow and at rest following flow cessation.
2) To develop a microstructural model that relates individual particle conformations with the rheo-optical response of dilute and semi-dilute CNT suspensions.
3) To investigate the rheological non-linearities of concentrated carbon nanotube suspensions (shear-thinning, normal stresses, shear stress overshoots, etc.) for varying parameters such as concentration, shear intensity and flow directionality.
4) To develop a microstructural model able to explain the shear rate dependency of the microstructure and comparison of the predictions with rheological data for concentrated CNT suspensions.

3.2 Summary of the articles

The above mentioned research objectives are developed in three articles that constitute the body of this thesis.

The first article, Chapter 4, focuses on the orientation dynamics of MWCNTs dispersed in a Newtonian epoxy matrix. The first and second specific objectives are here developed. Dichroism in parallel disks and Couette flow geometries was studied as a mean to correlate the complex part of the refractive index tensor with the orientation evolution of the microstructure. Only dilute and semi-dilute regimes were investigated since higher concentrations caused the suspensions to be too opaque.

The relaxation behavior of these suspensions was found to be in good agreement with the Doi and Edwards (1986) theory. However a quite disordered system was found experimentally, where the orientation angle with the flow direction was far from zero even at high Pe numbers. To explain this peculiar behavior, we suggested that the highly disordered microstructure could be a consequence of the bent conformation and flexibility of the rods. To model this behavior, we followed the approach of Strautins and Latz (2007) and described flexible rods with a two-rod model. We modified their bending potential that allows only straight rods at equilibrium with a harmonic cosine expression.

Furthermore, the interplay between hydrodynamic and bending contributions caused an orientation evolution completely different with respect to the one for slender rigid rods, which perfectly align in the flow direction. Particles kept tumbling even if their aspect ratio is infinite because of the bending torque.

The third and fourth specific objectives are undertaken in Chapters 5 and 6. In Chapter 5, the steady state rheology of MWCNT suspensions is investigated in simple shear flow. The attention is focused on the derivation of a simple description to explain the strong shear-thinning behavior of untreated CNTs.

From dilute to concentrated regimes, different concentrations were prepared and analysed. A cone and plate geometry was chosen in order to obtain a homogenous simple shear flow and to capture the first normal stress difference (N_1). To describe the shear-thinning behavior and the apparent yield stress exhibited by these suspensions, a new set of rheological equations was developed. The MWCNTs were modelled as rigid rods dispersed in a Newtonian matrix and rod-rod interactions were assumed to be the controlling mechanism. The particle-particle interactions were modelled by a non-linear lubrication force (a power-law function of the relative velocity at the contact point). To link the microstructure evolution with the macroscopic stress tensor, the constitutive equation was obtained while accounting for, in addition to the matrix contribution, hydrodynamic forces and rod-rod interactions. The model predictions showed a good agreement with the steady shear data of CNT/epoxy systems as well as for suspensions of glass fibers in polybutene (data from Sepehr *et al.* (2004b)) demonstrating its ability to describe the behavior of micro and nano scale particle suspensions.

The non-linearity of the interactions with respect to the macroscopic shear rate was used to describe the local effect of "extra" forces (van der Waals, or caused by squeezing flows between rods) during the interaction event. This simple argument led to a microstructure which depended directly on the shear rate applied to the system and, furthermore, it demonstrated that shear thinning can be a consequence of interactions simply viscous in nature.

In Chapter 6, the model predictions are tested in transient shear flow. Transient shear flow data of a concentrated MWCNT suspension in a Newtonian epoxy matrix were analyzed. Multiple shearing and rest steps were used to probe the non-linear rheological response of this system. Stress overshoots appeared at small deformation during forward and reverse flow experiments, and their intensity increased with rest time between two consecutive flows, during which the suspension structure was reconstructed and by increasing the shear rate. However, the position of overshoots was found to be independent of the shear rate, implying that there was a characteristic deformation for the network to break down.

The model predictions showed that interactions disordered the orientation state of the rods. The effect of shear rate was directly accounted by the model, which predicted the need to reach a critical shear rate to break down the structure and let the rods orient in the flow direction. In addition, the model predictions were confronted with the rheological data of a glass fiber-filled polybutene [Sepehr *et al.* (2004b)]. For this micro size particles, the model pointed to the hydrodynamic contribution as the controlling contribution for their rheological response, while in the case of CNTs, the rod-rod interactions were dominant.

CHAPTER 4 ARTICLE 1: RHEO-OPTICAL RESPONSE OF CARBON NANOTUBE SUSPENSIONS

G. Natale [a], N. K. Reddy [b], G. Ausias [c], J. Férec [c], M.C. Heuzey [a] and P.J. Carreau [a]

[a] Research Center for High Performance Polymer and Composite Systems (CREPEC), Chemical Engineering Department, Polytechnique Montreal, PO Box 6079, Stn Centre-Ville, Montreal, QC, Canada H3C 3A7

[b] Department of Chemical Engineering, K.U. Leuven, W. de Croylaan 46, B-3001 Leuven, Belgium

[c] Laboratoire d'Ingénierie des MATériaux de Bretagne (LIMATB) Univ. Bretagne-Sud, EA 4250, LIMATB, F-56100 Lorient, France

4.1 Synopsis

In this work, the rheo-optical response of multi-walled carbon nanotube (MWCNT) suspensions was analyzed. Dichroism was obtained using a polarization-modulation technique in parallel disks and for the first time for these particles in a Couette flow geometry. MWCNTs were dispersed in a Newtonian epoxy matrix, at different concentrations covering the dilute and semi-dilute regimes. Measurements of dichroism were performed as functions of shear rate and nanotube concentration. Surprisingly, the ultimate average orientation angle with respect to the flow direction was far from zero degree, even at high Peclet (Pe) numbers in very dilute suspensions. To explain this peculiar behavior, a new model for flexible rods, valid in the dilute regime, is proposed. It is based on the development of Strautins and Latz (2007) that considers flexible rods made of beads and connectors. We modified their bending potential that allows only straight rods at equilibrium with a harmonic cosine expression. This simple modification changes drastically the behavior of these flexible particles that exhibit a non negligible orientation in the vorticity direction under steady state.

4.2 Introduction

The increasing demand for more efficient processing schemes for colloidal suspensions requires a complete understanding of the fundamentals of their flow behavior. This knowledge can open up new routes not only to optimize tools to control such processes, but also to tailor materials based on predicted microstructure-macroscopic properties interplay. Colloidal suspensions of highly anisotropic particles attract increasing interest because of the number of potential applications, from organic electronics to micromechanics and composites. In this class of particles, carbon nanotubes (CNTs) are fascinating because they exhibit features at the frontier between a semi-flexible macromolecule and a micro-size fiber. Furthermore, their quasi-one-dimensional structure gives them unique thermal and electrical properties that have made CNTs the polymer filler of choice for the creation of multi functional composites [Du *et al.* (2004), Abdel-Goad and Pötschke (2005), Hu *et al.* (2006)].

Many publications have recently appeared on the rheology of CNT suspensions. See for examples Fan and Advani (2007) and Hobbie and Fry (2007). In small amplitude oscillatory flows (SAOS), suspensions of unmodified CNTs exhibit mild elasticity (low values of G') at very low concentration [Rahatekar *et al.* (2006a), Ma *et al.* (2008)]. Crossing the limit of percolation, the tube network contribution becomes predominant with the storage modulus, G', that overcomes the loss counterpart, G''. In addition, both moduli of percolated systems present a non-terminal character at low frequencies [Abdel-Goad and Pötschke (2005), Hu *et al.* (2006)]. Percolation concentration thresholds are strongly dependent on the particle aspect ratio if well dispersed systems are compared [Huang *et al.* (2006), Abbasi *et al.* (2009a)]. Furthermore, the moduli are functions of the thermo-mechanical history. Increasing pre-shearing intensity before an SAOS test causes a reduction of G' that increases with time, indicative of a structure build up until it reaches a new meta-stable equilibrium state [Khalkhal *et al.* (2011)]. The pre-shearing step causes a destruction of the network by orienting the tubes in the flow direction. During rest time, Brownian motion dominates, re-establishing the network by interlocking the tubes in a new state. This evolution of the structure upon rest was also confirmed by transient tests consisting of multiple shear start-ups spaced out with rest steps [Wu *et al.* (2007), Khalkhal and Carreau (2012)]. Recently, Pujari *et al.* (2009b) and (2011) linked directly microstructure and rheological features

by probing concentrated CNT suspensions by small- and wide-angle x-ray scattering (SAXS and WAXS). The rheological and orientation data were discussed in terms of distortion, breakdown, and reformation of percolated multi-walled carbon nanotube (MWCNT) networks.

Another rheological characteristic of CNT suspensions is their marked shear-thinning behavior during steady shear rate ramp tests [Rahatekar *et al.* (2006a)]. Non negligible first normal stress difference, N_1, was also reported in cone-and-plate flow rheometry [Natale *et al.* (2014)].

The optical contrast between CNTs and most typical polymers make CNT suspensions good candidates to be probed with rheo-optical techniques, especially considering that these suspensions exhibits reasonably strong anisotropy [Hobbie (2004)]. Rheo-optical techniques are extremely useful to link in real time rheological information to microstructure evolution. In flow dichroism and birefringence studies, the material property of interest is the refractive index tensor, $\mathbf{n} = \mathbf{n}' - i\mathbf{n}''$. The real part of this tensor, $\mathbf{n}'$, causes the phase shift in the transmitted light while the imaginary component, $\mathbf{n}''$, characterizes the attenuation. When the refractive index tensor is anisotropic, the differences in the principal eigenvalues of its real $\Delta n'$ and imaginary $\Delta n''$ parts are defined as birefringence and dichroism, respectively. Following the approach of Onuki and Doi (1986), Hobbie (2004) derived an expression for the dielectric tensor of CNT suspensions valid in the dilute and semi-dilute regimes and as function of concentration, spatial fluctuation and orientation of the rods.

The first published rheo-optical study of CNT suspensions was performed by Fry *et al.* (2006). They studied single- and multi-walled CNTs suspended in various media using parallel plate (disk) flow geometry. Their results were in qualitative agreement with the theoretical predictions of Doi and Edwards (1986) at low Pe number, while at high Pe the degree of nanotube alignment scaled with $Pe^{1/6}$.

The Doi-Edwards model [Doi and Edwards (1978a)] and his extension for polydisperse systems called the "DEMG model" [Marrucci and Grizzuti (1983)] were used in the past to describe the rheo-optical response of collagen proteins in transient flows [Chow *et al.* (1985a, b)]. The DEMG model was able to account correctly for polydispersity of the aspect ratio of the systems. However, the birefringence overshoots were always underestimated. This was mainly attributed to the flexibility of the particles, which was not accounted for in the model.

An alternative approach to take into account flexibility was proposed by Strautins and Latz (2007). Their model consists of a semi-flexible system of three beads and two connectors, subjected to a bending potential. In their work, they allowed only small deviations from straight rod conformation in order to obtain simple closures for the evolution equations of the second order orientation tensors. For shear flow, this assumption results in a completely aligned system in absence of Brownian motion while we would suspect flexibility to play an important role on the final orientation of the system. Furthermore, the effects of the bending potential are important only in flow fields where the second order derivative of the velocity is non zero. This implies that for simple shear flow (or in general for many rheological flows), flexibility would not have any effect in contrast with the experimental literature [Keshtkar *et al.* (2010)] and other models for semi-flexible fibers [Rajabian *et al.* (2005), Rajabian *et al.* (2008)]. The approach of Strautins and Latz (2007) was extended by Ortman *et al.* (2012) who introduced an isotropic diffusion coefficient, suggested by Folgar and Tucker (1984), in order to consider contacts between particles. In addition they were able to calculate the stress contribution due to fiber bending, and obtain a semi-quantitative agreement with the experimental rheological response of long glass fiber suspensions in a sliding plate rheometer. The presence of the diffusion coefficient drives the orientation of the fibers to a random state and, consequently, bending as well. This way, the bending potential contributes to the dynamics of the system also in simple shear flow. However, the model is only valid for semi-flexible fibers.

In this work, the flow dichroism of multi-walled carbon nanotubes (MWCNTs) dispersed in a Newtonian epoxy was investigated. The dichroic response of this system was studied in parallel disks and, for the first time, in a Couette (concentric cylinders) flow geometry as functions of particle concentration and shear rate. The use of the Couette geometry allows monitoring the orientation of the MWCNTs with respect to the flow direction and, as a consequence, provides information about their conformation. In addition, we propose a modification of the Strautins and Latz model in order to account for the effect of flexibility in simple shear flow, and we extend their model to describe particles that are completely flexible. This new model is used to explain the peculiar response of dilute MWCNT suspensions at high Pe number.

4.3 Materials and experimental methodology

An epoxy (Epon 828, MOMENTIVE Speciality Chemicals Inc., Columbus, OH, USA) with a density of 1.16 g/mL and a viscosity, η_0, of 12.3 Pa·s (at 25 °C) was used as the dispersing medium of the multi walled carbon nanotubes (MWCNTs) obtained from Cheap Tubes Inc. (Cambridgeport, MA, USA). The average length *L* of the tubes was 670 nm while the mean value of the outer diameter *d* was 15 nm. The particles were polydisperse with an aspect ratio *r* varying between 4 and 314 [Khalkhal *et al.* (2011)].

The MWCNT-epoxy suspensions were prepared using an EXAKT three-roll mill (from EXAKT Technologies Inc. Oklahoma city, OK, USA) at room temperature. The MWCNTs were mixed as received with the epoxy without any surfactant or additive. The samples were initially manually blended with a spatula in a glove box, and then were poured into the three-roll mill. Each sample was circulated between the rolls once at 100 and 50 μm gap sizes, twice at 20 and 10 μm gap sizes and four times at a 5 μm gap. During this procedure, the speed of the rolls was maintained constant at 150 rpm. A typical MWCNT-epoxy suspension is shown in the TEM micrograph reported in Figure 4.1.

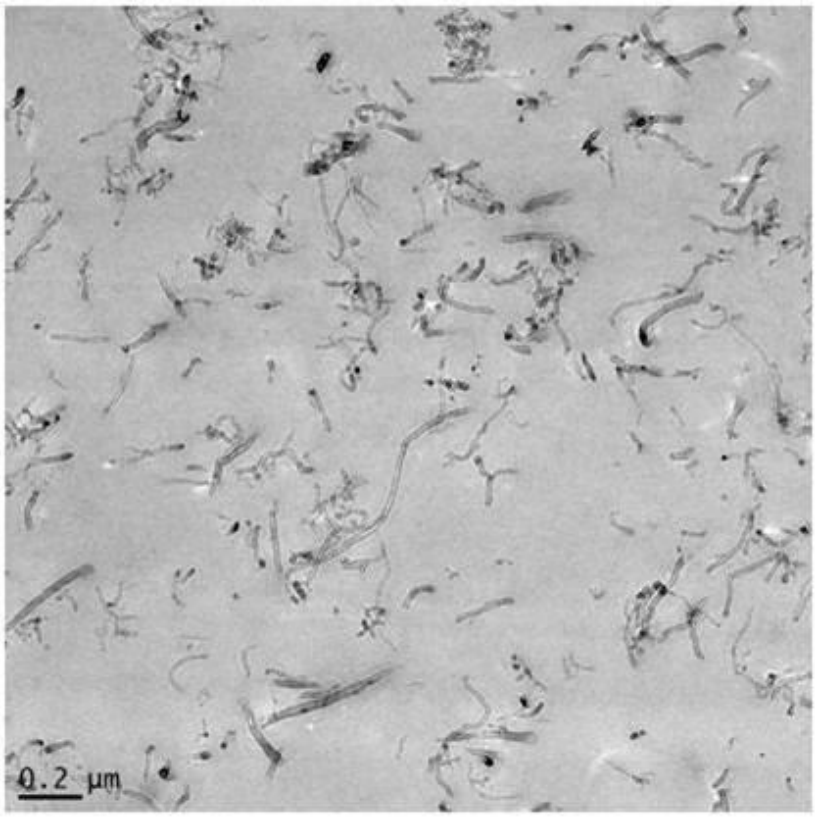

Figure 4.1 TEM micrograph of a cured epoxy-based suspension containing 3wt% MWCNTs.

Flow dichroism experiments were performed using a Couette cell (CC) and a parallel disk (PP) setup. In the case of the Couette cell, the forward scattering data was collected in the flow-gradient plane. The Couette cell had a height of 21 mm and inner and outer radii of 16.95 and 17.95 mm, respectively. The top and the bottom parts were made of quartz to send and collect the laser light in the vorticity direction. Similarly, for the parallel disk setup the top and the bottom disks were made of quartz. The disks had a diameter of 40 mm and the gap was varied from 0.75 to 1.0 mm, depending on the concentration of MWCNTs such that the sample was not opaque.

A home-built optical setup was employed to obtain dichroism data. The optical train is based on field effect modulator as proposed by Frattini and Fuller (1984). A modulated polarization vector of light is generated by sending the light source (λ = 632.8 nm, 10 mW He-Ne laser) through a Glan-Thompson polarizer, P_1-0° (Newport, RI, USA), which is parallel to the laser direction, a photoelastic modulator, PEM-45° (Beaglehole Instruments, New Zealand) oriented at 45° with respect to P_1- 0° and a quarter wave plate, Q-0°, (Newport, RI, USA) oriented at 0° with respect to

P_1-0°. The modulated light is then sent through the sample by a set of prisms. The harmonic parts of the scattering data from the photodiode are sent to two lock-in amplifiers (Stanford Research Systems model 530, Sunnyvale, CA, USA) and the intensity of the first harmonic (R_1) and the second harmonic (R_2) data are recorded using a Labview program. The optical train is arranged such that the scattering due to particle orientation in the flow direction corresponds to a positive dichroism. The required flow field was applied using a MCR300 controlled stress rheometer (Anton-Paar, Graz, Austria).

The flow dichroism is calculated from the extinction coefficient given by Fuller (1995):

$$\delta'' = \left(sign\left(R_2\right)\right)\tanh^{-1}\left[\frac{1}{2}\sqrt{\left(\frac{R_1}{-J_1\left(A\right)}\right)^2+\left(\frac{R_2}{-J_2\left(A\right)}\right)^2}\right] \tag{4.1}$$

where $J_1(A)$ and $J_2(A)$ are Bessel functions of the first kind and A is the amplitude of the photoelastic modulator adjusted to have $J_0(A)=0$. The extinction coefficient and flow dichroism are related by the wavelength and the optical path length (sample thickness) via [Fuller and Mikkelsen (1989)]:

$$\Delta n'' = \frac{\delta''\lambda}{2\pi l} \tag{4.2}$$

where l is the optical path length. Similarly, the orientation angle, χ, of the particles with respect to the flow direction can be calculated using the data obtained by the two lock-in amplifiers:

$$\chi = \frac{1}{2}\tan^{-1}\left[\frac{R_1/J_1\left(A\right)}{R_2/J_2\left(A\right)}\right] \tag{4.3}$$

It should be noted that the orientation angle of the particles is only measurable in the Couette flow cell because, in this case, the scattering data is collected in the vorticity direction. For parallel disk geometry the measured orientation angle cannot be interpreted in a simple way and this is out of scope for the current work.

Two tests were performed on the different samples and they are defined in this paper as “shear ramp” and “start-up” tests. In shear ramp tests the samples were first allowed to rest for a sufficiently long time in order to reach an isotropic initial orientation state before starting the ramp in shear rates. In start-up tests, the samples were allowed to relax to an isotropic state between each shear start-up at different imposed rates. A comparison of the results obtained at each shear rate for the two tests will give us information about the influence of the initial orientation state to the microstructure. Relaxation experiments were performed in the high Pe regime so that all the particles were oriented and once the flow was stopped, particles underwent relaxation to come back to an isotropic state due to Brownian motion. For all tests, the noise is always lower than 9 % of the signal magnitude.

In order to obtain an initial isotropic orientation state, after loading the sample and before all the tests, we applied a pre-shearing step at a rate of 10 s^{-1} for 100 s. Then, we let the samples relax until all the dichroism vanished by observing its decay. Once the dichroism reached the lowest value and was steady for 5 min (meaning the sample orientation state was isotropic) the lock-in amplifiers were re-normalized to zero (the last value of dichroism was the baseline). The MWCNT volume fraction, ϕ, varied between 5.6×10^{-7} and 1.39×10^{-3} from dilute to semi-dilute regime. The limits between the two regimes are defined according to Doi and Edwards (1986) and to Larson (1999) as:

$$\begin{aligned} &cL^2d<1,\ cL^3<1 \text{ dilute;} \\ &cL^2d<1,\ cL^3>1 \text{ semi-dilute.} \end{aligned} \qquad (4.4)$$

where c is the number of particle per unit volume. Thus, the dilute regime for the MWCNT particles (average L = 670 nm and d = 15 nm) is $\phi<3.8*10^{-4}$, while the upper limit of the semi-dilute regime is $\phi\approx1.74*10^{-2}$.

4.4 Dichroism in parallel disk and Couette flow geometries

The shear-induced dichroism, $\Delta n''$, of the MWCNT suspensions in the disk (or parallel plate, PP) flow geometry for different volume fractions is reported in Figure 4.2.

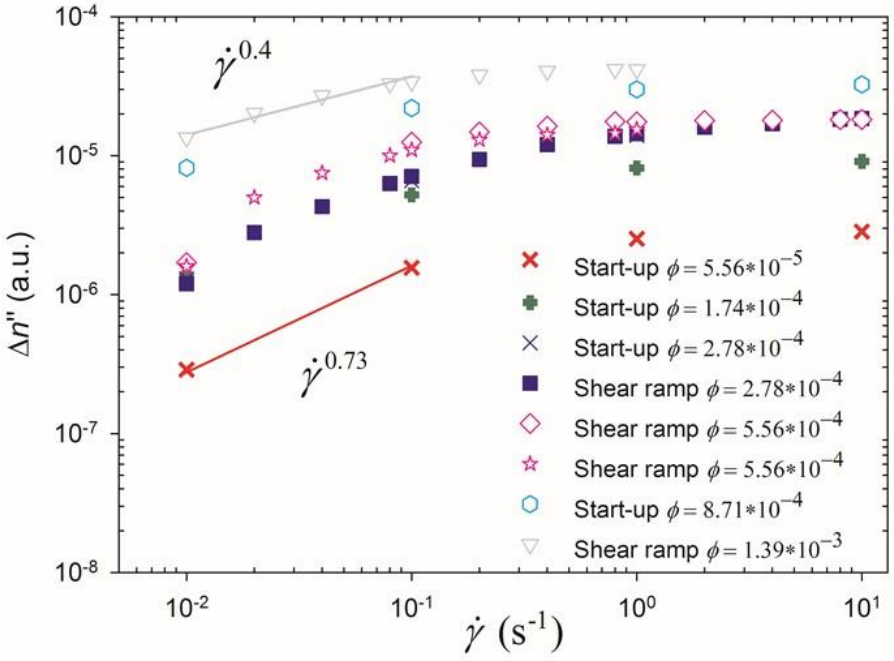

Figure 4.2 Dichroism as function of shear rate for different volume fractions in parallel disk flow geometry. Open symbols indicate concentrations in the semi-dilute regime.

The dichroic response increases monotonically as function of shear rate for the entire volume fraction range analyzed. The trend shows significant changes in the dichroism values only for shear rate lower than 1 s^{-1} where $\Delta n"$ is shown by the solid lines in the Figure 4.2 to be proportional to $\dot{\gamma}^{0.73}$ and $\dot{\gamma}^{0.40}$ for volume fractions of $5.6*10^{-5}$ and $1.39*10^{-3}$, respectively. At higher shear rates, the dichroism levels off without showing any important variation. The signal intensity increases linearly with the volume fraction, as shown in Figure 4.3.

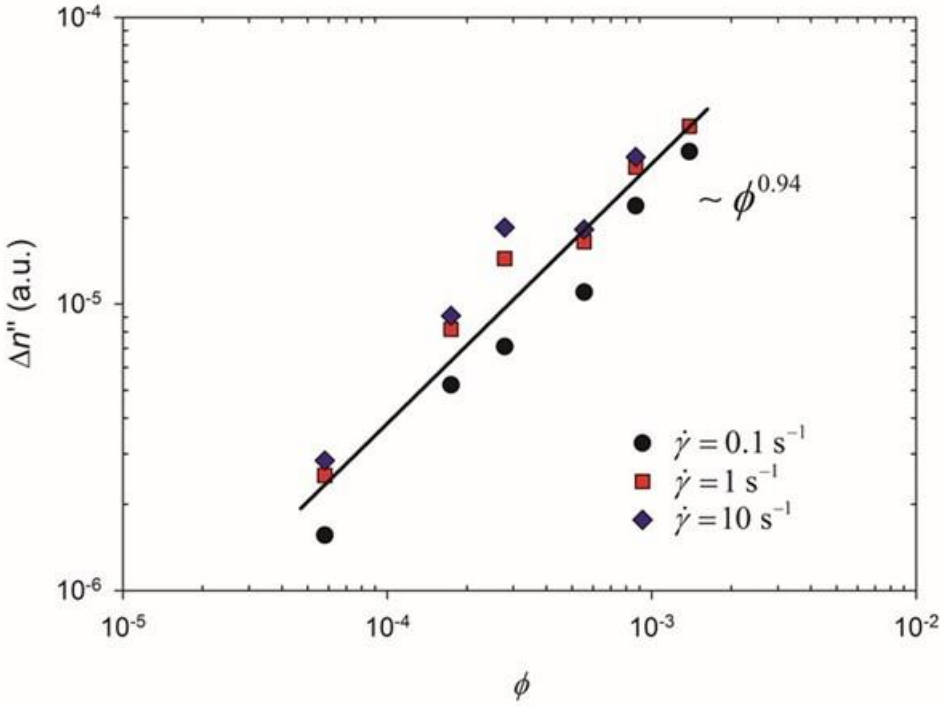

Figure 4.3 Dichroism as function of volume fraction for different shear rates in parallel disk flow geometry.

Hobbie (2004) derived the following expression for the first order term of dichroism for anisotropic particle suspensions:

$$\Delta n'' \approx \frac{1}{2}\phi\left(\alpha_{\parallel}''-\alpha_{\perp}''\right)\Delta S+... \qquad (4.5)$$

where $\alpha_{\parallel}''$ and $\alpha_{\perp}''$ are the complex part of the dielectric constants along and normal to the local symmetry axis of the nanotube, respectively, while ΔS is the difference in the Eigen values of the second order orientation tensor (the choice of the difference of Eigen values involved in Eq. 4.5 depends on the flow plane perpendicular to the light beam considered). For the interested reader, other authors obtained analogous expressions for rigid-type polymer chains [Fuller (1995)] and for rod-like particles [Lenstra *et al.* (2001)].

Eq. 4.5 links the overall orientation of the system with the variation in dichroism. For a perfectly isotropic orientation distribution, the optical response of the system will be about zero (in a homogeneous system), while it will reach a maximum for a completely aligned state. According to Eq. 4.5, the optical response in Figure 4.2 is principally due to a more oriented system with increasing flow intensity. At a shear rate larger than 1 s^{-1}, the intensity does not change anymore because of an already saturated orientation state. In the first decade of shear rate, the slopes of the dichroism curves decrease with the volume fraction, going from $\dot{\gamma}^{0.73}$ to $\dot{\gamma}^{0.4}$ for $\phi = 1.39 * 10^{-3}$ and $\phi = 5.6 * 10^{-5}$, respectively. In the dilute regime, the rods are free to rotate in periodic orbits and, on average, align with the flow direction. As we move into the semi-dilute regime, the interactions between the rods become more important since they scale $O(\phi^2)$ and higher. The contacts between the rods cause a randomizing effect on the orientation distribution of the fibers that is reflected in the shear rate dependency [Natale *et al.* (2014)].

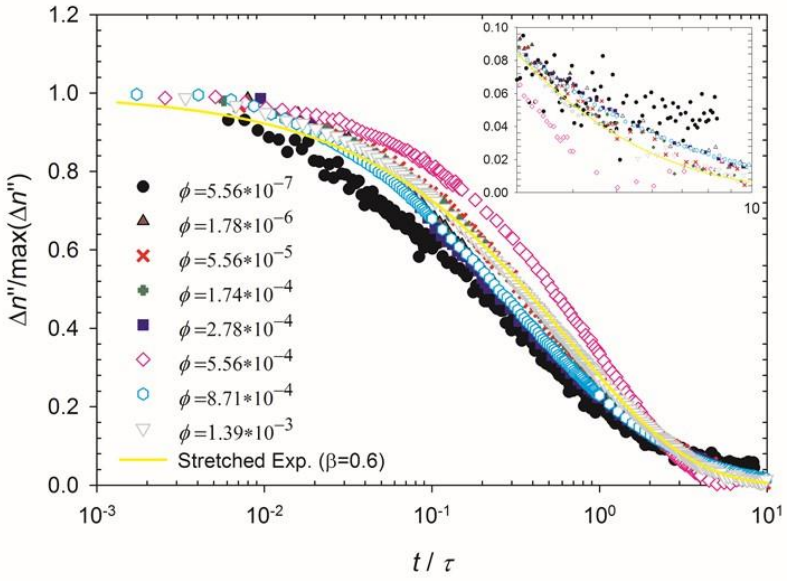

Figure 4.4 Normalized dichroism as function of scaled time during relaxation after shearing at 10 s^{-1} in parallel disk flow geometry. The data at each concentration are scaled with the average relaxation time calculated at that concentration. The solid line represents a stretched exponential function for the α = 0.02 s^{-1} and β = 0.6. The insert is a zoom of the results at long t/τ. Open symbols indicate concentration in the semi-dilute regime.

The dichroism data relative to the relaxation step successive to shearing at 10 s^{-1} are reported in Figure 4.4 for different MWCNT concentrations. The curves are fitted with a stretched exponential function, since a simple exponential function was not able to reproduce correctly the relaxation behavior of these MWCNT suspensions:

$$\frac{\Delta n''}{\max(\Delta n'')} = \exp\left[-(\alpha t)^{\beta}\right] \tag{4.6}$$

The need for the stretched exponential is an evidence of multiple relaxation times in the system, principally due to the polydispersed aspect ratio and flexibility of the MWCNTs. Conversely, one can write the stretched exponential function as a sum of pure exponential decays weighted by a particular probability distribution function of α for a given value of β [Johnston (2006)]. For each concentration, it is possible to calculate an average relaxation time from fitting the data of Figure 4.4:

$$\tau = \int_0^{\infty} \mathrm{e}^{-(\alpha t)^{\beta}} dt = \frac{1}{\alpha\beta}\Gamma\left(\frac{1}{\beta}\right) \tag{4.7}$$

where Γ is the gamma function. Once the relaxation time is known, the rotary diffusion coefficient is evaluated as $D_r \approx (6\tau)^{-1}$ [Fuller (1995)]. The values obtained for α, β and D_r are reported in Figure 4.5 and a stretched exponential function is reported in Figure 4.4 for average values of α and β.

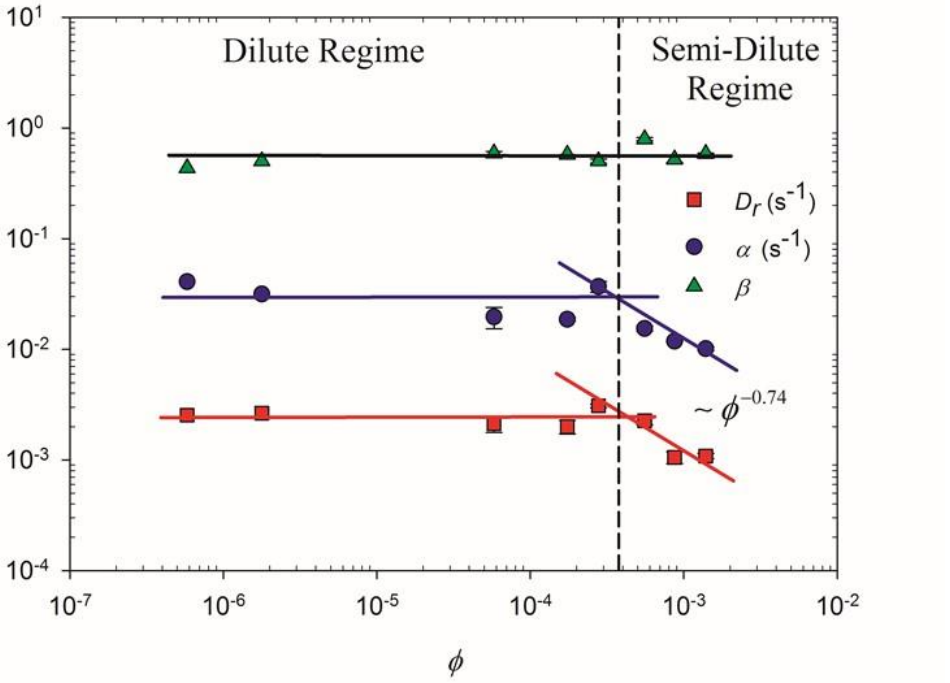

Figure 4.5 Rotary diffusion, α and β (of the stretched exponential function) as functions of volume fraction. The vertical dashed line represents the theoretical limit between the dilute and semi-dilute regimes [Doi and Edwards (1986)]. The solid lines are guidelines.

The rotary diffusion coefficient has a constant value in the dilute regime ($\phi < 3.8 * 10^{-4}$). The average value of D_r^{-1} obtained from the experimental data is 393 s, while the one calculated according to the theory of Doi and Edwards (1986) is

$$D_r^{-1} = \frac{\pi \eta_0 L^3}{3 k_B T \left[\ln(r) - 0.8\right]} = 314 \text{ s} \qquad (4.8)$$

where k_B and T are the Boltzmann constant and the absolute temperature, respectively. The limit between the dilute and semi-dilute regimes is correctly predicted by Doi and Edwards (1986) as showed in Figure 4.5. For all the calculation, average values for the diameter and length of the MWCNTs were considered. As soon as the limit between the dilute and semi-dilute regimes is reached, the rotary diffusion coefficient decreases with increasing volume fraction. However, the power-law coefficient of - 0.74 is quite far from the - 2 proposed by Doi and Edwards (1986). This

discrepancy could be attributed to the fact that only four points were considered to determine this slope. More data in the semi-dilute regime would be needed to confirm this result. Unfortunately, suspensions with higher MWCNT contents were too opaque to be probed experimentally. In addition, a transition zone, where the volume fraction power-law index changes gradually from 0 to - 2 between the two regimes, is expected. This transition zone is the result of the polydispersity and flexibility of the particles that is not directly accounted for by Doi and Edwards (1986). Since the analyzed semi-dilute volume fractions are close to the frontier between the two regimes, they are possibly located in this transition zone, explaining the low value of the power-law index (- 0.74) found experimentally.

The average β value of the stretched exponential is around 0.6 and seems to be independent of the volume fraction. As mentioned above, it is related to the polydispersity of the aspect ratio and possible flexibility of the MWCNTs that result in a spectrum of relaxation times. On the other hand, the value of α has a similar behavior to the rotary diffusion and has units of s^{-1}. Thus, it describes the effect of excluded volume interactions between the rods [Bellini *et al.* (1989)].

The first order term of the refractive index tensor suggests (as shown in Eq. 4.5) a linear dependency with the volume fraction. This is consistent with the scaling behavior firstly reported by Fry *et al.* (2006).

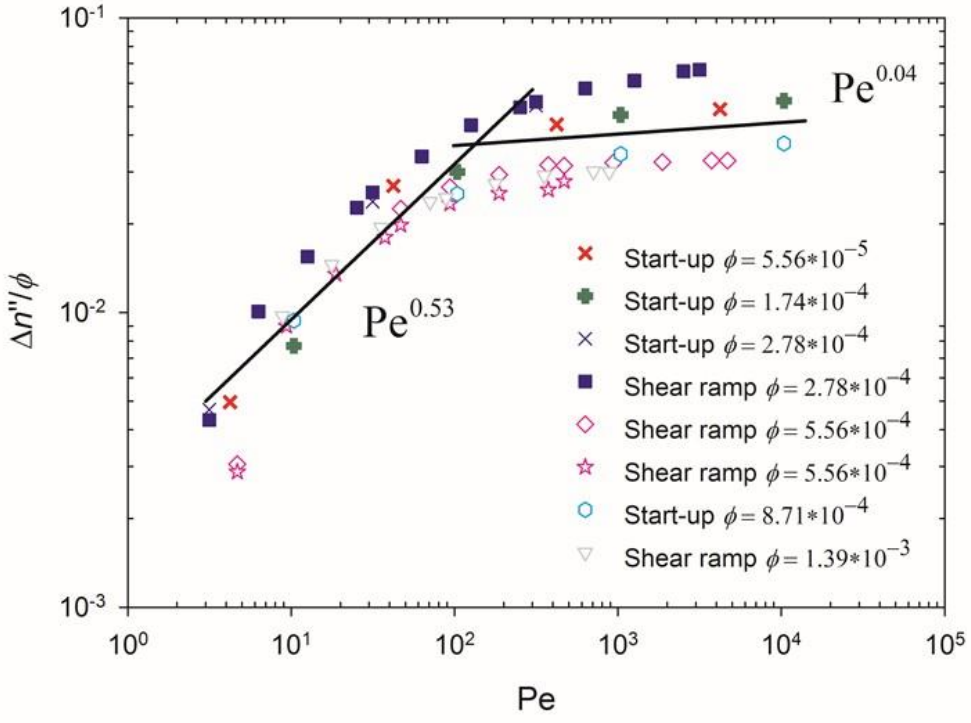

Figure 4.6 Dichroism scaled with volume fraction as function of Peclet number in parallel disk flow geometry. Open symbols indicate concentrations in the semi-dilute regime.

In Figure 4.6, the scaled dichroism is reported for the parallel disk data as a function of the rotational Peclet number $\mathrm{Pe} = \dot{\gamma}/D_r$. Data for the different concentrations are overlapping. The scaled dichroism increases mainly for Pe lower than 10^2, where it is proportional to $\mathrm{Pe}^{1/2}$. This zone is followed by a plateau where the dichroism changes slightly ($\sim\mathrm{Pe}^{0.04}$). This is in contrast with the scaling behavior proposed by Fry *et al.* (2006). They found for their MWCNTs (with *r* four times larger than the particles used in this work) at high Pe ($10^4 \le \mathrm{Pe} \le 10^9$) that $\Delta n''/\phi$ was proportional to $\mathrm{Pe}^{0.16}$. This discrepancy might be because their suspensions were mainly in the semi-dilute regime, implying that particle-particle interactions worked strongly against the progressive alignment of the nanotubes.

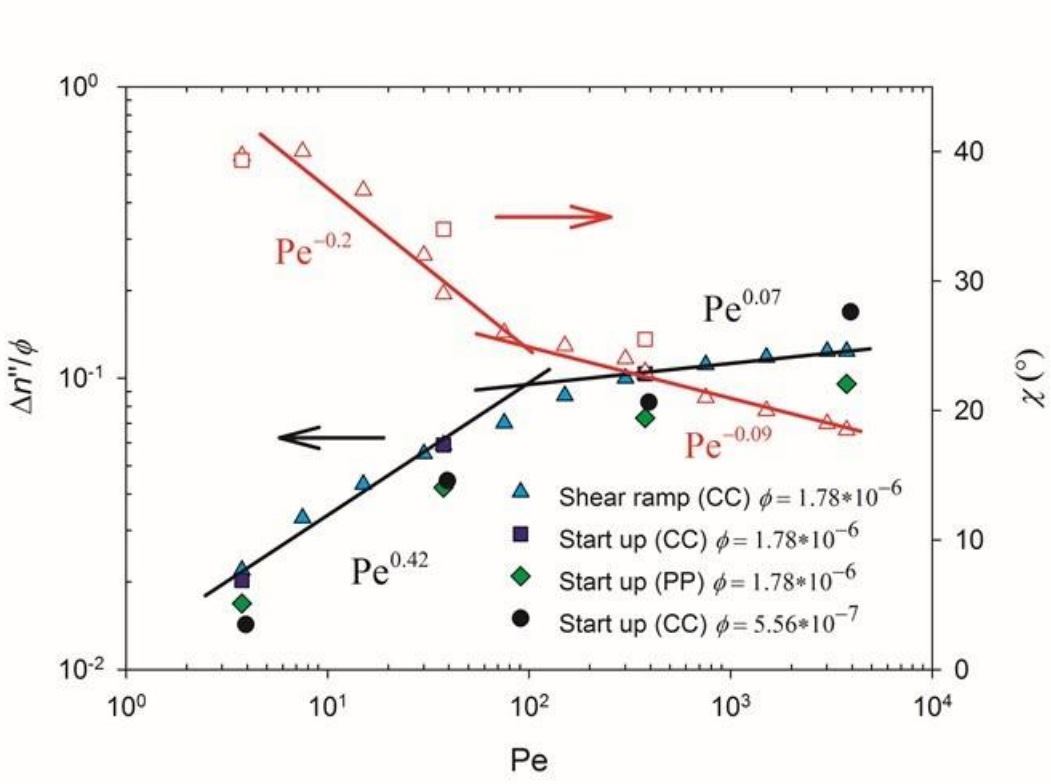

Figure 4.7 Dichroism scaled with volume fraction and orientation angle as functions of Peclet number. The data were obtained in Couette cell (CC) and PP flow geometries. Open symbols refer to the orientation angle.

The same scaling is used in Figure 4.7, where the values of dichroism and orientation angle obtained in a Couette cell flow geometry for the dilute suspensions ($\phi < 3.8*10^{-4}$) are reported. In this case, the light beam was perpendicular to the flow and velocity gradient plane, allowing for direct evaluation of the angle χ between the principal axis of the particle and the flow direction.

It should be noted that for the lowest concentration ($\phi = 5.56*10^{-7}$) the dichroism signal was quite low and it was not possible to obtain values for the orientation angle.

The dichroism shows a similar behavior to the results obtained in the disk or PP flow geometry. For $Pe < 10^2$, $\Delta n''/\phi$ scales as $\propto Pe^{0.42}$, hence with a slightly lower power-law index compared to the one found for the PP geometry (0.53). For Pe < 1, it is expected that the first deviation from an isotropic orientation state would be linear in the flow-gradient plane, while quadratic in the flow-vorticity plane [Doi and Edwards (1986)]. Hence at low Pe, this could explain why a stronger rate

dependency is found in the PP geometry with respect to the one found in the Couette flow cell. At high Pe, the slope of the dichroism curve tends to zero since change in orientation is negligible (negligible slope for the orientation angle). The marginal effect of the Brownian motion of these suspensions is clearly seen for $Pe < 10^2$ where the orientation angle changes quickly with increasing shear rate. Surprisingly, the orientation angle is far from zero even at high Pe where it reaches the minimum value of 18° at $Pe = 4*10^3$. For concentrated MWCNT suspensions, Pujari *et al.* (2011) found lower values of the orientation angle ($\approx 5^\circ$) from SAXS at $\dot{\gamma} = 10\ s^{-1}$. However, this shear rate for their combination of MWCNTs and matrix corresponded to $Pe \approx 10^6$, three order of magnitude higher than the maximum Pe probed in our work.

At high shear rates, the hydrodynamic force dominates the Brownian motion; hence, the randomizing effect of the rotary diffusion cannot be the cause of the misalignment. In addition, interactions between rods can also be excluded as a possible cause considering the very low volume fraction (dilute regime) used in these experiments. The only other possible answer to explain this peculiar behavior needs to be in the conformation of the rods. The TEM micrograph in Figure 4.1 obtained on a cured epoxy suspension shows that the equilibrium conformation of these particles is far from being straight. This is mainly due to the presence of structural defects at the MWCNT walls, which cause them to be bent [Hobbie (2004)].

The bending of the particles might be the cause of the behavior observed in Figure 4.7 and its effect is analyzed in the next section. For this purpose, a new model is developed based on the hypothesis that the equilibrium conformations of MWCNTs are not straight but actually bent. More specifically, we try to answer the following question: Is it possible that the misalignment with respect to the flow direction at high Pe is due to the flexibility and bending of the rods, as illustrated in Figure 4.1?

4.5 Model

4.5.1 Definitions and hypotheses

Following Strautins and Latz (2007), we consider flexible rods made of three spheres and two infinitely thin connectors of lengths L_α and L_β (Figure 4.8).

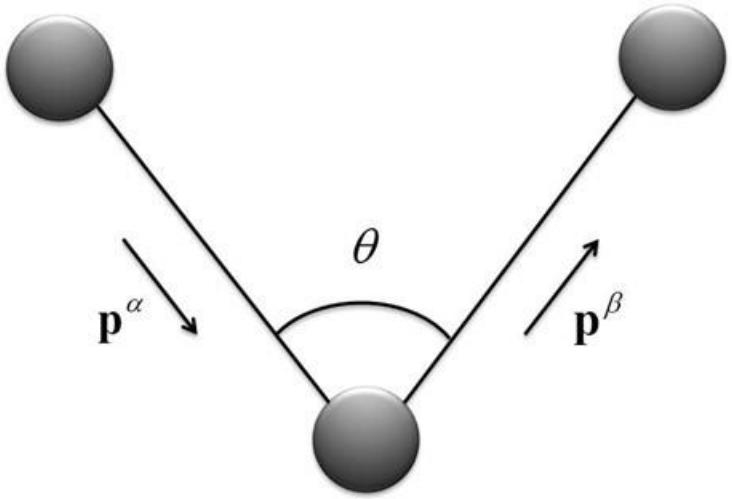

Figure 4.8 Flexible particle scheme.

The central bead is located at $\mathbf{r}_c$ with respect to a fixed reference system $\mathbf{R}$. The other two beads (named alpha and beta) are located respectively at $\mathbf{r}_c - L_\alpha \mathbf{p}^\alpha$ and $\mathbf{r}_c + L_\beta \mathbf{p}^\beta$. The quantities $\mathbf{p}^\alpha$ and $\mathbf{p}^\beta$ are two unit vectors oriented from bead alpha to the center bead and from the center bead to the beta one, respectively. As previously mentioned, the reason behind the orientation results obtained in the Couette flow geometry needs to be connected with the single particle dynamics and in particular, with particle conformation. The following hypotheses are stated for developing the model to describe the behavior at high Pe number and in the dilute concentration regime:

1. All beads have the same mass and radius.
2. The particles are considered inertialess and the gravitational effect is negligible.
3. The suspended particles are assumed to be distributed uniformly, i.e., there is no concentration gradient.
4. The bulk flow is assumed to be homogeneous and the velocity gradient $(\nabla \mathbf{v}^\infty = \boldsymbol{\kappa}^\dagger)$ is constant over the particle length.
5. The particles have large aspect ratio and, hence, Brownian motion is neglected.
6. The matrix is considered incompressible and Newtonian with a viscosity η_0.

7. The particle flexibility is described according to a cosine harmonic potential and the equilibrium positions of the particles are bent.
8. Particle-particle interactions are neglected.

4.5.2 Equations

4.5.2.1 Particle rotary velocity

In their work, Strautins and Latz (2007) proposed the following elastic potential to describe flexibility:

$$U = \tilde{k}\left[1-\left(\mathbf{p}^{\alpha}\cdot\mathbf{p}^{\beta}\right)\right] \tag{4.9}$$

where $\tilde{k}$ characterizes the resistance to bending. This potential allows only straight rods at equilibrium or, in other words, it exhibits a minimum when the two rods are on a straight line. This implies that in the absence of external forces the particles tend to simply assume a straight rod configuration. As shown previously in Figure 4.1, the MWCNTs are bent at equilibrium; hence, to describe this behavior, a cosine harmonic potential [Bulacu *et al.* (2013)] is considered to be acting on the particle to describe the bending resistance:

$$U = \frac{1}{2}k\left[e-\left(\mathbf{p}^{\alpha}\cdot\mathbf{p}^{\beta}\right)\right]^{2} \tag{4.10}$$

The parameter *k* represents the stiffness of the particle while $\cos^{-1}(e)$ is the equilibrium angle between $\mathbf{p}^{\alpha}$ and $\mathbf{p}^{\beta}$. This potential is a restricted bending potential and allows us to describe particles whose equilibrium position is far from a straight rod. An alternative approach was used in Brownian dynamics simulations where the bending potential of Eq. 4.10 was coupled with *a priori* chosen bent configuration [Cruz *et al.* (2012)].

To evaluate the rotary velocity of these flexible particles, it is necessary to write the evolution of each connector. The hydrodynamic and bending forces act on each bead. From the force balance derived in Appendix A, it is shown that the particle center of mass moves affinely with the flow

velocity. Hence, the spatial distribution of the rod center of mass remains homogenous under flow. Considering the reference system on the central bead, the torque due to the hydrodynamic force (proportional to the relative velocity between the fluid and the particle) on bead alpha is written as:

$$\mathbf{T}_H^\alpha = -L_\alpha \mathbf{p}^\alpha \times \mathbf{F}_H^\alpha = -L_\alpha \mathbf{p}^\alpha \times \varsigma \left[+\boldsymbol{\kappa} \cdot \left(-L_\alpha \mathbf{p}^\alpha \right) + L_\alpha \dot{\mathbf{p}}^\alpha \right] \tag{4.11}$$

where ς is the drag coefficient on a sphere.

In addition, the bending potential causes an intra-particle torque equal to:

$$\mathbf{T}_B^\alpha = -\mathbf{p}^\alpha \times \frac{\partial U}{\partial \mathbf{p}^\alpha} = -\mathbf{p}^\alpha \times \left[-k \left(e - \mathbf{p}^\alpha \cdot \mathbf{p}^\beta \right) \left(\boldsymbol{\delta} - \mathbf{p}^\alpha \mathbf{p}^\alpha \right) \cdot \mathbf{p}^\beta \right] \tag{4.12}$$

where $\boldsymbol{\delta}$ is the unit tensor. The intensity of the bending torque is proportional to how far from equilibrium the angle between the two rods is and its direction is perpendicular to the unit vector $\mathbf{p}^\alpha$.

The sum of the two torques is equal to zero because of the inertialess assumption. After some manipulations, the expression for the rotary velocity of the connector alpha is finally obtained:

$$\dot{\mathbf{p}}^\alpha = \boldsymbol{\kappa} \cdot \mathbf{p}^\alpha - \boldsymbol{\kappa} : \mathbf{p}^\alpha \mathbf{p}^\alpha \mathbf{p}^\alpha + \frac{k}{\varsigma L_\alpha^{\,2}} \left(e - \mathbf{p}^\alpha \cdot \mathbf{p}^\beta \right) \left(\boldsymbol{\delta} - \mathbf{p}^\alpha \mathbf{p}^\alpha \right) \cdot \mathbf{p}^\beta \tag{4.13}$$

Following the same procedure on the bead beta, the rotary velocity of $\mathbf{p}^\beta$ is calculated as:

$$\dot{\mathbf{p}}^\beta = \boldsymbol{\kappa} \cdot \mathbf{p}^\beta - \boldsymbol{\kappa} : \mathbf{p}^\beta \mathbf{p}^\beta \mathbf{p}^\beta + \frac{k}{\varsigma L_\beta^{\,2}} \left(e - \mathbf{p}^\alpha \cdot \mathbf{p}^\beta \right) \left(\boldsymbol{\delta} - \mathbf{p}^\beta \mathbf{p}^\beta \right) \cdot \mathbf{p}^\alpha \tag{4.14}$$

In Eqs. 4.13 and 4.14, the orientation evolution is composed of two parts. The first two terms on the right side of the equations correspond to the Jeffery equation for an ellipsoid of infinite aspect ratio, while the last term is the coupling effect between the orientation of $\mathbf{p}^\alpha$ and $\mathbf{p}^\beta$ due to the introduction of the bending potential.

For the sake of completeness, the expression for the stress tensor is derived in Appendix B and an approach to solve a modified Fokker-Planck equation for flexible rods is presented in Appendix C. The approach leads to two new fourth-order non-symmetric tensors that require closure approximations to solve the sets of equations. Instead of proposing questionable closure approximations at this point, we use particle based simulations as described in the next section.

4.5.2.2 Particle based simulations

As discussed in Appendix C, we were not able to close the problem obtained writing the orientation distribution function (ODF) moments evolution. In order to have first insights on the predictions of the model, we proceed in this work with a particle-based simulation approach. It consists in following the orientation evolution of a numerically significant number of particles to accurately compute average properties. We are not required to solve the equation of the center of mass velocity since we already know that the particles move homogenously with respect to the fluid element at the same position. The numerical solution is obtained through a more simple set of ordinary differential equations (ODEs). Thus, we firstly set a random initial orientation for *N* particles. Then, we solve the ODEs (Eqs. 4.13 and 4.14) for each particle. Once we know the orientation evolution of the *N* particles constituting the suspensions, we are able to calculate $\mathbf{a}_2 = \iint \mathbf{p}^\alpha \mathbf{p}^\alpha \psi d\mathbf{p}^\alpha d\mathbf{p}^\beta$, $\mathbf{b}_2 = \iint \mathbf{p}^\alpha \mathbf{p}^\beta \psi d\mathbf{p}^\alpha d\mathbf{p}^\beta$ and $\mathbf{c}_2 = \iint \mathbf{p}^\beta \mathbf{p}^\beta \psi d\mathbf{p}^\alpha d\mathbf{p}^\beta$ (Appendix C) by numerically solving the integrals. For clarity, if we consider the tensor $\mathbf{a}_2$, it is calculated as follows:

$$\mathbf{a}_2 \equiv \iint \mathbf{p}^\alpha \mathbf{p}^\alpha \psi d\mathbf{p}^\alpha d\mathbf{p}^\beta = \frac{1}{N} \sum_{n=1}^{N} \mathbf{p}^{\alpha^{(n)}} \mathbf{p}^{\alpha^{(n)}} \tag{4.15}$$

The value *N* is obtained numerically by finding the minimum number of particles above which the values of the second order tensors become independent of *N*. It was found that *N* = 500 was a sufficient number of particles and the following results are obtained with this value.

Since we assign randomly the initial position of each connector, we might start to shear a system that it is not at equilibrium because some particles could be in a given conformation that is far from their equilibrium. To avoid this problem, the initialization step is followed by a rest stage where we solve Eqs. 4.13 and 4.14 for a shear rate equal to zero until steady state and only at this point,

we start shearing the system. The rest step allows the particles to relax until they reach their equilibrium positions or, in other words, it allows dissipating the non-zero components of the stress tensor due to the bending potential.

It is important to underline that since we are solving Eqs. 4.13 and 4.14, the particles are non-Brownian. This implies that the predictions of the model are physically valid only at high Pe numbers, which is fortunately the region of interest for this work.

4.6 Parametric analysis

The introduction of the bending potential brings into the model two adjustable parameters that characterize the particles. The stiffness coefficient *k* has units of [N·m] and it controls the flexibility of the particles (higher *k* means lower flexibility). The equilibrium conformation *e* defines the angle between $\mathbf{p}^{\alpha}$ and $\mathbf{p}^{\beta}$, when the bending potential reaches a minimum. In this and following sections, we consider particles with connectors of the same length ($L = L_{\alpha} = L_{\beta}$) and beads of the same diameter for simplicity purposes. From Eqs. 4.13 and 4.14, we can define the following parameter:

$$k_S = \frac{1}{t_B} = \frac{k}{\varsigma L^2} \tag{4.16}$$

where k_S has units of s^{-1} and it represents the inverse of the characteristic bending time t_B. It is chosen instead of parameter *k* avoiding defining particle length and diameter.

To better understand the predictions of the model, a first interesting aspect to analyze is the period of rotation of these flexible particles. For a clear representation, let us consider a single particle in simple shear flow. To follow its evolution, it is straightforward to consider the projection of one of the two unit vectors, i.e. $\mathbf{p}^{\alpha}$, on the flow direction $\boldsymbol{\delta}_1$ ($p_1 = \mathbf{p}^{\alpha} \cdot \boldsymbol{\delta}_1$). For the simulations reported in this section, the equilibrium conformation *e* is chosen to be equal to 0.7 (corresponding to 134.5 ^{o} for the angle between the two rods of Figure 4.8). This value was chosen arbitrarily, but it does not affect the validity of the following discussion. In addition, the shear rate used for these simulations was set equal to 1 s^{-1}.

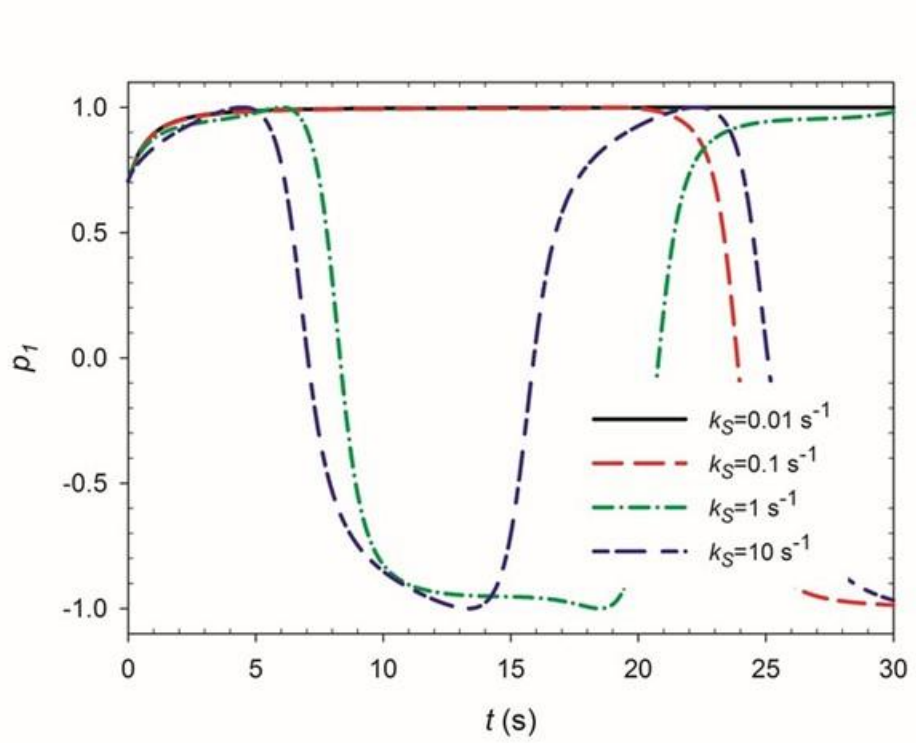

Figure 4.9 Evolution of the flow direction component of the unit vector $\mathbf{p}^{\alpha}$ for different values of k_S at a shear rate equal to 1 s^{-1}.

We report in Figure 4.9 the evolution of p_1 as a function of time for values of k_S varying between 10^{-2} and 10 s^{-1}. For low k_S, the rotary velocity of the particle is dominated by the hydrodynamic contribution. In particular, when k_S is equal to 10^{-2} s^{-1}, the particle aligns with the flow direction and stays in this position indefinitely. This peculiar behavior can be understood by analyzing Eqs. 4.13 and 4.14. When $k_S \approx \dot{\gamma}$, the coupling term between $\mathbf{p}^{\alpha}$ and $\mathbf{p}^{\beta}$ becomes negligible and the particle behaves as a rod of infinite aspect ratio, accordingly to the Jeffery equation. With increasing values of k_S, the particle becomes more and more rigid and it rotates in the gradient-flow plane. The period of rotation becomes shorter as k_S increases since the torque due to the bending potential is more intense. Each connector pulls and pushes the other one during the rotation, keeping the angle between $\mathbf{p}^{\alpha}$ and $\mathbf{p}^{\beta}$ around the equilibrium position.

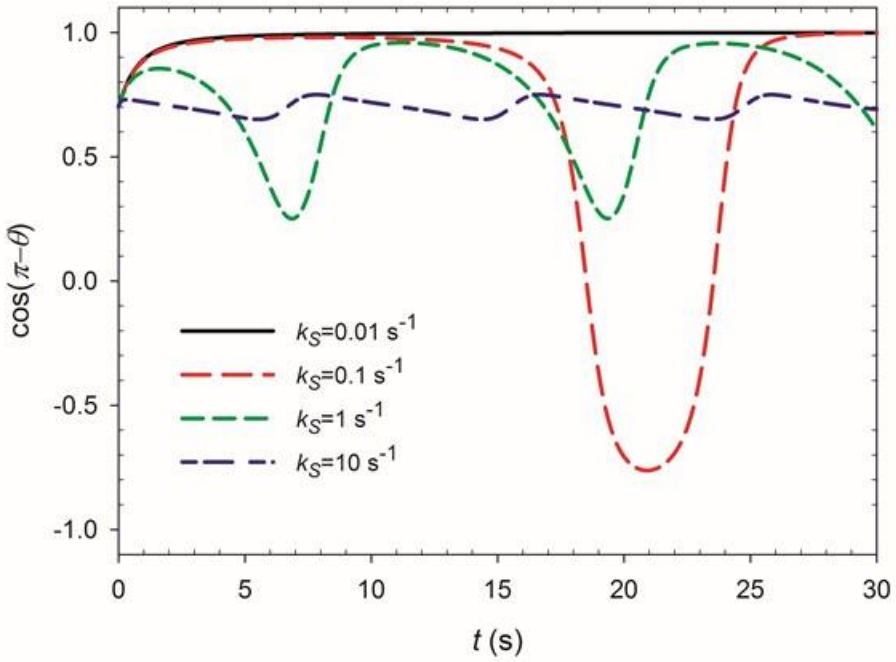

Figure 4.10 Evolution of cos (π-θ) (angle between $\mathbf{p}^{\alpha}$ and $\mathbf{p}^{\beta}$) for different values of k_S at a shear rate of 1 s^{-1}.

The evolution of the angle θ between $\mathbf{p}^{\alpha}$ and $\mathbf{p}^{\beta}$ on a plane containing the two unit vectors is reported during particle rotation in Figure 4.10. In the case of $k_S = \dot{\gamma}$, the cosine of θ is equal to 1. The flow stretches the particle in a straight rod configuration. Increasing k_S, cos(π-θ) oscillates around the equilibrium conformation with a decreasing period and intensity. Hence, the particle becomes more rigid and the torque is minimized due to the bending potential during the rotation.

When we consider a suspension in the dilute regime, all the particles are rotating independently. However, the overall system has a well-defined orientation obtained by averaging all the particles orientations at each instant. This is shown in Figure 4.11 where we report the normal component of the tensor $\mathbf{a}_2$ in the flow direction, i.e. a_{11}, and the trace of $\mathbf{b}_2$.

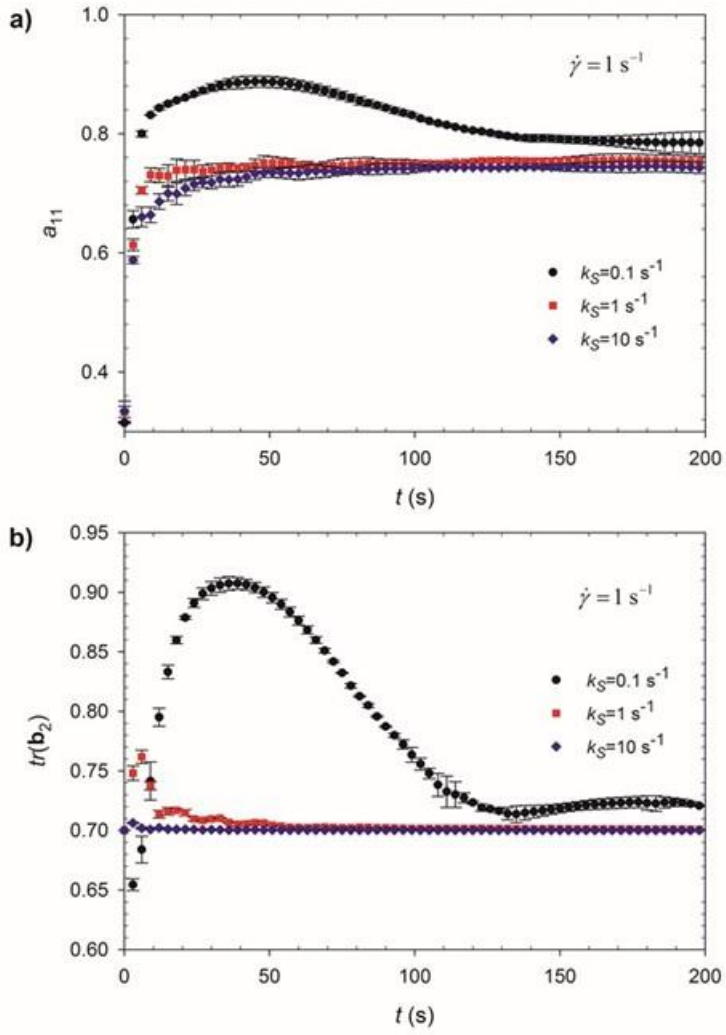

Figure 4.11 Evolution of a) a_{11} component and b) trace of $\mathbf{b}_2$ for different values of k_S at a shear rate of 1 s^{-1}.

More in details, we report in Figure 4.11 the averages of four simulations with the relative standard deviations (error bars). This is because the initial condition is always random and, hence, each simulation starts from a slightly different condition, like in an experimental rheological test. Since we start from an isotropic state, the evolutions of the $\mathbf{c}_2$ components are similar to the ones of $\mathbf{a}_2$, and for the sake of brevity are not reported here. The a_{11} component (Figure 4.11a) presents a significant overshoot for $k_S < \dot{\gamma}$ while it increases monotonically for $k_S \geq \dot{\gamma}$ to reach rapidly steady state. Under steady state, the more flexible particles ($k_S = 0.1\ s^{-1}$) get more aligned in the flow

direction. Analyzing the trace of $\mathbf{b}_2$ in Figure 4.11b, which represents the average cosine of the angle between the connectors $\mathbf{p}^{\alpha}$ and $\mathbf{p}^{\beta}$ [Ortman *et al.* (2012)], it becomes clear that the overshoot in a_{11} for $k_S < \dot{\gamma}$ is due to the stretching effect of the shear flow that opens up the particles in a "rod-like" configuration, and aligns them in the flow direction. In this case, the trace of $\mathbf{b}_2$ presents a large overshoot and then levels off towards the equilibrium value. As k_S increases, the intensity of the overshoot decreases until almost disappearing. This behavior is due to the fact that the average conformation angle does not vary significantly with respect to the chosen equilibrium position.

On the other hand, parameter *e* controls the equilibrium angle θ between the two connectors. It does not influence the time evolution of the particles, but it determines variations in the degree of orientation under steady state (not shown here). The straighter the particles are, the more they tend to align in the flow direction as they slow down their rotation when in the flow direction. Again, these considerations are valid only in the dilute regime.

Concluding this section, a distinction needs to be made between quenched and strain-induced bending. In our simple model, the parameter *e* controls the particle equilibrium conformation; hence, it determines the "frozen" or quenched bent conformation. When the particle is in this conformation, no torque due to the bending potential acts on the particle arms. In the presence of flow, the hydrodynamic torques can displace the arms from the equilibrium position, causing stretching or more pronounced bending. The competition between the hydrodynamic and bending torques, which is controlled by the ratio $k_S/\dot{\gamma}$, will determine the evolution of the conformation of the particle during flow. In this scenario, we refer to strain-induced bending. Finally, no thermal bending is present in the model since the effect of Brownian motion is neglected here.

4.7 Predictions at high Pe

We are interested now in explaining the high values of the orientation angle shown in Figure 4.7. To quantify the flexibility of the rods, the effective stiffness is calculated as $S^{eff} = E_Y \pi / 64 \eta_s \dot{\gamma} r^4$ [Switzer III and Klingenberg (2003)] where E_Y is the Young modulus of the MWCNTs and is considered to be 40 GPa according to Hobbie and Fry (2007). We underline that a precise value for the Young modulus might be highly depending of the specific sample, but the following

analysis is sensitive only to order of magnitude changes. Using an average aspect ratio *r* of 45, the value of S^{eff} can be estimated to be in the range of 3.8 to 38.5 for our MWCNTs. Hence, we can consider that on average these particles are moderately stiff in the range of shear rates analyzed.

To represent this complex system with our mathematical description, we chose a value of 1 s^{-1} for the parameter k_S that is of the same order of the shear rates analyzed $k_S/\dot{\gamma} \in [0.1,1]$, guaranteeing that the particles are sufficiently stiff in comparison with the flow intensity. Parameter *e* was obtained by fitting the steady-state values of the orientation angle at each shear rate. The effective stiffness S^{eff} presents a strong dependency on the aspect ratio. Our MWCNTs are polydispersed in length and diameter and, nevertheless, they act overall as moderately stiff, a spectrum of behaviors ranging from rigid to completely flexible is present. Therefore, the equilibrium angle is assumed to be a function of the shear rate in order to keep into consideration this large range of behaviors.

Following Fuller (1995) who expressed dichroism and orientation angle for rigid rod suspensions as functions of the orientation tensor, the expression is here modified to account for the particles made of two connectors as follows:

$$\Delta n'' = M\frac{\phi}{2}\left[\left(a_{11}^2 - a_{22}^2 + 4a_{12}^2\right)^{0.5} + \left(c_{11}^2 - c_{22}^2 + 4c_{12}^2\right)^{0.5}\right]$$

$$\tan(2\chi) = \frac{1}{2}\left[\left(\frac{2a_{12}}{a_{11} - a_{22}}\right) + \left(\frac{2c_{12}}{c_{11} - c_{22}}\right)\right] \tag{4.17}$$

where M is a proportionality constant associated with the intrinsic optical anisotropy of the system and is determined by comparing the predictions with the experimental values. Since our particles are made of two arms, $\Delta n''$ and χ are obtained as algebraic means of the alpha and beta connector contributions.

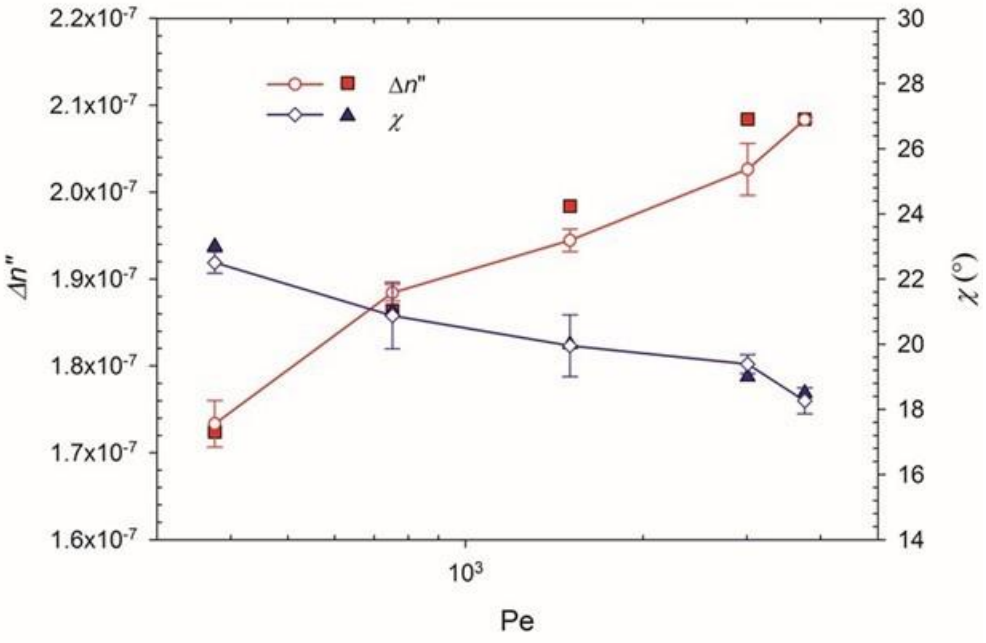

Figure 4.12 Comparison between experimental (filled) and predicted (unfilled) values of dichroism and orientation angle obtained in the Couette flow geometry.

Figure 4.12 compares the experimental and predicted values for dichroism and orientation angle for $\mathrm{Pe} > 10^2$ obtained in the Couette flow geometry using k_S equal to 1 s^{-1} and e as a fitting parameter. As previously discussed, the predictions of the model obtained for particle-based simulations without the addition of stochastic terms to represent Brownian motion are physically valid only in this high Pe regime. As seen in Figure 4.12, the model is able to correctly predict the rheo-optical behavior of the dilute epoxy-MWCNT system, confirming that the equilibrium conformation of these MWCNTs is not straight but bent. The values of e obtained by fitting the orientation angle are presented in Figure 4.13.

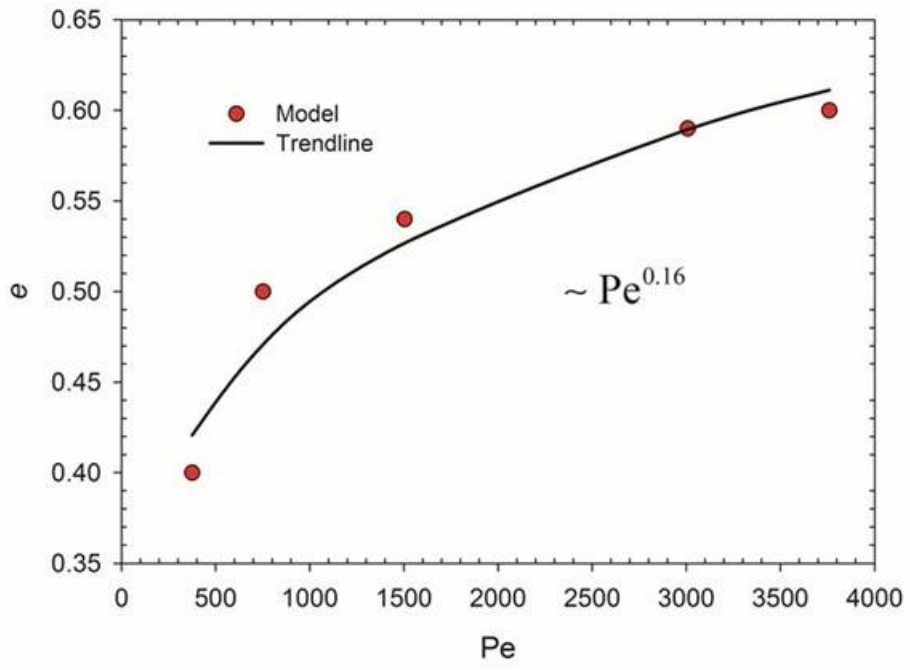

Figure 4.13 Fitted values for the equilibrium position *e* as a function of Pe. The trendline represents the regression of the data with a power-law expression.

As the intensity of the flow increases, the particles get more and more straight. The equilibrium position scales as $\propto \mathrm{Pe}^{0.16}$ showing a stronger dependency than the one found experimentally for the orientation angle $\propto \mathrm{Pe}^{-0.09}$ (Figure 4.7). The value of the exponent (0.16) in Figure 4.13 is obtained by a regression of the data with a power-law expression. Conversely, the flow efficiency in aligning the particles is here lowered due to the fact that the particles can bend to disperse the flow energy.

From the ratio between the predicted and experimental dichroism, the value of M, which is related to the intrinsic anisotropy and polarizability of MWCNTs in epoxy, is found to be 2×10^{-17} mL, about 5 order of magnitude larger than the values reported by Chow *et al.* (1985a) for collagen in a glycerin-water mixture.

Concluding, the high values of the orientation angle with respect to the flow direction are found, with the help of a simple model, to be caused by particle bending and flexibility. Indeed, particle stretching induces a more oriented system, as confirmed by the good agreement between the model

predictions and experimental data for $\Delta n''$ and χ. This is a consequence of the interplay between particle conformations and hydrodynamic torques. The hydrodynamic torque for these slender bodies exhibits a minimum in the case of straight particles perfectly oriented in the flow direction. Hence, the system tries to reach that state, but is limited by the imposed bending potential that traps the system in a different conformation which depends on the imposed shear rate.

4.8 Concluding remarks

Dichroism evolution of non-Brownian epoxy-based MWCNT suspensions can be divided into two regimes. For $Pe < 10^2$, MWCNTs are partially aligned in the flow direction due to hydrodynamic forces, while for higher Pe, the already saturated orientation state of the system changes slightly. Doi and Edwards (1986) theory was found to predict correctly the limit between the dilute and semi-dilute regimes. However, their theory predicts that dichroism scales with $Pe^{0.25}$ in the case of semi-dilute suspensions at modest Peclet numbers and this is not in agreement with our experimental findings ($Pe^{0.53}$ and $Pe^{0.42}$ in the case of PP and CC geometry, respectively).

Unlike other rod-like particles, for example collagen, MWCNTs show high values of the orientation angle (~ 18°) in the high Pe region investigated in this work. Our simple model confirmed that this behavior is mainly due to a non-straight equilibrium conformation of the particles. In the model, orientation dynamic of flexible slender bodies is controlled by hydrodynamic and bending torques. The bending torque is caused by a cosine harmonic potential assumed to be acting between the two connectors of a particle. This potential is also responsible for the bent configuration at equilibrium. We found that the interplay between hydrodynamic and bending contributions causes an orientation evolution completely different with respect to the one for slender rigid rods, which completely align in the flow direction. Particles keep tumbling even if their aspect ratio is infinite because of the bending torque.

In addition, we found that the high values of the orientation angle are well predicted by the model and the slight change of dichroism intensity in this saturated orientation level is mainly due to rod stretching. On average, particles become straighter with increasing shear rate.

Particle-based simulations were used here in order to confront experimental data with model predictions. However, the absence of stochastic terms in the simulations limits the predictions to the regime where the Brownian contribution to the orientation evolution is negligible. Future work will focus on the introduction of a stochastic term or in the solution of the modified Fokker-Planck equation for flexible rods (Eq. 4C.1 of Appendix C). Furthermore, it would be most useful to find a solution for the closure problem in solving fourth order orientation tensors, which are non-symmetric tensors. Finally, another interesting aspect to be analyzed is the direct introduction of polydispersity, not only in the connector lengths, but also in the equilibrium conformation. This will introduce a continuous spectrum of relaxation times that could explain the mild elasticity (low values of G') found for dilute MWCNT suspensions in small amplitude oscillatory flow [Ma *et al.* (2008)] and, in addition, the fast change in anisotropy during rest after shearing brought to light by Pujari *et al.* (2011).

4.9 Acknowledgements

This work was funded by NSERC (Natural Science and Engineering Research Council of Canada). The authors are profoundly thankful to Dr. Jan Vermant and Dr. Paula Moldenaers for providing access to their rheo-optical setup at KU Leuven and for insightful discussions.

4.10 Appendix A: Force Balance

Since $\partial U/\partial \mathbf{r} = 0$ and the beads are inertialess and non-Brownian, the only force acting on the beads is the hydrodynamic force:

$$\varsigma\left[3\boldsymbol{\kappa}\cdot\mathbf{r}_c - 3\dot{\mathbf{r}}_c + \boldsymbol{\kappa}\cdot\left(L_\beta\mathbf{p}^\beta - L_\alpha\mathbf{p}^\alpha\right) + \left(L_\alpha\dot{\mathbf{p}}^\alpha - L_\beta\dot{\mathbf{p}}^\beta\right)\right] = 0 \tag{4A.1}$$

The position of the center of mass $\mathbf{r}_{cm}$ considering the three beads having the same mass is

$$\mathbf{r}_{cm} = \frac{3\mathbf{r}_c - L_\alpha\mathbf{p}^\alpha + L_\beta\mathbf{p}^\beta}{3} \tag{4A.2}$$

and its velocity $\dot{\mathbf{r}}_{cm}$ is

$$\dot{\mathbf{r}}_{cm} = \frac{3\dot{\mathbf{r}}_c - L_\alpha \dot{\mathbf{p}}^\alpha + L_\beta \dot{\mathbf{p}}^\beta}{3} \tag{4A.3}$$

Substituting Eqs. 4A.2 and 4A.3 into Eq. 4A.1, we obtain:

$$\begin{aligned} &\varsigma\left[\boldsymbol{\kappa}\cdot\mathbf{r}_{cm} - \dot{\mathbf{r}}_{cm}\right] = 0 \\ &\dot{\mathbf{r}}_{cm} = \boldsymbol{\kappa}\cdot\mathbf{r}_{cm} \end{aligned} \tag{4A.4}$$

The center of mass has an affine motion with the fluid velocity, hence no spatial gradients are present in the system. This respects the third hypothesis.

4.11 Appendix B: Derivation of the stress tensor

In this section, we report for completeness the derivation of the stress tensor for our flexible particle model. The contribution to the stress tensor due to the presence of particles in the matrix is defined according to the Kramers-Kirkwood expression [Bird *et al.* (1987)] as follows:

$$\boldsymbol{\sigma}_p = \frac{1}{V}\sum_i \left\langle \mathbf{r}_i \mathbf{F}_i \right\rangle = \frac{1}{V}\sum_i \left\langle \mathbf{r}_i \mathbf{F}_i^H \right\rangle + \frac{1}{V}\sum_i \left\langle \mathbf{r}_i \mathbf{F}_i^B \right\rangle \tag{4B.1}$$

where $\mathbf{F}_i^H$, $\mathbf{F}_i^B$ and $\mathbf{r}_i$ are the hydrodynamic force, the bending force and the position of the bead *i*. Let us start analyzing the hydrodynamic contribution to the stress tensor:

$$\begin{aligned} \sum_i \mathbf{r}_i \mathbf{F}_i^H = {} & \varsigma \mathbf{r}_c \left[3\left(\boldsymbol{\kappa}\cdot\mathbf{r}_c - \dot{\mathbf{r}}_c\right) + \boldsymbol{\kappa}\cdot\left(L_\beta \mathbf{p}^\beta - L_\alpha \mathbf{p}^\alpha\right) + \left(L_\alpha \dot{\mathbf{p}}^\alpha - L_\beta \dot{\mathbf{p}}^\beta\right)\right] \\ & -\varsigma L_\alpha \mathbf{p}^\alpha \left[\left(\boldsymbol{\kappa}\cdot\mathbf{r}_c - \dot{\mathbf{r}}_c\right) + \boldsymbol{\kappa}\cdot\left(-L_\alpha \mathbf{p}^\alpha\right) + L_\alpha \dot{\mathbf{p}}^\alpha \right] \\ & +\varsigma L_\beta \mathbf{p}^\beta \left[\left(\boldsymbol{\kappa}\cdot\mathbf{r}_c - \dot{\mathbf{r}}_c\right) + \boldsymbol{\kappa}\cdot\left(L_\beta \mathbf{p}^\beta\right) - L_\beta \dot{\mathbf{p}}^\beta \right] \end{aligned} \tag{4B.2}$$

The first bracket on the right is equal to zero since the particle center of the mass moves with the fluid element. We can write $\left(\boldsymbol{\kappa}\cdot\mathbf{r}_c - \dot{\mathbf{r}}_c\right)$ as a function of the position of the center of mass from Eq. 4A.1 obtaining:

$$\left(\boldsymbol{\kappa}\cdot\mathbf{r}_c-\dot{\mathbf{r}}_c\right)=\left(\boldsymbol{\kappa}\cdot\mathbf{r}_{cm}-\dot{\mathbf{r}}_{cm}\right)+\frac{\left(\boldsymbol{\kappa}\cdot\left(L_\alpha\mathbf{p}^\alpha\right)-L_\alpha\dot{\mathbf{p}}^\alpha\right)}{3}+\frac{\left(\boldsymbol{\kappa}\cdot\left(-L_\beta\mathbf{p}^\beta\right)+L_\beta\dot{\mathbf{p}}^\beta\right)}{3} \tag{4B.3}$$

The first term on the right-end side of Eq. 4B.3 is zero for affine motion. Substituting Eq. 4B.3 in Eq. 4B.2, we obtain:

$$\begin{aligned}\sum_i\mathbf{r}_i\mathbf{F}_i^H=&-\varsigma L_\alpha\mathbf{p}^\alpha\left[\frac{2}{3}\left(\boldsymbol{\kappa}\cdot\left(-L_\alpha\mathbf{p}^\alpha\right)+L_\alpha\dot{\mathbf{p}}^\alpha\right)-\frac{\boldsymbol{\kappa}\cdot\left(L_\beta\mathbf{p}^\beta\right)-L_\beta\dot{\mathbf{p}}^\beta}{3}\right]\\&+\varsigma L_\beta\mathbf{p}^\beta\left[\frac{2}{3}\left(\boldsymbol{\kappa}\cdot\left(L_\beta\mathbf{p}^\beta\right)-L_\beta\dot{\mathbf{p}}^\beta\right)-\frac{\boldsymbol{\kappa}\cdot\left(-L_\alpha\mathbf{p}^\alpha\right)+L_\alpha\dot{\mathbf{p}}^\alpha}{3}\right]\end{aligned} \tag{4B.4}$$

and assuming affine rotation, we finally get:

$$\begin{aligned}\sum_i\mathbf{r}_i\mathbf{F}_i^H=&-\varsigma L_\alpha\mathbf{p}^\alpha\left[-\frac{2}{3}L_\alpha\boldsymbol{\kappa}:\mathbf{p}^\alpha\mathbf{p}^\alpha\mathbf{p}^\alpha-\frac{1}{3}L_\beta\boldsymbol{\kappa}:\mathbf{p}^\beta\mathbf{p}^\beta\mathbf{p}^\beta\right]\\&+\varsigma L_\beta\mathbf{p}^\beta\left[\frac{2}{3}L_\beta\boldsymbol{\kappa}:\mathbf{p}^\beta\mathbf{p}^\beta\mathbf{p}^\beta+\frac{1}{3}L_\alpha\boldsymbol{\kappa}:\mathbf{p}^\alpha\mathbf{p}^\alpha\mathbf{p}^\alpha\right]\end{aligned} \tag{4B.5}$$

Hence, the contribution to the stress due to the hydrodynamic force is:

$$\begin{aligned}\boldsymbol{\tau}_H=&\frac{1}{V}\sum_i\left\langle\mathbf{r}_i\mathbf{F}_i^H\right\rangle=\\&+n\varsigma\left[\frac{2}{3}L_\alpha^2\boldsymbol{\kappa}:\iint\mathbf{p}^\alpha\mathbf{p}^\alpha\mathbf{p}^\alpha\mathbf{p}^\alpha\psi d\mathbf{p}^\alpha d\mathbf{p}^\beta+\frac{1}{3}L_\alpha L_\beta\boldsymbol{\kappa}:\iint\mathbf{p}^\beta\mathbf{p}^\beta\mathbf{p}^\alpha\mathbf{p}^\beta\psi d\mathbf{p}^\alpha d\mathbf{p}^\beta\right]\\&+n\varsigma\left[\frac{2}{3}L_\beta^2\boldsymbol{\kappa}:\iint\mathbf{p}^\beta\mathbf{p}^\beta\mathbf{p}^\beta\mathbf{p}^\beta\psi d\mathbf{p}^\alpha d\mathbf{p}^\beta+\frac{1}{3}L_\alpha L_\beta\boldsymbol{\kappa}:\iint\mathbf{p}^\alpha\mathbf{p}^\alpha\mathbf{p}^\beta\mathbf{p}^\alpha\psi d\mathbf{p}^\alpha d\mathbf{p}^\beta\right]\end{aligned} \tag{4B.6}$$

Now, let us calculate the contribution to the stress tensor due to the bending potential:

$$\sum_i \mathbf{r}_i \mathbf{F}_i^B = \mathbf{r}_c \left[-\frac{k}{L_\alpha}\left(e - \mathbf{p}^\alpha \cdot \mathbf{p}^\beta\right)\left(\boldsymbol{\delta} - \mathbf{p}^\alpha \mathbf{p}^\alpha\right)\cdot \mathbf{p}^\beta + \frac{k}{L_\beta}\left(e - \mathbf{p}^\alpha \cdot \mathbf{p}^\beta\right)\left(\boldsymbol{\delta} - \mathbf{p}^\beta \mathbf{p}^\beta\right)\cdot \mathbf{p}^\alpha \right]$$
$$-L_\alpha \mathbf{p}^\alpha \left[-\frac{k}{L_\alpha}\left(e - \mathbf{p}^\alpha \cdot \mathbf{p}^\beta\right)\left(\boldsymbol{\delta} - \mathbf{p}^\alpha \mathbf{p}^\alpha\right)\cdot \mathbf{p}^\beta \right] \qquad (4B.7)$$
$$+L_\beta \mathbf{p}^\beta \left[+\frac{k}{L_\beta}\left(e - \mathbf{p}^\alpha \cdot \mathbf{p}^\beta\right)\left(\boldsymbol{\delta} - \mathbf{p}^\beta \mathbf{p}^\beta\right)\cdot \mathbf{p}^\alpha \right]$$

The first term on the right-end side of Eq. 4B.7 is zero since $\int \mathbf{r}_c d\mathbf{r}_c = 0$. Simplifying, we get:

$$\sum_i \mathbf{r}_i \mathbf{F}_i^B = \mathbf{p}^\alpha \left[k\left(e - \mathbf{p}^\alpha \cdot \mathbf{p}^\beta\right)\left(\boldsymbol{\delta} - \mathbf{p}^\alpha \mathbf{p}^\alpha\right)\cdot \mathbf{p}^\beta \right]$$
$$\mathbf{p}^\beta \left[k\left(e - \mathbf{p}^\alpha \cdot \mathbf{p}^\beta\right)\left(\boldsymbol{\delta} - \mathbf{p}^\beta \mathbf{p}^\beta\right)\cdot \mathbf{p}^\alpha \right] \qquad (4B.8)$$

Hence, the contribution to the stress tensor due to the bending potential is:

$$\boldsymbol{\tau}_B = \frac{1}{V}\sum_i \left\langle \mathbf{r}_i \mathbf{F}_i^B \right\rangle =$$
$$nk\left[\iint \left(e - \mathbf{p}^\alpha \cdot \mathbf{p}^\beta\right)\left(\mathbf{p}^\alpha \mathbf{p}^\beta - \left(\mathbf{p}^\alpha \cdot \mathbf{p}^\beta\right)\mathbf{p}^\alpha \mathbf{p}^\alpha\right)\psi d\mathbf{p}^\alpha d\mathbf{p}^\beta \right] \qquad (4B.9)$$
$$+nk\left[\iint \left(e - \mathbf{p}^\alpha \cdot \mathbf{p}^\beta\right)\left(\mathbf{p}^\beta \mathbf{p}^\alpha - \left(\mathbf{p}^\alpha \cdot \mathbf{p}^\beta\right)\mathbf{p}^\beta \mathbf{p}^\beta\right)\psi d\mathbf{p}^\alpha d\mathbf{p}^\beta \right]$$

After some rearrangements, the bending contribution to the stress tensor is given by:

$$\boldsymbol{\tau}_B = nke\left(\mathbf{b}_2 + \mathbf{b}_2^\dagger\right)$$
$$-nk\iint \left(\mathbf{p}^\alpha \cdot \mathbf{p}^\beta\right)\left(\mathbf{p}^\alpha \mathbf{p}^\beta + \mathbf{p}^\beta \mathbf{p}^\alpha + e\mathbf{p}^\alpha \mathbf{p}^\alpha + e\mathbf{p}^\beta \mathbf{p}^\beta\right)\psi d\mathbf{p}^\alpha d\mathbf{p}^\beta \qquad (4B.10)$$
$$+nk\iint \left(\mathbf{p}^\alpha \cdot \mathbf{p}^\beta\right)^2 \left(\mathbf{p}^\alpha \mathbf{p}^\alpha + \mathbf{p}^\beta \mathbf{p}^\beta\right)\psi d\mathbf{p}^\alpha d\mathbf{p}^\beta$$

The total stress tensor can now be calculated by adding the matrix contribution to the hydrodynamic and bending contributions obtained in Eqs. 4B.6 and 4B.10.

4.12 Appendix C: Second order orientation tensors

The multitude of particles constituting a suspension requires a statistical description of the problem. Therefore, an orientation distribution function, $\psi = \psi\left(\mathbf{p}^{\alpha}, \mathbf{p}^{\beta}, t\right)$, is introduced (valid for a spatially homogeneous system). It describes the probability of finding particles whose connectors have a certain orientation in space at a given instant. The orientation distribution function (ODF) can be regarded as a convected variable in the R^5 space described by all the possible configuration of $\mathbf{p}^{\alpha}$ and $\mathbf{p}^{\beta}$. Hence, the dynamics of a system under the hypotheses previously stated is depicted by the following modified Fokker-Planck equation for flexible rods:

$$\frac{D\psi}{Dt} = -\frac{\partial}{\partial \mathbf{p}^{\alpha}} \cdot \left(\dot{\mathbf{p}}^{\alpha}\psi\right) - \frac{\partial}{\partial \mathbf{p}^{\beta}} \cdot \left(\dot{\mathbf{p}}^{\beta}\psi\right) + D_r \left(\frac{\partial^2}{\partial \mathbf{p}^{\alpha 2}} + \frac{\partial^2}{\partial \mathbf{p}^{\beta 2}} \right) \psi \qquad (4C.1)$$

In Eq. 4C.1, a diffusion term, representing the effect of the rotary Brownian motion, is added in order to have a description valid for all Pe numbers and aspect ratios. In this section, hypothesis 5 is removed to obtain equations with a more general form. The numerical solution of this partial differential equation would require an enormous computational effort since a nonstandard R^4 space and time variable are required to be meshed. Consequently, a different strategy needs to be adopted.

One possibility is the definition of appropriate orientation tensors to describe the overall orientation evolution of the system [Advani and Tucker (1987)]. Of course, the information contained in a finite number of ODF moments is inferior to the knowledge of the full ψ. However, it is often sufficient to calculate average quantities of interest, i.e. stress tensor components, dichroism and average orientation angle. For our system, the time evolution of three second order orientation tensors is needed to completely describe the change in the microstructure. This comes out naturally from the mathematical development below. Following Ortman *et al.* (2012), an obvious choice of a second order tensor is the one related to the orientation of the connectors from the bead alpha to the central one: $\mathbf{a}_2 = \iint \mathbf{p}^{\alpha}\mathbf{p}^{\alpha}\psi d\mathbf{p}^{\alpha} d\mathbf{p}^{\beta}$.

The time evolution of $\mathbf{a}_2$ is calculated as follows:

$$\frac{D\mathbf{a}_2}{Dt} = \iint \dot{\mathbf{p}}^{\alpha}\mathbf{p}^{\alpha}\psi d\mathbf{p}^{\alpha}d\mathbf{p}^{\beta} + \iint \mathbf{p}^{\alpha}\dot{\mathbf{p}}^{\alpha}\psi d\mathbf{p}^{\alpha}d\mathbf{p}^{\beta} \tag{4C.2}$$

Substituting Eq. 4.13 in the last equation and after some lengthy calculations, we obtain:

$$\begin{aligned}\frac{D\mathbf{a}_2}{Dt} = &-\frac{1}{2}(\boldsymbol{\omega}\cdot\mathbf{a}_2 - \mathbf{a}_2\cdot\boldsymbol{\omega}) + \frac{1}{2}(\dot{\boldsymbol{\gamma}}\cdot\mathbf{a}_2 + \mathbf{a}_2\cdot\dot{\boldsymbol{\gamma}} - 2\dot{\boldsymbol{\gamma}}:\mathbf{a}_4) + 2D_r\left(\boldsymbol{\delta} - 3\mathbf{a}_2\right) \\ &+ \frac{k}{\varsigma L_{\alpha}{}^2}e\left(\mathbf{b}_2 + \mathbf{b}_2^{\dagger} - 2\iint\left(\mathbf{p}^{\alpha}\cdot\mathbf{p}^{\beta}\right)\mathbf{p}^{\alpha}\mathbf{p}^{\alpha}\psi d\mathbf{p}^{\alpha}d\mathbf{p}^{\beta}\right) \\ &- \frac{k}{\varsigma L_{\alpha}{}^2}\left(\iint\left(\mathbf{p}^{\alpha}\cdot\mathbf{p}^{\beta}\right)\left(\mathbf{p}^{\alpha}\mathbf{p}^{\beta} + \mathbf{p}^{\beta}\mathbf{p}^{\alpha}\right)\psi d\mathbf{p}^{\alpha}d\mathbf{p}^{\beta} - 2\iint\left(\mathbf{p}^{\alpha}\cdot\mathbf{p}^{\beta}\right)^2\mathbf{p}^{\alpha}\mathbf{p}^{\alpha}\psi d\mathbf{p}^{\alpha}d\mathbf{p}^{\beta}\right)\end{aligned} \tag{4C.3}$$

where $\mathbf{b}_2 = \iint \mathbf{p}^{\alpha}\mathbf{p}^{\beta}\psi d\mathbf{p}^{\alpha}d\mathbf{p}^{\beta}$ and $\mathbf{a}_4 = \iint \mathbf{p}^{\alpha}\mathbf{p}^{\alpha}\mathbf{p}^{\alpha}\mathbf{p}^{\alpha}\psi d\mathbf{p}^{\alpha}d\mathbf{p}^{\beta}.\dot{\boldsymbol{\gamma}}$ and $\boldsymbol{\omega}$ are the deformation rate and the vorticity tensor. The presence of the fourth order orientation tensor $\mathbf{a}_4$ implies the need of a closure approximation to solve the problem. Further approximations are also necessary to compute the last three integrals on the right side of Eq. 4C.3. It is important to underline that the second order tensor $\mathbf{b}_2$ is not symmetric. This is due to the fact that we removed the hypothesis of semi-flexibility ($\mathbf{p}^{\alpha} \approx \mathbf{p}^{\beta}$) that guaranteed the symmetry of the mixed tensor in the work of Ortman *et al.* (2012).

It can be easily seen that to compute the rate of change of $\mathbf{a}_2$, Eq. 4C.3 requires knowledge of the evolution for the second order tensor $\mathbf{b}_2$. Following the same procedure applied for $\mathbf{a}_2$ and making use of Eqs. 4.13 and 4.14, the rate of change for $\mathbf{b}_2$ is written as

$$\begin{aligned}\frac{D\mathbf{b}_2}{Dt} &= -\frac{1}{2}\left(\boldsymbol{\omega}\cdot\mathbf{b}_2-\mathbf{b}_2\cdot\boldsymbol{\omega}\right)+\frac{1}{2}\left(\dot{\boldsymbol{\gamma}}\cdot\mathbf{b}_2-\mathbf{b}_2\cdot\dot{\boldsymbol{\gamma}}\right)-2D_r\left(\mathbf{b}_2+\mathbf{b}_2{}^{\dagger}\right)\\ &-\frac{1}{2}\left(\dot{\boldsymbol{\gamma}}:\iint\mathbf{p}^{\alpha}\mathbf{p}^{\alpha}\mathbf{p}^{\alpha}\mathbf{p}^{\beta}\psi d\mathbf{p}^{\alpha}d\mathbf{p}^{\beta}+\dot{\boldsymbol{\gamma}}:\iint\mathbf{p}^{\beta}\mathbf{p}^{\beta}\mathbf{p}^{\alpha}\mathbf{p}^{\beta}\psi d\mathbf{p}^{\alpha}d\mathbf{p}^{\beta}\right)\\ &+\frac{ke}{\varsigma}\left(\frac{\mathbf{a}_2}{L_\beta^2}+\frac{\mathbf{c}_2}{L_\alpha^2}-\left(\frac{1}{L_\alpha^2}+\frac{1}{L_\beta^2}\right)\iint\left(\mathbf{p}^{\alpha}\cdot\mathbf{p}^{\beta}\right)\mathbf{p}^{\alpha}\mathbf{p}^{\beta}\psi d\mathbf{p}^{\alpha}d\mathbf{p}^{\beta}\right)\\ &-\frac{k}{\varsigma}\left(\iint\left(\mathbf{p}^{\alpha}\cdot\mathbf{p}^{\beta}\right)\left(\frac{\mathbf{p}^{\beta}\mathbf{p}^{\beta}}{L_\alpha^2}+\frac{\mathbf{p}^{\alpha}\mathbf{p}^{\alpha}}{L_\beta^2}\right)\psi d\mathbf{p}^{\alpha}d\mathbf{p}^{\beta}-\left(\frac{1}{L_\alpha^2}+\frac{1}{L_\beta^2}\right)\iint\left(\mathbf{p}^{\alpha}\cdot\mathbf{p}^{\beta}\right)^2\mathbf{p}^{\alpha}\mathbf{p}^{\beta}\psi d\mathbf{p}^{\alpha}d\mathbf{p}^{\beta}\right)\end{aligned} \tag{4C.4}$$

The tensor $\mathbf{b}_2$ contains information regarding the average spatial conformation of the particles. In particular, the trace of $\mathbf{b}_2$ is equal to $\iint\left(\mathbf{p}^{\alpha}\cdot\mathbf{p}^{\beta}\right)\psi d\mathbf{p}^{\alpha}d\mathbf{p}^{\beta}$ and it represents the average cosine of the angle between the connectors $\mathbf{p}^{\alpha}$ and $\mathbf{p}^{\beta}$ [Ortman *et al.* (2012)]. As a consequence, the trace of $\mathbf{b}_2$ is no longer unitary as for the other non-mixed second order tensors presented here. It varies between 0 and 1 corresponding to a system of bent or straight particles, respectively.

The time evolution of the mixed tensor $\mathbf{b}_2$ introduces the need of a time evolution for a third orientation tensor $\mathbf{c}_2=\iint\mathbf{p}^{\beta}\mathbf{p}^{\beta}\psi d\mathbf{p}^{\alpha}d\mathbf{p}^{\beta}$. It represents the average orientation of the connectors $\mathbf{p}^{\beta}$. Proceeding as previously, its time evolution can be obtained as:

$$\begin{aligned}\frac{D\mathbf{c}_2}{Dt} &= -\frac{1}{2}\left(\boldsymbol{\omega}\cdot\mathbf{c}_2-\mathbf{c}_2\cdot\boldsymbol{\omega}\right)+\frac{1}{2}\left(\dot{\boldsymbol{\gamma}}\cdot\mathbf{c}_2+\mathbf{c}_2\cdot\dot{\boldsymbol{\gamma}}-2\dot{\boldsymbol{\gamma}}:\mathbf{c}_4\right)+2D_r\left(\boldsymbol{\delta}-3\mathbf{a}_2\right)\\ &+\frac{k}{\varsigma L_\beta{}^2}e\left(\mathbf{b}_2+\mathbf{b}_2^{\dagger}-2\iint\left(\mathbf{p}^{\alpha}\cdot\mathbf{p}^{\beta}\right)\mathbf{p}^{\beta}\mathbf{p}^{\beta}\psi d\mathbf{p}^{\alpha}d\mathbf{p}^{\beta}\right)\\ &-\frac{k}{\varsigma L_\beta{}^2}\left(\iint\left(\mathbf{p}^{\alpha}\cdot\mathbf{p}^{\beta}\right)\left(\mathbf{p}^{\alpha}\mathbf{p}^{\beta}+\mathbf{p}^{\beta}\mathbf{p}^{\alpha}\right)\psi d\mathbf{p}^{\alpha}d\mathbf{p}^{\beta}-2\iint\left(\mathbf{p}^{\alpha}\cdot\mathbf{p}^{\beta}\right)^2\mathbf{p}^{\beta}\mathbf{p}^{\beta}\psi d\mathbf{p}^{\alpha}d\mathbf{p}^{\beta}\right)\end{aligned} \tag{4C.5}$$

where $\mathbf{c}_4 = \iint \mathbf{p}^\beta \mathbf{p}^\beta \mathbf{p}^\beta \mathbf{p}^\beta \psi d\mathbf{p}^\alpha d\mathbf{p}^\beta$. These three orientation tensors contain sufficient information to calculate average quantities of interest.

Ortman *et al.* (2012) proposed a simple approximation for the integrals containing the dot product between $\mathbf{p}^\alpha$ and $\mathbf{p}^\beta$. As an example, let us consider the integral $\iint \left(\mathbf{p}^\alpha \cdot \mathbf{p}^\beta\right) \mathbf{p}^\alpha \mathbf{p}^\alpha \psi d\mathbf{p}^\alpha d\mathbf{p}^\beta$. It can be written as follows:

$$\iint \left(\mathbf{p}^\alpha \cdot \mathbf{p}^\beta\right) \mathbf{p}^\alpha \mathbf{p}^\alpha \psi d\mathbf{p}^\alpha d\mathbf{p}^\beta \approx \iint \left(\mathbf{p}^\alpha \cdot \mathbf{p}^\beta\right) \psi d\mathbf{p}^\alpha d\mathbf{p}^\beta \cdot \iint \mathbf{p}^\alpha \mathbf{p}^\alpha \psi d\mathbf{p}^\alpha d\mathbf{p}^\beta = tr\left(\mathbf{b}_2\right) \cdot \mathbf{a}_2 \qquad (4C.6)$$

One could similarly approximate the other integrals that contains the dot product between $\mathbf{p}^\alpha$ and $\mathbf{p}^\beta$. Unfortunately, we are still not able to close the problem due to the presence of two new fourth order orientation tensors in Eq. 4C.4: $\iint \mathbf{p}^\alpha \mathbf{p}^\alpha \mathbf{p}^\alpha \mathbf{p}^\beta \psi d\mathbf{p}^\alpha d\mathbf{p}^\beta$ and $\iint \mathbf{p}^\beta \mathbf{p}^\beta \mathbf{p}^\alpha \mathbf{p}^\beta \psi d\mathbf{p}^\alpha d\mathbf{p}^\beta$. These last two tensors are non-symmetric tensors, while all the closure approximations reported in the literature have been developed in order to preserve the symmetry of fourth order orientation tensors like $\mathbf{a}_4$ and $\mathbf{c}_4$ [Advani and Tucker (1987), Cintra and Tucker (1995)]. Hence, their proposed closure approximations would not work in this particular case. For the first time, the closure approximation problem is here extended to anti-symmetric tensors. To our knowledge, no solution is available in the literature and thus, we open up this question to the scientific community.

4.13 References

Abbasi S., P. Carreau, A. Derdouri and M. Moan, "Rheological properties and percolation in suspensions of multiwalled carbon nanotubes in polycarbonate," Rheologica Acta **48**, 943-959 (2009).

Abdel-Goad M. and P. Pötschke, "Rheological characterization of melt processed polycarbonate-multiwalled carbon nanotube composites," Journal of Non-Newtonian Fluid Mechanics **128**, 2-6 (2005).

Advani S. G. and C. L. Tucker, "The use of tensors to describe and predict fiber orientation in short fiber composites," Journal of Rheology **31**, 751-784 (1987).

Bellini T., F. Mantegazza, R. Piazza and V. Degiorgio, "Stretched-exponential relaxation of electric birefringence in a polydisperse colloidal solution," EPL (Europhysics Letters) **10**, 499 (1989).

Bird R. B., C. F. Curtiss, R. C. Armstrong and O. Hassager, *Dynamics of polymeric liquids. Volume 2, Kinetic theory* (Wiley, New York, 1987).

Bulacu M., N. Goga, W. Zhao, G. Rossi, L. Monticelli, X. Periole, D. P. Tieleman and S. J. Marrink, "Improved Angle Potentials for Coarse-Grained Molecular Dynamics Simulations," Journal of Chemical Theory and Computation **9**, 3282-3292 (2013).

Chow A. W., G. G. Fuller, D. G. Wallace and J. A. Madri, "Rheooptical response of rodlike chains subject to transient shear flow. 2. Two-color flow birefringence measurements on collagen protein," Macromolecules **18**, 793-804 (1985a).

Chow A. W., G. G. Fuller, D. G. Wallace and J. A. Madri, "Rheooptical response of rodlike, shortened collagen protein to transient shear flow," Macromolecules **18**, 805-810 (1985b).

Cintra J. J. S. and C. L. Tucker, "Orthotropic closure approximations for flow-induced fiber orientation," Journal of Rheology **39**, 1095-1122 (1995).

Cruz C., L. Illoul, F. Chinesta and G. Régnier, "Shear-strain step response in linear regime of dilute suspensions of naturally bent carbon nanotubes," Journal of Applied Polymer Science **125**, 4347-4357 (2012).

Doi M. and S. F. Edwards, "Dynamics of rod-like macromolecules in concentrated solution. Part 1," J. Chem. Soc., Faraday Trans. 2 **74**, 560-570 (1978).

Doi M. and S. F. Edwards, "The theory of polymer dynamics," Clarendon, Oxford (1986).

Du F., R. C. Scogna, W. Zhou, S. Brand, J. E. Fischer and K. I. Winey, "Nanotube Networks in Polymer Nanocomposites: Rheology and Electrical Conductivity," Macromolecules **37**, 9048-9055 (2004).

Fan Z. and S. G. Advani, "Rheology of multiwall carbon nanotube suspensions," Journal of Rheology **51**, 585-604 (2007).

Folgar F. P. and C. L. Tucker, "Orientation behavior of fibers in concentrated suspensions," J. Reinf. Plast. Compos. **3**, 99 (1984).

Frattini P. L. and G. G. Fuller, "The dynamics of dilute colloidal suspensions subject to time-dependent flow fields by conservative dichroism," Journal of Colloid and Interface Science **100**, 506-518 (1984).

Fry D., B. Langhorst, H. Wang, M. L. Becker, B. J. Bauer, E. A. Grulke and E. K. Hobbie, "Rheo-optical studies of carbon nanotube suspensions," The Journal of Chemical Physics **124**, 054703 (2006).

Fuller G. G., *Optical rheometry of complex fluids* (Oxford University Press, 1995).

Fuller G. G. and K. J. Mikkelsen, "Note: Optical Rheometry Using a Rotary Polarization Modulator," Journal of Rheology (1978-present) **33**, 761-769 (1989).

Hobbie E. K., "Optical anisotropy of nanotube suspensions," The Journal of Chemical Physics **121**, 1029-1037 (2004).

Hobbie E. K. and D. J. Fry, "Rheology of concentrated carbon nanotube suspensions," The Journal of Chemical Physics **126**, 124907-7 (2007).

Hu G., C. Zhao, S. Zhang, M. Yang and Z. Wang, "Low percolation thresholds of electrical conductivity and rheology in poly(ethylene terephthalate) through the networks of multi-walled carbon nanotubes," Polymer **47**, 480-488 (2006).

Huang Y. Y., S. V. Ahir and E. M. Terentjev, "Dispersion rheology of carbon nanotubes in a polymer matrix," Physical Review B **73**, 125422 (2006).

Johnston D. C., "Stretched exponential relaxation arising from a continuous sum of exponential decays," Physical Review B **74**, 184430 (2006).

Keshtkar M., M.-C. Heuzey, P. J. Carreau, M. Rajabian and C. Dubois, "Rheological properties and microstructural evolution of semi-flexible fiber suspensions under shear flow," Journal of Rheology (1978-present) **54**, 197-222 (2010).

Khalkhal F. and P. J. Carreau, "Critical shear rates and structure build-up at rest in MWCNT suspensions," Journal of Non-Newtonian Fluid Mechanics **171–172**, 56-66 (2012).

Khalkhal F., P. J. Carreau and G. Ausias, "Effect of flow history on linear viscoelastic properties and the evolution of the structure of multiwalled carbon nanotube suspensions in an epoxy," Journal of Rheology **55**, 153-175 (2011).

Larson R. G., "The Structure and Rheology of Complex fluids," Journal (1999).

Lenstra T. A. J., Z. Dogic and J. K. G. Dhont, "Shear-induced displacement of isotropic-nematic spinodals," The Journal of Chemical Physics **114**, 10151-10162 (2001).

Ma W. K. A., F. Chinesta, A. Ammar and M. R. Mackley, "Rheological modeling of carbon nanotube aggregate suspensions," Journal of Rheology **52**, 1311-1330 (2008).

Marrucci G. and N. Grizzuti, "The effect of polydispersity on rotational diffusivity and shear viscosity of rodlike polymers in concentrated solutions," Journal of Polymer Science: Polymer Letters Edition **21**, 83-86 (1983).

Natale G., M. C. Heuzey, P. J. Carreau, G. Ausias and J. Férec, "Rheological modeling of carbon nanotube suspensions with rod–rod interactions," AIChE Journal **60**, 1476-1487 (2014).

Onuki A. and M. Doi, "Flow birefringence and dichroism of polymers. I. General theory and application to the dilute case," The Journal of Chemical Physics **85**, 1190-1197 (1986).

Ortman K., D. Baird, P. Wapperom and A. Whittington, "Using startup of steady shear flow in a sliding plate rheometer to determine material parameters for the purpose of predicting long fiber orientation," Journal of Rheology (1978-present) **56**, 955-981 (2012).

Pujari S., S. Rahatekar, J. W. Gilman, K. K. Koziol, A. H. Windle and W. R. Burghardt, "Shear-induced anisotropy of concentrated multiwalled carbon nanotube suspensions using x-ray scattering," Journal of Rheology (1978-present) **55**, 1033-1058 (2011).

Pujari S., S. S. Rahatekar, J. W. Gilman, K. K. Koziol, A. H. Windle and W. R. Burghardt, "Orientation dynamics in multiwalled carbon nanotube dispersions under shear flow," The Journal of Chemical Physics **130**, - (2009).

Rahatekar S. S., K. K. K. Koziol, S. A. Butler, J. A. Elliott, M. S. P. Shaffer, M. R. Mackley and A. H. Windle, "Optical microstructure and viscosity enhancement for an epoxy resin matrix

containing multiwall carbon nanotubes," Journal of Rheology (1978-present) **50**, 599-610 (2006).

Rajabian M., C. Dubois and M. Grmela, "Suspensions of Semiflexible Fibers in Polymeric Fluids: Rheology and Thermodynamics," Rheologica Acta **44**, 521-535 (2005).

Rajabian M., C. Dubois, M. Grmela and P. Carreau, "Effects of polymer–fiber interactions on rheology and flow behavior of suspensions of semi-flexible fibers in polymeric liquids," Rheologica Acta **47**, 701-717 (2008).

Strautins U. and A. Latz, "Flow-driven orientation dynamics of semiflexible fiber systems," Rheologica Acta **46**, 1057-1064 (2007).

Switzer III L. H. and D. J. Klingenberg, "Rheology of sheared flexible fiber suspensions via fiber-level simulations," Journal of Rheology **47**, 759-778 (2003).

Wu D., L. Wu and M. Zhang, "Rheology of multi-walled carbon nanotube/poly(butylene terephthalate) composites," Journal of Polymer Science Part B: Polymer Physics **45**, 2239-2251 (2007).

CHAPTER 5 ARTICLE 2: RHEOLOGICAL MODELING OF CARBON NANOTUBE SUSPENSIONS WITH ROD-ROD INTERACTIONS

G. Natale [a], G. Ausias [b], J. Férec [b], M.C. Heuzey [a] and P.J. Carreau [a]

[a] *Center for Applied Research on Polymers and Composites (CREPEC),*

Chemical Engineering Department, École Polytechnique de Montréal,

PO Box 6079, Stn Centre-Ville, Montreal, QC, Canada H3C3A7

[b] *Laboratoire d'Ingénierie des MATériaux de Bretagne (LIMATB)*

Université Européenne de Bretagne, rue de St Maudé, 56325 Lorient, France

5.1 Synopsis

To explain the shear-thinning behavior of untreated carbon nanotube (CNT) suspensions in a Newtonian matrix, a new set of rheological equations is developed. The CNTs are modelled as rigid rods dispersed in a Newtonian matrix and the evolution of the system is controlled by hydrodynamic and rod-rod interactions. The particle-particle interactions is modelled by a non-linear lubrication force, function of the relative velocity at the contact point, and weighted by the contact probability. The stress tensor is calculated from the known fourth-order orientation tensor and a new fourth-order interaction tensor. The Fokker-Planck equation is numerically solved for steady simple shear flows using a finite volume method. The model predictions show a good agreement with the steady shear data of CNTs dispersed in a Newtonian epoxy matrix as well as for suspensions of glass fibers in polybutene1, demonstrating its ability to describe the behavior of micro and nano scale particle suspensions.

KEYWORDS: Modeling of suspensions, carbon nanotubes (CNTs), interaction tensors, Fokker-Planck equation, steady shear flow, shear thinning behavior.

5.2 Introduction

The popularity of carbon nanotubes (CNTs) as polymer fillers can be easily understood considering the high added value achievable for creating multi-functional composites. However, an essential requirement for CNT success in potential applications is a clear understanding and control of material properties' evolution during flow and processing. Hence, the rheology of CNT suspensions has been intensely investigated in the last few decades by different authors: Du *et al.* (2004), Huang *et al.* (2006), Fan and Advani (2007), Hobbie and Fry (2007), Wu *et al.* (2007), etc.

CNTs dispersed in a matrix form complex microstructures due to their high aspect ratio, and van der Waals forces. The microstructure is a function of CNT concentration, aspect ratio and dispersion, and it evolves with and without flow with corresponding changes in the rheological properties [Du *et al.* (2004), Fan and Advani (2007), Song and Youn (2005), Hu *et al.* (2006)]. Many rheological studies have been published on the linear viscoelastic behavior and on the non-terminal character (in percolated systems) of the storage modulus and complex viscosity at low frequencies, considered as the rheological signature of an established filler network [Abdel-Goad

and Pötschke (2005), Hu *et al.* (2006), Wu *et al.* (2007)]. In addition, small amplitude oscillatory shear (SAOS) measurements have been used as an indirect method to characterize the suspension, correlating mixing time, dispersion state and network elasticity [Huang *et al.* (2006)].

The nanotubes form an elastic network with a characteristic shear modulus and yield stress, both of which increase with CNT concentration [Abbasi *et al.* (2009a), Hobbie and Fry (2007)]. The network structure is very sensitive and it can be easily destroyed by steady shear and large amplitude oscillatory shear (LAOS) deformation. However, the microstructure keeps evolving under quiescent conditions and a network reorganization takes place, as illustrated by the behavior of the stress overshoot in reverse flow as function of rest time [Wu *et al.* (2007), Khalkhal and Carreau (2012)] or by the storage modulus as function of time [Khalkhal *et al.* (2011)].

Direct and indirect rheo-optical studies have shown evidences that the anisotropy is enhanced with increasing shear rate and/or volume fraction, due to rotational excluded-volume interactions [Hobbie *et al.* (2003), Fan and Advani (2005), Fry *et al.* (2006)]. Mechanical interlock of the nanotubes caused by inter-particle collisions in confined geometry was also shown by Ma *et al.* (2007). Another unique rheological characteristic is the shear-thinning behavior of CNT-based suspensions, even when the carbon nanotubes are added to a Newtonian matrix. The viscosity at low-shear rates can be several orders of magnitude higher than that of the neat medium, while it tends to level off asymptotically towards that of the latter at high-shear rates [Rahatekar *et al.* (2006b)]. There is not a univocal explanation for this shear-thinning phenomenon, but shear thinning seems to be due to a combination of nanotube orientation and agglomerates break-up.

To entirely characterize such a complex system, it is necessary to grasp the interplay between the different mechanisms that control the evolution of the microstructure such as hydrodynamic forces, Brownian motion, attractive forces and particle interactions. Modeling is a powerful tool to understand the causes behind the microstructure evolution and thus, can open new routes to specifically develop enhanced composite properties and processing schemes.

The first successful attempt to model anisotropic particles was achieved by Jeffery (1922). In his work, he described the orientation evolution of a single spheroid in a Newtonian medium in the absence of Brownian motion and particle interactions. He showed that a particle rotates around the vorticity axis and remains in the same orbit forever. However, most of the real suspensions (blood,

composites, paints) contain many particles and direct and indirect interactions play a major role in their rheological properties. Models have been developed based on the presence of hydrodynamic interactions [Dinh and Armstrong (1984), Shaqfeh and Fredrickson (1990)]. Hydrodynamic interactions happen when a particle is in the vicinity of a second particle, causing disturbances in the flow field as seen by the second particle. This introduces fluctuations in the orbits before steady-state is reached.

Later, Petrich *et al.* (2000) showed experimentally that particle interactions becomes more and more important as the particle concentration increased, but the hydrodynamic theories were not able to capture the enhancement in viscosity and first normal stress differences. An original approach aimed at including these effects was proposed by Folgar and Tucker (1984) and Advani and Tucker (1987), introducing an empirical diffusional term into the Jeffery equation

$$\dot{\mathbf{p}} = -\frac{1}{2}\boldsymbol{\omega}\cdot\mathbf{p} + \frac{1}{2}\lambda(\dot{\boldsymbol{\gamma}}\cdot\mathbf{p} - \dot{\boldsymbol{\gamma}} : \mathbf{ppp}) - C_I\left|\dot{\gamma}\right|\frac{\partial \ln(\psi)}{\partial \mathbf{p}}, \qquad (5.1)$$

where $\mathbf{p}$ is the unit vector directed along the particle principal axis, $\boldsymbol{\omega}$ and $\dot{\boldsymbol{\gamma}}$ are the vorticity and deformation rate tensors, respectively, and the shape factor $\lambda = (r^2-1)/(r^2+1)$ is a parameter related to the particle aspect ratio $r = L/D$. The phenomenological term (last term in Eq. 5.1) is proportional to the effective deformation rate $\left|\dot{\gamma}\right| = \sqrt{\dot{\boldsymbol{\gamma}} : \dot{\boldsymbol{\gamma}}/2}$ and to a constant diffusion coefficient C_I. Several authors have proposed formulations for the diffusion coefficient as function of fiber aspect ratio and volume fraction [Bay (1991), Phan-Thien *et al.* (2002), Ranganathan and Advani (1991)].

Recently, Ma *et al.* (2008) showed that a Fokker-Planck advection-diffusion description, with a constant rotary diffusion, failed to capture the experimentally observed rheological responses of untreated CNT suspensions. They proposed an innovative approach named the "aggregation/orientation" (AO) model that takes into account the different possible microstructures in a CNT suspension, but its predictions were limited to low CNT volume fractions and different adjustable parameters were needed for each concentration. Following this trend, Chinesta (2013) proposed a realistic model based on a double-scale kinetics theory, considering at a first scale the kinematics of the clusters and at a second one, the kinematics of the rods constituting the clusters.

A more complete theory for concentrated rod-like suspensions with strong particle interactions was presented by Sandstrom (1993) and Sandstrom and Tucker (1993). They modeled the interparticle contacts as a linear lubrication force. This work was extended by Servais *et al.* (1999a) and Servais *et al.* (1999b), assuming that in addition to the lubrication force at each contact point there were a Coulombic friction force and a normal force of elastostatic origin. Furthermore, Djalili-Moghaddam and Toll (2005) proposed a nonlinear formulation of the model and considered the total stress as the sum of the contributions of the matrix, hydrodynamic forces and interaction forces. However, only short-range hydrodynamic interactions were taken into account. Finally, Férec *et al.* (2009) generalized their work, not neglecting any term in the particle relative velocity expression, and constructed a new conformation tensor called the interaction tensor.

A different approach was undertaken by Le Corre *et al.* (2004) based on a deterministic upscaling technique to establish the fundamental properties of the macroscopic mechanical behavior of planar distributed fiber networks, and it was later extended for the case of high concentrated fiber bundle suspensions dispersed in a non-Newtonian power-law fluid [Le Corre *et al.* (2005)]. The shear-thinning behavior was also considered by Guiraud *et al.* (2012) to evaluate the average contact force, and in addition to the approach of Servais *et al.* (1999a), two new aspects were examined: (i) the dependence of contact surfaces on fiber bundle orientation and (ii) the influence of the confining pressure.

The aforementioned approaches have an important point in common: they provide a description of the suspension system at a mesoscopic scale where the microstructure is defined by a distribution function that depends on time, physical space and chosen conformational coordinates. This choice is convenient because it guarantees a good compromise between a fine description and computational time. On the other hand, direct simulations can give specific insights on the mechanisms behind particle-particle interactions, but this microscopic description is achieved at a high computational cost. The reader is referred to interesting examples of direct simulations [Switzer III and Klingenberg (2003), Yamanoi *et al.* (2010)].

Nevertheless, no matter what approach or length scale is privileged, a model able to capture the well-known shear-thinning and normal stress differences in all the concentration regimes of CNT suspensions is still missing in the literature. In this work we favor the mesoscopic scale and propose a novel expression for the lubrication force, which is non linear with respect to the relative particle

velocity at the contact point. A new rheological model is developed and a new conformation tensor is obtained. In addition, the modified Fokker-Planck equation is numerically solved for steady shear flow, eliminating the inconvenient introduction of closure approximations. The new model contains only four adjustable parameters obtained by fitting experimental data, and its predictions are confronted for two different systems in order to cover both micro and nano scale particles. The first system is composed of CNTs dispersed in an epoxy matrix, and the second consists of a glass fiber-filled polybutene.

5.3 Model formulation

5.3.1 Definitions and hypotheses

A representative volume element (RVE) containing a large number of rods is chosen large enough to have the same behavior as the bulk of the suspension. The number of particles per unit volume is n and the particle volume fraction is represented by ϕ. In the following, the superscript α refers to the test rod while β is used for the neighboring rods. The mass center position of the test rod is defined by the vector expressed with respect to a fixed coordinate system R. The unit vector $\mathbf{p}^{\alpha}$ along the major axis of the rod describes its orientation. The arc length, s^{α}, is measured along the rod axis with $s^{\alpha} = 0$ at the center. The rod orientation contained in the RVE can be calculated using the orientation distribution function $\psi_{\mathbf{p}^{\alpha}}$ which is a continuous function of the unit vector $\mathbf{p}^{\alpha}$ over the RVE. Each element of fluid has a velocity $\mathbf{v}^{\infty}$ in **R**, and the surrounding fluid angular velocity is defined by $\boldsymbol{\Omega}^{\infty} = \frac{1}{2}\nabla \times \mathbf{v}^{\infty}$. The model is based on the following hypotheses

(1) All particles are considered as straight and rigid rods of uniform length *L* and constant diameter *D*.

(2) The bulk flow is assumed to be homogeneous, whereas the velocity gradient is constant over the rod length ($\nabla \mathbf{v}^{\infty} = \boldsymbol{\kappa}^{\dagger}$), so the fluid velocity is given by $\mathbf{v}^{\infty} = \boldsymbol{\kappa} \cdot \mathbf{r}_{\mathbf{C}}^{\alpha}$.

(3) The suspended rods are assumed to be distributed uniformly, i.e. there is no concentration gradient.

(4) The particles are considered inertialess and the gravitational effect is negligible.

(5) The matrix is assumed to be incompressible and a continuous Newtonian medium with a viscosity η_0. The fluid motion is determined by the Stokes equation (negligible translational and rotational fluid inertia).

(6) The particle-particle interaction force is non-linear (power-law form) with respect to the relative velocity at the contact point.

(7) Affine motion and rotation are assumed.

(8) The particles have large aspect ratio, $r = L/D >> 1$, and hence, Brownian motion is neglected.

5.3.2 Equations for rod motion

Following Kim and Karrila (1991) and Férec *et al.* (2009), we assume that the test rod α suspended in a Newtonian fluid is subjected to an external force caused by a neighboring interacting rod β. For the case of rod motion with interactions, the time evolution for a test prolate spheroid α, written in **R**, is

$$\dot{\mathbf{p}}^{\alpha} = \boldsymbol{\varpi}^{\alpha} \times \mathbf{p}^{\alpha} = \left[\boldsymbol{\Omega}^{\infty} + \mathbf{C}^{-1} \cdot \left(\mathbf{H} : \dot{\boldsymbol{\gamma}} + \mathbf{T}_{\mathrm{I}} \right) \right] \times \mathbf{p}^{\alpha}, \tag{5.2}$$

where $\boldsymbol{\varpi}^{\alpha}$ is the angular velocity of rod α and $\mathbf{T}_{\mathrm{I}}$ represents the global torque due to the interactions between the test rod α and all neighboring rods. The three terms on the right hand-side of Eq. 5.2 refer to the rotations due to the rigid-body, the fluid deformation and the interaction torque, respectively. **C** and **H** are resistance tensors expressed as $\mathbf{C} = \eta_0 L^3 \left[Y_C \boldsymbol{\delta} + \left(X_C - Y_C \right) \mathbf{p}^{\alpha} \mathbf{p}^{\alpha} \right]$ and $\mathbf{H} = -\frac{1}{2} \eta_0 L^3 Y_H \left(\boldsymbol{\varepsilon} \cdot \mathbf{p}^{\alpha} \right) \mathbf{p}^{\alpha}$, respectively, where **ε** is the third order permutation tensor and X_C, Y_C and Y_H are resistance functions. For the dilute regime (low concentration suspensions), we find that the rotational drag coefficients are expressed as $X_C = 4\pi/r^2$ and $Y_C = 1/6$.

To calculate the overall interaction torque $\mathbf{T}_{\mathrm{I}}$, it is necessary to integrate the differential interaction moment $d\mathbf{T}_{\mathrm{I}}$, which is simply the lever arm times the applied differential force $d\mathbf{f}_{\mathrm{I}}$

$$d\mathbf{T}_\mathbf{I} = s^\alpha \mathbf{p}^\alpha \times d\mathbf{f}_\mathbf{I} . \tag{5.3}$$

If a linear lubrication is assumed [Férec *et al.* (2009)], the interaction force results in

$$\mathbf{f}_\mathbf{I} = D\eta_0 k \Delta\dot{\mathbf{r}} , \tag{5.4}$$

where k is a dimensionless geometric factor and $\Delta\dot{\mathbf{r}}$ is the time derivative of the shortest distance between two fibers $\Delta\mathbf{r}$. However, while two rods approach each other, the fluid between them is squeezed and this causes a flow that is a non-linear function of $\Delta\dot{\mathbf{r}}$. To take into account this effect, we propose a new expression for $\mathbf{f}_\mathbf{I}$

$$\mathbf{f}_\mathbf{I} = Dkb(\Delta\dot{\mathbf{r}} \cdot \Delta\dot{\mathbf{r}})^{\frac{m-1}{2}} \Delta\dot{\mathbf{r}} , \tag{5.5}$$

where b and m are the consistency and the power-law exponent, respectively, of the rod-rod interaction force. We note that the last equation reduces to Eq. 5.4 when $m = 1$ and $b = \eta_0$.

To satisfy the requirement for material objectivity, the relative rod velocity, $\Delta\dot{\mathbf{r}}$, has to be expressed in a co-rotational frame (denoted by the superscript *crf*) and thus, it reduces to the following formFérec *et al.* (2009)

$$\Delta\dot{\mathbf{r}}^{crf} = \frac{s^\beta}{2}\left(\dot{\boldsymbol{\gamma}} \cdot \mathbf{p}^\beta - \dot{\boldsymbol{\gamma}} : \mathbf{p}^\beta \mathbf{p}^\beta \mathbf{p}^\beta\right) - \frac{s^\alpha}{2}\left(\dot{\boldsymbol{\gamma}} \cdot \mathbf{p}^\alpha - \dot{\boldsymbol{\gamma}} : \mathbf{p}^\alpha \mathbf{p}^\alpha \mathbf{p}^\alpha\right) . \tag{5.6}$$

The expression of $\Delta\dot{\mathbf{r}}^{crf}$ is then substituted in Eq. 5.5 to calculate the interaction force. In doing so, we first calculate the dot product in Eq. 5.7

$$\begin{aligned}\Delta\dot{\mathbf{r}}^{crf}\cdot\Delta\dot{\mathbf{r}}^{crf} &= \left(\frac{s^{\beta}}{2}\right)^{2}\left[\dot{\boldsymbol{\gamma}}^{2}:\mathbf{p}^{\beta}\mathbf{p}^{\beta}-\left(\dot{\boldsymbol{\gamma}}:\mathbf{p}^{\beta}\mathbf{p}^{\beta}\right)^{2}\right]\\ &+\left(\frac{s^{\alpha}}{2}\right)^{2}\left[\dot{\boldsymbol{\gamma}}^{2}:\mathbf{p}^{\alpha}\mathbf{p}^{\alpha}-\left(\dot{\boldsymbol{\gamma}}:\mathbf{p}^{\alpha}\mathbf{p}^{\alpha}\right)^{2}\right] \qquad (5.7)\\ &-\frac{s^{\alpha}s^{\beta}}{2}\left[(\dot{\boldsymbol{\gamma}}\cdot\mathbf{p}^{\beta}-\dot{\boldsymbol{\gamma}}:\mathbf{p}^{\beta}\mathbf{p}^{\beta}\mathbf{p}^{\beta})\cdot(\dot{\boldsymbol{\gamma}}\cdot\mathbf{p}^{\alpha}-\dot{\boldsymbol{\gamma}}:\mathbf{p}^{\alpha}\mathbf{p}^{\alpha}\mathbf{p}^{\alpha})\right].\end{aligned}$$

For the sake of simplicity and without losing too much information about the physics (i.e. having the same shear-rate dependency), Eq. 5.7 can be written as

$$\left(\Delta\dot{\mathbf{r}}^{crf}\cdot\Delta\dot{\mathbf{r}}^{crf}\right)^{\frac{m-1}{2}}\approx\left|\frac{s^{\alpha}}{2}\dot{\boldsymbol{\gamma}}:\mathbf{p}^{\alpha}\mathbf{p}^{\alpha}\right|^{m-1}. \qquad (5.8)$$

This choice is based on two observations. First, the retained scalar has the simplest expression among the other scalars and second, it has a form already reported in the literature by different authors [Souloumiac and Vincent (1998), Gibson and Toll (1999)]. We finally obtain the new form for the interaction force

$$\mathbf{f}_{\mathbf{I}}=Dkb\left|\frac{s^{\alpha}}{2}\dot{\boldsymbol{\gamma}}:\mathbf{p}^{\alpha}\mathbf{p}^{\alpha}\right|^{m-1}\Delta\dot{\mathbf{r}}^{crf}. \qquad (5.9)$$

In order to calculate the elementary interaction force, we need to weight $\mathbf{f}_{\mathbf{I}}$ by the contact probability P_C that represents the probability that a neighboring rod interacts with the test rod. Doi and Edwards (1978a), and then Sandstrom (1993) have proposed an evaluation of this probability as

$$P_C=2nD\left|\mathbf{p}^{\alpha}\times\mathbf{p}^{\beta}\right|\psi_{\mathbf{p}^{\beta}}d\mathbf{p}^{\beta}ds^{\alpha}ds^{\beta}, \qquad (5.10)$$

where n is the number density of the rods and $\psi_{\mathbf{p}^{\beta}}$ is the probability to find the interacting rod with an orientation $\mathbf{p}^{\beta}$.

Combining Eqs. (5.9) and (5.10), the new elementary interaction force can be written as

$$d\mathbf{f}_{\mathbf{I}} = 2nD^2kb\left|\frac{s^{\alpha}}{2}\right|^{m-1}\left|\dot{\boldsymbol{\gamma}}:\mathbf{p}^{\alpha}\mathbf{p}^{\alpha}\right|^{m-1}\Delta\dot{\mathbf{r}}^{crf}\left|\mathbf{p}^{\alpha}\times\mathbf{p}^{\beta}\right|\psi_{\mathbf{p}^{\beta}}d\mathbf{p}^{\beta}ds^{\alpha}ds^{\beta}, \tag{5.11}$$

Once we obtain the expression for $d\mathbf{f}_{\mathbf{I}}$, it is possible to evaluate the global torque, $\mathbf{T_I}$, integrating Eq. 5.3 over the neighboring and test rod lengths and over all directions of $\mathbf{p}^{\beta}$. This is equivalent in saying that the "interaction event" can happen with the same probability at any combination of points on the test and neighboring rods (described by the arc lengths s^{α} and s^{β}), but the rod-rod interaction depends on the orientation of the neighboring rods. With these considerations, the global torque is evaluated and consequently, the expression of the orientation time evolution for the test fiber α is obtained

$$\dot{\mathbf{p}}^{\alpha} = \dot{\mathbf{p}}_H^{\alpha} - \phi M_I\int\frac{1}{2}(\dot{\boldsymbol{\gamma}}\cdot\mathbf{p}^{\alpha} - \dot{\boldsymbol{\gamma}}:\mathbf{p}^{\alpha}\mathbf{p}^{\alpha}\mathbf{p}^{\alpha})\left|\mathbf{p}^{\alpha}\times\mathbf{p}^{\beta}\right|\left|\dot{\boldsymbol{\gamma}}:\mathbf{p}^{\alpha}\mathbf{p}^{\alpha}\right|^{m-1}\psi_{\mathbf{p}^{\beta}}d\mathbf{p}^{\beta} \tag{5.12}$$

,

where ϕ is the volume fraction of the rods and $M_I \equiv \frac{kbL^{m-1}}{2^{2m-3}(m+2)\eta_0\pi Y_C}$, called rod-rod interaction intensity factor, and $\dot{\mathbf{p}}_H^{\alpha}$ is given by the Jeffery (1922) with $\lambda = 1$

$$\dot{\mathbf{p}}_H^{\alpha} = -\frac{1}{2}\boldsymbol{\omega}\cdot\mathbf{p}^{\alpha} + \frac{1}{2}(\dot{\boldsymbol{\gamma}}\cdot\mathbf{p}^{\alpha} - \dot{\boldsymbol{\gamma}}:\mathbf{p}^{\alpha}\mathbf{p}^{\alpha}\mathbf{p}^{\alpha}). \tag{5.13}$$

Following Folgar and Tucker (1984), we consider that the interactions also modify the fiber rotation, and a perturbation velocity, proportional to the effective deformation rate $|\dot{\gamma}|$, is introduced

$$\dot{\mathbf{p}}^{\alpha} = \dot{\mathbf{p}}_H^{\alpha} - \phi M_I\int\frac{1}{2}(\dot{\boldsymbol{\gamma}}\cdot\mathbf{p}^{\alpha} - \dot{\boldsymbol{\gamma}}:\mathbf{p}^{\alpha}\mathbf{p}^{\alpha}\mathbf{p}^{\alpha} + 2q|\dot{\gamma}|\frac{\partial\ln\psi_{\mathbf{p}^{\alpha}}}{\partial\mathbf{p}^{\alpha}}) \left|\mathbf{p}^{\alpha}\times\mathbf{p}^{\beta}\right|\left|\dot{\boldsymbol{\gamma}}:\mathbf{p}^{\alpha}\mathbf{p}^{\alpha}\right|^{m-1}\psi_{\mathbf{p}^{\beta}}d\mathbf{p}^{\beta}, \tag{5.14}$$

where *q* is a dimensionless interaction coefficient. This diffusional term (the third term in the brackets in Eq. 5.14 is not due to the Brownian motion, but represents the rotational fluctuations undergoing by the test fiber, when the suspension is under flow.

5.4 Rod orientation distribution

A suspension is composed of a multitude of particles dispersed in a medium, and to deal with a rod population instead of a single rod, it is necessary to use the orientation distribution function $\psi_{\mathbf{p}^\alpha}$ [Advani and Tucker (1987)]. Thus, the probability to find a particle between $\mathbf{p}^\alpha$ and $\left(\mathbf{p}^\alpha + d\mathbf{p}^\alpha\right)$ is represented by $\psi_{\mathbf{p}^\alpha}$. Considering that when a particle leaves one orientation it must appear in another one, $\psi_{\mathbf{p}^\alpha}$ can be regarded as a convected scalar. From Bird *et al.* (1987), the continuity relation can be expressed as

$$\frac{D}{Dt}\psi_{\mathbf{p}^\alpha} = -\frac{\partial}{\partial \mathbf{p}^\alpha}\cdot\left(\dot{\mathbf{p}}^\alpha \psi_{\mathbf{p}^\alpha}\right), \tag{5.15}$$

where *D/Dt* represents the material derivative. Before combining the last expression with the equation of motion, it is convenient to rewrite Eq. 5.15 in a more compact way. First we define two new expressions

$$\lambda_{\mathbf{p}^\alpha} = 1 - \phi M_I \int \left|\mathbf{p}^\alpha \times \mathbf{p}^\beta\right| \left|\dot{\boldsymbol{\gamma}} : \mathbf{p}^\alpha \mathbf{p}^\alpha\right|^{m-1} \psi_{\mathbf{p}^\beta} d\mathbf{p}^\beta , \tag{5.16}$$

$$\dot{\mathbf{p}}_I^\alpha = -\frac{1}{2}\boldsymbol{\omega}\cdot\mathbf{p}^\alpha + \frac{1}{2}\lambda_{\mathbf{p}^\alpha}\left(\dot{\boldsymbol{\gamma}}\cdot\mathbf{p}^\alpha - \dot{\boldsymbol{\gamma}} : \mathbf{p}^\alpha\mathbf{p}^\alpha\mathbf{p}^\alpha\right), \tag{5.17}$$

where $\dot{\mathbf{p}}_I^{\boldsymbol{\alpha}}$ reduces to the Jeffery (1922) equation with $\lambda = 1$ when the concentration of particles in the system tends towards zero. According to the above definitions, it is possible now to rewrite Eq. 5.14 as follows

$$\dot{\mathbf{p}}^{\alpha} = \dot{\mathbf{p}}_I^{\alpha} - q|\dot{\gamma}|\left(1-\lambda_{\mathbf{p}^{\alpha}}\right)\frac{\partial \ln \psi_{\mathbf{p}^{\alpha}}}{\partial \mathbf{p}^{\alpha}}. \tag{5.18}$$

Finally, we can obtain the time evolution for the probability distribution function by substituting Eq. 5.18 in Eq. 5.15

$$\frac{D}{Dt}\psi_{\mathbf{p}^{\alpha}} = -\frac{\partial}{\partial \mathbf{p}^{\alpha}}\cdot\left(\dot{\mathbf{p}}_I^{\alpha}\psi_{\mathbf{p}^{\alpha}}\right) + q|\dot{\gamma}|\frac{\partial}{\partial \mathbf{p}^{\alpha}}\cdot\left[\left(1-\lambda_{\mathbf{p}^{\alpha}}\right)\frac{\partial \psi_{\mathbf{p}^{\alpha}}}{\partial \mathbf{p}^{\alpha}}\right]. \tag{5.19}$$

This expression simplifies into the pure convective Fokker-Planck equation [Doi and Edwards (1986)] when the concentration of particles is very low.

5.5 Stress determination

Following to Férec *et al.* (2009), the overall stress is the sum of the matrix, the hydrodynamic and the rod interactions contributions and hence, the deviatoric form of the stress $\boldsymbol{\tau}$ becomes

$$\boldsymbol{\tau} = \eta_0\dot{\boldsymbol{\gamma}} + \eta_0\phi N_P\dot{\boldsymbol{\gamma}} : \mathbf{a_4} + n\iint s^{\alpha}\mathbf{p}^{\alpha}d\mathbf{f}_{\mathbf{I}}\psi_{\mathbf{p}^{\alpha}}d\mathbf{p}^{\alpha}, \tag{5.20}$$

where $N_P = X_A r^2/6\pi$, X_A is the parallel drag coefficient of the rods and $\mathbf{a_4}$ is the well-known fourth order orientation tensor defined by Advani and Tucker (1987)

$$\mathbf{a_4} = \int \mathbf{p}^{\alpha}\mathbf{p}^{\alpha}\mathbf{p}^{\alpha}\mathbf{p}^{\alpha}\psi_{\mathbf{p}^{\alpha}}d\mathbf{p}^{\alpha}. \tag{5.21}$$

Developing the integral in Eq. 5.20 using Eqs. 5.6 and 5.11, the contribution to the stress due to rod interactions is obtained

$$\boldsymbol{\tau}_{\mathbf{I}} \equiv n\iint s^{\alpha}\mathbf{p}^{\alpha}d\mathbf{f}_{\mathbf{I}}\psi_{\mathbf{p}^{\alpha}}d\mathbf{p}^{\alpha} = 2\phi^2 M_I\frac{r^2\eta_0 Y_C}{\pi}\dot{\boldsymbol{\gamma}} : \mathbf{b_4}^{(m)}, \tag{5.22}$$

with $\mathbf{b_4}^{(m)}$, the new form of the interaction tensor, defined as

$$\mathbf{b}_4^{(m)} = \int\int \mathbf{p}^\alpha \mathbf{p}^\alpha \mathbf{p}^\alpha \mathbf{p}^\alpha \left|\mathbf{p}^\alpha \times \mathbf{p}^\beta\right| \left|\dot{\boldsymbol{\gamma}} : \mathbf{p}^\alpha \mathbf{p}^\alpha\right|^{m-1} \psi_{\mathbf{p}^\alpha} \psi_{\mathbf{p}^\beta} d\mathbf{p}^\alpha d\mathbf{p}^\beta . \tag{5.23}$$

The interaction tensor is completely symmetric and it shows a direct dependence on the rate of deformation. Finally, the total stress tensor accounting the effects of rod interactions is given by

$$\boldsymbol{\sigma} = -P\boldsymbol{\delta} + \eta_0 \dot{\boldsymbol{\gamma}} + \phi\eta_0 X_A \frac{r^2}{6\pi} \dot{\boldsymbol{\gamma}} : \mathbf{a}_4 + 2\phi^2 M_I \frac{r^2 \eta_0 Y_C}{\pi} \dot{\boldsymbol{\gamma}} : \mathbf{b}_4^{(m)}, \tag{5.24}$$

where P is the pressure. We note that Eq. 5.24 reduces to the constitutive equation proposed by Férec *et al.* (2009) for $m = 1$ and $b = \eta_0$. Moreover, when the rod volume fraction, ϕ, is very small, the contribution due to interactions is negligible and the total stress reduces to that obtained by Dinh and Armstrong (1984) which is valid in the dilute concentration regime.

5.6 Numerical method

For the case of steady-state shear flow, the viscosity and the first normal stress difference are deduced from Eq. 5.24 and can be written as

$$\begin{aligned} \eta &= \eta_0 + 2\phi\eta_0 N_P a_{1122} + 4\phi^2 M_I \frac{r^2 \eta_0 Y_C}{\pi} b_{1122}^{(m)} \\ N_1 &= 2\phi\eta_0 N_P \dot{\gamma}_{12} \left(a_{1112} - a_{1222}\right) + 4\phi^2 M_I \frac{r^2 \eta_0 Y_C}{\pi} \dot{\gamma}_{12} \left(b_{1112}^{(m)} - b_{1222}^{(m)}\right) \end{aligned} . \tag{5.25}$$

Eqs. 4.25 show that key components of the fourth-order orientation and interaction tensors are needed to evaluate the viscosity and the first normal stress material functions. Generally closure approximations are used to express the fourth-order tensors in terms of the second-order ones [Advani and Tucker III (1990), Cintra and Tucker III (1995), Chung and Kwon (2001), Férec *et al.* (2008)]. Despite the fact that closure approximations are more and more accurate, they always lead to some unavoidable errors. To circumvent this barrier, a possible strategy is to use the probability distribution function evaluated for steady-state. Hence, Eq. 5.19 becomes

$$\frac{\partial}{\partial \mathbf{p}^{\alpha}} \cdot \left(\dot{\mathbf{p}}_I^{\alpha} \psi_{\mathbf{p}^{\alpha}} \right) = q |\dot{\gamma}| \frac{\partial}{\partial \mathbf{p}^{\alpha}} \cdot \left[\left(1 - \lambda_{\mathbf{p}^{\alpha}} \right) \frac{\partial \psi_{\mathbf{p}^{\alpha}}}{\partial \mathbf{p}^{\alpha}} \right]. \tag{5.26}$$

This Fokker-Planck equation is strongly non-linear as both $\dot{\mathbf{p}}_I^{\alpha}$ and $\lambda_{\mathbf{p}^{\alpha}}$ are functions of $\psi_{\mathbf{p}^{\alpha}}$. Therefore, no simple analytic solution exists and a numerical resolution is required. Eq. 5.26 is numerically solved using a finite volume method as previously performed by Férec *et al.* (2008) (see Férec *et al.* (2008) for more details about the mesh and the treatment of the periodic boundary conditions). The central scheme has been implemented in order to interpolate properties between the nodes. To obtain a physically steady-state solution, a constraint is added to the numerical system in order to respect the normalization condition. For a given shear rate, the nonlinear terms are evaluated using successive iterations for the probability distribution function, starting with an initial guess of $1/4\pi$. Convergence is reached when the error between two successive iterations is less than 10^{-3}. Once the distribution function is numerically computed, the orientation and interaction tensor components are straightforwardly obtained for any shear rate using Eqs. 5.21 and 5.23.

5.6.1 Isotropic orientation distribution

In order to understand how the model predictions are influenced by the non-linear interactions, a first set of simulations was computed imposing an isotropic orientation distribution. This condition was chosen because it guarantees the maximum number of interactions at each shear rate and hence, it enhances the effect of the interactions on the overall computations. All the predictions presented in this section and the next were obtained for the following conditions: $\eta_0 = 25$ Pa.s, $\phi = 0.10$ and $r = 30.$ In the case of constant isotropic orientation distribution, the only adjustable parameters are M_I, N_P and *m*. While *m* is responsible for how the interaction contribution in the macroscopic stress tensor depends on the shear rate, M_I and N_P that control the intensity of the mechanical (rod-rod) and hydrodynamic interactions, respectively, are taken to be both equal to 100, which is a typical value for our experimental suspensions. In the case of simple shear flow and for $m = 0.3$, the different contributions to the steady-state reduced viscosity of a filled system are illustrated in Figure 5.1.

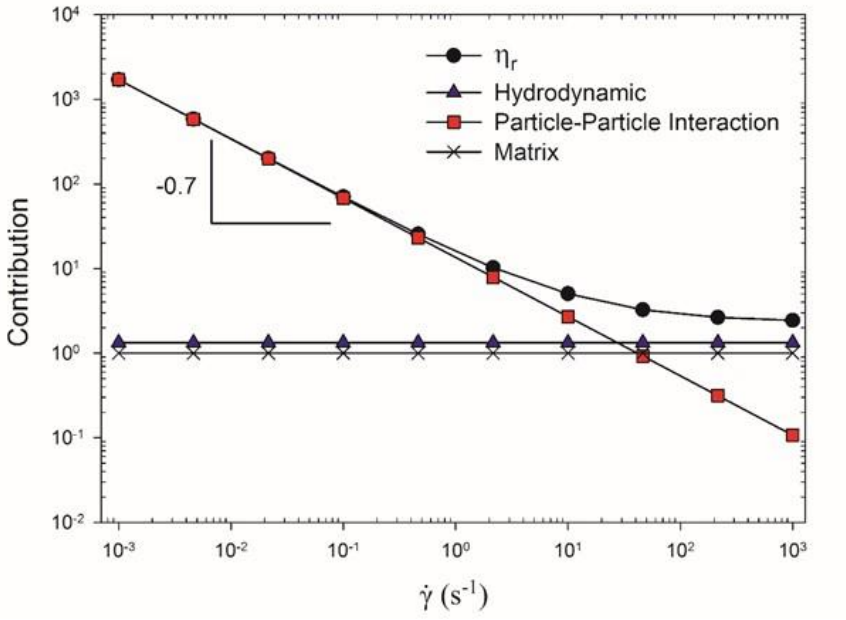

Figure 5.1 Individual and overall contributions to the steady-state reduced viscosity of a filled system in simple shear flow. The results were obtained in the case of isotropic orientation distribution and m=0.3.

The hydrodynamic contribution is independent of the shear rate while the one due to rod-rod interactions show a decreasing trend. At low shear rates, the mechanical (rod-rod) interactions are the dominant mechanism while, at high shear rates, the hydrodynamic contribution becomes controlling. The transition between the two mechanisms is clearly represented by the trend of the reduced viscosity that goes from a shear-thinning behavior to a plateau-like at high shear rates that approaches the viscosity of the matrix. In the case of an isotropic orientation distribution the first normal stress difference is null, independently of the shear rate, because the components of $\mathbf{a}_4$ and $\mathbf{b}_4^{(m)}$ involved in the expression of N_1 are equal to each other.

The model was also tested for the case of elongational flow, resulting in similar behaviors (results not shown here).

5.6.2 Parametric analysis

When the condition on the isotropic orientation distribution is removed, the model has a fourth adjustable parameter, q, which controls the perturbation on the particle rotational velocity due to the interactions, and that is modeled mathematically as a diffusion term in Eq. 5.19. The effects of q and N_P on the model predictions are well-known from the literature [Férec *et al.* (2009, Sepehr *et al.* (2004a)]. The steady-state viscosity is almost independent of q whereas it increases with N_P, and the first normal stress difference rises with q and N_P. With the introduction of the non-linear elementary rod-rod interaction force, two additional adjustable parameters have entered the model (M_I and m) and the interactions between particles can also be controlled by tuning their values. The set of parameters used for the following simulation results are reported in

Table 5.1.

Table 5.1 Parameters used for the parametric analysis on the steady shear viscosity, normal stress difference and $\mathbf{a}_2$ components predictions.

	Test A	Test B
N_P	100	100
M_I (s^{m-1})	[0.1, 0.3, 0.5, 0.7]	0.5
q	0.1	0.1
m	0.5	[0.3, 0.5, 0.7, 1]

Increasing M_I (Test A) is equivalent to increasing the intensity of the interactions and this is clearly shown by the higher steady shear viscosity and enhanced shear-thinning illustrated in Figure 5.2.

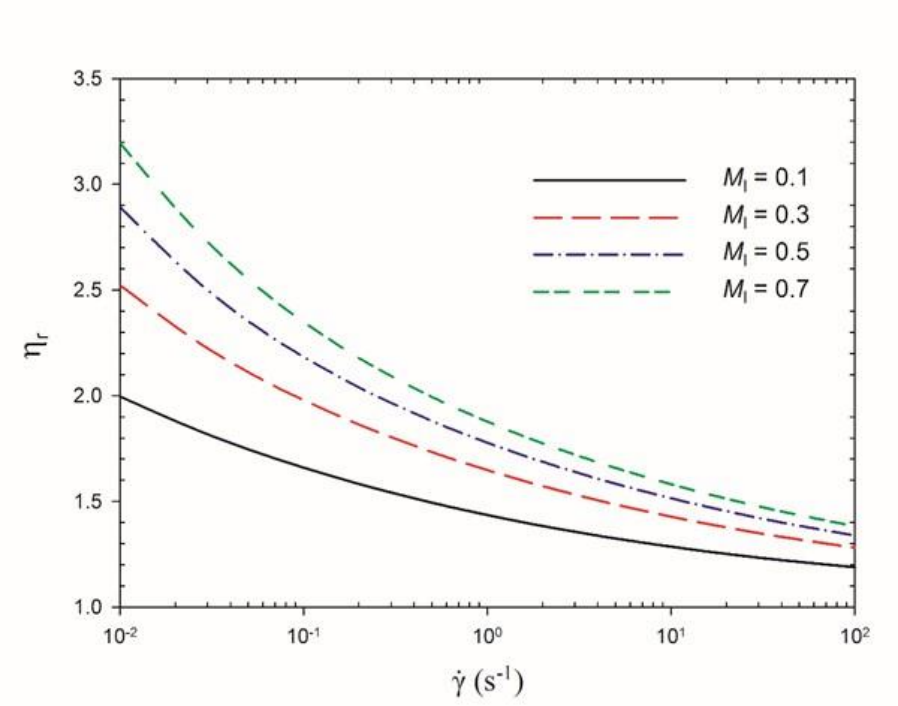

Figure 5.2 Reduced steady-shear viscosity predictions as function of shear rate for different values of MI. The values of the other three adjustable parameters are reported in Table 5.1 (Test A).

By the analysis of the second order tensor component a_{11} (where 1 is the flow direction), the interactions prevent rods from getting aligned in the flow direction, which is physically realistic as depicted in Figure 5.3.

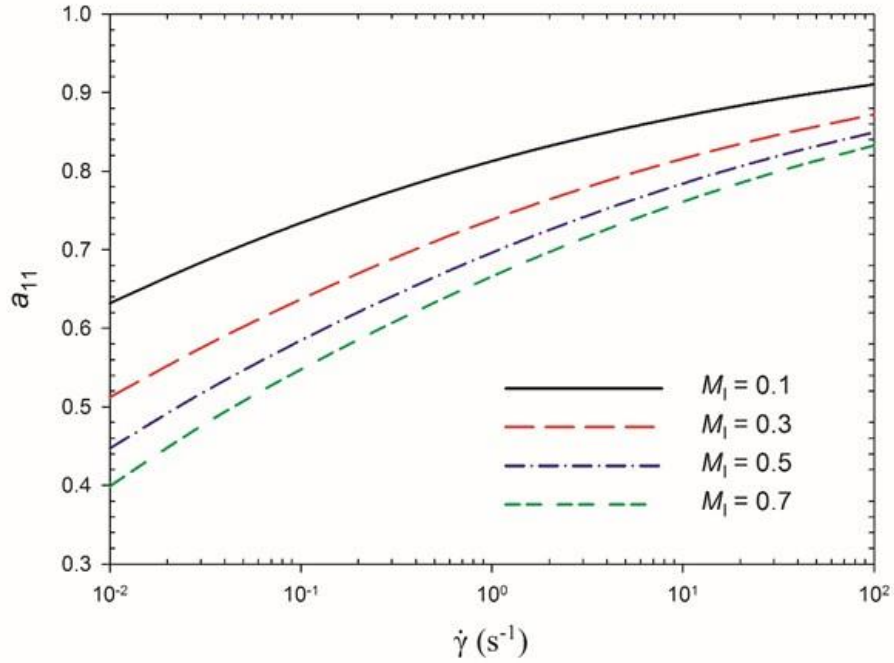

Figure 5.3 Component a11 of the second order orientation tensor as function of shear rate for different values of MI. The values of the other three adjustable parameters are reported in Table 5.1 (Test A).

Modern theories of anisotropic particle suspensions attribute the origin of the normal force to particles sticking out of the flow plane due to interactions [Dinh and Armstrong (1984), Folgar and Tucker (1984), Férec *et al.* (2009)]. The model predictions are in agreement with this last statement as shown by the increase of the first normal stress difference presented in Figure 5.4.

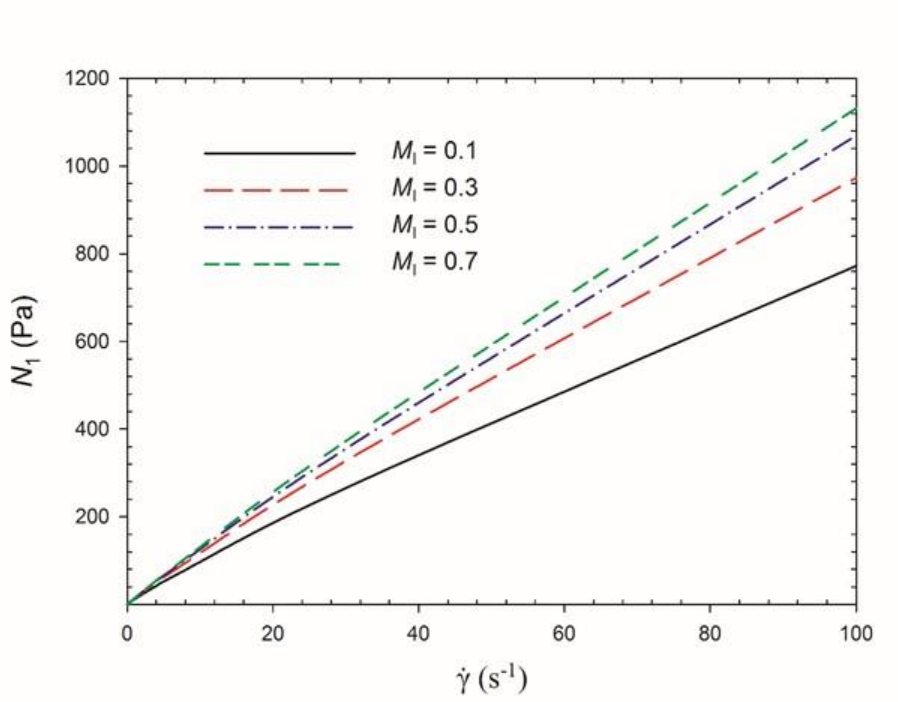

Figure 5.4 First normal stress difference predictions as function of shear rate for various values of M_I. The values of the three other adjustable parameters are reported in Table 5.1 (Test A).

Conversely, the initial condition of an isotropic orientation is characterized by the obvious fact that the particle orientation distribution is spherically symmetric at equilibrium. However, shear flow will distort the distribution, making it "ellipsoidal". Normal stresses can be associated to the tendency of the distorted distribution to relax back to the spherical shape, implying a compression orthogonal to the shear direction. The rod-rod interactions influence how the orientation distribution is distorted by the shear flow.

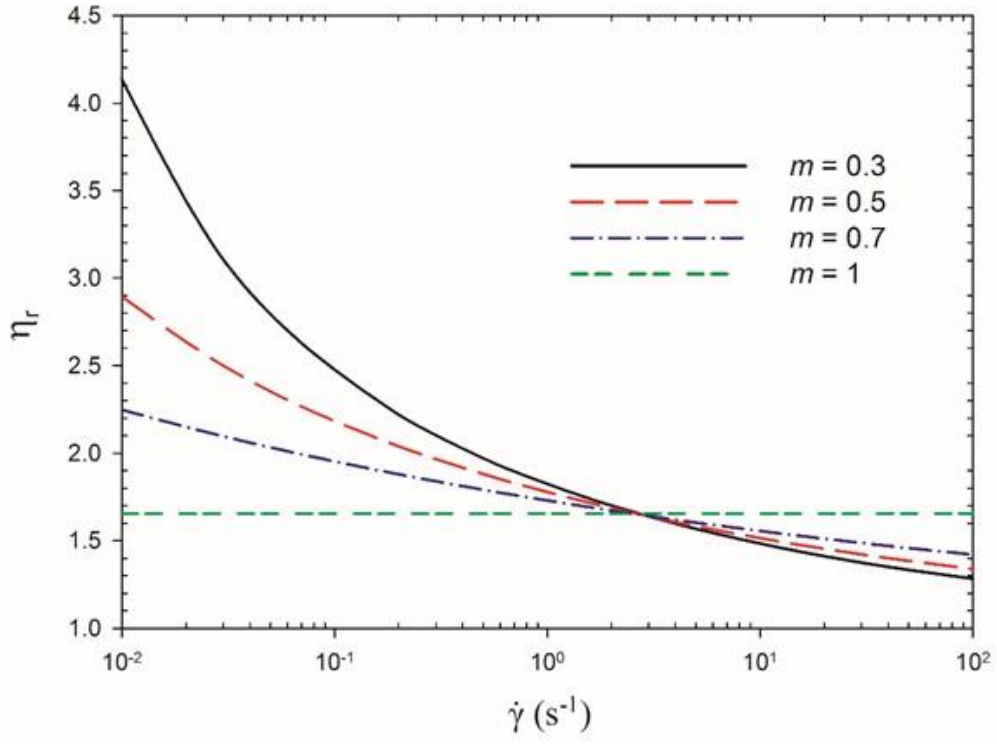

Figure 5.5 Reduced steady shear viscosity predictions as function of shear rate for different values of m. The values of the other three adjustable parameters are reported in Table 5.1 (Test B).

The effect of parameter *m* on the reduced steady shear viscosity is highlighted in Figure 5.5 (parameters of Test B in Table 5.1). Varying *m* from 0 to 1, a full spectrum of behavior is obtained, from shear-thinning ($m<1$) to Newtonian ($m=1$); hence, parameter *m* clearly controls the dependency with shear rate of the interactions.

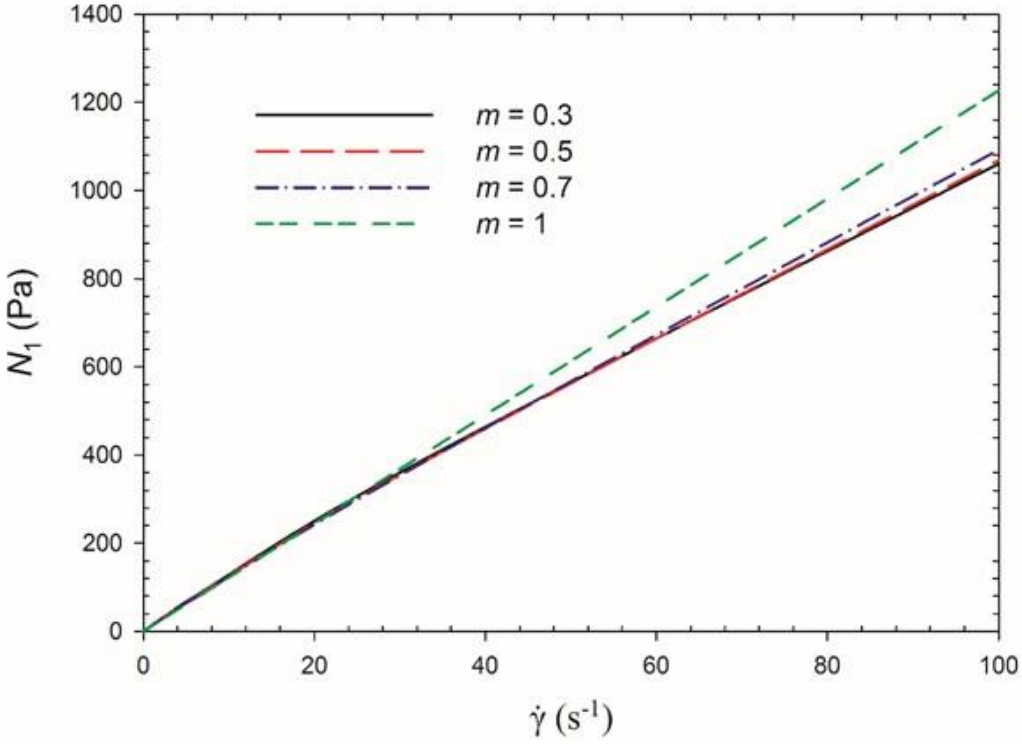

Figure 5.6 First normal stress difference predictions as function of shear rate for different values of m. The values of the other three adjustable parameters are reported in Table 5.1 (Test B).

The first normal stress difference does not show significant variations as illustrated in Figure 5.6; however, it shows a decreasing trend with increasing value of *m.* This effect is more significant at high shear rates since *m* influences the dependency of the interactions with shear rate. Lower values of N_1 imply a more oriented network of rods and this scenario is confirmed by the behavior of a_{11} in Figure 5.7.

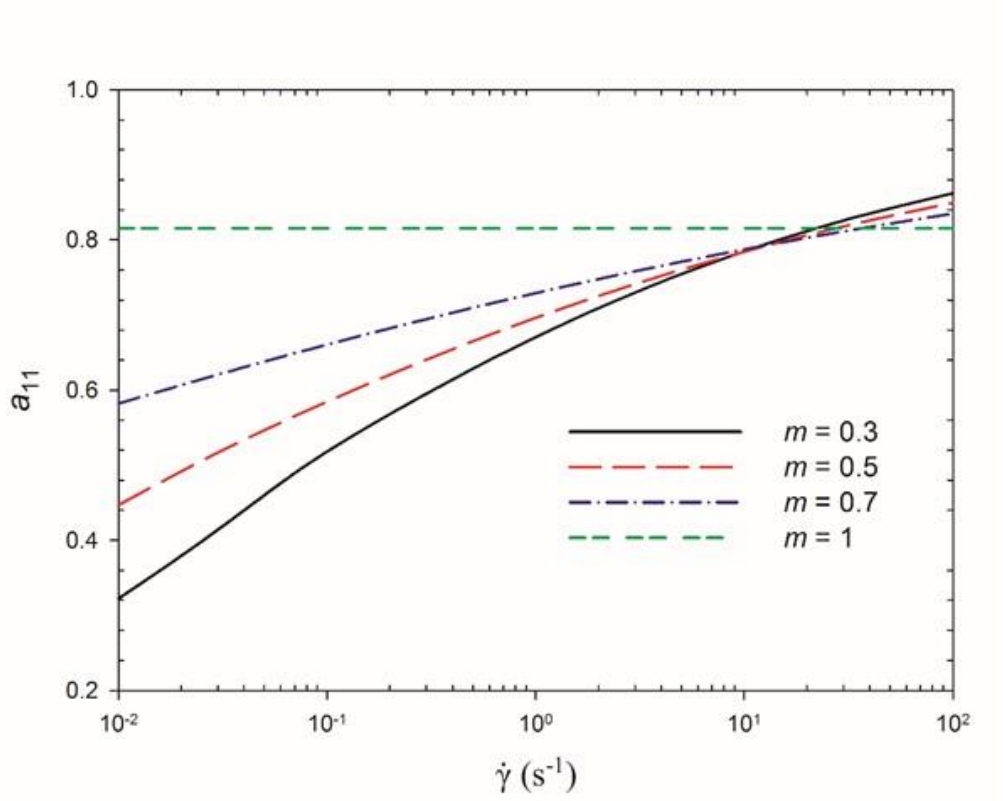

Figure 5.7 Component a11 of the second-order orientation tensor as function of shear rate for different values of m. The values of the other three adjustable parameters are reported in Table 5.1 (Test B).

In addition, the model is able to predict a shear-thickening behavior for ($m > 1$) (results not shown).

5.7 Materials and experimental methodology

A Newtonian low viscosity matrix was chosen in order to emphasize the rheological features due to the carbon nanotubes in the suspension. An epoxy (Epon 828, HEXION Specialty Chemicals Inc.) with a density of 1.16 g/mL and a viscosity of 12.3 Pa.s (at 25 °C) was used as the dispersing medium. Multiwalled carbon nanotubes (MWCNTs) from Cheap Tubes Inc. were characterized in a previous work [Khalkhal *et al.* (2011)]. The main characteristics of the suspensions investigated in this work are given in Table 5.2. The table also reports the corresponding characteristics of glass fiber suspensions in a polybutene taken from Sepehr *et al.* (2004b).

Table 5.2 Characteristics of the materials used in this work.

Suspensions	Matrix	Viscosity η_0 (Pa.s)	Fiber volume % range	Fiber length L (μm)	Fiber diameter D (μm)	Aspect ratio r
EPO-CNT	Epoxy	12.3	0.59 – 2.36	0.1 – 2.2	$7 \cdot 10^{-3}$ – $2.5 \cdot 10^{-2}$	4 – 314
PB-GF	Polybutene	24.0	1.58 – 7.06	260	14	20

In addition, the CNTs can be considered as rigid rods in the range of shear rates studied here according to Switzer III and Klingenberg (2003) assuming a Young modulus of 40 GPa [Hobbie and Fry (2007)].

The suspensions of CNT-epoxy were prepared using an EXAKT three-roll mill (from EXAKT Technologies, Inc.) at room temperature. The CNTs were mixed as received with the epoxy without any surfactant or additive. The samples were initially manually blended with a spatula in a glove box, and then were poured into the three-roll mill (3RM). To break the CNT agglomerates and avoid a reduction in the aspect ratio during mixing, the gaps between the mill rolls were equally set and gradually reduced from 100 to 5 μm. Each sample was circulated between the gaps of the rolls once at the 100 and 50 μm gap sizes, twice at the 20 and 10 μm gap sizes and four times at the 5 μm gap size. During this procedure, the speed of the rollers was maintained constant at 150 rpm.

In order to verify the degree of dispersion, a suspension containing 4.4 wt% CNTs was prepared and transmission electron microscopy (TEM) analysis was performed after thermal curing. The curing agent used was a commercial product, JEFFAMINE® T-403 polyetheramine. After preparation with the three-roll mill, suspension samples were gently hand-mixed with the curing agent at room temperature to avoid formation of bubbles. The composition of the final system was 32 wt% T-403 and 68 wt% epoxy/CNT suspension. Hence, the addition of T-403 resulted in a dilution of CNTs in the system, from 4.4 to 3 wt%. After mixing with the curing agent, the samples

were left to rest for 1 h in a vacuum oven at room temperature to remove any bubbles and finally, always under vacuum, the temperature was increased to 80 ºC for 2 h to obtain a fully set system. TEM analysis was performed on thin sections of samples ultramicrotomed with a diamond knife at room temperature. Figure 5.8 shows TEM images for two magnifications of the cured sample.

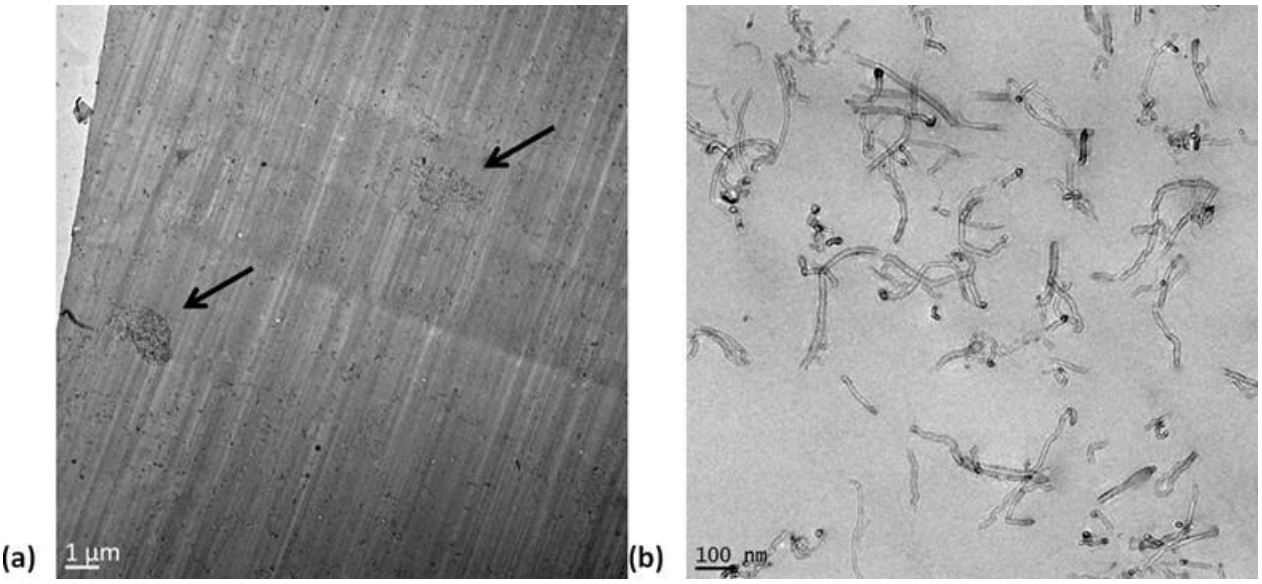

Figure 5.8 TEM images of a cured suspension containing 3 wt% CNTs at lower (a) and at higher (b) magnification. The arrows are used to indicate the agglomerates.

Both images depict a good degree of dispersion of the CNTs with the chosen mixing procedure. Only few agglomerates are observable in the lower magnification image (shown by the arrow in Figure 5.8a) and individual nanotubes, many in contact with neighbors, are detected in the high magnification view (Figure 5.8b). We believe that the few small agglomerates, as seen in Figure 5.8a, have little influence on the rheological behavior of these CNT suspensions.

A Physica MCR502 (Anton Paar) rheometer with a cone-and-plate flow geometry (CP50 with the diameter of 50 mm and an angle of 2°) was used to perform the rheological measurements at 25 °C. The cone-and-plate geometry allows a homogeneous shear flow, which makes it preferable not only to achieve precise rheological data but also to recreate the flow conditions used for the model calculations. The gap at the center of the cone is 51 µm, which is about 80 times larger than the average length of the carbon nanotubes. Moreover, the absence of wall effects was assessed by comparing results from the cone-and-plate geometry with data from a parallel-plate flow geometry (PP50 with a diameter of 49.96 mm, 1 mm gap) corrected according to Carreau *et al.* (1997) (data

not reported). The temperature during the tests was controlled at 25 °C by a Peltier (P-PTD 200) system. All experiments were run one day after sample preparation in order to avoid aging effects.

To cover all concentration regimes, four volume fractions of carbon nanotubes were chosen. According to the work of Khalkhal *et al.* (2011), the limits between the different regimes can be distinguished from rheological measurements based on the reduced viscosity η_r as a function of volume fraction ϕ. The authors found that the boundary between the dilute and the semi-dilute regime was at $\phi \approx 0.9\%$ while the concentrated regime was reached for $\phi \geq 2.05\%$. Hence, one concentration representative of the dilute regime ($\phi = 0.59\%$) or 1 wt%, two for the semi-dilute ($\phi = 1.18\%, 1.77\%$) or 2 and 3 wt%, and one for the concentrated regime were investigated ($\phi = 2.36\%$) or 4 wt%.

5.8 Data and predictions

Network formation, particles orientation and interactions play an important role on the rheological properties of CNT suspensions. While the steady-state viscosity for the neat epoxy is Newtonian over the entire range of shear rate investigated (constant viscosity of 12.3 Pa.s), with the addition of the filler the system exhibits a shear-thinning behavior with a significant enhancement of the viscosity at low shear rates, as illustrated in Figure 5.9.

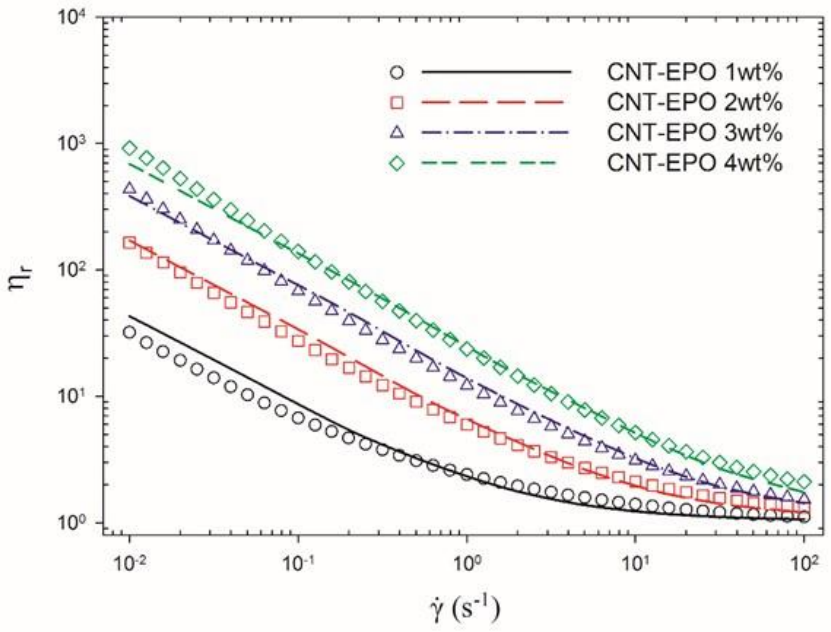

Figure 5.9 Reduced steady shear viscosity data (symbols) for the four CNT concentrations dispersed in an epoxy matrix. The experimental results are compared with the model predictions (lines). The fitting parameter values are reported in Table 5.3.

Table 5.3 Adjustable parameter values obtained by fitting the experimental steady shear viscosity and normal stress difference data for carbon nanotubes dispersed in epoxy (CNT-EPO) and glass fibers dispersed in polybutene (PB-GF) [Sepehr *et al.* (2004b)].

Suspensions	Parallel drag coefficient N_P	Interaction coefficient q	Rod-rod Interaction intensity factor M_I (s^{m-1})	Interaction power-law exponent m
EPO-CNT	146.6	0.06	75.1	0.28
PB-GF	82	5.92	0.07	0.77

The lines are the model predictions using the parameters reported in Table 5.3 and the aspect ratio for the CNTs of 182, which is consistent with the experimental range reported in Table 5.2. As stated before, the model contains four independent adjustable parameters: q, N_P, M_I and m. A least square method was used to solve the fitting problem and only one set of parameters was necessary to predict both the reduced steady shear viscosity and first normal stress difference (Figure 5.10)

for the four CNT concentrations. The model predicts very well the effect of CNT concentration as well as the shear-thinning behavior.

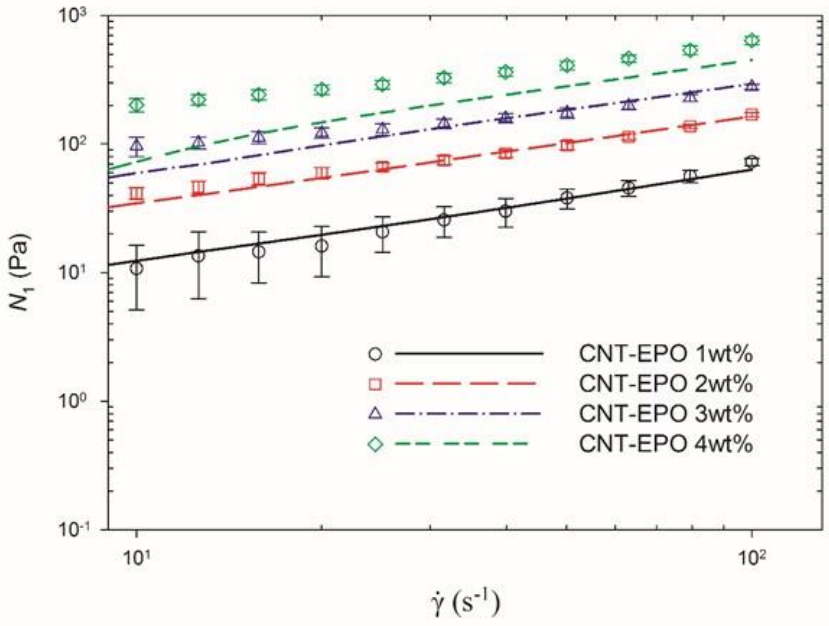

Figure 5.10 First normal stress difference data (symbols) for the four CNT concentrations dispersed in an epoxy matrix. The experimental results are compared with the model predictions (lines). The fitting parameter values are reported in Table 5.3.

By increasing the CNT content, nanotube-nanotube interactions become progressively dominant. The higher is the concentration, the smaller the relative inter-particle distance. This eventually leads to a percolated network throughout the system which restrains the long-range motion of the polymer chains [Hobbie and Fry (2007)], responsible for a further increase in the viscosity at low shear rates. However, the shear flow is able to break down the network between MWNTs and the individual particles get oriented in the flow direction [Fan and Advani (2007)]. This promotes the shear-thinning behavior reported in Figure 5.9. The steady shear viscosity data obeys a power-law expression at low shear rates. The slope of the log-log plots decreases slightly with the loading, varying from -0.67 (1 wt%) to -0.82 (4 wt%), whereas the model predicts an unique slope of -0.72. Thus, the behavior tends to the solid-like limit, which is characterized by a theoretical slope of -1.

The presence of carbon nanotubes in a Newtonian matrix causes the appearance of normal stresses during shear flow, as shown in Figure 5.10. Normal stresses increase with shear rate and CNT concentration (data also become less noisy). This suggests that the enhancement of the normal force is a result of the combination of particle interactions [Sepehr *et al.* (2004a)] and network elasticity developed by the interconnections between the high aspect ratio CNTs in the medium. The lines in Figure 5.10 are the model predictions using the same parameters as for the fitting of the steady shear viscosity of Figure 5.9 (see Table 5.3). The model predicts correctly the trend with shear rate; however the effect of CNT concentration is underpredicted. The rod-rod interactions are not sufficient to predict the high values of the first normal stress difference as observed at low-shear rates for the more concentrated CNT suspension. This aspect is intrinsically connected with the formation of a network (percolation) resulting from the contact of multiple particles and, hence, another mechanism has to be introduced to describe the network elasticity.

Many authors have reported the establishment of a particle network in their system by showing the classical plateau of the storage modulus (G') at low frequencies in small amplitude oscillatory shear (SAOS) measurements [Du *et al.* (2004), Fan and Advani (2007), Hobbie and Fry (2007)]. In addition, many others have reported the tangent of the phase angle for CNT suspensions showing the transition from a viscous to an elastic system coinciding with the establishment of a network (or percolation threshold) [Abdel-Goad and Pötschke (2005), Abbasi *et al.* (2009a)].

In order to separate the effect of a network formation from those of the particle-particle interactions, it is useful to compare the experimental findings of suspensions of nanoparticles with those of classical micro-scale suspensions. This helps to highlight the importance of a network on the rheological results of the CNT suspensions, and also to validate the versatility of the model proposed. Hence, the CNT-epoxy system is compared with a Newtonian polybutene filled with glass fibers (data from Sepehr *et al.* (2004b)). The information regarding the matrix and the filler are reported and compared with the respective characteristics of the CNT-epoxy system in Table 5.2.

Three different weight fractions of glass fibers (GFs) were used [4.3% (PB05), 8.7% (PB10), and 17.6% (PB20)]. More information regarding the preparation conditions of the suspensions can be found in Sepehr *et al.* (2004b). Glass fibers (GFs) do not form networks and, when dispersed in a Newtonian matrix, they do not induce elasticity to the system. Consequently they show a moderate

shear-thinning behavior and no tendency towards an infinite viscosity at low shear rates (or presence of a yield stress), even at high concentrations. The behavior is illustrated in Figure 5.11, which compares the steady shear viscosity data to the model predictions.

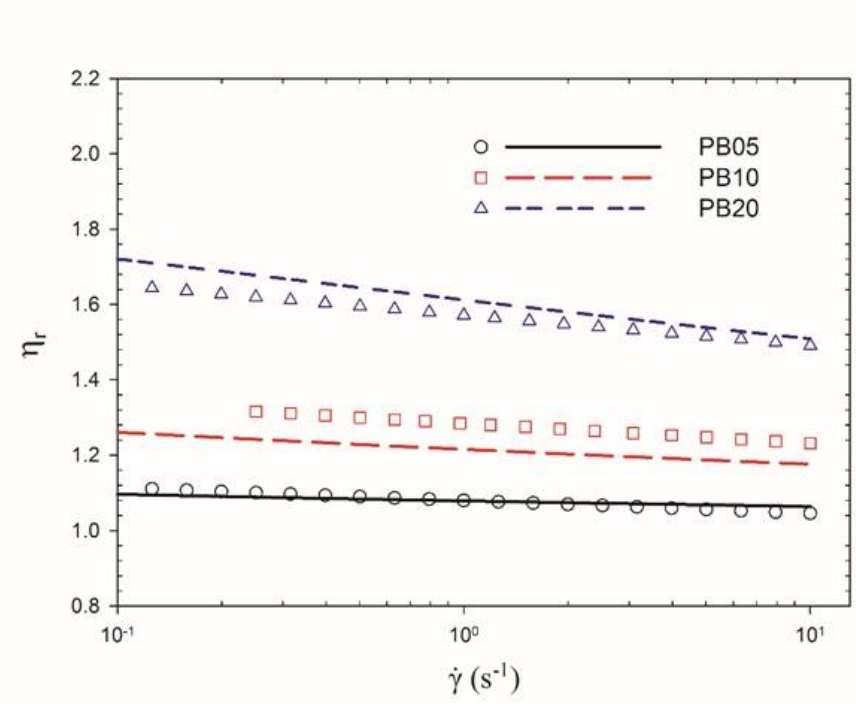

Figure 5.11 Reduced steady shear viscosity data (symbols) of the three GF concentrations dispersed in a polybutene matrix. The experimental results are compared with the model predictions (lines). The fitting parameter values are reported in Table 5.3. The experimental data are taken from Sepehr *et al.* (2004b).

Since no network is established, the shear-thinning must be mainly due to fiber orientation under flow. As for the CNT systems, only one set of the adjustable parameters was required in order to predict all the experimental findings (Figure 5.11 and Figure 5.12).

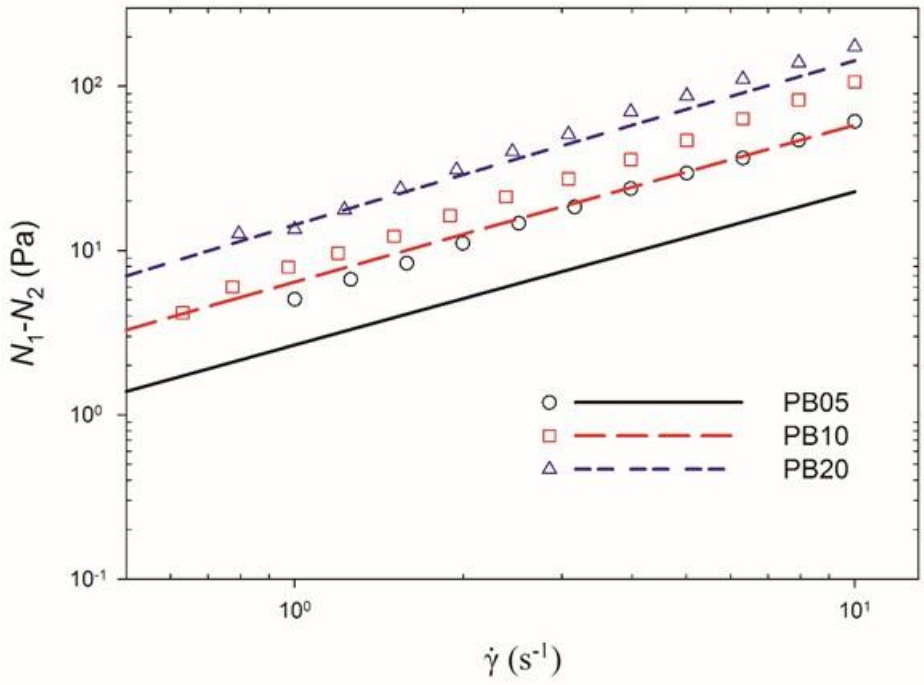

Figure 5.12 Normal stress difference data (symbols) of the three GF concentrations dispersed in a polybutene matrix. The experimental results are compared with the model predictions (lines). The fitting parameter values are reported in Table 5.3. The experimental data are taken from Sepehr *et al.* (2004b).

The values of the parameters for the GF systems are also reported in Table 5.3 and the aspect ratio used in the model is reported in Table 5.2. The model describes reasonably well the data and the shear-thinning is well predicted, but the effect of fiber concentration on the steady-state viscosity is overpredicted. We note from Table 5.3 that the mechanical (rod-rod) interaction intensity factor (M_I) for the glass fiber suspensions is almost zero (0.07) compared to a very large value for the CNT suspensions (75.1).

Figure 5.12 compares the normal stress difference (N_1-N_2) data (obtained from parallel plate geometry) and the model predictions as functions of the shear rate for the different concentrations of glass fibers dispersed in the polybutene matrix. The same parameters for predicting the viscosity were used (see Table 5.3). The normal stress difference exhibits a slope of 1 and its magnitude increases with fiber content as fairly well predicted by the model. The effect of concentration is

too pronounced as observed by the lower values predicted at the lowest fiber concentration (5 wt%). This behavior has been documented in the literature [Goto *et al.* (1986), Petrich *et al.* (2000)]. The enhancement of the normal stresses in the presence of fibers in a Newtonian fluid is largely due to fiber-fiber interactions. The slope of 1 is well predicted by different models [Folgar and Tucker (1984), Djalili-Moghaddam and Toll (2005), Férec *et al.* (2009)] and they all have in common the assumption that collisions between particles are the major cause for nonzero normal stresses in steady shear flows.

In comparison, the slope of the normal stress difference N_1 between 40 and 100 s^{-1} for the CNT suspensions decreases with CNT content, from 0.93 for the 1 wt% to 0.6 for the 4 wt% (Figure 5.10). For the suspension with 1 wt% of CNTs, the network is not fully established since the percolation threshold is somewhere between 1 and 2 wt% as showed by Khalkhal *et al.* (2011). This implies that the increase in normal stresses is mainly due to the interactions between the rods. Thus, the N_1 dependency with shear rate for the lowest CNT concentration is similar to the one reported for GFs, and the slope is indeed close to 1 (0.93). However, with increasing concentration of CNTs, or equivalently building a network between the dispersed particles, the system behaves more like a viscoelastic fluid and the first normal stress difference is the result of two contributions: rod-rod interactions and network elasticity. The rod-rod interaction contribution is a linear function of the shear rate whereas, as showed by the steady-state viscosity in Figure 5.9, the network tends to be destroyed with the intensity of the shear flow, thus the network elasticity contribution must decrease with shear rate. Increasing CNT loading, the contribution due to network elasticity is more important, as shown by the high values of N_1 at low shear rates. Consequently, the relative importance of the network elasticity with respect to the rod-rod interactions grows and, hence, the value of the slope of N_1 vs. $\dot{\gamma}$ (log-log plot) decreases with CNT concentration.

From the model predictions, it is possible to obtain microstructural information. More precisely, the second order orientation tensor can be used as a compact representation of the overall orientation of the particles without significant loss of information. For carbon nanotube suspensions, the components of the second order orientation tensor, calculated for the parameter values given in Table 5.3, are illustrated in Figure 5.13a and b.

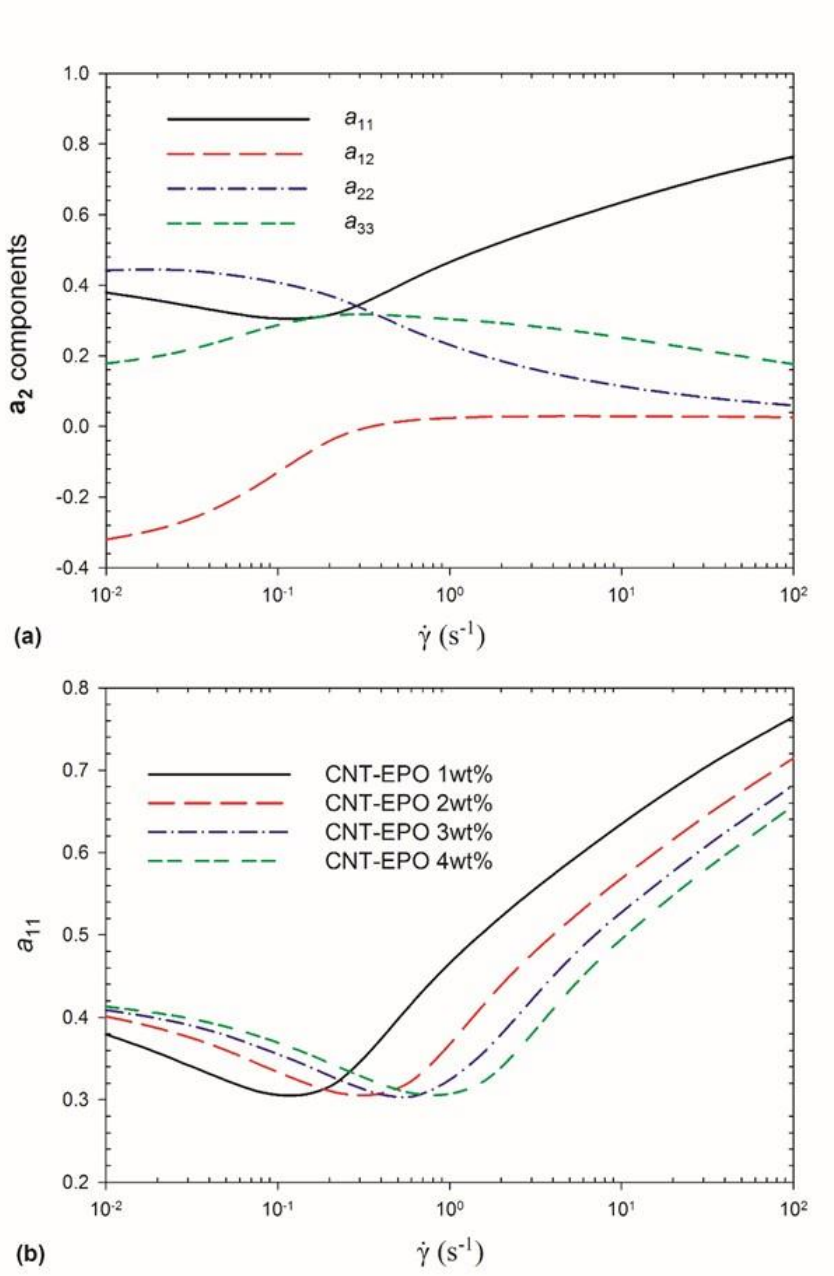

Figure 5.13 (a) Variations of the $\mathbf{a}_2$ components as functions of shear rate for the 1 wt% CNT suspension. (b) Variation of the a_{11} component as function of shear rate for various CNT concentrations.

Initially, the rods tend towards an isotropic orientation at a shear rate around 10^{-1} s^{-1} for the suspension containing 1 wt% CNT and only at larger shear rates do they orient along the flow direction. Increasing the concentration has an effect also on the position of the a_{11} minimum that

is shifted to higher shear rates. Until the shear rate at which the minimum appears, the tendency of the rods to get oriented in the flow direction is overcome by the particle-particle interactions. At higher shear rates the hydrodynamic interactions gain more importance and the rods get oriented. Again, larger is the number of particles dispersed in the system, higher is the average number of contacts for tubes and hence, the overall degree of orientation is lower.

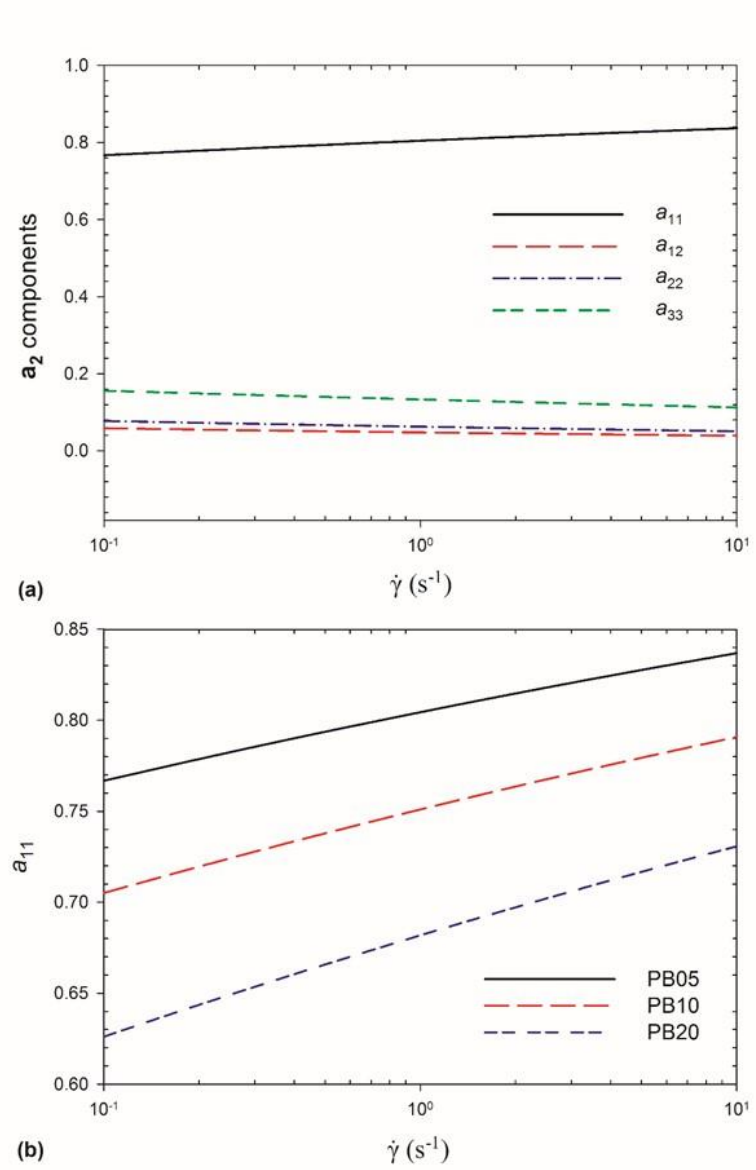

Figure 5.14 (a) Variations of the $\mathbf{a}_2$ components as functions of shear rate for the 5 wt% GF suspension (PB05). (b) Variation of the a_{11} component as function of shear rate for different GF concentrations.

In the case of glass fibers, the components of $\mathbf{a}_2$ show a monotonic behavior as functions of shear rate and the fibers tend to get oriented in the flow direction (Figure 5.14a and b). With increasing fiber concentration, the fiber-fiber interaction contribution becomes more important, provoking a randomizing effect on the overall orientation distribution and causing a lower degree of orientation, as shown in Figure 5.14b.

By comparing the two set of parameters reported in Table 5.3, we underline how the model recognizes the differences between a micro-size and a nano-size filled system. In particular, the nature of the interactions for the two systems is completely different and it is characterized by the two parameters M_I and m. In the case of CNTs, the rod-rod interaction intensity factor (M_I) is three orders of magnitude larger than the one for glass fiber suspension, while the interaction power-law exponent (m) shows a stronger dependency on shear rate. The description of the interaction nature obtained from the model is in agreement with the CNTs higher aspect ratio with respect to GFs, and with the additional contribution due to attractive forces for nano-particles [Yamanoi *et al.* (2010)]. In addition, we find that the value of N_P for the glass fiber system is very close to that obtained by Sepehr *et al.* (2004a) using the Folgar and Tucker (1984) model.

5.9 Concluding remarks

Unlike well-known rheological models for anisotropic particle suspensions at the mesoscopic scale, the new constitutive equation proposed in this work includes a term representative of particle-particle interactions that depends directly on the shear rate. Once the solution of the modified Fokker-Planck equation is obtained for steady-state, it provides the orientation distribution function, the viscosity and normal stress differences without the need of closure approximations. As a consequence of the non-linear function proposed to describe particle-particle interactions, the relative importance of interaction and hydrodynamic contributions depends on shear rate. For an index m between 0 and 1, particle interactions become predominant at low shear rates, exhibiting an apparent yield stress as observed for many non-dilute suspensions, while at high-shear rates the hydrodynamic contribution becomes dominant.

The model predictions are in good agreement with the experimental findings for both the CNT-epoxy and GF-polybutene systems. For the CNT suspensions, the proposed interaction force is not sufficient to completely predict the first normal stress difference data as observed at low shear rates

for the more concentrated suspension. Therefore, another mechanism should be taken into account to fully describe the CNT network elasticity.

Furthermore, the model is found to recognize the differences between micro and nano-size filled composites, mainly distinguishing the relative importance of the particle-particle interactions and network formation.

In this work, we were able to avoid the use of closure approximations by solving numerically the modified Fokker-Planck equation for steady-state. However, closure approximations might be necessary to calculate the predictions in transient flows since the non-linearity present in the modified Fokker-Planck equation will result in very long computational times. Hence, a closed form for the time evolution of the second order orientation tensor will need to be developed. Recently, numerical strategies called proper generalized decomposition (PGD) [Ammar *et al.* (2006), Ammar *et al.* (2007)] have been proposed to overcome the high-dimensional problems (time, physical space and conformational coordinates) involved in complex flows. These techniques may represent alternatives to overcome the limitations of classical approaches.

5.10 Acknowledgments

This work was funded by NSERC (Natural Science and Engineering Research Council of Canada). The authors are thankful to Dr. Daniel Therriault for providing access to the three-roll mill at the composite laboratory in the Mechanical Engineering Department of Ecole Polytechnique.

5.11 References

Abbasi S., P. Carreau, A. Derdouri and M. Moan, "Rheological properties and percolation in suspensions of multiwalled carbon nanotubes in polycarbonate," Rheologica Acta **48**, 943-959 (2009).

Abdel-Goad M. and P. Pötschke, "Rheological characterization of melt processed polycarbonate-multiwalled carbon nanotube composites," Journal of Non-Newtonian Fluid Mechanics **128**, 2-6 (2005).

Advani S. G. and C. L. Tucker, "The use of tensors to describe and predict fiber orientation in short fiber composites," Journal of Rheology **31**, 751-784 (1987).

Advani S. G. and C. L. Tucker III, "Closure approximations for three-dimensional structure tensors," Journal of Rheology **34**, 367-386 (1990).

Ammar A., B. Mokdad, F. Chinesta and R. Keunings, "A new family of solvers for some classes of multidimensional partial differential equations encountered in kinetic theory modeling of complex fluids," Journal of Non-Newtonian Fluid Mechanics **139**, 153-176 (2006).

Ammar A., B. Mokdad, F. Chinesta and R. Keunings, "A new family of solvers for some classes of multidimensional partial differential equations encountered in kinetic theory modelling of complex fluids: Part II: Transient simulation using space-time separated representations," Journal of Non-Newtonian Fluid Mechanics **144**, 98-121 (2007).

Bay R. S., "Fiber orientation in injection-molded composites: A comparison of theory and experiment," Ph.D. dissertation, University of Illinois at Urbana-Champaign, Illinois, United States, 1991.

Bird R. B., C. F. Curtiss, R. C. Armstrong and O. Hassager, *Dynamics of polymeric liquids. Volume 2, Kinetic theory* (Wiley, New York, 1987).

Carreau P. J., D. De Kee and R. P. Chhabra, *Rheology of polymeric systems: Principles and applications* (Hanser, Munich, 1997).

Chinesta F., "From Single-Scale to Two-Scales Kinetic Theory Descriptions of Rods Suspensions," Archives of Computational Methods in Engineering **20**, 1-29 (2013).

Chung D. H. and T. H. Kwon, "Improved model of orthotropic closure approximation for flow induced fiber orientation," Polymer Composites **22**, 636-649 (2001).

Cintra J. J. S. and C. L. Tucker III, "Orthotropic closure approximations for flow-induced fiber orientation," Journal of Rheology **39**, 1095-1122 (1995).

Dinh S. M. and R. C. Armstrong, "A rheological equation of state for semiconcentrated fiber suspensions," Journal of Rheology **28**, 207-227 (1984).

Djalili-Moghaddam M. and S. Toll, "A model for short-range interactions in fibre suspensions," Journal of Non-Newtonian Fluid Mechanics **132**, 73-83 (2005).

Doi M. and S. F. Edwards, "Dynamics of rod-like macromolecules in concentrated solution. Part 1," J. Chem. Soc., Faraday Trans. 2 **74**, 560-570 (1978).

Du F., R. C. Scogna, W. Zhou, S. Brand, J. E. Fischer and K. I. Winey, "Nanotube Networks in Polymer Nanocomposites: Rheology and Electrical Conductivity," Macromolecules **37**, 9048-9055 (2004).

Edwards M. D. a. S. F., *The theory of polymer dynamics* (New York, 1986).

Fan Z. and S. G. Advani, "Characterization of orientation state of carbon nanotubes in shear flow," Polymer **46**, 5232-5240 (2005).

Fan Z. and S. G. Advani, "Rheology of multiwall carbon nanotube suspensions," Journal of Rheology **51**, 585-604 (2007).

Ferec J., G. Ausias, M. C. Heuzey and P. J. Carreau, "Modeling fiber interactions in semiconcentrated fiber suspensions," Journal of Rheology **53**, 49-72 (2009).

Férec J., M. Heniche, M. C. Heuzey, G. Ausias and P. J. Carreau, "Numerical solution of the Fokker–Planck equation for fiber suspensions: Application to the Folgar–Tucker–Lipscomb model," Journal of Non-Newtonian Fluid Mechanics **155**, 20-29 (2008).

Folgar F. P. and C. L. Tucker, "Orientation behavior of fibers in concentrated suspensions," J. Reinf. Plast. Compos. **3**, 99-119 (1984).

Fry D., B. Langhorst, H. Wang, M. L. Becker, B. J. Bauer, E. A. Grulke and E. K. Hobbie, "Rheo-optical studies of carbon nanotube suspensions," The Journal of Chemical Physics **124**, 054703 (2006).

Gibson A. G. and S. Toll, "Mechanics of the squeeze flow of planar fibre suspensions," Journal of Non-Newtonian Fluid Mechanics **82**, 1-24 (1999).

Goto S., H. Nagazono and H. Kato, "The flow behavior of fiber suspensions in Newtonian fluids and polymer solutions," Rheologica Acta **25**, 246-256 (1986).

Guiraud O., L. Orgeas, P. J. J. Dumont and S. R. d. Roscoat, "Microstructure and deformation micromechanisms of concentrated fiber bundle suspensions: An analysis combining x-ray microtomography and pull-out tests," Journal of Rheology **56**, 593-623 (2012).

Hobbie E. K. and D. J. Fry, "Rheology of concentrated carbon nanotube suspensions," The Journal of Chemical Physics **126**, 124907-7 (2007).

Hobbie E. K., H. Wang, H. Kim, S. Lin-Gibson and E. A. Grulke, "Orientation of carbon nanotubes in a sheared polymer melt," Physics of Fluids **15**, 1196-1202 (2003).

Hu G., C. Zhao, S. Zhang, M. Yang and Z. Wang, "Low percolation thresholds of electrical conductivity and rheology in poly(ethylene terephthalate) through the networks of multi-walled carbon nanotubes," Polymer **47**, 480-488 (2006).

Huang Y. Y., S. V. Ahir and E. M. Terentjev, "Dispersion rheology of carbon nanotubes in a polymer matrix," Physical Review B **73**, 125422 (2006).

Jeffery G. B., "The motion of ellipsoidal particles immersed in a viscous fluid," Proceedings of the Royal Society of London Serie A **102**, 161-179 (1922).

Khalkhal F. and P. J. Carreau, "Critical shear rates and structure build-up at rest in MWCNT suspensions," Journal of Non-Newtonian Fluid Mechanics **171–172**, 56-66 (2012).

Khalkhal F., P. J. Carreau and G. Ausias, "Effect of flow history on linear viscoelastic properties and the evolution of the structure of multiwalled carbon nanotube suspensions in an epoxy," Journal of Rheology **55**, 153-175 (2011).

Kim S. and S. J. Karrila, *Microdynamics: Principles and selected applications* (Butterworth - Heinemann, Boston, 1991).

Le Corre S., D. Caillerie, L. Orgéas and D. Favier, "Behavior of a net of fibers linked by viscous interactions: theory and mechanical properties," Journal of the Mechanics and Physics of Solids **52**, 395-421 (2004).

Le Corre S., P. Dumont, L. Orgeas and D. Favier, "Rheology of highly concentrated planar fiber suspensions," Journal of Rheology **49**, 1029-1058 (2005).

Ma A., M. Mackley and S. Rahatekar, "Experimental observation on the flow-induced assembly of Carbon nanotube suspensions to form helical bands," Rheologica Acta **46**, 979-987 (2007).

Ma W. K. A., F. Chinesta, A. Ammar and M. R. Mackley, "Rheological modeling of carbon nanotube aggregate suspensions," Journal of Rheology **52**, 1311-1330 (2008).

Petrich M. P., D. L. Koch and C. Cohen, "An experimental determination of the stress-microstructure relationship in semi-concentrated fiber suspensions," Journal of Non-Newtonian Fluid Mechanics **95**, 101-133 (2000).

Phan-Thien N., X. J. Fan, R. I. Tanner and R. Zheng, "Folgar-Tucker constant for a fibre suspension in a Newtonian fluid," Journal of Non-Newtonian Fluid Mechanics **103**, 251-260 (2002).

Rahatekar S. S., K. K. K. Koziol, S. A. Butler, J. A. Elliott, M. S. P. Shaffer, M. R. Mackley and A. H. Windle, "Optical microstructure and viscosity enhancement for an epoxy resin matrix containing multiwall carbon nanotubes," Journal of Rheology **50**, 599-610 (2006).

Ranganathan S. and S. G. Advani, "Fiber-fiber interactions in homogeneous flows of nondilute suspensions," Journal of Rheology **35**, 1499-1522 (1991).

Sandstrom C. R., "Interactions and orientation in concentrated suspensions of rigid rods: theory and experiment," Ph.D. thesis, University of Illinois, Urbana-Champaign, 1993.

Sandstrom C. R. and C. L. Tucker, "A theory for concentrated fiber suspensions with strong fiber-fiber interactions," Makromolekulare Chemie-Macromolecular Symposia **68**, 291-300 (1993).

Sepehr M., G. Ausias and P. J. Carreau, "Rheological properties of short fiber filled polypropylene in transient shear flow," Journal of Non-Newtonian Fluid Mechanics **123**, 19-32 (2004a).

Sepehr M., P. J. Carreau, M. Moan and G. Ausias, "Rheological properties of short fiber model suspensions," Journal of Rheology **48**, 1023-1048 (2004b).

Servais C., A. Luciani and J.-A. E. Manson, "Fiber--fiber interaction in concentrated suspensions: Dispersed fiber bundles," Journal of Rheology **43**, 1005-1018 (1999a).

Servais C., J.-A. E. Manson and S. Toll, "Fiber--fiber interaction in concentrated suspensions: Disperse fibers," Journal of Rheology **43**, 991-1004 (1999b).

Shaqfeh E. S. G. and G. H. Fredrickson, "The hydrodynamic stress in a suspension of rods," Physics of Fluids a-Fluid Dynamics **2**, 7-24 (1990).

Song Y. S. and J. R. Youn, "Influence of dispersion states of carbon nanotubes on physical properties of epoxy nanocomposites," Carbon **43**, 1378-1385 (2005).

Souloumiac B. and M. Vincent, "Steady shear viscosity of short fibre suspensions in thermoplastics," Rheologica Acta **37**, 289-298 (1998).

Switzer III L. H. and D. J. Klingenberg, "Rheology of sheared flexible fiber suspensions via fiber-level simulations," Journal of Rheology **47**, 759-778 (2003).

Wu D., L. Wu and M. Zhang, "Rheology of multi-walled carbon nanotube/poly(butylene terephthalate) composites," Journal of Polymer Science Part B: Polymer Physics **45**, 2239-2251 (2007).

Yamanoi M., C. Leer, F. W. J. van Hattum, O. S. Carneiro and J. M. Maia, "Direct fibre simulation of carbon nanofibres suspensions in a Newtonian fluid under simple shear," Journal of Colloid and Interface Science **347**, 183-191 (2010).

CHAPTER 6 ARTICLE 3: MODELING INTERACTIONS IN CARBON NANOTUBE SUSPENSIONS: TRANSIENT SHEAR FLOW

G. Natale [a], G. Ausias [b], J. Férec [b], M.C. Heuzey [a] and P.J. Carreau [a]

[a] Research Center for High Performance Polymer and Composite Systems (CREPEC), Chemical Engineering Department, Polytechnique Montreal, PO Box 6079, Stn Centre-Ville, Montreal, QC, Canada H3C 3A7

[b] Laboratoire d'Ingénierie des MATériaux de Bretagne (LIMATB) Univ. Bretagne-Sud, EA 4250, LIMATB, F-56100 Lorient, France

6.1 Synopsis

Transient shear flow data of untreated multiwalled carbon nanotubes (MWCNTs) dispersed in a Newtonian epoxy matrix are analyzed. A sequence of shearing and rest steps were applied to characterize the transient responses of the suspensions. Stress overshoots appeared at very small deformation during forward and reverse flow experiments and their intensity increased with rest time between two consecutive flows, during which the suspension structure was reconstructed. The transient behavior of the MWCNT suspensions is explained with the help of a recently proposed model [Natale *et al.* (2014)]. The MWCNTs are described as rigid rods dispersed in a Newtonian matrix, and the evolution of the system is controlled by hydrodynamics, rod-rod interactions and Brownian motion. The force due to the interactions is modeled as a non-linear lubrication force and the total stress tensor is evaluated introducing a fourth-order interaction tensor. The Fokker-Planck equation is numerically solved for transient simple shear flow using a finite volume method, avoiding the need of closure approximations. The model predictions show that interactions slow down the orientation evolution of the rods. For the first time, the effect of shear rate is directly accounted by the model, which predicts that a critical shear rate is necessary to break down the structure and let the rods orient in the flow direction. In addition, we confronted the model predictions with the rheological data of a glass fiber-filled polybutene [Sepehr *et al.* (2004b)], demonstrating its ability to describe the behavior of micro and nano-scale particle suspensions.

6.2 Introduction

Since their discovery, the scientific interest towards carbon nanotubes (CNTs) has been increasing due to their quasi unidimensional structure responsible of unique properties (high electrical and thermal conductivities and excellent mechanical strength). Industrial applications for these inorganic nanoparticles vary over a wide range of possibilities, from biological sensing devices to multifunctional composites [Abbasi *et al.* (2009b), Gupta and Choudhary (2011)] .

CNTs can be considered somewhere in between a micro-size fiber and a semi-flexible polymer, and when suspended in liquids their rheological behavior reflects these characteristics. At low volume fractions, CNT suspensions show mild elasticity (low values of storage modulus, G') in Newtonian matrices, which is a proof of inner flexibility [Ma *et al.* (2008), Cruz *et al.* (2012)].

Under shear flow, the rods tend to get more and more oriented in the flow direction as proven by rheo-optical analysis [Hobbie (2004), Fry *et al.* (2006), Pujari *et al.* (2009a), Pujari *et al.* (2011)]. The bent equilibrium conformation of multiwalled carbon nanotubes (MWCNTs) is also responsible for non-zero hydrodynamic torques even when aligned in the flow direction, causing a reduction in the overall orientation state [Natale *et al.* (2015)]. At increasing volume fractions, CNTs form a network stabilized by attractive van der Waals forces. In small amplitude oscillatory shear (SAOS), Du *et al.* (2004) showed that the establishment of a percolated network is responsible for the non-terminal character of the storage modulus, *G'*, and loss modulus, *G"*, with *G'* exhibiting larger values than the viscous counterpart (forming a weak gel). During flow, hydrodynamic forces are able to break down the overall structure. After a pre-shearing step, Khalkhal *et al.* (2011) found that *G'* decreased and its reduction was proportional to the intensity of the applied shear flow. In quiescent state, the structure keeps evolving due to Brownian motion, which makes particles interlock again, hence restoring *G'*. The presence of overshoots has also been reported in the shear stress response to a step increase in shear rate [Khalkhal and Carreau (2012)]. This overshoot appears at smaller deformation compared to a glass fiber system [Sepehr *et al.* (2004a)]. If a sequence of shear and rest steps is applied to the system, the shear stress overshoot disappears in the second shear step when no rest time is allowed. While, after a rest interval, overshoots slowly reappear with an intensity proportional to the rest time [Wu *et al.* (2007), Khalkhal and Carreau (2012)].

Modeling the rheological behavior of colloidal suspensions is of fundamental importance to design and optimize processing schemes where the final goal is to obtain specific microstructural states and to achieve desired macroscopic properties. Furthermore, modeling can be used to separate and quantify the impact of different microscopic mechanisms, which is rarely possible experimentally. On the other hand modeling anisotropic particle suspensions is still a challenge, especially in concentrated regimes where most commercial applications occur. One of the main difficulties in modeling anisotropic particles in the concentrated regime resides in finding a successful kinetic theory to include the effects of particle-particle interactions.

For rods with high aspect ratios (as CNTs) in the dilute regime, the leading order of the velocity disturbance due to the presence of a particle, according to the slender body theory, scales as

~1/ln(r), r being the particle aspect ratio [Batchelor (1970)]. Multibody hydrodynamic interactions become more and more important as the concentration increases. In the semi-dilute regime, Shaqfeh and Fredrickson (1990) demonstrated using a multiple scattering theory that an intermediate range of screening exists. The presence of many particles in a system causes a screening effect for the hydrodynamic interactions and the screening length, ξ, has the following dependency:

$$\xi \approx D\left[\frac{3\left|\ln(\phi)\right|}{20\phi}\right]^{1/2} \tag{6.1}$$

where ϕ is the particle volume fraction. The dominant term of the screening length, reported in Eq. 6.1, is independent of the overall system orientation. On a length scale larger than ξ, an individual rod would perceive on average the rest of the system as a viscous medium with an effective viscosity. At shorter length scales, an individual particle would see a depletion in particle concentration and, hence, it would be surrounded by the pure matrix. In addition, Shaqfeh and Fredrickson (1990) derived the first order term of the hydrodynamic contribution to the stress tensor in the semi-dilute regime, extending the pioneering work of Batchelor (1971). However, the hydrodynamic theories' predictions were not sufficient to explain the enhancement in viscosity and first normal stress differences found experimentally by Petrich *et al.* (2000). This "extra" contribution to the stress tensor was attributed to fiber-fiber interactions.

Modeling rod interactions is a challenging task. Folgar and Tucker (1984) and Advani and Tucker (1987) described the randomizing effect of particle-particle interactions by the addition of an effective diffusion coefficient proportional to the shear rate. More recently, Sandstrom (1993) and Sandstrom and Tucker (1993) modeled interactions between fibers as a linear lubrication force. Sundararajakumar and Koch (1997) studied the effect of mechanical contacts in the absence of hydrodynamic interactions with direct simulations. They found that the collisions between particles caused less orientation in the flow direction. Further progress was achieved by Djalili-Moghaddam and Toll (2005) by adding to the total stress a contribution due to interaction forces, in addition to the matrix and hydrodynamics contributions. Férec *et al.* (2009) extended this work by developing a continuum equivalent model and described the relative velocity between pairs of rods without

neglecting any terms. Furthermore, they were able to predict correctly the transient viscosity and the change in sign of the normal stress differences in reverse flows for glass fiber suspensions.

In simple shear flow, CNT suspensions in Newtonian matrices present a strong shear-thinning behavior. Many authors have suggested that the shear-thinning signature is due to a combination between agglomerate break-up, particle-particle interactions and rod orientations [Rahatekar *et al.* (2006b), Hobbie and Fry (2007), Ma *et al.* (2008)]. However, in well-dispersed systems, the shear-thinning phenomenon is still present. Hence, Natale *et al.* (2014) pointed to particle-particle interactions and rod orientations as being mainly responsible for this effect. The complete avoidance of agglomerates is experimentally challenging since in a concentrated system an ideal dispersion state is almost impossible to achieve. However, even in a scenario where agglomerates are present, particle-particle interactions would still play a major role. Under flow, the agglomerates would break down causing many particles to be at distances of the order of a particle diameter. Hence, short-range interaction forces would be dominant. In a recent publication, Natale *et al.* (2014) modeled MWCNTs as thin rods interacting with each other by a non-linear lubrication force. The multibody long range hydrodynamic interactions were neglected when calculating the rod rotary velocity, but a perturbation velocity was introduced as previously done by Folgar and Tucker (1984). The interaction force used to model the mechanical contacts allowed for the first time to have a direct shear-rate dependency of the microstructure, this interaction force being responsible for the shear-thinning phenomenon. In this work, we extend the analysis of the proposed model to transient shear flow by solving the non-linear Fokker-Planck equation using a finite volume method (FVM), hence without the need of questionable closure approximations. We analyze the model predictions, comparing them with experimental data obtained for a multi-walled carbon nanotube (MWCNT)-epoxy system in the concentrated regime. Furthermore, the model predictions are also confronted with the experimental data of a micro-size glass fiber-filled polybutene [Sepehr *et al.* (2004b)].

6.3 Model

In this section, the main equations of the model obtained by Natale *et al.* (2014) are reported, but the interested reader is referred to our previous work for the full derivation.

In concentrated thin rods suspensions, a complete description of the hydrodynamic interactions is not yet available and it would be a difficult task to derive a set of equations to precisely account for it. Consequently, a phenomenological route is undertaken here.

Particles are considered as long and thin rods of length L and diameter D and are subjected to a homogeneous flow. At high volume fractions, a rod is surrounded by many neighboring particles at short length scale ~D and, hence, its motion is strongly influenced by direct (or mechanical) contacts with these particles. The long range hydrodynamic interactions can be considered negligible when compared to mechanical contacts in this regime, because they are mainly screened by the presence of particles. In the following development, direct contacts are considered the controlling mechanism for the overall dynamics of the suspension and they contribute significantly to the rheological response of the system. To take into consideration these interactions, an extra force needs to be introduced. Recently, Natale *et al.* (2014) proposed a non-linear (power-law) lubrication force in the relative velocity of the rods

$$\mathbf{f}_\mathbf{I} = Dkb(\Delta\dot{\mathbf{r}} \cdot \Delta\dot{\mathbf{r}})^{\frac{m-1}{2}} \Delta\dot{\mathbf{r}} \tag{6.2}$$

where b and m are the consistency and the power-law exponent, respectively, of the rod-rod interaction force, k is a dimensionless geometric factor and $\Delta\dot{\mathbf{r}}$ is the approaching velocity of two rods at the interaction point. The argument at the base of this choice is that during an interaction event, the approaching rods feel a shear rate that does not scale linearly with the macroscopic shear rate, $\dot{\gamma}$. This can be the consequence of a squeezed fluid between two approaching rods, or of additional forces (van der Waals, electrostatic, etc.), which may act at such short ranges and cause the approaching velocity to be non-linear in terms of $\Delta\dot{\mathbf{r}}$. This interaction force is purely viscous in nature (hydrodynamic friction) and Natale *et al.* (2014) demonstrated that it was able to accurately predict shear-thinning.

Once the interaction torque is derived and considering that interactions between the rods create a dispersion effect which is modeled as a perturbation velocity, similarly to Folgar and Tucker (1984), the rotary velocity of the test rod is defined as

$$\dot{\mathbf{p}}^{\alpha} = -\frac{1}{2}\boldsymbol{\omega}\cdot\mathbf{p}^{\alpha} + \frac{1}{2}\lambda_{\mathbf{p}^{\alpha}}\left(\dot{\boldsymbol{\gamma}}\cdot\mathbf{p}^{\alpha} - \dot{\boldsymbol{\gamma}}:\mathbf{p}^{\alpha}\mathbf{p}^{\alpha}\mathbf{p}^{\alpha}\right) - q\left|\dot{\gamma}\right|\left(1-\lambda_{\mathbf{p}^{\alpha}}\right)\frac{\partial \ln \psi_{\mathbf{p}^{\alpha}}}{\partial \mathbf{p}^{\alpha}} \tag{6.3}$$

where $\boldsymbol{\omega}$ and $\dot{\boldsymbol{\gamma}}$ are the vorticity and deformation rate tensor, respectively, and q is a dimensionless interaction coefficient. The effective form factor $\lambda_{\mathbf{p}^{\alpha}}$ is

$$\lambda_{\mathbf{p}^{\alpha}} = 1 - \phi M_I \left|\dot{\boldsymbol{\gamma}}:\mathbf{p}^{\alpha}\mathbf{p}^{\alpha}\right|^{m-1} \int \left|\mathbf{p}^{\alpha}\times\mathbf{p}^{\beta}\right| \psi_{\mathbf{p}^{\beta}} d\mathbf{p}^{\beta} \tag{6.4}$$

with $M_I \equiv \dfrac{kbL^{m-1}}{2^{2m-3}(m+2)\eta_0 \pi Y_C}$ which represents the interactions intensity, η_0 is the matrix viscosity and Y_C a resistance function.

In the dilute regime (ϕ tends to zero), Eq. 6.3 reduces to the Jeffery equation for particles with high aspect ratio [Jeffery (1922)]. A general form of Eq. 6.3 can be rewritten as

$$\dot{\mathbf{p}}^{\alpha} = -\frac{1}{2}\boldsymbol{\omega}\cdot\mathbf{p}^{\alpha} + \frac{1}{2}\lambda\left(\dot{\boldsymbol{\gamma}}\cdot\mathbf{p}^{\alpha} - \dot{\boldsymbol{\gamma}}:\mathbf{p}^{\alpha}\mathbf{p}^{\alpha}\mathbf{p}^{\alpha}\right) - C\frac{\partial \ln \psi_{\mathbf{p}^{\alpha}}}{\partial \mathbf{p}^{\alpha}} \tag{6.5}$$

Eq. 6.5 is composed of a convective part (the first two terms on the right side) and a diffusion one (last term on the right side). In the literature, different models have proposed a similar description for the test rod rotary velocity, but with different expressions for the parameters λ and C. These are summarized in Table 6.1.

Table 6.1 Expressions for λ and C from previous models reported in the literature.

Authors	λ	C
Jeffery (1922)	$\dfrac{r^2-1}{r^2+1}$	0
Folgar and Tucker (1984)	1	$C_I\left\|\dot{\gamma}\right\|$
Advani and Tucker (1987)	$\dfrac{r^2-1}{r^2+1}$	$C_I\left\|\dot{\gamma}\right\|$
Férec *et al.* (2009)	$1-\phi M_I\int\left\|\mathbf{p}^{\alpha}\times\mathbf{p}^{\beta}\right\|\psi_{\mathbf{p}^{\beta}}d\mathbf{p}^{\beta}$	$q\left\|\dot{\gamma}\right\|\phi M_I\int\left\|\mathbf{p}^{\alpha}\times\mathbf{p}^{\beta}\right\|\psi_{\mathbf{p}^{\beta}}d\mathbf{p}^{\beta}$

The parameter λ in the classical papers of Jeffery (1922) and Advani and Tucker (1987) represents the shape of the spheroid and can vary between 0 (sphere) and 1 (rod of infinite aspect ratio). In the work of Férec *et al.* (2009) and Natale *et al.* (2014), the parameter λ is a pseudo-shape factor. It tends asymptotically towards the value of 1 when the rods are all aligned parallel to the flow streamlines and depending on the product ϕM_I it can take values of $|\lambda| \geq 1$. Moreover, stable steady-state orientations for axisymmetric bodies with $|\lambda| \geq 1$ were found to be independent of the initial orientation state [see for examples: Ericksen (1960), Bretherton (1962), and Brenner (1974)]. Physically, Eq. 6.3 represents on average the rotary velocity of a rod surrounded by neighbors. The information regarding the interactions are all contained in $\lambda_{\mathbf{p}^\alpha}$. This effective "shape factor" evolves during flow, meaning that the test rod sees around itself rods with which it interacts and the ultimate effect of these interactions is comparable to a change in the physical shape of the test rod. Furthermore, the interactions depend on the orientation of the test rod α, on the shear rate applied and on the rod orientation distribution. It is important to underline that the contact probability chosen to calculate the average interaction torque is correct only for uncorrelated long and thin rods at equilibrium [Doi and Edwards (1978b)]. When shear flow is applied to the system, dynamical correlations are considered insignificant and not perturbing the pair-correlation function. In other words the orientation evolution of a generic rod in the suspension is hindered by the other rods, and this happens at a much longer time scale than the one related to the evolution of its center of mass. Hence, the effect of shear flow on positional correlations is much less pronounced than its alignment effect on the probability density function. This is an assumption often used for rods with high aspect ratio [Dhont and Briels (2003b), Djalili-Moghaddam and Toll (2005), Férec *et al.* (2009)]. The difficulty in defining a precise evolution for the pair-correlation function in simple shear flow for rod-like particles is due to the fact that shear flow is a non-conservative external force field, for which no potential energy can be defined [Dhont and Briels (2003a)].

To close Eq. 6.3, the time evolution of the rod orientation distribution, $\psi_{\mathbf{p}^\alpha}$, is required. $\psi_{\mathbf{p}^\alpha}$ can be considered as a convected scalar [Bird *et al.* (1987)] and the continuity relation can be expressed as

$$\frac{D}{Dt}\psi_{\mathbf{p}^\alpha} = -\frac{\partial}{\partial \mathbf{p}^\alpha}\cdot\left(\dot{\mathbf{p}}_I^\alpha \psi_{\mathbf{p}^\alpha}\right) + \frac{\partial}{\partial \mathbf{p}^\alpha}\cdot\left[q|\dot{\gamma}|\left(1-\lambda_{\mathbf{p}^\alpha}\right)\frac{\partial \psi_{\mathbf{p}^\alpha}}{\partial \mathbf{p}^\alpha} + D_r\frac{\partial \psi_{\mathbf{p}^\alpha}}{\partial \mathbf{p}^\alpha}\right] \tag{6.6}$$

where *D/Dt* represents the material derivative, D_r is the rotary diffusion coefficient introduced to take into account the Brownian motion effects and $\dot{\mathbf{p}}_I^\alpha$ represents the first two terms of Eq. 6.3. This is a non-linear Fokker-Planck equation since $\lambda_{\mathbf{p}^\alpha}$ and $\dot{\mathbf{p}}_I^\alpha$ both contain an integral dependency on $\psi_{\mathbf{p}^\alpha}$. To relate the microstructure evolution to the macroscopic rheological response of the system, a constitutive equation is necessary. Following Djalili-Moghaddam and Toll (2005) and Férec *et al.* (2009), Natale *et al.* (2014) calculated the stress tensor accounting for the effect of interactions as

$$\boldsymbol{\sigma} = -P\boldsymbol{\delta} + \eta_0\dot{\boldsymbol{\gamma}} + \phi\eta_0 N_P\dot{\boldsymbol{\gamma}} : \mathbf{a}_4 + 2\phi^2 M_I\frac{r^2\eta_0 Y_C}{\pi}\dot{\boldsymbol{\gamma}} : \mathbf{b}_4{}^{(m)} + 3\phi\eta_0 D_r\mathbf{a}_2 \tag{6.7}$$

where P is the hydrostatic pressure, $N_P = X_A r^2/6\pi$, X_A is the parallel drag coefficient of the rods and $\mathbf{a}_4$ is the well-known fourth-order orientation tensor defined by Advani and Tucker (1987)

$$\mathbf{a}_4 = \int \mathbf{p}^\alpha\mathbf{p}^\alpha\mathbf{p}^\alpha\mathbf{p}^\alpha\psi_{\mathbf{p}^\alpha}d\mathbf{p}^\alpha \tag{6.8}$$

$\mathbf{b}_4{}^{(m)}$ is a fourth-order interaction tensor defined as

$$\mathbf{b}_4{}^{(m)} = \int \mathbf{p}^\alpha\mathbf{p}^\alpha\mathbf{p}^\alpha\mathbf{p}^\alpha\left|\dot{\boldsymbol{\gamma}} : \mathbf{p}^\alpha\mathbf{p}^\alpha\right|^{m-1}\int\left|\mathbf{p}^\alpha\times\mathbf{p}^\beta\right|\psi_{\mathbf{p}^\beta}d\mathbf{p}^\beta\psi_{\mathbf{p}^\alpha}d\mathbf{p}^\alpha \tag{6.9}$$

On the right-end side of Eq. 6.7, the first three terms are the hydrostatic pressure, the matrix and the hydrodynamic contributions, respectively, while the last two terms are related to the interactions, which scale as $\sim\dot{\gamma}^m$, and to Brownian motion, respectively. Furthermore, Eq. 6.7 reduces to the constitutive equation proposed by Férec *et al.* (2009) in the absence of Brownian motion and for the power-law exponent $m=1$ and the consistency parameter $b=\eta_0$. When a homogenous flow is applied, Eqs. 6.6 and 6.7 constitute a closed set of equations, which links the

microscopic evolution of a suspension of rigid rods in a Newtonian matrix to the macroscopic stress tensor.

6.4 Numerical method

The presence of two fourth-order tensors, $\mathbf{a}_4$ and $\mathbf{b}_4^{(m)}$, in the constitutive equation (Eq. 6.7) requires the knowledge of the orientation distribution evolution. Since only moments of the orientation distribution are needed, many authors suggested that the evolution of the second-order tensor $\mathbf{a}_2 = \int \mathbf{p}^\alpha \mathbf{p}^\alpha \psi_{\mathbf{p}^\alpha} d\mathbf{p}^\alpha$ would contain sufficient information to describe the stress tensor [Advani and Tucker (1987), Férec *et al.* (2014)]. As shown in Appendix A, in this work the evolution of the orientation second-order tensor is coupled with tensors $\mathbf{a}_4$ and $\mathbf{b}_4^{(m)}$ and, consequently, implies the need for an approximated closure to the problem. Instead of proposing arguable closure approximations, a complete solution for Eq. 6.6 is developed. The Fokker-Planck equation, Eq. 6.6, which controls the evolution of the microstructure, is strongly non-linear and no simple analytical solution exists. In this work Eq. 6.6 is numerically solved using a finite volume method, as previously performed by Férec *et al.* (2008). The finite volume method was chosen for its well-known conservativeness property needed to respect the normalization condition [Versteeg and Malalasekera (1995)]. Thanks to the symmetries of $\psi_{\mathbf{p}^\alpha}$, the computation time was reduced by meshing only one half of the unit sphere which is the domain of the rod orientation distribution. The surface of the sphere was discretized where the area of one cell is $\Delta A = \sin\theta \Delta\vartheta \Delta\theta$, with ϑ and θ the two spherical coordinates moving on the surface of the unit sphere. The same number of nodes were used in the ϑ and θ directions. Solutions independent of the number of nodes were obtained for 80 nodes in the θ (or ϑ) direction. A power-law scheme was implemented in order to interpolate properties between the nodes and periodic boundary conditions were applied [Férec *et al.* (2008)].

The non-linear lubrication force brings in flux terms, which depends on $\left|\dot{\boldsymbol{\gamma}} : \mathbf{p}^\alpha \mathbf{p}^\alpha\right|^{m-1}$. This term can diverge in some positions of the unit vector $\mathbf{p}^\alpha$ on the unit sphere (for examples in the poles of the sphere) because of the power-law expression. Physically, these positions are not accessible to the particles since the diffusion term diverges the same way because it is proportional to

$\left|\dot{\boldsymbol{\gamma}} : \mathbf{p}^{\alpha}\mathbf{p}^{\alpha}\right|^{m-1}$ as well. This implies that the particles are always pushed away from those regions of the sphere. For the numerical solutions, we limited the values of the components of $\mathbf{p}^{\alpha}$ to extremely low but non zero values. This is equivalent to exclude extremely small region of the sphere and this is necessary in order to maintain the conservativeness of the numerical method. For all the simulations, the minimum value allowed for the components of $\mathbf{p}^{\alpha}$ was of 10^{-10}. The sensitivity of the numerical results to the chosen value was studied and shown not to have significant effects for values below 10^{-4}.

For a given shear rate and at each time step, the non-linear terms were evaluated using successive iterations for the rod orientation distribution, using as initial guess the value of $\psi_{\mathbf{p}^{\alpha}}$ calculated from the previous time step, and starting with a guess of $1/4\pi$ (isotropic state) for the first time step. The error between two consecutive iterations was required to be less than 10^{-3} before the numerical procedure could move on to the next time step. Once the distribution function was numerically computed, the stress tensor components were straightforwardly obtained at each time step using Eq. 6.7.

6.5 Materials and experimental

A Newtonian epoxy (Epon 828, HEXION Specialty Chemicals Inc.) with a density of 1.16 g/mL and a viscosity of 12.3 Pa.s at 25 °C was used as the dispersing medium. Multiwalled carbon nanotubes (MWCNTs) from Cheap Tubes Inc. were characterized in a previous work [Khalkhal *et al.* (2011)]. The main characteristics of the suspensions investigated in this work are given in Table 6.2, which also reports the corresponding characteristics of glass fiber suspensions in a polybutene (PB-GF) taken from the work of Sepehr *et al.* (2004b).

Table 6.2 Characteristics of the materials analyzed in this work.

Suspensions	Matrix	Viscosity η_0 (Pa·s)	Fiber volume fraction ϕ %	Rod length L (μm)	Rod diameter D (μm)	Aspect ratio r
EPO-CNT	Epoxy	12.3	1.17	0.1 – 2.2	$(0.7 – 2.5)\times10^{-2}$	4 – 314
PB-GF	Polybutene	24	7.06	260	14	20

Homogenization of the CNT suspensions is a difficult task because of strong attractive van der Waals forces between nanotubes and, furthermore, the dispersion strongly depends on the chemical nature of the matrix. The degree of dispersion is, however, of great importance since all the macroscopic properties of composite materials will strongly be influenced by it. At the laboratory scale, successful dispersion states have been reported when mixing CNTs to a Newtonian epoxy with the aid of a mechanical mixer named three roll mill (3RM) [see for example Schulz *et al.* (2011), Khalkhal *et al.* (2011), Olowojoba *et al.* (2013)]. For this work, the suspensions of CNT-epoxy (EPO-CNT) were prepared using an EXAKT 3RM (from EXAKT Technologies, Inc.) at room temperature. The details of the suspension preparation and the verification of the dispersion state can be found in previous investigations [Khalkhal *et al.* (2011), Natale *et al.* (2014)].

A Physica MCR502 (Anton Paar) rheometer with a cone-and-plate flow geometry (CP50 with the diameter of 50 mm and an angle of 2°) was used to perform the rheological measurements at 25 °C. The cone-and-plate geometry allows a homogeneous shear flow, which makes it preferable not only to achieve precise rheological data but also to recreate the flow conditions used for the model calculations. The gap at the center of the cone is 51 μm, which is about 80 times larger than the average length of the carbon nanotubes. Moreover, the absence of wall effects was assessed by comparing results from the cone-and-plate geometry with data from a parallel-plate flow geometry (PP50 with a diameter of 49.96 mm, 1 mm gap), corrected according to Carreau *et al.* (1997) (data not reported here). The temperature during the tests was controlled at 25 °C by a Peltier (P-PTD 200) system. All experiments were run one day after sample preparation in order to avoid aging effects. Once the samples were positioned and trimmed, they were allowed to relax for 1 h in order to be in an isotropic initial state and to eliminate any residual stresses. After this relaxation step, different stress growth experiments were performed. The first stress growth was in counter clock-

wise (CCW) direction followed by two stress growths in clock-wise (CW) direction. These stress growths were separated by two rest steps of equal length, where the sample was allowed to relax for times from 0 s to 1 h. This procedure was repeated for shear rates of 1, 5 and 10 s^{-1}.

Unfortunately, the normal forces exerted by the EPO-CNT system were in the range of sensitivity of the instrument for the experimental conditions studied in this work, and since the noise to signal ratio was always above 50%, they are not discussed here.

6.6 Data and predictions

6.6.1 MWCNT suspensions

Natale *et al.* (2014) compared the model predictions of the steady-state shear viscosity and first normal stress difference, N_1, for different concentrations of MWCNTs dispersed in epoxy (using the same materials than in this work, i.e. EPO-CNT in Table 6.2). They found that the model was able to quantitatively predict the viscosity shear-thinning behavior and N_1 values at steady-state, for different concentrations of MWCNTs ranging from dilute to concentrated regime. Only one set of adjustable parameters, named here EPO-CNT $^{(SS)}$, was required and their values are reported in Table 6.3. The superscript SS stands for steady-state.

Table 6.3 Parameter values obtained by fitting the transient experimental data for carbon nanotubes dispersed in epoxy (EPO-CNT $^{(T)}$). The parameter values obtained by fitting the steady-state values of viscosity and first normal stresses difference, N_1, of carbon nanotubes (1.17 vol%) dispersed in epoxy (EPO-CNT $^{(SS)}$) obtained from Natale *et al.* (2014) are also reported.

Suspensions	Parallel drag coefficient N_P	Interaction coefficient q	Rod-rod Interaction intensity factor M_I (s^{m-1})	Interaction power-law exponent m	Rotary Diffusion D_r (s^{-1})
EPO-CNT $^{(T)}$	154	2.1×10^{-2}	862	0.49	1.3×10^{-4}
EPO-CNT $^{(SS)}$	147	6×10^{-2}	75	0.28	0

"T" for transient, "SS" for steady-state conditions

We proceed here by extending the analysis of the model predictions [Natale *et al.* (2014)] to transient shear flows. The first verification that comes to mind is to confront the model predictions

using the parameters obtained for steady-state (EPO-CNT $^{(SS)}$) with the rheological response to a stress growth experiment of the EPO-CNT suspension. The experimental and modeling results are reported in Figure 6.1.

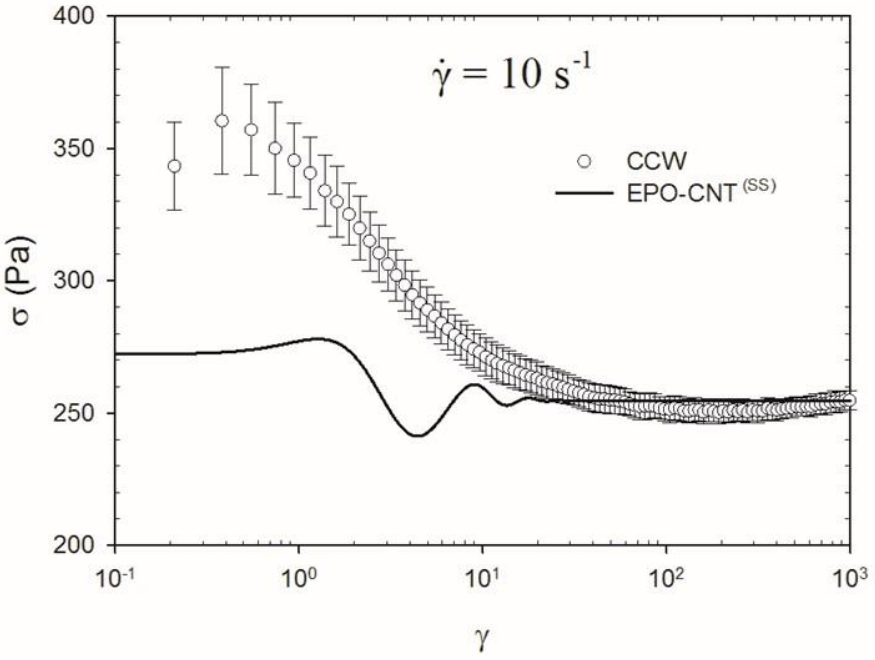

Figure 6.1 Comparison between stress growth experimental data and model prediction for the EPO-CNT system in CCW direction at 10 s^{-1} using the set of parameters EPO-CNT $^{(SS)}$.

As discussed in the introduction, concentrated MWCNT suspensions have an interesting rheological behavior because of the anisotropic nature of the particles and their colloidal character. When a constant shear flow is applied (CCW run in Figure 6.1), the shear stress presents a strong overshoot at low deformation (about 0.45) and it gradually levels off to the steady-state value at a strain of 20. From Figure 6.1, it is clear that the predictions obtained with the parameters EPO-CNT $^{(SS)}$ in Table 6.3 show an oscillatory character, which is not present experimentally. In addition, even if the steady-state value is correctly predicted the results from the model show a less intense overshoot positioned at larger strain (about 1.5), compared with the one found experimentally. Since analytical expressions for the adjustable parameters are not yet available, it is necessary to verify if the model is otherwise able to capture the transient response of MWCNT suspensions. To answer this question, a new set of adjustable parameters (EPO-CNT $^{(T)}$) was found

by fitting only the experimental transient data and they are reported in Table 6.3. The new model predictions are reported in the following analysis. At the end of this section, the model predictions with the set of parameters EPO-CNT $^{(T)}$ are also confronted with the steady-state data from Natale *et al.* (2014).

Figure 6.2 reports stress growth experiments at 10 s^{-1} where the direction of the flow is inverted from CCW to CW with an interval between the two steps, where the system is allowed to relax from 0 to 1000 s. As already seen in Figure 6.1, a strong overshoot is present in the first CCW run at a strain of about 0.45.

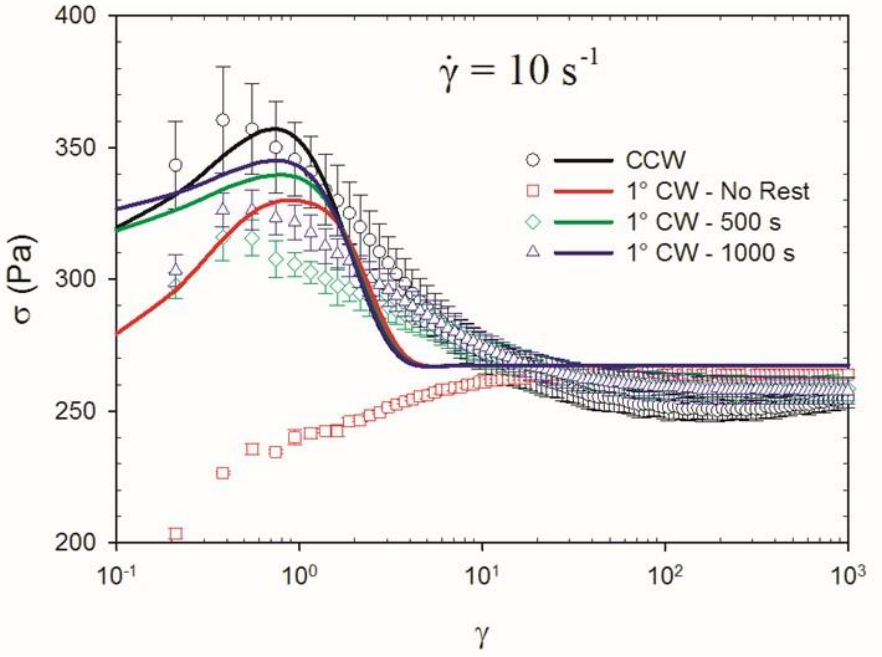

Figure 6.2 Comparison between stress growth experimental data and model predictions for the EPO-CNT system in CCW and CW directions for different rest times (0 s, 500 s and 1000 s) at 10 s^{-1} using the set of parameters EPO-CNT $^{(T)}$.

By inverting the flow direction (square symbols in Figure 6.2) without allowing the system to relax, a pseudo-plateau is observed at a strain similar to the CCW overshoot position. This pseudo-plateau slowly disappears and the shear stress tends smoothly to its steady-state value at a deformation of about 10. If the system is allowed to relax for 500 or 1000 s, the characteristic overshoot reappears and its intensity increases with the rest time until obtaining the initial amplitude of the CCW step

after a rest time of 3600 s (not shown here for clarity). The pseudo-plateau found by inverting the flow direction is not present if the second run is in the same flow direction as the first. This is clearly shown in Figure 6.3 where consecutive shear flows at 10 s^{-1} in the CW direction are applied. The absence of the pseudo-plateau when no rest time is allowed implies that the microstructure is sensitive to the flow direction. The kinetics of the structure build-up and the shape (width and intensity) of the overshoots are similar to the one reported in Figure 6.2.

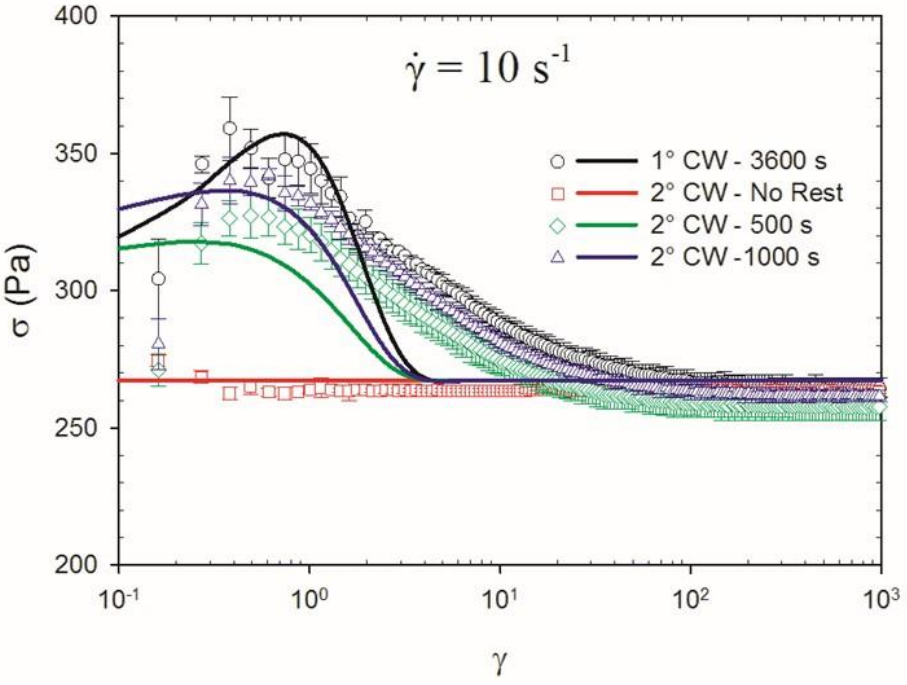

Figure 6.3 Comparison between two consecutive stress growth experimental data and model predictions for the EPO-CNT system in the CW direction for different rest times (0 s, 500 s and 1000 s) at 10 s^{-1} using the set of parameters EPO-CNT $^{(T)}$.

It is worth underlining that the only cases that strongly depend on the flow direction are the ones with no rest time allowed. This is consistent with the idea of a microstructure that evolves according to the Brownian motion during rest or, in other words, which moves towards an isotropic state where no preferential orientation is present.

The model predictions using the new set of parameters, i.e. EPO-CNT $^{(T)}$, reported in Table 6.3 are shown in Figure 6.2 and Figure 6.3 by the solid lines. Only one set of parameters is used for all the

EPO-CNT curves reported in this work. Overall, the model is able to correctly predict the transient rheological response of CNT suspensions and correctly account for the evolution of the microstructure during cessation of flow. The major deviations appear in the case when flow direction is inverted without rest time since the model predicts an overshoot almost as important as the initial CCW one (Figure 6.2). Experimentally, pseudo plateaus were also found in the case of glass fibers by Sepehr *et al.* (2004b) and they can be explained by the fact that less hydrodynamic resistance is associated with an aligned rod structure. The model over predicts the effect of inverting the flow direction since, as we will see later, the predicted microstructure is not much oriented in the flow direction. Although the intensity of the overshoots and the deformation at which they appear are well predicted, their widths are always underestimated by the model. Experimental polydispersity in particle dimensions (length and diameter) and particle flexibility may be the main reasons behind these differences, since they are not accounted for in the mathematical description. The shorter deformation required by the model to reach the steady-state value is a consequence of the single relaxation time ($\sim 1/D_r$) present in the case of the modeled monodispersed system, while the particle are polydispersed, implying a range of relaxation times.

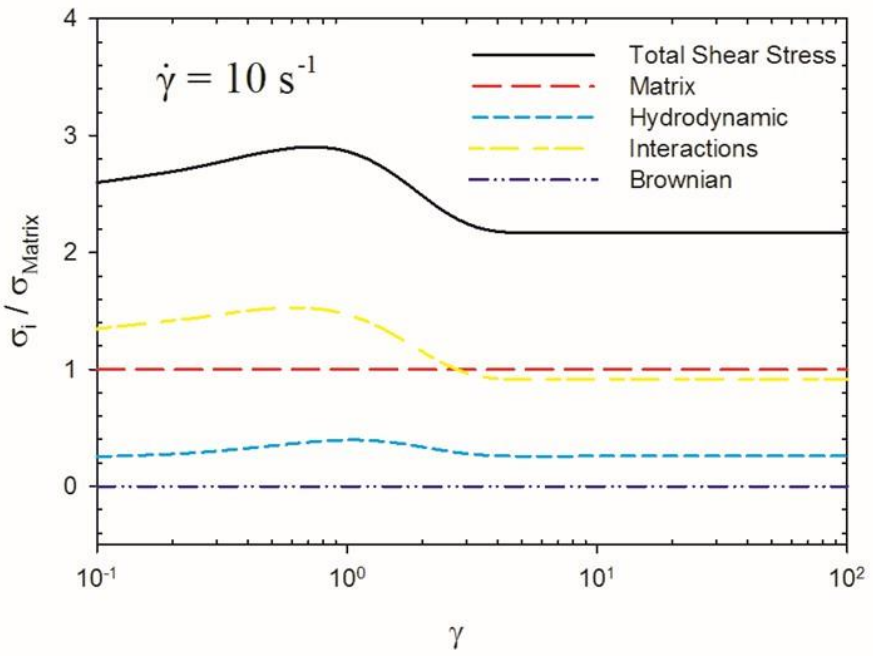

Figure 6.4 Predictions of the different contributions to the shear stress and total shear stress normalized with respect to the matrix contribution for the EPO-CNT system in the CCW run at 10 s-1 using the set of parameters EPO-CNT (T).

To explain the presence of the overshoots, the different contributions to the stress tensor are separated and normalized by the Newtonian matrix contribution in Figure 6.4. It is clear that the interaction contribution is significant and it accounts on average for 42% of the total shear stress. In addition, the particle interactions are mainly responsible for the characteristic overshoots observed experimentally. The hydrodynamic contribution alone would not be able to explain this rheological behavior and accounts for only 11% of the total shear stress, as shown in Figure 6.4. The Newtonian matrix contributes for about 46% of the total stress while the Brownian motion can be considered negligible. In addition, the low value of the rotary diffusion coefficient predicted by the model for MWCNTs (1.3×10^{-4} s^{-1}, Table 6.2) confers to the microstructural description a thixotropic character, according to the definition of Larson (2015). The Brownian diffusion term included in Eq. 6.6 causes a weak restoring force, which leads to a slow structural recovery on cessation of flow. However, the stress contribution due to Brownian motion is negligible during flow, as seen in Figure 6.4.

Similar trends as presented in Figure 6.2 and Figure 6.3 were observed for shear rates of 1 and 5 s^{-1} (not shown here). In Figure 6.5, a comparison of the first CCW run at $\dot{\gamma}$ of 1, 5 and 10 s^{-1} is reported. The shear stress magnitude increases with the applied shear rate, but the deformations at which the maximum yielding is observed and where the data reach steady-state are practically independent of the applied shear rate. The model correctly predicts the effect of shear rate, due to the non-linearity introduced that causes the interaction contribution to be proportional to $\dot{\gamma}^m$. This is clearly the case experimentally, as seen in Figure 6.5, where the steady-state values of the shear stress is only doubled in the case of a five time increase in the shear rate intensity (comparing the curves at $\dot{\gamma}$ of 1 and 5 s^{-1}).

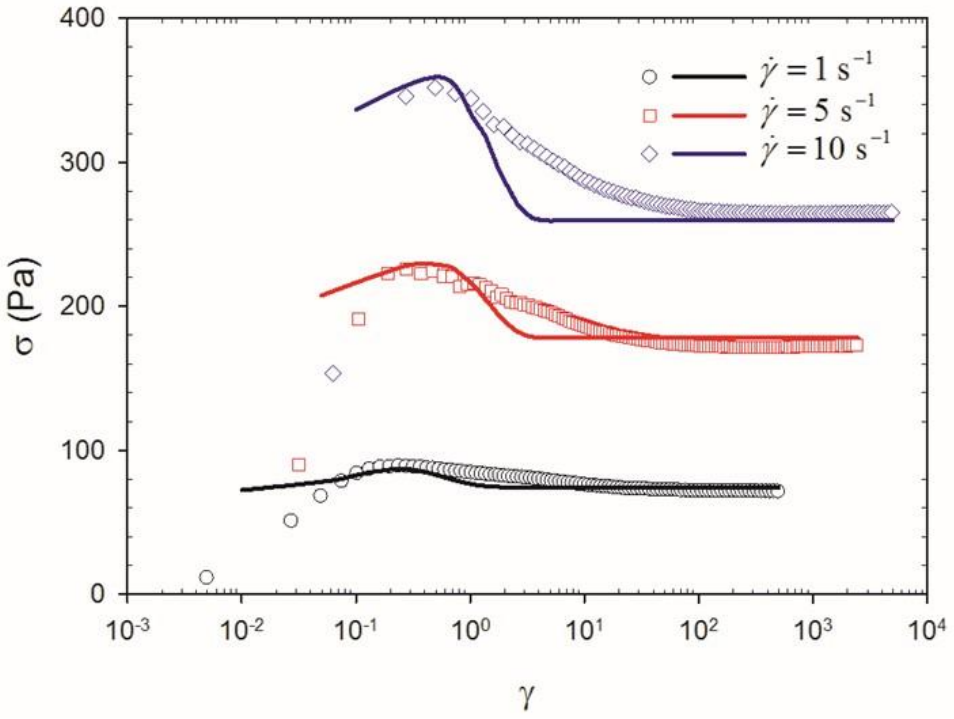

Figure 6.5 Comparison between stress growth experimental data and model predictions in the CCW direction at different shear rates for the CNT-EPO system using the set of parameters EPO-CNT (T).

The model also gives information regarding the microstructure evolution and more precisely, about the suspension orientation state. The classical description based on the second-order moment of

the orientation distribution, $\mathbf{a}_2$, is employed. Surprisingly, the model predicts a disordered microstructure for the EPO-CNT system with an important spreading of the rods orientation and an anisotropy with respect to the flow direction, as shown in Figure 6.6.

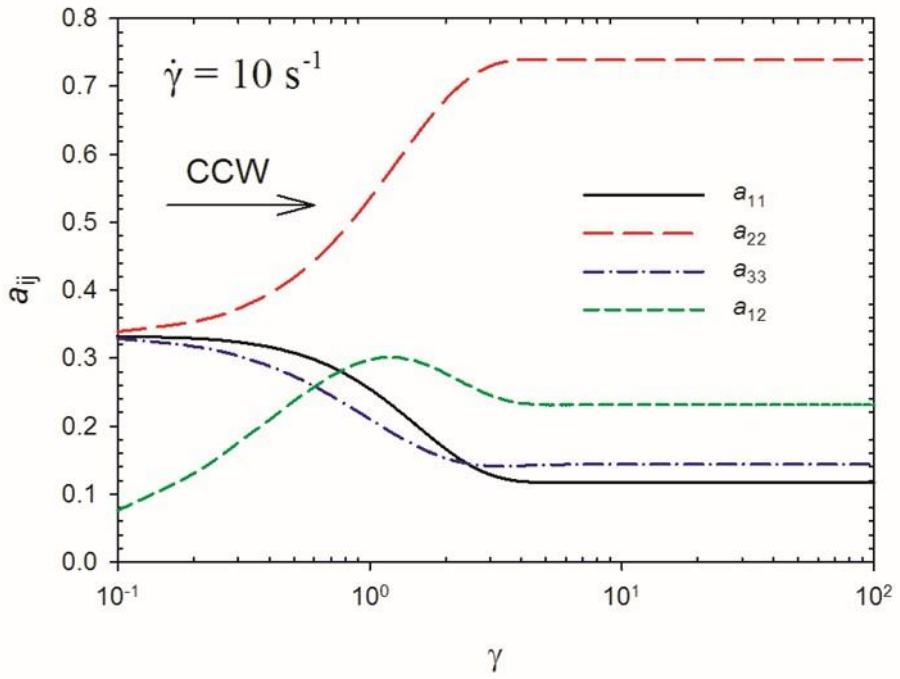

Figure 6.6 Model predictions of a2 components for the EPO-CNT system in CCW direction at 10 s-1 using the set of parameters EPO-CNT (T).

The strain at which we observe the overshoot in the a_{12} (subscripts 1 and 2 stand for flow and gradient direction, respectively) component corresponds to the characteristic deformation for the overshoot in the shear stress. Hence, the shear stress overshoots are found when the majority of the rods are located in the flow-gradient (12) plane. The value of a_{22} is always larger than a_{11}. A similar behavior was also encountered by Sundararajakumar and Koch (1997) in direct simulation of mono-dispersed rod suspension interacting with a linear lubrication force.

To complete the picture, it is interesting to show how the predicted orientation state changes with the applied shear rate and the predictions for steady-state with the parameters EPO-CNT $^{(T)}$ of Table 6.3 are presented in Figure 6.7.

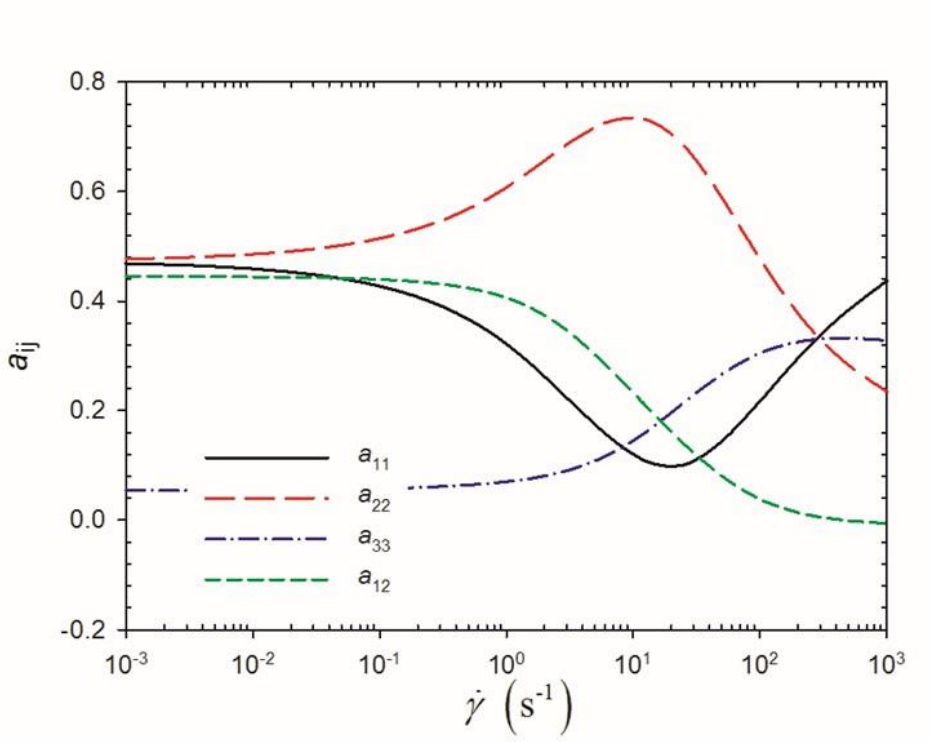

Figure 6.7 Model predictions of $\mathbf{a}_2$ components for the EPO-CNT system in steady state as function of shear rate using the set of parameters EPO-CNT $^{(T)}$.

The model predictions of the microstructure orientation depend strongly on the applied shear rate, which is typical for colloidal suspensions [Mobuchon *et al.* (2009b), Pujari *et al.* (2009a), Khalkhal *et al.* (2011)] and two regions can be identified. At shear rates lower than 20 s^{-1}, the model predicts a highly disordered system with rods that are unable to orient in the flow direction because of the interactions. With increasing shear rate the intensity of the flow is able to break this network of interactions and the rods tend slowly to orient in the flow direction. Hence, the model predicts a critical shear rate above which the system starts to orient. These results are coherent with the low levels of orientation found in the dichroic response of dilute MWCNT suspensions found by Natale *et al.* (2015). This critical shear rate is dependent on the interaction parameters and on the concentration of rods used in the simulations. A similar scenario has already been reported experimentally in the literature [Hobbie and Fry (2006), Niu *et al.* (2014)], however more work is required to verify experimentally the predicted orientation evolution.

It is worthwhile to compare the experimental data with the predictions of the model with the parameter values obtained from the transient data (EPO-CNT $^{(T)}$) and the ones obtained by Natale *et al.* (2014) using only steady-state data (EPO-CNT $^{(SS)}$). The results are reported in Figure 6.8 and the experimental data are taken from Natale *et al.* (2014).

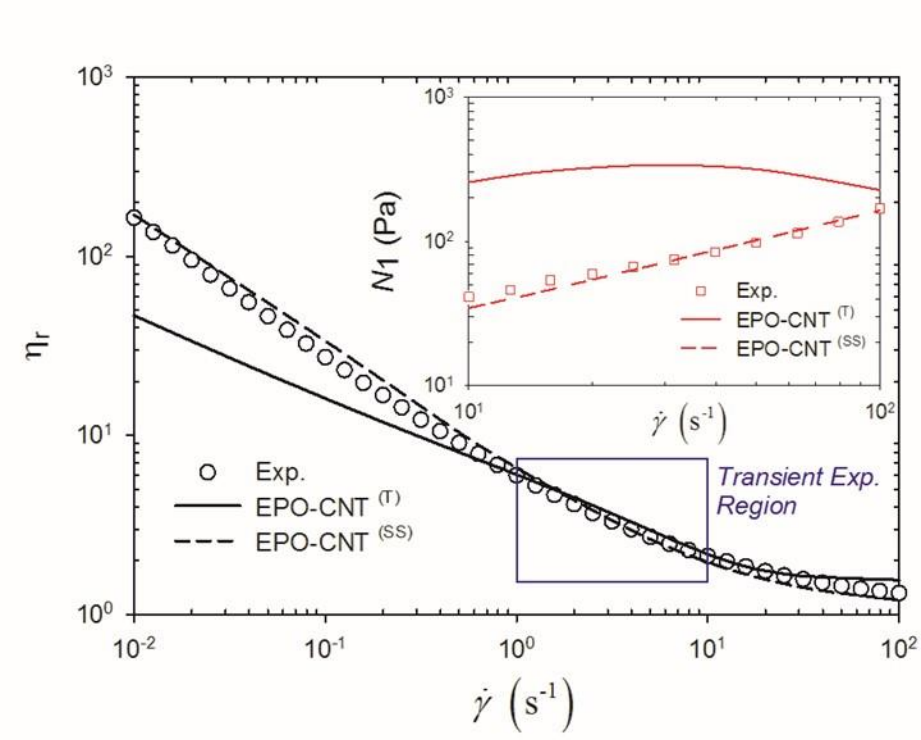

Figure 6.8 Comparison of the reduced steady-shear viscosity and first normal stress difference (insert) for the EPO-CNT system containing 1.17 vol% of carbon nanotubes with the model predictions using the two set of parameters reported in Table 6.3.

As shown in Figure 6.8 the EPO-CNT system containing 1.17 vol% of carbon nanotubes show experimentally a strong shear-thinning behavior and positive first normal stress differences. Natale *et al.* (2014) modeling results based on steady-state data for different concentrations using the parameters EPO-CNT $^{(SS)}$ (Table 6.3) show a good agreement with experiments (solid lines in the figure). However, the model predictions calculated with the new parameters obtained from the transient data (EPO-CNT $^{(T)}$) show lower values with respect to the experimental results for the reduced steady shear viscosity at shear rates below 1 s^{-1} (dashed lines). Furthermore, the predictions fail to capture N_1. In the case of the parameters EPO-CNT $^{(SS)}$ in Table 6.3, the predicted N_1

increases monotonically with the shear rate as observed experimentally. With a lower M_I (75), the difference $|a_{11}- a_{22}|$ keeps increasing in the region of shear rates between 10 and 10^2 s^{-1}.

In this section, we have demonstrated that the model is able to capture the mean features of the transient rheology of MWCNT suspensions using a simple power-law expression to describe the interactions between rods. However, three main weaknesses were encountered in the analysis: the presence of an overshoot in the reverse flow without rest (Figure 6.2), the underestimation of the steady-state viscosity at low shear rates and failure in predicting N_1 at steady-state (Figure 6.8).

By analyzing the parameter values reported in Table 6.3, the major differences are observed in the two parameters that control the rod-rod interactions: m and M_I. The power-law index, m, is lower (0.28 instead of 0.49) when obtained with the steady-state values (EPO-CNT $^{(SS)}$), since it is required to capture the higher slope at low shear rates, which in the model is about (1-m). It is important to underline that the quality of the fit is strongly dependent on the extent of experimental conditions examined. The steady-shear viscosity does not have a unique slope for the all range of shear rate. The transient data analyzed here are concentrated in the range of shear rates between 1 and 10 s^{-1} (box-contained region in Figure 6.8) where the shear-thinning is moderate and consequently, the predictions based on the transient data are in good agreement only for shear rates larger than 1 s^{-1}. The intensity of the interactions, M_I, required to predict the strong overshoot is about 10 times larger in transient regime than the one obtained using steady-state data and this causes also the stronger intensity of N_1. From this analysis, it is tempting to imagine that the two parameters controlling the interactions should be considered as functions of the shear rate as well of volume fraction, rod aspect ratio, etc.). This, however, introduces complexities that go beyond the scope of the present paper.

6.6.2 Glass fiber suspensions

The model predictions are also verified for a micro-size filled system: glass fibers dispersed in a polybutene matrix (PB-GF). The experimental results are taken from the work of Sepehr *et al.* (2004b) and key material properties of the PB-GF system are reported in Table 6.2. Glass fiber suspensions do not form a network throughout the system since they are not Brownian and no attractive forces are present. Furthermore, Férec *et al.* (2009) showed that a simple linear lubrication force was sufficient to predict the transient rheological response for this system. The

comparison between the model predictions and the experimental data for the PB-GF system has two main goals: first to verify that a simple linear lubrication force is indeed the correct expression for the interaction force, and second to demonstrate the versatility of the new model. In addition, it was possible to obtain experimentally a convincing response for the normal stress differences in this system, which was not the case for the EPO-CNT suspensions.

Since a parallel plate (PP) flow geometry was used to perform rheological measurements for the PB-GF system, the model predictions, which are based on the assumption of a homogenous flow, are corrected to take into account the radial dependency of the shear flow. Hence, the shear viscosity and the normal stress differences (predicted by the model) are corrected according to the following equations [Carreau *et al.* (1997)]

$$\eta(\gamma_R) = \frac{4}{\gamma_R^{\,4}} \int_0^{\gamma_R} \eta(\gamma)\gamma^3 d\gamma \tag{6.10}$$

$$N_1(\gamma_R) - N_2(\gamma_R) = \frac{2}{\gamma_R^{\,2}} \int_0^{\gamma_R} \left[N_1(\gamma) - N_2(\gamma) \right] \gamma d\gamma \tag{6.11}$$

In addition, the glass fibers are not Brownian particles ($D_r = 0$) and, experimentally, it was not possible to achieve a reproducible initial condition when positioning the samples between the plates. Hence, a first shear-rate step was imposed in the CW direction in order to precondition the samples and start successive stress growth measurements from a reproducible initial condition. This shear-rate step was followed by another CW run and, then, a CCW step. In the following, the CCW step data will be used for the comparison with the model predictions since, at this state, any unknown regarding the initial orientation state of the system has been removed. Furthermore, the initial condition for the CCW step in the simulations was obtained by numerically shearing the system in the CW direction until the relative steady-state value was obtained and the final orientation state was used as the initial condition for the CCW step.

As in the case of the MWCNT data, the model predictions calculated with the parameters obtained in steady-state by Natale *et al.* (2014) (PB-GF $^{(SS)}$) fail to predict the transient response of glass fibers suspensions (data not shown). Hence, a new set of parameter is again necessary to verify the

model predictions in transient shear flows. The values of the new set of parameters (PB-GF $^{(T)}$) and of the one obtained at steady-state by Natale *et al.* (2014) are reported in Table 6.4.

Table 6.4 Adjustable parameter values obtained by fitting the transient experimental data for glass fibers (7.06 vol.%) dispersed in polybutene (PB-GF $^{(T)}$). The parameter values obtained by fitting the steady-state values of the viscosity and first normal stresses difference, N_1- N_2, of glass fibers (7.06 vol.%) dispersed in polybutene (PB-GF $^{(SS)}$) obtained from Natale *et al.* (2014) are also reported.

Suspensions	Parallel drag coefficient N_P	Interaction coefficient q	Rod-rod Interaction intensity factor M_I (s^{m-1})	Interaction power-law exponent m	Rotary Diffusion D_r (s^{-1})
PB-GF $^{(T)}$	203	2.4×10^{-2}	5×10^{-2}	0.93	0
PB-GF $^{(SS)}$	82	5.92	7×10^{-2}	0.77	0

"T" for transient, "SS" for steady-state conditions

By reversing the flow, the shear stress response of the PB-GF system presents a long plateau followed by an overshoot at a much higher deformation (about 20) than the EPO-CNT system (about 0.45). This is shown in Figure 6.9 where the shear stress growth data during the CCW step for shear rates $\dot{\gamma}$ of 0.1 s^{-1}, 1 s^{-1} and 5 s^{-1} are reported.

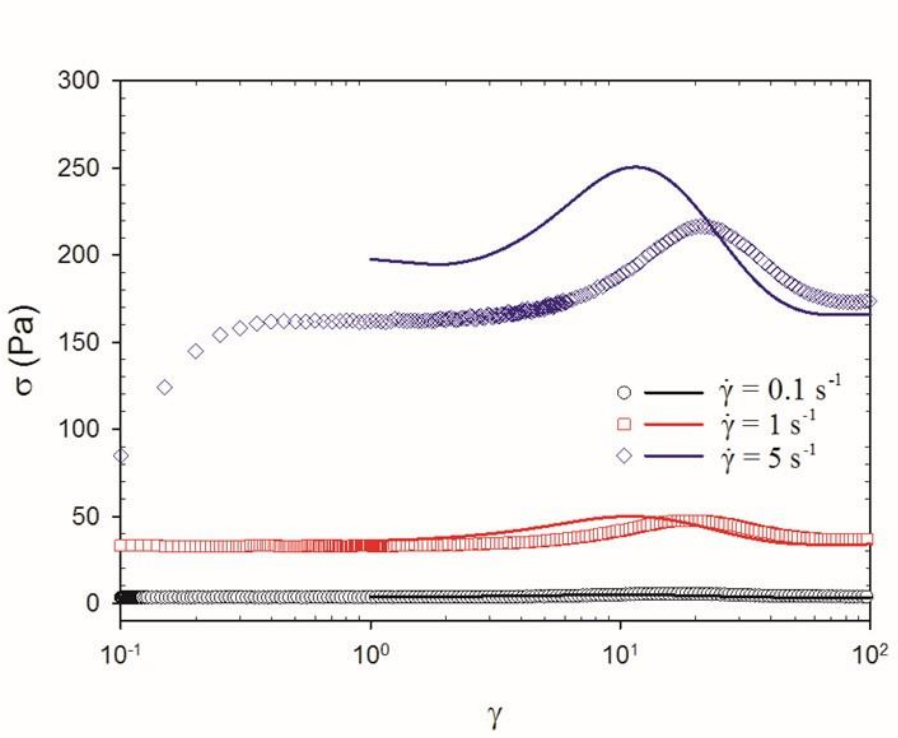

Figure 6.9 Comparison between experimental reversed stress growth data at different shear rates and model predictions in the CCW direction immediately following an initial CW test for the PB-GF (7.06 vol.%) system using the set of parameters PB-GF $^{(T)}$. Data from Sepehr *et al.* (2004b).

All the shear stress overshoots, independently of the applied shear rate, appear at a strain of about 20. Concentrated glass fiber suspensions form a "crystalline" structure, due to the aligning effect of the shear flow. By inverting the flow direction, the aligned fibers tilt over in order to adapt to the new flow condition [Sepehr *et al.* (2004b)]. This is at the base of the reverse peak in the shear stress reported in Figure 6.9. The effect of inversion in flow direction is even more dramatic in the case of the normal stress differences (N_1-N_2), as shown in Figure 6.10. Negative values at low strain are followed by a fast change in sign and at deformation of about 40 an overshoot is observed. This behavior is present independently of the applied shear rate.

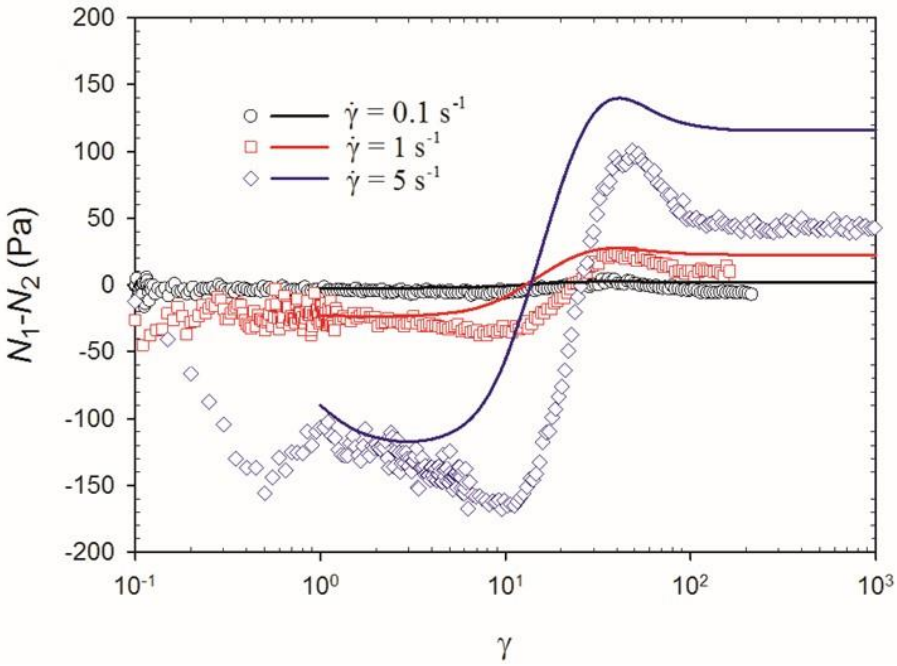

Figure 6.10 Comparison between experimental N_1-N_2 responses to reversed stress growth at different shear rates and model predictions in the CCW direction following immediately an initial CW test for the PB-GF (7.06 vol.%) system using the set of parameters PB-GF $^{(T)}$. Data from Sepehr *et al.* (2004b).

The model captures adequately the behavior for this micro-sized filled system. The shear stress overshoots are predicted at slightly shorter strain, but the predictions for the steady-state values for the shear stress are in good quantitative agreement with the experiments, with just one set of parameters for all the three shear rates examined. Furthermore, the change in sign of the N_1-N_2 curves observed experimentally after the inversion of the flow is predicted by the model. Even though the change in sign is seen at a lower strain (~13) than experimentally (~23), the overshoot positions and intensities are adequately captured. However, the model always overestimates the steady-state values for the normal stress differences.

As done for the EPO-CNT system, it is interesting to show the different contributions to the shear stress and their relative importance for this micro-size filled system. The results are presented in Figure 6.11 for a shear rate of 5 s^{-1}, but the conclusions are also valid for the other shear rates examined. In contrast with the EPO-CNT system, the dominant contribution in the case of GF

suspensions is due to the matrix, while the interactions have a negligible influence on the overall shear stress. The hydrodynamic contribution due to fiber orientation is responsible for the shear stress overshoots. It is worth noting that even if the PB-GF shear stress is controlled by the hydrodynamic contribution, the particle-particle interactions play an important role in slowing down the microstructure evolution due to the perturbation velocity used to simulate the long range hydrodynamic interactions, the last term of Eq. 6.3, which has an indirect influence on the rheological response. In other words, the characteristic strains (at which the overshoots or the change in sign appear) are overall correctly predicted because the model accounts for mechanical contacts.

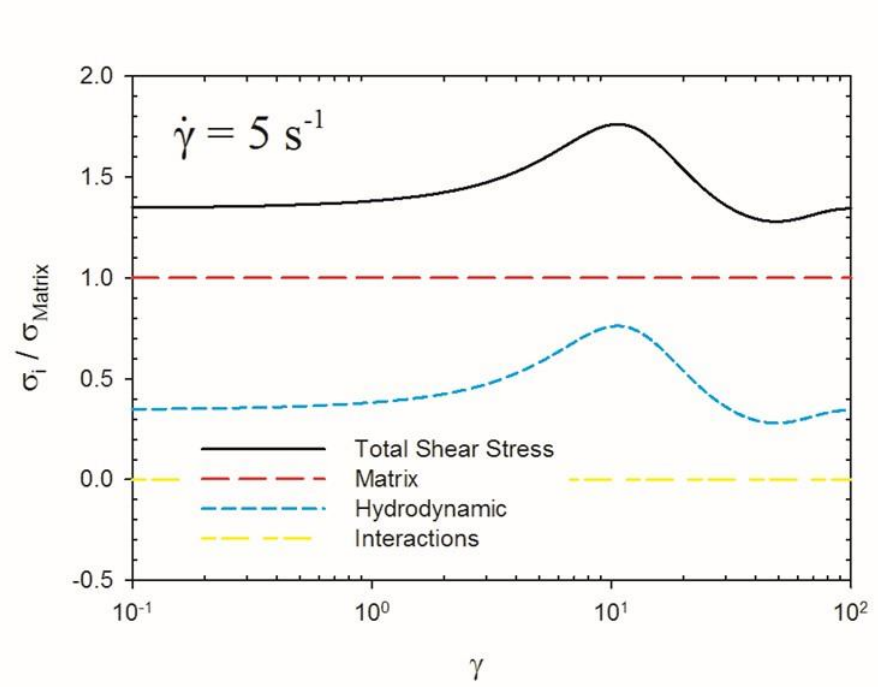

Figure 6.11 Model predictions of the different contributions to the shear stress and total shear stress normalized with respect to the matrix contribution for the PB-GF (7.06 vol.%) system in the CCW stress growth test at 5 s^{-1} using the set of parameters PB-GF $^{(T)}$.

By comparing the predictions regarding the relative importance of the different contributions to the shear stress for the two systems, the model clearly distinguishes between a nano and micro size filled system. MWCNTs create a network through the suspension and each rod is in contact with multiple other particles. When a shear flow is applied, particle-particle interactions are frequent and dominate the overall rheological response, especially at low deformations where the deviation

from the isotropic orientation state is still small. The GFs are not able to form a network since they are not Brownian. Consequently, less (in number and intensity) interactions are expected. It is the overall orientation dynamic (such tilting by reversing the flow) that controls the PB-GF system rheology. These differences are also clear by comparing the numerical values for the adjustable parameters obtained by the fitting procedure of the transient data of the two systems reported in Table 6.3 and Table 6.4. The strength of interactions is controlled by the parameter M_I and there are four order of magnitude in difference between the values for MWCNTs and GFs. The deviation from a simple linear lubricated interaction (m = 0.49) for the nanoparticles is much more important than in the case of the glass fibers (m = 0.93). This result confirms that a linear lubrication force is an appropriate description for the GF system and is in agreement with the results obtained by Férec *et al.* (2009). Glass fibers interaction force scales linearly with the macroscopic shear rate, while in the case of MWCNTs this linear relationship is lost, implying a much more complex interaction behavior.

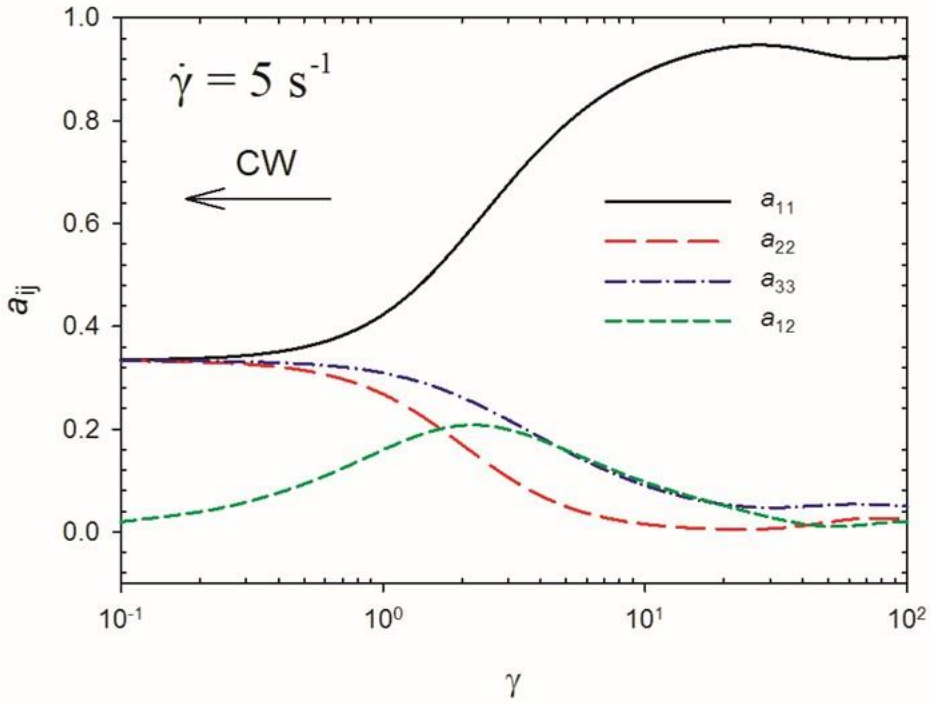

Figure 6.12 Model predictions of $\mathbf{a}_2$ components for the PB-GF (7.06 vol.%) system in the CW direction at 5 s^{-1}.

The predicted EPO-CNT orientation state differs strongly with the orientation distribution found for the GF suspensions. The GFs orient easily around the flow direction (values of a_{11} approaching 1 as seen in Figure 6.12), in agreement with the observations of Férec *et al.* (2009). The differences in the predicted orientation state are a consequence of the much more intense interactions between MWCNTs than for GFs. To complete the analysis, the predictions of the model with the parameter values obtained from the transient data (PB-GF $^{(T)}$) are compared with the one obtained by Natale *et al.* (2014) for steady state (PB-GF $^{(SS)}$) and the experimental data for the steady-state viscosity and normal stress differences, N_1-N_2 . The results are reported in Figure 6.13 and the experimental data are taken from Sepehr *et al.* (2004b).

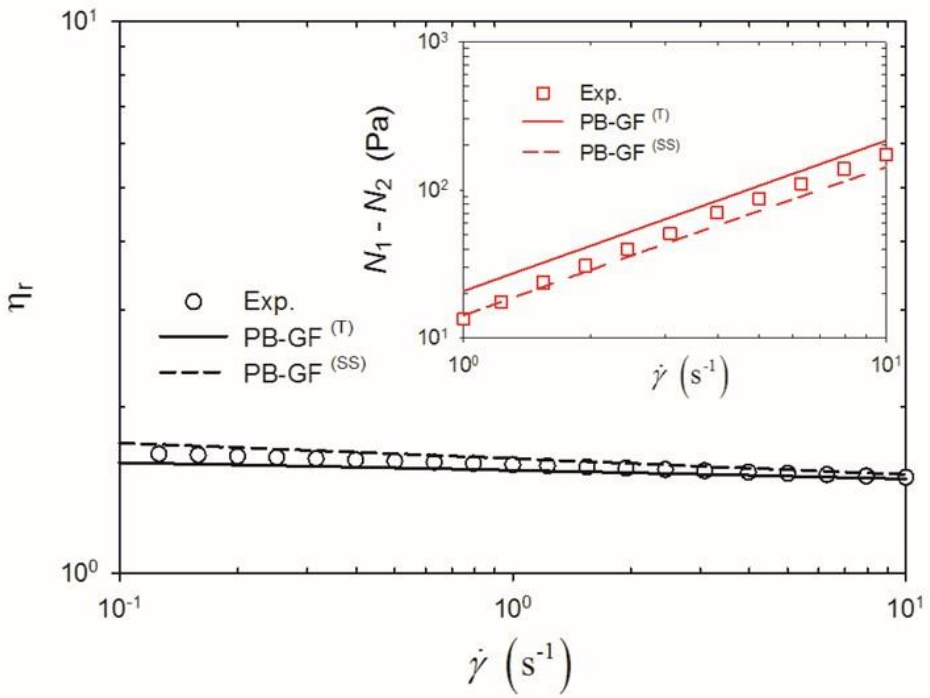

Figure 6.13 Comparison of the reduced steady-shear viscosity and first normal stress differences (inset) for PB-GF (7.06 vol.%) system with model predictions with the two set of parameters reported in Table 6.4.

The PB-GF system shows in Figure 6.13 a very moderate shear-thinning behavior in the range of shear rates analyzed, while the N_1-N_2 grows linearly with the applied shear rate. The behavior is a

consequence of the interactions between rods, as discussed by Sepehr *et al.* (2004b) and Natale *et al.* (2014). Contrary to the EPO-CNT case, both set of parameters show a good quantitative agreement with the experimental data. The model using the parameters PB-GF $^{(T)}$ overestimates slightly the normal stress differences, but the linear slope is well predicted. The good agreement is not surprising since the experimental window for the transient data in the case of PB-GF covers almost completely the steady-state data. Hence, quantitative predictions for the PB-GF system are obtained for transient and steady-state rheology with only one set of parameters. Contrary to the EPO-CNT case, the major differences between the parameter values reported in Table 6.4 are observed in the two parameters related to hydrodynamic interactions: q and N_P. This is a clear consequence of the results reported in Figure 6.11: the non-linear lubrication interaction contribution to the shear stress is negligible for the PB-GF system. Furthermore, this implies a more moderate shear-thinning behavior in the case of glass fiber since the contribution to the shear viscosity due to the hydrodynamic interactions does not depend directly on the shear rate [Natale *et al.* (2014)].

6.7 Concluding remarks

Stress growth experiments of concentrated MWCNT suspensions were performed to study the microstructure evolution during non-linear deformation. In quiescent state, MWCNTs are able to build a network throughout the system due to Brownian motion. When a constant shear rate is applied, the shear stress exhibits a strong overshoot. The deformation at the overshoots was found to be about 0.45 independently of the shear rate intensity for shear rate between 1 and 10 s^{-1}. When rest was allowed, no influence of the applied flow direction was found on the overshoots, confirming the hypothesis of an evolution controlled by Brownian motion during the quiescent state.

The transient response of these concentrated MWCNT suspensions was explained with the aid of a micro structural description based on the simple argument that the interaction force between two rods scales as a power-law with shear rate. The model predictions showed clearly that the overshoots were due to interactions between CNTs and that the interaction contribution to the shear stress overcame the hydrodynamic one. Furthermore, the model was able to correctly predict the effect of shear rate on the transient shear stress response. However, the model underestimated the

reduced steady-state viscosity at low shear rates. On the other hand, a linear lubrication force was sufficient to describe the rheological response of glass fiber suspensions and our modeling results are in agreement with those of Férec *et al.* (2009).

The good agreement between the model predictions and rheological response for the suspensions investigated and the shear-rate dependent microstructure are very encouraging results for the proposed interaction force, especially in the case of the EPO-CNT system. The proposed model can capture the transient rheological behavior of MWCNT and GF suspensions. Moving from micro to nano size filler, the model is able to recognize differences in the type of interactions, microstructural evolution and, consequently, in the rheological response. Further studies should focus on the numerical solution of the Fokker-Planck equation in more complex flows to completely test the model predictions, on the development of valid closure approximation for the interaction tensors, $\mathbf{b}_2^{(m)}$ and $\mathbf{b}_4^{(m)}$, and on the definition of the physical dependencies for the interaction parameters, m and M_I.

In addition to the dependencies of the interaction parameters (m and M_I) on shear rate, some improvements to the model predictions could be brought by accounting for the rotational hindering introduced in concentrated systems, and a more complex diffusion coefficient than the simple isotropic one used here [Doi and Edwards (1986), Phelps and Tucker (2009)]. Furthermore, flexibility and polydispersity appears to have a strong effect on the width of the overshoots. Finally, a major focus should be given to the development of a more accurate contact probability function and to determine fully its validity under shear flow.

6.8 Acknowledgements

This work was funded by NSERC (Natural Science and Engineering Research Council of Canada).

6.9 Appendix A: Evolution of a2

To reduce the numerical cost of solving the full Fokker-Planck equation, one possibility is to obtain the evolution of the relative second-order tensor $\mathbf{a}_2 = \iint \mathbf{p}^\alpha \mathbf{p}^\alpha \psi_{\mathbf{p}^\alpha} d\mathbf{p}^\alpha d\mathbf{p}^\beta$. Even if the information contained in $\mathbf{a}_2$ is inferior to the knowledge of the full $\psi_{\mathbf{p}^\alpha}$, it is sufficient to calculate average

quantities of interest, i.e. stress tensor components, dichroism and average orientation angle. The time evolution of $\mathbf{a}_2$ is calculated as follows

$$\frac{D\mathbf{a}_2}{Dt} = \int \dot{\mathbf{p}}^\alpha \mathbf{p}^\alpha \psi_{\mathbf{p}^\alpha} d\mathbf{p}^\alpha + \int \mathbf{p}^\alpha \dot{\mathbf{p}}^\alpha \psi_{\mathbf{p}^\alpha} d\mathbf{p}^\alpha \tag{6A.1}$$

Substituting Eq. 6.8 in the last equation and after some calculations, we obtain

$$\begin{aligned}\frac{D\mathbf{a}_2}{Dt} = &-\frac{1}{2}(\boldsymbol{\omega}\cdot\mathbf{a}_2 - \mathbf{a}_2\cdot\boldsymbol{\omega}) + \frac{1}{2}(\dot{\boldsymbol{\gamma}}\cdot\mathbf{a}_2 + \mathbf{a}_2\cdot\dot{\boldsymbol{\gamma}} - 2\dot{\boldsymbol{\gamma}}:\mathbf{a}_4) + 2D_r(\boldsymbol{\delta} - 3\mathbf{a}_2) \\ &-\frac{1}{2}\phi M_I\left(\dot{\boldsymbol{\gamma}}\cdot\mathbf{b}_2{}^{(m)} + \mathbf{b}_2{}^{(m)}\cdot\dot{\boldsymbol{\gamma}} - 2\dot{\boldsymbol{\gamma}}:\mathbf{b}_4{}^{(m)}\right) \\ &-\phi M_I q|\dot{\gamma}|\iint|\mathbf{p}^\alpha\times\mathbf{p}^\beta|\psi_{\mathbf{p}^\beta}d\mathbf{p}^\beta\left|\dot{\boldsymbol{\gamma}}:\mathbf{p}^\alpha\mathbf{p}^\alpha\right|^{m-1}\frac{\partial\psi_{\mathbf{p}^\alpha}}{\partial\mathbf{p}^\alpha}\cdot\frac{\partial\mathbf{p}^\alpha\mathbf{p}^\alpha}{\partial\mathbf{p}^\alpha}d\mathbf{p}^\alpha\end{aligned} \tag{6A.2}$$

where $\mathbf{b}_2{}^{(m)} = \int \mathbf{p}^\alpha\mathbf{p}^\alpha\left|\dot{\boldsymbol{\gamma}}:\mathbf{p}^\alpha\mathbf{p}^\alpha\right|^{m-1}\int|\mathbf{p}^\alpha\times\mathbf{p}^\beta|\psi_{\mathbf{p}^\beta}d\mathbf{p}^\beta\psi_{\mathbf{p}^\alpha}d\mathbf{p}^\alpha$. By pre-averaging the last term, we can rewrite Eq. 6A.2 as

$$\begin{aligned}\frac{D\mathbf{a}_2}{Dt} = &-\frac{1}{2}(\boldsymbol{\omega}\cdot\mathbf{a}_2 - \mathbf{a}_2\cdot\boldsymbol{\omega}) + \frac{1}{2}(\dot{\boldsymbol{\gamma}}\cdot\mathbf{a}_2 + \mathbf{a}_2\cdot\dot{\boldsymbol{\gamma}} - 2\dot{\boldsymbol{\gamma}}:\mathbf{a}_4) \\ &-\frac{1}{2}\phi M_I\left(\dot{\boldsymbol{\gamma}}\cdot\mathbf{b}_2{}^{(m)} + \mathbf{b}_2{}^{(m)}\cdot\dot{\boldsymbol{\gamma}} - 2\dot{\boldsymbol{\gamma}}:\mathbf{b}_4{}^{(m)}\right) \\ &+2\left(D_r + \phi M_I q|\dot{\gamma}|f\right)(\boldsymbol{\delta} - 3\mathbf{a}_2)\end{aligned} \tag{6A.3}$$

with *f* the trace of $\mathbf{b}_2{}^{(m)}$. Eq. 6A.3 demonstrates that the evolution of $\mathbf{a}_2$ is coupled with three tensors ($\mathbf{b}_2{}^{(m)}, \mathbf{b}_4{}^{(m)}$ and $\mathbf{a}_4$) for which the introduction of closure approximations is required.

In the case of an isotropic orientation distribution, $\mathbf{b}_4{}^{(m)}$ components can be determined analytically. In particular, the Osanger potential $|\mathbf{p}^\alpha\times\mathbf{p}^\beta|$ can be simplified by expanding it using Taylor series expansion until the first-order that gives [Dhont and Briels (2003b)]

$$|\mathbf{p}^\alpha\times\mathbf{p}^\beta| \approx \frac{5\pi}{16}\left(1 - \frac{3}{5}\mathbf{p}^\alpha\mathbf{p}^\alpha:\mathbf{p}^\beta\mathbf{p}^\beta\right) \tag{6A.4}$$

Therefore, the fourth-order interaction tensor defined in Eq. 6.14 for $m = 0$ becomes

$$\mathbf{b}_4^{(m=0)} = \frac{5}{16^2\pi}\int \mathbf{p}^\alpha\mathbf{p}^\alpha\mathbf{p}^\alpha\mathbf{p}^\alpha \left|\dot{\boldsymbol{\gamma}} : \mathbf{p}^\alpha\mathbf{p}^\alpha\right|^{-1}\int\left(1-\frac{3}{5}\mathbf{p}^\alpha\mathbf{p}^\alpha : \mathbf{p}^\beta\mathbf{p}^\beta\right) d\mathbf{p}^\beta d\mathbf{p}^\alpha \tag{6A.5}$$

Consequently, the component of $\mathbf{b}_4^{(m=0)}$ involved in the calculation of the shear stress (Eq. 6.12) results equal to [Férec *et al.* (2015)]

$$b_{1122}{}^{(m=0)} = \frac{1}{12\left|\dot{\gamma}\right|} \tag{6A.6}$$

In the case of $m = 1$, it is easy to demonstrate that

$$b_{1122}{}^{(m=1)} = \frac{\pi}{60} \tag{6A.7}$$

By imposing $b_{1122}{}^{(m=0)} = b_{1122}{}^{(m=1)}$, it is possible to calculate the shear rate at which all the $b_{1122}{}^{(m)}$ intersect. This shear rate is equal to $5/\pi$ and the generic form valid in isotropic state for the $b_{1122}{}^{(m)}$ is then easily obtained as

$$b_{1122}{}^{(m)} = \frac{\pi}{60}\left|\frac{\dot{\gamma}\pi}{5}\right|^{m-1} \tag{6A.8}$$

This result also implies that it is possible to obtain an analytical solution for the stress tensor in the isotropic state.

6.10 References

Abbasi S., P. J. Carreau, A. Derdouri and M. Moan, "Rheological properties and percolation in suspensions of multiwalled carbon nanotubes in polycarbonate," Rheologica acta **48**, 943-959 (2009).

Advani S. G. and C. L. Tucker, "The use of tensors to describe and predict fiber orientation in short fiber composites," Journal of Rheology **31**, 751-784 (1987).

Batchelor G. K., "Slender-body theory for particles of arbitrary cross-section in Stokes flow," Journal of Fluid Mechanics **44**, 419-440 (1970).

Batchelor G. K., "The stress generated in a non-dilute suspension of elongated particles by pure straining motion," Journal of Fluid Mechanics **46**, 813-829 (1971).

Bird R. B., C. F. Curtiss, R. C. Armstrong and O. Hassager, *Dynamics of polymeric liquids. Volume 2, Kinetic theory* (Wiley, New York, 1987).

Brenner H., "Rheology of a dilute suspension of axisymmetric Brownian particles," International Journal of Multiphase Flow **1**, 195-341 (1974).

Bretherton F. P., "The motion of rigid particles in a shear flow at low Reynolds number," Journal of Fluid Mechanics **14**, 284-304 (1962).

Carreau P. J., D. De Kee and R. P. Chhabra, *Rheology of polymeric systems: Principles and applications* (Hanser, Munich, 1997).

Cruz C., L. Illoul, F. Chinesta and G. Régnier, "Shear-strain step response in linear regime of dilute suspensions of naturally bent carbon nanotubes," Journal of Applied Polymer Science **125**, 4347-4357 (2012).

Dhont J. K. G. and W. J. Briels, "Inhomogeneous suspensions of rigid rods in flow," The Journal of Chemical Physics **118**, 1466-1478 (2003a).

Dhont J. K. G. and W. J. Briels, "Viscoelasticity of suspensions of long, rigid rods," Colloids and Surfaces A: Physicochemical and Engineering Aspects **213**, 131-156 (2003b).

Djalili-Moghaddam M. and S. Toll, "A model for short-range interactions in fibre suspensions," Journal of Non-Newtonian Fluid Mechanics **132**, 73-83 (2005).

Doi M. and S. F. Edwards, "Dynamics of rod-like macromolecules in concentrated solution. Part 2," Journal of the Chemical Society, Faraday Transactions 2: Molecular and Chemical Physics **74**, 918-932 (1978).

Doi M. and S. F. Edwards, "The theory of polymer dynamics," Clarendon, Oxford (1986).

Du F., R. C. Scogna, W. Zhou, S. Brand, J. E. Fischer and K. I. Winey, "Nanotube Networks in Polymer Nanocomposites: Rheology and Electrical Conductivity," Macromolecules **37**, 9048-9055 (2004).

Ericksen J. L., "Transversely isotropic fluids," Kolloid-Zeitschrift **173**, 117-122 (1960).

Férec J., E. Abisset-Chavanne, G. Ausias and F. Chinesta, "On the use of interaction tensors to describe and predict rod interactions in rod suspensions," Rheologica Acta **53**, 445-456 (2014).

Férec J., G. Ausias, M. C. Heuzey and P. J. Carreau, "Modeling fiber interactions in semiconcentrated fiber suspensions," Journal of Rheology **53**, 49-72 (2009).

Férec J., M. Heniche, M. C. Heuzey, G. Ausias and P. J. Carreau, "Numerical solution of the Fokker–Planck equation for fiber suspensions: Application to the Folgar–Tucker–Lipscomb model," Journal of Non-Newtonian Fluid Mechanics **155**, 20-29 (2008).

Férec J., A. Perrot and G. Ausias, "Toward modeling anisotropic yield stress and consistency induced by fiber in fiber-reinforced viscoplastic fluids," Journal of Non-Newtonian Fluid Mechanics **220**, 69-76 (2015).

Folgar F. P. and C. L. Tucker, "Orientation behavior of fibers in concentrated suspensions," J. Reinf. Plast. Compos. **3**, 99-119 (1984).

Fry D., B. Langhorst, H. Wang, M. L. Becker, B. J. Bauer, E. A. Grulke and E. K. Hobbie, "Rheo-optical studies of carbon nanotube suspensions," The Journal of Chemical Physics **124**, 054703 (2006).

Gupta A. and V. Choudhary, "Electromagnetic interference shielding behavior of poly(trimethylene terephthalate)/multi-walled carbon nanotube composites," Composites Science and Technology **71**, 1563-1568 (2011).

Hobbie E. K., "Optical anisotropy of nanotube suspensions," The Journal of Chemical Physics **121**, 1029-1037 (2004).

Hobbie E. K. and D. J. Fry, "Nonequilibrium Phase Diagram of Sticky Nanotube Suspensions," Physical Review Letters **97**, 036101 (2006).

Hobbie E. K. and D. J. Fry, "Rheology of concentrated carbon nanotube suspensions," The Journal of Chemical Physics **126**, 124907-7 (2007).

Jeffery G. B., "The motion of ellipsoidal particles immersed in a viscous fluid," Proceedings of the Royal Society of London Serie A **102**, 161-179 (1922).

Khalkhal F. and P. J. Carreau, "Critical shear rates and structure build-up at rest in MWCNT suspensions," Journal of Non-Newtonian Fluid Mechanics **171–172**, 56-66 (2012).

Khalkhal F., P. J. Carreau and G. Ausias, "Effect of flow history on linear viscoelastic properties and the evolution of the structure of multiwalled carbon nanotube suspensions in an epoxy," Journal of Rheology **55**, 153-175 (2011).

Larson R. G., "Constitutive equations for thixotropic fluids," Journal of Rheology (1978-present) **59**, 595-611 (2015).

Ma W. K. A., F. Chinesta, A. Ammar and M. R. Mackley, "Rheological modeling of carbon nanotube aggregate suspensions," Journal of Rheology **52**, 1311-1330 (2008).

Mobuchon C., P. J. Carreau and M.-C. Heuzey, "Structural analysis of non-aqueous layered silicate suspensions subjected to shear flow," Journal of Rheology (1978-present) **53**, 1025-1048 (2009).

Natale G., M. C. Heuzey, P. J. Carreau, G. Ausias and J. Férec, "Rheological modeling of carbon nanotube suspensions with rod–rod interactions," AIChE Journal **60**, 1476-1487 (2014).

Natale G., N. K. Reddy, G. Ausias, J. Férec, M. C. Heuzey and P. J. Carreau, "Rheo-optical response of carbon nanotube suspensions," Journal of Rheology (1978-present) **59**, 499-524 (2015).

Niu R., J. Gong, D. Xu, T. Tang and Z.-Y. Sun, "Flow-induced structure and rheological properties of multiwall carbon nanotube/polydimethylsiloxane composites," RSC Advances **4**, 62759-62768 (2014).

Olowojoba G., S. Sathyanarayana, B. Caglar, B. Kiss-Pataki, I. Mikonsaari, C. Hübner and P. Elsner, "Influence of process parameters on the morphology, rheological and dielectric

properties of three-roll-milled multiwalled carbon nanotube/epoxy suspensions," Polymer **54**, 188-198 (2013).

Petrich M. P., D. L. Koch and C. Cohen, "An experimental determination of the stress-microstructure relationship in semi-concentrated fiber suspensions," Journal of Non-Newtonian Fluid Mechanics **95**, 101-133 (2000).

Phelps J. H. and C. L. Tucker, "An anisotropic rotary diffusion model for fiber orientation in short- and long-fiber thermoplastics," Journal of Non-Newtonian Fluid Mechanics **156**, 165-176 (2009).

Pujari S., S. Rahatekar, J. W. Gilman, K. K. Koziol, A. H. Windle and W. R. Burghardt, "Shear-induced anisotropy of concentrated multiwalled carbon nanotube suspensions using x-ray scattering," Journal of Rheology (1978-present) **55**, 1033-1058 (2011).

Pujari S., S. S. Rahatekar, J. W. Gilman, K. K. Koziol, A. H. Windle and W. R. Burghardt, "Orientation dynamics in multiwalled carbon nanotube dispersions under shear flow," The Journal of Chemical Physics **130**, 214903 (2009).

Rahatekar S. S., K. K. K. Koziol, S. A. Butler, J. A. Elliott, M. S. P. Shaffer, M. R. Mackley and A. H. Windle, "Optical microstructure and viscosity enhancement for an epoxy resin matrix containing multiwall carbon nanotubes," Journal of Rheology **50**, 599-610 (2006).

Sandstrom C. R., "Interactions and orientation in concentrated suspensions of rigid rods: theory and experiment," Ph.D. thesis, University of Illinois, Urbana-Champaign, 1993.

Sandstrom C. R. and C. L. Tucker, "A theory for concentrated fiber suspensions with strong fiber-fiber interactions," Makromolekulare Chemie-Macromolecular Symposia **68**, 291-300 (1993).

Schulz S. C., G. Faiella, S. T. Buschhorn, L. A. S. A. Prado, M. Giordano, K. Schulte and W. Bauhofer, "Combined electrical and rheological properties of shear induced multiwall carbon nanotube agglomerates in epoxy suspensions," European Polymer Journal **47**, 2069-2077 (2011).

Sepehr M., G. Ausias and P. J. Carreau, "Rheological properties of short fiber filled polypropylene in transient shear flow," Journal of Non-Newtonian Fluid Mechanics **123**, 19-32 (2004a).

Sepehr M., P. J. Carreau, M. Moan and G. Ausias, "Rheological properties of short fiber model suspensions," Journal of Rheology **48**, 1023-1048 (2004b).

Shaqfeh E. S. G. and G. H. Fredrickson, "The hydrodynamic stress in a suspension of rods," Physics of Fluids a-Fluid Dynamics **2**, 7-24 (1990).

Sundararajakumar R. R. and D. L. Koch, "Structure and properties of sheared fiber suspensions with mechanical contacts," Journal of Non-Newtonian Fluid Mechanics **73**, 205-239 (1997).

Versteeg H. K. and W. Malalasekera, *An Introduction to Computational Fluid Dynamics: The Finite Volume Method* (Pearson Prentice Hall, Harlow, Toronto, 1995).

Wu D., L. Wu and M. Zhang, "Rheology of multi-walled carbon nanotube/poly(butylene terephthalate) composites," Journal of Polymer Science Part B: Polymer Physics **45**, 2239-2251 (2007).

CHAPTER 7 GENERAL DISCUSSION

In this thesis, the structural evolution of carbon nanotube suspensions was probed by direct and indirect methods. The bulk rheology of carbon nanotube suspensions was explained by linking experimentally the microstructure and macroscopic properties and with the aid of microstructural descriptions.

Relatively "short" MWCNTs were used in this work, with average diameter of about 15 nm and length of 670 nm. They were polydisperse in diameters and lengths with aspect ratios varying between 4 and 314. Assuming a Young modulus, E_Y, of 40 GPa [Hobbie and Fry (2007)] and an average aspect ratio, *r*, of 45, the effective stiffness parameter defined by Switzer III and Klingenberg (2003) is

$$S^{eff} = \frac{E_Y \pi}{2^6 \eta_0 \dot{\gamma} r^4} \approx \frac{40}{\dot{\gamma}} \tag{7.1}$$

where η_0 is the matrix viscosity and is equal to 12.3 Pa s. Hence, the MWCNTs used in this work can be considered sufficiently stiff in the range of shear rates commonly probed during rheological tests.

In dilute and semi-dilute regimes, the orientation dynamics of the system was much more complex than the behavior expected for rigid-rod suspensions. The evolution of dichroism as function of Pe presented clearly two stages (Figure 4.6). At low Pe, the dichroism evolved strongly coherently with the idea of particles orienting in the flow direction due to the applied shear flow. At high Pe, a saturated orientation state was reached and only a mild change of the orientation state was found. In dilute regime, the most puzzling result was the finding of a plateau for the average orientation angle at high values (~18°) in the high Pe range. This low anisotropy was explained by the assumption that nanotube conformation at equilibrium is anything but a straight rod.

This hypothesis was developed in a simple two-rod approach. The bending potential was modelled with a cosine-harmonic expression allowing bent conformations at the equilibrium. The model predictions were found in agreement with the experimental results in the high Pe region (Figure 4.12).

Bent conformations of the rods have important consequences on the orientation dynamic of the system. From an individual rod perspective, the interplay between bending and hydrodynamic torques in shear flow causes the particle to keep tumbling. Even when oriented in the flow direction, the bent conformation causes non-zero torques, provoking on average a less aligned microstructure.

A second important consequence is the introduction of a characteristic relaxation time in the modelled system. According to Duggal and Pasquali (2006), an average relaxation time due to elastic deformation , τ_r^B , for an isolated semi-flexible rod in a viscous matrix can be calculated as:

$$\tau_r^B \approx 0.512 \frac{\eta_0 r^4}{E_Y \ln(r)} \tag{7.2}$$

For the MWCNT/epoxy combination used here, this relaxation time is about 0.27 s for the highest aspect ratio rods. Hence, elastic relaxation was difficult to observe experimentally in the dichroism relaxation behavior. Moreover, Brownian motion was found to dictate the relaxation time observed by dichroism, in good agreement with the predictions of the Doi and Edwards (1986) theory for rigid-rods.

It is important to underline that the elastic relaxation time, τ_r^B , grows fast as function of the aspect ratio. This characteristic time was used to explain the fast relaxation behavior observed by Pujari *et al.* (2011) using SAXS when characterizing non-Brownian MWCNT suspensions. They used rods with aspect ratio one order of magnitude larger than the one used in this work, and their characteristic time was ~70 s.

Direct observations of CNT suspensions is a very challenging task. One possibility is to perform curing of CNT/epoxy composites. However, heat curing provokes an initial reduction of the medium viscosity which causes re-aggregation and, hence, changes in the dispersion and orientation state of the system. Also, UV curing can produce local stresses which would influence the microstructural state. In any case, only static information can be obtained. In addition to this

experimental problem, it is not straightforward how to correlate TEM images with orientation tensors.

TEM was employed to verify the dispersion state of the system in concentrated regime. Only few micro-sized aggregates were found, while the majority of the rods were homogeneously dispersed in the matrix (Figure 5.8).

A more interesting technique is confocal microscopy. In comparison with optical microscopy, this has the advantage to collect light only from a thin layer of the sample which is selectively excited by a laser, guaranteeing higher definition images. For the combination of MWCNTs and epoxy used in this work, it was possible to use the confocal microscope in reflective mode without the need of any fluorescent dye and chemical or physical surface treatments. An example of the possible results achievable with this technique and more details on the instrumental setup are reported in Appendix B. Coupled with a shear platform, confocal microscopy could be used to obtain direct information on the orientation and structure evolution of CNT suspensions. However, the achievable range of shear rates is limited by the required scanning time and resolution, which are at the limit of this instrument for the MWCNTs employed here. Longer carbon nanotubes could be successfully used with this technique.

A similar problem was encountered by employing *in situ* small angle light scattering (SALS) in order to have structural information. A parallel disks geometry with quartz plates and a He-Ne laser with an emission wavelength of 632 nm were used. In dilute regime, the patterns obtained with the rheo-SALS Anton Paar apparatus appeared completely isotropic independently of the Pe number. The characteristic length scale of the system ($\sim 1/L$) was at the limit of the scattering vector range detectable with our apparatus. Furthermore, the range of concentration was limited at because of the high opacity of the samples. In dilute regime successful results could be obtained with longer carbon nanotubes.

In order to probe the structure evolution of suspensions in a more concentrated regime, bulk rheology was used to obtain indirect information. Increasing nanotube concentration, a network is developed in the system as a consequence of Brownian motion and attractive van der Waals interactions. By applying a steady shear flow, this network of rods is destroyed. Rod-rod

interactions and orientation control the evolution of the microstructure, and the steady-state shear viscosity presents a strong shear-thinning behavior.

The slope of the steady shear viscosity at low shear rates was found to decrease with increasing MWCNT concentration, moving towards the theoretical slope of -1 (Figure 5.9) [Folgar and Tucker (1984), Djalili-Moghaddam and Toll (2005), Férec *et al.* (2009)]. The apparent yield stress reported is also an indirect confirmation of the good dispersion achieved. Furthermore, the rheological measurements were conducted by using a cone-and-plate geometry, which guarantees a homogenous shear flow. Positive first normal stress differences, N_1, were also obtained in steady state. They increased monotonously with increasing shear rate. Many authors have reported negative N_1, which are caused by the formation of more complex agglomerate structure (helical banding) and inhomogeneity in the system.

In these more concentrated suspensions, rod-rod interactions were assumed controlling the rheological response of the system. In order to simplify the description, particles were considered as rigid-rods. The "test" rod orientation evolution was derived including the effect of the interacting neighbors. The interactions were simply modelled as a non-linear lubrication force.

The idea behind this choice was based on the assumption that during the interaction event, the particles feel locally a shear rate which is different from the macroscopic one. With this simple description, the strong shear-thinning behavior and first normal stress difference of MWCNT suspensions were correctly predicted. Four adjustable parameters were identified by fitting the rheological data for steady state.

To further test this description and to complete the rheological characterization of MWCNT suspensions, transient shear flows were used in order to characterize the non-linear rheological response of the system. A concentrated MWCNT suspension was used and a series of shear flow and rest steps were applied to the system.

Applying a constant shear flow, the shear stress presented a strong overshoot at very small strain (about 0.4). The deformation at which the system yielded was found to be independent of the shear rate applied and hence, the network breaking point is reached only when the system has been subjected to a sufficient deformation. The overshoots intensity grows with shear rate. During rest, Brownian motion and attractive van der Waals interactions bring the system towards an isotropic

state and the network is reformed. To monitor this evolution, stress growth experiments were performed after different rest time. The structural build up was confirmed by the increase in overshoot intensity with the imposed rest time (Figure 6.2).

When no rest time was allowed, no shear stress overshoot was encountered. However, the system rheology showed dependency on the flow directionality. By shearing in the same direction, steady-state values were immediately reached while by inverting the flow direction, the shear stress presented a pseudo plateau. This experimental finding is still puzzling. This peculiar evolution could be due to rods still unaligned after the first shear step.

Regarding rheological measurements, a comment on the use of a pre-shearing step needs to be made. Pre-shearing is often used in the rheology of structured fluids to erase mechanical history and start rheological tests from a more reproducible initial state. However, this step is only necessary when the system is non-Brownian. For the MWCNT/epoxy system used in this work pre-shearing was not used and actually avoided. When a MWCNT suspensions is loaded in the rheometer, the squeezing flow developed between the plates determines an initial microstructure which will influence the rheological response of the system. By applying a pre-shearing step, a certain orientation in the system is imposed. This guarantees more reproducible rheological data but the initial orientation state is difficult to determine. This becomes very important when an initial condition for the orientation distribution function is required for the modeling. Instead of applying a pre-shear step, a more correct choice is to let the system completely relax and reach an isotropic orientation state, thanks to the Brownian motion. This guarantees an orientation state consistent for all the tests and also free of unknown initial conditions to solve the orientation distribution evolution. The main drawback of this choice is the time required for the relaxation, which in the case of MWCNT/epoxy in the concentrated regime was larger than 1 h.

The model predictions were also tested against transient shear flow data. The model was able to overall predict the structure build up and capture the transient rheology of the MWCNT suspensions.

However, aspects like the overshoot widths and the evolution during rest were not perfectly predicted. These differences can be attributed to some of the modelling hypotheses. Polydispersity and particles flexibility could introduce longer relaxation time widening the shear stress

overshoots. Moreover, when the model predictions were optimized for the transient shear flows, the model under predicted the steady state viscosity for low shear rates values. More work is hence required in the analysis of the adjustable parameters and into the definition of their functional forms. Direct simulation could help to fill this gap.

The most interesting and innovative aspect of the proposed model regards the predicted microstructural state. During transient shear flow, the predicted orientation state of the system was disordered with low anisotropy. In steady state, the microstructure was found to be directly dependent on shear rate. At low shear rates, interactions were dominant and the rods were far from being aligned in the flow direction. Only at high shear rate, when the network of interactions was broken, the rods could finally orient. The experimental verification of this predicted scenario is still challenging and incomplete in the concentrated regime. Methods like small and wide angle x-ray scattering could eventually give more insights on these predictions.

CHAPTER 8 CONCLUSIONS AND RECOMMENDATIONS

In this thesis, the dynamics of carbon nanotube suspensions were characterized by rheological and optical techniques. The orientation evolution was experimentally linked to the rheological response by rheo-optical technique and by modeling. Summarizing, the main contributions of this research are:

1) Orientation dynamics of MWCNT suspensions were directly probed by a rheo-optical method in dilute and semi-dilute regimes under shear-flow and at rest. Dichroism and orientation angle were obtained as functions of the Peclet number. In the non-Brownian regime, the average orientation angle was found to saturate at high values (~18°). Direct information on the relaxation behavior of these suspensions was also obtained.

2) A new model for flexible particles in the dilute regime was developed. Particles are described with a modified two-rod model that allowed non-straight particle conformations at equilibrium. This enabled to explain the disordered system observed in dichroism.

3) Steady-state shear viscosity and first normal stress differences were investigated in shear flow using a cone-and-plate flow geometry. These suspensions presented a strong shear-thinning behavior. The apparent yield stress was found to be a function of concentration. This is coherent with the idea of a network being developed in the system. Also, positive N_1 were measured and explained as the result of network elasticity and rod-rod interactions.

4) A new rheological model for rigid-rods valid in different concentration regimes was developed. Interactions between rods were assumed to control the rheology of these suspensions and were described as a non-linear lubrication force. The predicted microstructure was shear dependent, in agreement with the rheology of colloidal suspensions and the shear-thinning phenomenon was well predicted.

5) Non-linear transient rheology of concentrated suspensions was investigated in simple shear flow. When a constant shear rate was applied, strong shear stress overshoots were found at low strain. The position of the overshoots was independent of the shear rate. The microstructure was found to be independent of flow directionality and it kept evolving

during rest due to Brownian motion. This structural build-up during rest was confirmed by the intensity of the overshoots that increased with the allowed rest time.

6) The mechanism of the structure evolution during shear flow and at rest was quantified by comparing the model predictions with the rheological response of the system. According to the model description, interactions were found to be dominant and the primary cause of the observed overshoots. A disordered orientation state was predicted.

Recommendations:

In order to complete the link between rheology and microstructural evolution, confocal microscopy is probably the most interesting avenue. The use of carbon nanotubes with an average length between 1-10 microns would allow to collect structural and orientation information. The main limitation of this technique is the time required to scan a section of interest in the sample. During flow, this limits the range of Pe accessible. One possibility to overcome this problem is to vary the medium viscosity and temperature in order to increase the range of Pe obtainable.

An important aspect that requires further investigation is the effect of polydispersity. Gel permeation/size exclusion columns could be used to obtain monodisperse samples. A comparison of the rheology of mono and poly dispersed samples could clarify the effect of this parameter on the dynamic of the system and, in particular, on the overshoot widths in transient shear flows. The effect of polydispersity should be also investigate in SAOS at low frequencies and in dilute regime; comparisons between the predictions of the proposed two-rod model and rheological data could give insights regarding the mild elasticity (low values of G') reported in the literature [Ma *et al.* (2008)].

It would be particularly interesting to study the evolution of the microstructure by X-ray diffraction, which would give access to information at the nanoscale and in more concentrated regimes. This would provide more precise insights on the local rearrangements, responsible for the thixotropic behavior of the system. Furthermore, a comparison between the microstructural information obtained by dichroism and SAXS would cover the microstructure evolution over a wide range of length scales.

As for the mathematical description, more work is required to introduce interactions in the suggested two-rod description. This could overcome the difficulty that the linear or non-linear

lubrication interactions are a purely viscous type of interactions. The coupling between interactions and bending elasticity would results in an interesting relaxation behavior. Anisotropy in the system could be generated even during rest.

The lubricated interaction chosen depends directly on the macroscopic shear rate. This suggests that in absence of flow, the rods are free and do not “see” each other. It would be interesting to couple Brownian motion with lubricated interactions. A relaxation time which directly depends on the orientation state of the system and concentration could be obtained.

Another open question regards the contact probability used. This is valid only for long and thin rods at equilibrium. A very challenging task would be to determine a contact probability accounting for the effect of shear flow.

BIBLIOGRAPHY

Abbasi S., P. Carreau, A. Derdouri and M. Moan, "Rheological properties and percolation in suspensions of multiwalled carbon nanotubes in polycarbonate," Rheologica Acta **48**, 943-959 (2009a).

Abbasi S., P. J. Carreau, A. Derdouri and M. Moan, "Rheological properties and percolation in suspensions of multiwalled carbon nanotubes in polycarbonate," Rheologica acta **48**, 943-959 (2009b).

Abdel-Goad M. and P. Pötschke, "Rheological characterization of melt processed polycarbonate-multiwalled carbon nanotube composites," Journal of Non-Newtonian Fluid Mechanics **128**, 2-6 (2005).

Abisset-Chavanne E., R. Mezher, S. Le Corre, A. Ammar and F. Chinesta, "Kinetic theory microstructure modeling in concentrated suspensions," Entropy **15**, 2805-2832 (2013).

Advani S. G. and C. L. Tucker, "Closure approximations for three-dimensional structure tensors," Journal of Rheology **34**, 367-386 (1990).

Advani S. G. and C. L. Tucker, "The use of tensors to describe and predict fiber orientation in short fiber composites," Journal of Rheology **31**, 751-784 (1987).

Advani S. G. and C. L. Tucker III, "Closure approximations for three-dimensional structure tensors," Journal of Rheology **34**, 367-386 (1990).

Allen R., G. G. Fuller and Z. Bao, "Aligned SWNT Films from Low-Yield Stress Gels and Their Transparent Electrode Performance," ACS applied materials & interfaces **5**, 7244-7252 (2013).

Ammar A., B. Mokdad, F. Chinesta and R. Keunings, "A new family of solvers for some classes of multidimensional partial differential equations encountered in kinetic theory modeling of complex fluids," Journal of Non-Newtonian Fluid Mechanics **139**, 153-176 (2006).

Ammar A., B. Mokdad, F. Chinesta and R. Keunings, "A new family of solvers for some classes of multidimensional partial differential equations encountered in kinetic theory modelling of complex fluids: Part II: Transient simulation using space-time separated representations," Journal of Non-Newtonian Fluid Mechanics **144**, 98-121 (2007).

Ávila-Orta C. A., V. J. Cruz-Delgado, M. G. Neira-Velázquez, E. Hernández-Hernández, M. G. Méndez-Padilla and F. J. Medellín-Rodríguez, "Surface modification of carbon nanotubes with ethylene glycol plasma," Carbon **47**, 1916-1921 (2009).

Badaire S., C. Zakri, M. Maugey, A. Derré, J. N. Barisci, G. Wallace and P. Poulin, "Liquid Crystals of DNA-Stabilized Carbon Nanotubes," Advanced Materials **17**, 1673-1676 (2005).

Batchelor G. K., "Slender-body theory for particles of arbitrary cross-section in Stokes flow," Journal of Fluid Mechanics **44**, 419-440 (1970).

Batchelor G. K., "The stress generated in a non-dilute suspension of elongated particles by pure straining motion," Journal of Fluid Mechanics **46**, 813-829 (1971).

Baughman R. H., A. A. Zakhidov and W. A. de Heer, "Carbon nanotubes--the route toward applications," Science **297**, 787-792 (2002).

Bay R. S., "Fiber orientation in injection-molded composites: A comparison of theory and experiment," Ph.D. dissertation, University of Illinois at Urbana-Champaign, Illinois, United States, 1991.

Bellini T., F. Mantegazza, R. Piazza and V. Degiorgio, "Stretched-exponential relaxation of electric birefringence in a polydisperse colloidal solution," EPL (Europhysics Letters) **10**, 499 (1989).

Bhattacharyya A. R., T. V. Sreekumar, T. Liu, S. Kumar, L. M. Ericson, R. H. Hauge and R. E. Smalley, "Crystallization and orientation studies in polypropylene/single wall carbon nanotube composite," Polymer **44**, 2373-2377 (2003).

Bird R. B., C. F. Curtiss, R. C. Armstrong and O. Hassager, *Dynamics of polymeric liquids. Volume 2, Kinetic theory* (Wiley, New York, 1987).

Brenner H., "Rheology of a dilute suspension of axisymmetric Brownian particles," International Journal of Multiphase Flow **1**, 195-341 (1974).

Bretherton F. P., "The motion of rigid particles in a shear flow at low Reynolds number," Journal of Fluid Mechanics **14**, 284-304 (1962).

Bulacu M., N. Goga, W. Zhao, G. Rossi, L. Monticelli, X. Periole, D. P. Tieleman and S. J. Marrink, "Improved Angle Potentials for Coarse-Grained Molecular Dynamics Simulations," Journal of Chemical Theory and Computation **9**, 3282-3292 (2013).

Carreau P. J., D. De Kee and R. P. Chhabra, *Rheology of polymeric systems: Principles and applications* (Hanser, Munich, 1997).

Chinesta F., "From Single-Scale to Two-Scales Kinetic Theory Descriptions of Rods Suspensions," Archives of Computational Methods in Engineering **20**, 1-29 (2013).

Chow A. W., G. G. Fuller, D. G. Wallace and J. A. Madri, "Rheooptical response of rodlike chains subject to transient shear flow. 2. Two-color flow birefringence measurements on collagen protein," Macromolecules **18**, 793-804 (1985a).

Chow A. W., G. G. Fuller, D. G. Wallace and J. A. Madri, "Rheooptical response of rodlike, shortened collagen protein to transient shear flow," Macromolecules **18**, 805-810 (1985b).

Chung D. H. and T. H. Kwon, "Improved model of orthotropic closure approximation for flow induced fiber orientation," Polymer Composites **22**, 636-649 (2001).

Cintra J. J. S. and C. L. Tucker, "Orthotropic closure approximations for flow-induced fiber orientation," Journal of Rheology **39**, 1095-1122 (1995).

Cintra J. J. S. and C. L. Tucker III, "Orthotropic closure approximations for flow-induced fiber orientation," Journal of Rheology **39**, 1095-1122 (1995).

Cruz C., L. Illoul, F. Chinesta and G. Régnier, "Shear-strain step response in linear regime of dilute suspensions of naturally bent carbon nanotubes," Journal of Applied Polymer Science **125**, 4347-4357 (2012).

Davis V. A., L. M. Ericson, A. N. G. Parra-Vasquez, H. Fan, Y. Wang, V. Prieto, J. A. Longoria, S. Ramesh, R. K. Saini, C. Kittrell, W. E. Billups, W. W. Adams, R. H. Hauge, R. E. Smalley and M. Pasquali, "Phase Behavior and Rheology of SWNTs in Superacids," Macromolecules **37**, 154-160 (2003).

Dhont J. K. G. and W. J. Briels, "Inhomogeneous suspensions of rigid rods in flow," The Journal of Chemical Physics **118**, 1466-1478 (2003a).

Dhont J. K. G. and W. J. Briels, "Viscoelasticity of suspensions of long, rigid rods," Colloids and Surfaces A: Physicochemical and Engineering Aspects **213**, 131-156 (2003b).

Dinh S. M. and R. C. Armstrong, "A rheological equation of state for semiconcentrated fiber suspensions," Journal of Rheology **28**, 207-227 (1984).

Djalili-Moghaddam M. and S. Toll, "A model for short-range interactions in fibre suspensions," Journal of Non-Newtonian Fluid Mechanics **132**, 73-83 (2005).

Doi M. and S. F. Edwards, "Dynamics of rod-like macromolecules in concentrated solution. Part 1," J. Chem. Soc., Faraday Trans. 2 **74**, 560-570 (1978a).

Doi M. and S. F. Edwards, "Dynamics of rod-like macromolecules in concentrated solution. Part 2," Journal of the Chemical Society, Faraday Transactions 2: Molecular and Chemical Physics **74**, 918-932 (1978b).

Doi M. and S. F. Edwards, "The theory of polymer dynamics," Clarendon, Oxford (1986).

Du F., J. E. Fischer and K. I. Winey, "Effect of nanotube alignment on percolation conductivity in carbon nanotube/polymer composites," Physical Review B **72**, 121404 (2005).

Du F., R. C. Scogna, W. Zhou, S. Brand, J. E. Fischer and K. I. Winey, "Nanotube Networks in Polymer Nanocomposites: Rheology and Electrical Conductivity," Macromolecules **37**, 9048-9055 (2004).

Duggal R. and M. Pasquali, "Dynamics of Individual Single-Walled Carbon Nanotubes in Water by Real-Time Visualization," Physical Review Letters **96**, 246104 (2006).

Ericksen J. L., "Transversely isotropic fluids," Kolloid-Zeitschrift **173**, 117-122 (1960).

Eslami H. and M. Grmela, "Mesoscopic formulation of reptation," Rheologica Acta **47**, 399-415 (2008).

Eslami H., M. Grmela and M. Bousmina, "Linear and nonlinear rheology of polymer/layered silicate nanocomposites," Journal of Rheology **54**, 539-562 (2010).

Eslami H., M. Grmela and M. Bousmina, "A mesoscopic rheological model of polymer/layered silicate nanocomposites," Journal of Rheology **51**, 1189-1222 (2007).

Eslami H., M. Grmela and M. Bousmina, "A mesoscopic tube model of polymer/layered silicate nanocomposites," Rheologica acta **48**, 317-331 (2009).

Esumi K., M. Ishigami, A. Nakajima, K. Sawada and H. Honda, "Chemical treatment of carbon nanotubes," Carbon **34**, 279-281 (1996).

Fan Z. and S. G. Advani, "Characterization of orientation state of carbon nanotubes in shear flow," Polymer **46**, 5232-5240 (2005).

Fan Z. and S. G. Advani, "Rheology of multiwall carbon nanotube suspensions," Journal of Rheology **51**, 585-604 (2007).

Faraoni V., M. Grosso, S. Crescitelli and P. L. Maffettone, "The rigid-rod model for nematic polymers: An analysis of the shear flow problem," Journal of Rheology **43**, 829-843 (1999).

Férec J., E. Abisset-Chavanne, G. Ausias and F. Chinesta, "On the use of interaction tensors to describe and predict rod interactions in rod suspensions," Rheologica Acta **53**, 445-456 (2014).

Férec J., G. Ausias, M. C. Heuzey and P. J. Carreau, "Modeling fiber interactions in semiconcentrated fiber suspensions," Journal of Rheology **53**, 49-72 (2009).

Férec J., M. Heniche, M. C. Heuzey, G. Ausias and P. J. Carreau, "Numerical solution of the Fokker–Planck equation for fiber suspensions: Application to the Folgar–Tucker–Lipscomb model," Journal of Non-Newtonian Fluid Mechanics **155**, 20-29 (2008).

Férec J., A. Perrot and G. Ausias, "Toward modeling anisotropic yield stress and consistency induced by fiber in fiber-reinforced viscoplastic fluids," Journal of Non-Newtonian Fluid Mechanics **220**, 69-76 (2015).

Folgar F. P. and C. L. Tucker, "Orientation behavior of fibers in concentrated suspensions," J. Reinf. Plast. Compos. **3**, 99-119 (1984).

Frattini P. L. and G. G. Fuller, "The dynamics of dilute colloidal suspensions subject to time-dependent flow fields by conservative dichroism," Journal of Colloid and Interface Science **100**, 506-518 (1984).

Fry D., B. Langhorst, H. Wang, M. L. Becker, B. J. Bauer, E. A. Grulke and E. K. Hobbie, "Rheo-optical studies of carbon nanotube suspensions," The Journal of Chemical Physics **124**, 054703 (2006).

Fuller G. G., *Optical rheometry of complex fluids* (Oxford University Press, 1995).

Fuller G. G. and K. J. Mikkelsen, "Note: Optical Rheometry Using a Rotary Polarization Modulator," Journal of Rheology **33**, 761-769 (1989).

Ghosh T., M. Grmela and P. J. Carreau, "Rheology of short fiber filled thermoplastics," Polymer Composites **16**, 144-153 (1995).

Gibson A. G. and S. Toll, "Mechanics of the squeeze flow of planar fibre suspensions," Journal of Non-Newtonian Fluid Mechanics **82**, 1-24 (1999).

Goto S., H. Nagazono and H. Kato, "The flow behavior of fiber suspensions in Newtonian fluids and polymer solutions," Rheologica Acta **25**, 246-256 (1986).

Grmela M., "Bracket formulation of diffusion-convection equations," Physica D: Nonlinear Phenomena **21**, 179-212 (1986).

Grmela M. and P. J. Carreau, "Conformation tensor rheological models," Journal of Non-Newtonian Fluid Mechanics **23**, 271-294 (1987).

Guiraud O., L. Orgeas, P. J. J. Dumont and S. R. d. Roscoat, "Microstructure and deformation micromechanisms of concentrated fiber bundle suspensions: An analysis combining x-ray microtomography and pull-out tests," Journal of Rheology **56**, 593-623 (2012).

Gupta A. and V. Choudhary, "Electromagnetic interference shielding behavior of poly(trimethylene terephthalate)/multi-walled carbon nanotube composites," Composites Science and Technology **71**, 1563-1568 (2011).

Han K.-H. and Y.-T. Im, "Modified hybrid closure approximation for prediction of flow-induced fiber orientation," Journal of Rheology **43**, 569-589 (1999).

Hinch E. and L. Leal, "The effect of Brownian motion on the rheological properties of a suspension of non-spherical particles," Journal of Fluid Mechanics **52**, 683-712 (1972).

Hinch E. and L. Leal, "Time-dependent shear flows of a suspension of particles with weak Brownian rotations," Journal of Fluid Mechanics **57**, 753-767 (1973).

Hobbie E., "Shear rheology of carbon nanotube suspensions," Rheologica Acta **49**, 323-334 (2010).

Hobbie E. K., "Optical anisotropy of nanotube suspensions," The Journal of Chemical Physics **121**, 1029-1037 (2004).

Hobbie E. K. and D. J. Fry, "Nonequilibrium Phase Diagram of Sticky Nanotube Suspensions," Physical Review Letters **97**, 036101 (2006).

Hobbie E. K. and D. J. Fry, "Rheology of concentrated carbon nanotube suspensions," The Journal of Chemical Physics **126**, 124907-7 (2007).

Hobbie E. K., H. Wang, H. Kim, S. Lin-Gibson and E. A. Grulke, "Orientation of carbon nanotubes in a sheared polymer melt," Physics of Fluids **15**, 1196-1202 (2003).

Hough L. A., M. F. Islam, P. A. Janmey and A. G. Yodh, "Viscoelasticity of Single Wall Carbon Nanotube Suspensions," Physical Review Letters **93**, 168102 (2004).

Hu G., C. Zhao, S. Zhang, M. Yang and Z. Wang, "Low percolation thresholds of electrical conductivity and rheology in poly(ethylene terephthalate) through the networks of multi-walled carbon nanotubes," Polymer **47**, 480-488 (2006).

Huang Y. Y., S. V. Ahir and E. M. Terentjev, "Dispersion rheology of carbon nanotubes in a polymer matrix," Physical Review B **73**, 125422 (2006).

Iijima S. and T. Ichihashi, "Single-shell carbon nanotubes of 1-nm diameter," (1993).

Jeffery G. B., "The motion of ellipsoidal particles immersed in a viscous fluid," Proceedings of the Royal Society of London Serie A **102**, 161-179 (1922).

Jin L., C. Bower and O. Zhou, "Alignment of carbon nanotubes in a polymer matrix by mechanical stretching," Applied Physics Letters **73**, 1197-1199 (1998).

Johnston D. C., "Stretched exponential relaxation arising from a continuous sum of exponential decays," Physical Review B **74**, 184430 (2006).

Keshtkar M., M.-C. Heuzey, P. J. Carreau, M. Rajabian and C. Dubois, "Rheological properties and microstructural evolution of semi-flexible fiber suspensions under shear flow," Journal of Rheology **54**, 197-222 (2010).

Khalkhal F., "Characterization of flow-induced structures in carbon nanotube suspensions," Ecole Polytechnique, Montreal, 2012.

Khalkhal F. and P. J. Carreau, "Critical shear rates and structure build-up at rest in MWCNT suspensions," Journal of Non-Newtonian Fluid Mechanics **171–172**, 56-66 (2012).

Khalkhal F., P. J. Carreau and G. Ausias, "Effect of flow history on linear viscoelastic properties and the evolution of the structure of multiwalled carbon nanotube suspensions in an epoxy," Journal of Rheology **55**, 153-175 (2011).

Kim K. S., D. J. Bae, J. R. Kim, K. A. Park, S. C. Lim, J. J. Kim, W. B. Choi, C. Y. Park and Y. H. Lee, "Modification of Electronic Structures of a Carbon Nanotube by Hydrogen Functionalization," Advanced Materials **14**, 1818-1821 (2002).

Kim S. and S. J. Karrila, *Microdynamics: Principles and selected applications* (Butterworth - Heinemann, Boston, 1991).

Koch D. L., "A model for orientational diffusion in fiber suspensions," Physics of Fluids **7**, 2086-2088 (1995).

Kuzuu N. and M. Doi, "Constitutive equation for nematic liquid crystals under weak velocity gradient derived from a molecular kinetic equation," Journal of the Physical Society of Japan **52**, 3486-3494 (1983).

Larson R. G., "Arrested tumbling in shearing flows of liquid-crystal polymers," Macromolecules **23**, 3983-3992 (1990).

Larson R. G., "Constitutive equations for thixotropic fluids," Journal of Rheology (1978-present) **59**, 595-611 (2015).

Larson R. G., "The Structure and Rheology of Complex fluids," Journal (1999).

Larson R. G. and H. C. Ottinger, "Effect of molecular elasticity on out-of-plane orientations in shearing flows of liquid-crystalline polymers," Macromolecules **24**, 6270-6282 (1991).

Le Corre S., D. Caillerie, L. Orgéas and D. Favier, "Behavior of a net of fibers linked by viscous interactions: theory and mechanical properties," Journal of the Mechanics and Physics of Solids **52**, 395-421 (2004).

Le Corre S., P. Dumont, L. Orgeas and D. Favier, "Rheology of highly concentrated planar fiber suspensions," Journal of Rheology **49**, 1029-1058 (2005).

Lee H. W., W. You, S. Barman, S. Hellstrom, M. C. LeMieux, J. H. Oh, S. Liu, T. Fujiwara, W. M. Wang, B. Chen, Y. W. Jin, J. M. Kim and Z. Bao, "Lyotropic Liquid-Crystalline Solutions of High-Concentration Dispersions of Single-Walled Carbon Nanotubes with Conjugated Polymers," Small **5**, 1019-1024 (2009).

Lee S. H., E. Cho, S. H. Jeon and J. R. Youn, "Rheological and electrical properties of polypropylene composites containing functionalized multi-walled carbon nanotubes and compatibilizers," Carbon **45**, 2810-2822 (2007).

Lenstra T. A. J., Z. Dogic and J. K. G. Dhont, "Shear-induced displacement of isotropic-nematic spinodals," The Journal of Chemical Physics **114**, 10151-10162 (2001).

Lin-Gibson S., J. A. Pathak, E. A. Grulke, H. Wang and E. K. Hobbie, "Elastic flow instability in nanotube suspensions," Physical Review Letters **92**, 048302 (2004).

Lipscomb G., M. Denn, D. Hur and D. Boger, "The flow of fiber suspensions in complex geometries," Journal of Non-Newtonian Fluid Mechanics **26**, 297-325 (1988).

Ma A., M. Mackley and S. Rahatekar, "Experimental observation on the flow-induced assembly of Carbon nanotube suspensions to form helical bands," Rheologica Acta **46**, 979-987 (2007).

Ma P.-C., N. A. Siddiqui, G. Marom and J.-K. Kim, "Dispersion and functionalization of carbon nanotubes for polymer-based nanocomposites: A review," Composites Part A: Applied Science and Manufacturing **41**, 1345-1367 (2010).

Ma W. K. A., F. Chinesta, A. Ammar and M. R. Mackley, "Rheological modeling of carbon nanotube aggregate suspensions," Journal of Rheology **52**, 1311-1330 (2008).

Mackaplow M. B. and E. S. Shaqfeh, "A numerical study of the rheological properties of suspensions of rigid, non-Brownian fibres," Journal of Fluid Mechanics **329**, 155-186 (1996).

Marrucci G. and N. Grizzuti, "The effect of polydispersity on rotational diffusivity and shear viscosity of rodlike polymers in concentrated solutions," Journal of Polymer Science: Polymer Letters Edition **21**, 83-86 (1983).

Meincke O., D. Kaempfer, H. Weickmann, C. Friedrich, M. Vathauer and H. Warth, "Mechanical properties and electrical conductivity of carbon-nanotube filled polyamide-6 and its blends with acrylonitrile/butadiene/styrene," Polymer **45**, 739-748 (2004).

Mickelson E. T., C. B. Huffman, A. G. Rinzler, R. E. Smalley, R. H. Hauge and J. L. Margrave, "Fluorination of single-wall carbon nanotubes," Chemical Physics Letters **296**, 188-194 (1998).

Mobuchon C., P. J. Carreau and M.-C. Heuzey, "Structural analysis of non-aqueous layered silicate suspensions subjected to shear flow," Journal of Rheology **53**, 1025-1048 (2009a).

Mobuchon C., P. J. Carreau and M.-C. Heuzey, "Structural analysis of non-aqueous layered silicate suspensions subjected to shear flow," Journal of Rheology **53**, 1025-1048 (2009b).

Natale G., M. C. Heuzey, P. J. Carreau, G. Ausias and J. Férec, "Rheological modeling of carbon nanotube suspensions with rod–rod interactions," AIChE Journal **60**, 1476-1487 (2014).

Natale G., N. K. Reddy, G. Ausias, J. Férec, M. C. Heuzey and P. J. Carreau, "Rheo-optical response of carbon nanotube suspensions," Journal of Rheology **59**, 499-524 (2015).

Niu R., J. Gong, D. Xu, T. Tang and Z.-Y. Sun, "Flow-induced structure and rheological properties of multiwall carbon nanotube/polydimethylsiloxane composites," RSC Advances **4**, 62759-62768 (2014).

Olowojoba G., S. Sathyanarayana, B. Caglar, B. Kiss-Pataki, I. Mikonsaari, C. Hübner and P. Elsner, "Influence of process parameters on the morphology, rheological and dielectric

properties of three-roll-milled multiwalled carbon nanotube/epoxy suspensions," Polymer **54**, 188-198 (2013).

Onuki A. and M. Doi, "Flow birefringence and dichroism of polymers. I. General theory and application to the dilute case," The Journal of Chemical Physics **85**, 1190-1197 (1986).

Ortman K., D. Baird, P. Wapperom and A. Whittington, "Using startup of steady shear flow in a sliding plate rheometer to determine material parameters for the purpose of predicting long fiber orientation," Journal of Rheology (1978-present) **56**, 955-981 (2012).

Petrich M. P., D. L. Koch and C. Cohen, "An experimental determination of the stress-microstructure relationship in semi-concentrated fiber suspensions," Journal of Non-Newtonian Fluid Mechanics **95**, 101-133 (2000).

Phan-Thien N., X. J. Fan, R. I. Tanner and R. Zheng, "Folgar-Tucker constant for a fibre suspension in a Newtonian fluid," Journal of Non-Newtonian Fluid Mechanics **103**, 251-260 (2002).

Phelps J. H. and C. L. Tucker, "An anisotropic rotary diffusion model for fiber orientation in short- and long-fiber thermoplastics," Journal of Non-Newtonian Fluid Mechanics **156**, 165-176 (2009).

Pötschke P., M. Abdel-Goad, I. Alig, S. Dudkin and D. Lellinger, "Rheological and dielectrical characterization of melt mixed polycarbonate-multiwalled carbon nanotube composites," Polymer **45**, 8863-8870 (2004).

Prashantha K., J. Soulestin, M. F. Lacrampe, P. Krawczak, G. Dupin and M. Claes, "Masterbatch-based multi-walled carbon nanotube filled polypropylene nanocomposites: Assessment of rheological and mechanical properties," Composites Science and Technology **69**, 1756-1763 (2009).

Pujari S., S. Rahatekar, J. W. Gilman, K. K. Koziol, A. H. Windle and W. R. Burghardt, "Shear-induced anisotropy of concentrated multiwalled carbon nanotube suspensions using x-ray scattering," Journal of Rheology **55**, 1033-1058 (2011).

Pujari S., S. S. Rahatekar, J. W. Gilman, K. K. Koziol, A. H. Windle and W. R. Burghardt, "Orientation dynamics in multiwalled carbon nanotube dispersions under shear flow," The Journal of Chemical Physics **130**, 214903 (2009a).

Pujari S., S. S. Rahatekar, J. W. Gilman, K. K. Koziol, A. H. Windle and W. R. Burghardt, "Orientation dynamics in multiwalled carbon nanotube dispersions under shear flow," The Journal of Chemical Physics **130**, - (2009b).

Qian D., G. J. Wagner, W. K. Liu, M.-F. Yu and R. S. Ruoff, "Mechanics of carbon nanotubes," Applied Mechanics Reviews **55**, 495-533 (2002).

Rahatekar S. S., K. K. K. Koziol, S. A. Butler, J. A. Elliott, M. S. P. Shaffer, M. R. Mackley and A. H. Windle, "Optical microstructure and viscosity enhancement for an epoxy resin matrix containing multiwall carbon nanotubes," Journal of Rheology (1978-present) **50**, 599-610 (2006a).

Rahatekar S. S., K. K. K. Koziol, S. A. Butler, J. A. Elliott, M. S. P. Shaffer, M. R. Mackley and A. H. Windle, "Optical microstructure and viscosity enhancement for an epoxy resin matrix containing multiwall carbon nanotubes," Journal of Rheology **50**, 599-610 (2006b).

Rahatekar S. S., A. Rasheed, R. Jain, M. Zammarano, K. K. Koziol, A. H. Windle, J. W. Gilman and S. Kumar, "Solution spinning of cellulose carbon nanotube composites using room temperature ionic liquids," Polymer **50**, 4577-4583 (2009).

Rajabian M., C. Dubois and M. Grmela, "Suspensions of Semiflexible Fibers in Polymeric Fluids: Rheology and Thermodynamics," Rheologica Acta **44**, 521-535 (2005).

Rajabian M., C. Dubois, M. Grmela and P. Carreau, "Effects of polymer–fiber interactions on rheology and flow behavior of suspensions of semi-flexible fibers in polymeric liquids," Rheologica Acta **47**, 701-717 (2008).

Ranganathan S. and S. G. Advani, "Fiber-fiber interactions in homogeneous flows of nondilute suspensions," Journal of Rheology **35**, 1499-1522 (1991).

Sandstrom C. R., "Interactions and orientation in concentrated suspensions of rigid rods: theory and experiment," Ph.D. thesis, University of Illinois, Urbana-Champaign, 1993.

Sandstrom C. R. and C. L. Tucker, "A theory for concentrated fiber suspensions with strong fiber-fiber interactions," Makromolekulare Chemie-Macromolecular Symposia **68**, 291-300 (1993).

Schulz S. C., G. Faiella, S. T. Buschhorn, L. A. S. A. Prado, M. Giordano, K. Schulte and W. Bauhofer, "Combined electrical and rheological properties of shear induced multiwall carbon nanotube agglomerates in epoxy suspensions," European Polymer Journal **47**, 2069-2077 (2011).

Sepehr M., G. Ausias and P. J. Carreau, "Rheological properties of short fiber filled polypropylene in transient shear flow," Journal of Non-Newtonian Fluid Mechanics **123**, 19-32 (2004a).

Sepehr M., P. J. Carreau, M. Moan and G. Ausias, "Rheological properties of short fiber model suspensions," Journal of Rheology **48**, 1023-1048 (2004b).

Servais C., A. Luciani and J.-A. E. Manson, "Fiber--fiber interaction in concentrated suspensions: Dispersed fiber bundles," Journal of Rheology **43**, 1005-1018 (1999a).

Servais C., J.-A. E. Manson and S. Toll, "Fiber--fiber interaction in concentrated suspensions: Disperse fibers," Journal of Rheology **43**, 991-1004 (1999b).

Sham M.-L. and J.-K. Kim, "Surface functionalities of multi-wall carbon nanotubes after UV/Ozone and TETA treatments," Carbon **44**, 768-777 (2006).

Shaqfeh E. S. G. and G. H. Fredrickson, "The hydrodynamic stress in a suspension of rods," Physics of Fluids a-Fluid Dynamics **2**, 7-24 (1990).

Song Y. S. and J. R. Youn, "Influence of dispersion states of carbon nanotubes on physical properties of epoxy nanocomposites," Carbon **43**, 1378-1385 (2005).

Souloumiac B. and M. Vincent, "Steady shear viscosity of short fibre suspensions in thermoplastics," Rheologica Acta **37**, 289-298 (1998).

Stevens J. L., A. Y. Huang, H. Peng, I. W. Chiang, V. N. Khabashesku and J. L. Margrave, "Sidewall Amino-Functionalization of Single-Walled Carbon Nanotubes through Fluorination and Subsequent Reactions with Terminal Diamines," Nano Letters **3**, 331-336 (2003).

Strand S. R., S. Kim and S. J. Karrila, "Computation of rheological properties of suspensions of rigid rods: stress growth after inception of steady shear flow," Journal of Non-Newtonian Fluid Mechanics **24**, 311-329 (1987).

Strautins U. and A. Latz, "Flow-driven orientation dynamics of semiflexible fiber systems," Rheologica Acta **46**, 1057-1064 (2007).

Sundararajakumar R. R. and D. L. Koch, "Structure and properties of sheared fiber suspensions with mechanical contacts," Journal of Non-Newtonian Fluid Mechanics **73**, 205-239 (1997).

Switzer III L. H. and D. J. Klingenberg, "Rheology of sheared flexible fiber suspensions via fiber-level simulations," Journal of Rheology **47**, 759-778 (2003).

Tagmatarchis N. and M. Prato, "Functionalization of carbon nanotubes via 1,3-dipolar cycloadditions," Journal of Materials Chemistry **14**, 437-439 (2004).

Thostenson E. T. and T.-W. Chou, "Aligned multi-walled carbon nanotube-reinforced composites: processing and mechanical characterization," Journal of physics D: Applied physics **35**, L77 (2002).

Thostenson E. T., Z. Ren and T.-W. Chou, "Advances in the science and technology of carbon nanotubes and their composites: a review," Composites science and technology **61**, 1899-1912 (2001).

Touhara H., J. Inahara, T. Mizuno, Y. Yokoyama, S. Okanao, K. Yanagiuch, I. Mukopadhyay, S. Kawasaki, F. Okino, H. Shirai, W. H. Xu, T. Kyotani and A. Tomita, "Property control of new forms of carbon materials by fluorination," Journal of Fluorine Chemistry **114**, 181-188 (2002).

Unger E., A. Graham, F. Kreupl, M. Liebau and W. Hoenlein, "Electrochemical functionalization of multi-walled carbon nanotubes for solvation and purification," Current Applied Physics **2**, 107-111 (2002).

Vaccaro A. and G. Marrucci, "A model for the nonlinear rheology of associating polymers," Journal of Non-Newtonian Fluid Mechanics **92**, 261-273 (2000).

Vermant J. and M. Solomon, "Flow-induced structure in colloidal suspensions," Journal of Physics: Condensed Matter **17**, R187 (2005).

Versteeg H. K. and W. Malalasekera, *An Introduction to Computational Fluid Dynamics: The Finite Volume Method* (Pearson Prentice Hall, Harlow, Toronto, 1995).

Wang D., P. Song, C. Liu, W. Wu and S. Fan, "Highly oriented carbon nanotube papers made of aligned carbon nanotubes," Nanotechnology **19**, 075609 (2008).

Wang S. C., K. S. Chang and C. J. Yuan, "Enhancement of electrochemical properties of screen-printed carbon electrodes by oxygen plasma treatment," Electrochimica Acta **54**, 4937-4943 (2009).

Wenseleers W., I. I. Vlasov, E. Goovaerts, E. D. Obraztsova, A. S. Lobach and A. Bouwen, "Efficient Isolation and Solubilization of Pristine Single-Walled Nanotubes in Bile Salt Micelles," Advanced Functional Materials **14**, 1105-1112 (2004).

Wu D., L. Wu and M. Zhang, "Rheology of multi-walled carbon nanotube/poly(butylene terephthalate) composites," Journal of Polymer Science Part B: Polymer Physics **45**, 2239-2251 (2007).

Yamanoi M., C. Leer, F. W. J. van Hattum, O. S. Carneiro and J. M. Maia, "Direct fibre simulation of carbon nanofibres suspensions in a Newtonian fluid under simple shear," Journal of Colloid and Interface Science **347**, 183-191 (2010).

Zhou W., M. F. Islam, H. Wang, D. L. Ho, A. G. Yodh, K. I. Winey and J. E. Fischer, "Small angle neutron scattering from single-wall carbon nanotube suspensions: evidence for isolated rigid rods and rod networks," Chemical Physics Letters **384**, 185-189 (2004a).

Zhou W., J. Vavro, C. Guthy, K. I. Winey, J. E. Fischer, L. M. Ericson, S. Ramesh, R. Saini, V. A. Davis, C. Kittrell, M. Pasquali, R. H. Hauge and R. E. Smalley, "Single wall carbon nanotube fibers extruded from super-acid suspensions: Preferred orientation, electrical, and thermal transport," Journal of Applied Physics **95**, 649-655 (2004b).

APPENDIX A – COEFFICIENT NUMERICAL DISCRETIZATION

In this appendix, we report the expressions for the coefficients a_E, a_W, a_N, a_S a_M and a_P used in the finite volume method described in section 2.2.11 for different spatial discretization. Following Férec *et al.* (2008), we have for the central scheme

$$\begin{aligned} a_E &= D_e - \frac{F_e}{2} \\ a_W &= D_w + \frac{F_w}{2} \\ a_N &= D_n - \frac{F_n}{2} \\ a_S &= D_s + \frac{F_s}{2} \end{aligned} \tag{A.1}$$

For Upwind differencing scheme, we have

$$\begin{aligned} a_E &= D_e + \max\left[0, -F_e\right] \\ a_W &= D_w + \max\left[0, F_w\right] \\ a_N &= D_n + \max\left[0, -F_n\right] \\ a_S &= D_s + \max\left[0, F_s\right] \end{aligned} \tag{A.2}$$

For Hybrid differencing scheme, we have

$$\begin{aligned} a_E &= \max\left[0, -F_e, \left(D_e - F_e/2\right)\right] \\ a_W &= \max\left[0, F_w, \left(D_w + F_w/2\right)\right] \\ a_N &= \max\left[0, -F_n, \left(D_n - F_n/2\right)\right] \\ a_S &= \max\left[0, F_s, \left(D_s + F_s/2\right)\right] \end{aligned} \tag{A.3}$$

For the power-law scheme, the coefficients a_E, a_W, a_N and a_S are defined as

$$
\begin{aligned}
a_E &= D_e \max\left[0,\left(1-0.1\left|Pe_e\right|\right)^5\right] + \max\left[-F_e,0\right] \\
a_W &= D_w \max\left[0,\left(1-0.1\left|Pe_w\right|\right)^5\right] + \max\left[F_w,0\right] \\
a_N &= D_n \max\left[0,\left(1-0.1\left|Pe_n\right|\right)^5\right] \max\left[-F_n,0\right] \\
a_S &= D_s \max\left[0,\left(1-0.1\left|Pe_s\right|\right)^5\right] + \max\left[F_s,0\right]
\end{aligned}
\tag{A.4}
$$

For all the schemes, the coefficients a_M and a_P and the fluxes are

$$
\begin{aligned}
a_M &= \frac{\sin\left(\theta_P\right)\Delta\theta\Delta\varphi}{\Delta t} \\
a_P &= a_E + a_W + a_N + a_S + F_e - F_w + F_n - F_s \\
D_e &= D_r \sin\left(\theta_e\right)\frac{\Delta\varphi}{\Delta\theta} \\
D_w &= D_r \sin\left(\theta_w\right)\frac{\Delta\varphi}{\Delta\theta} \\
D_n &= D_r \frac{\Delta\theta}{\sin\left(\theta_P\right)\Delta\varphi} \\
D_s &= D_r \frac{\Delta\theta}{\sin\left(\theta_P\right)\Delta\varphi} \\
F_e &= \dot{\theta}_e \sin\left(\theta_e\right)\Delta\varphi \\
F_w &= \dot{\theta}_w \sin\left(\theta_w\right)\Delta\varphi \\
F_n &= \sin\left(\theta_P\right)\dot{\varphi}_n\Delta\theta \\
F_s &= \sin\left(\theta_P\right)\dot{\varphi}_s\Delta\theta
\end{aligned}
\tag{A.5}
$$

APPENDIX B – CONFOCAL MICROSCOPY

Confocal microscopy can be used to visualize CNT suspensions in liquid state. Since the large difference in refractive index between the epoxy matrix and the nanotubes, confocal microscopy can be used in the reflective mode. Hence, the wavelengths of the laser and of the detector are focused on the same range. Consequently, major care needs to be taken to not overload the detector with high laser intensity. This can be avoided by slowly changing the laser intensity starting from low values (below 30 %).

An Argonne laser was used with a wavelength of 488 nm. In the following figure, a Zeiss confocal LSM 510 META microscope is equipped with the base of a Linkam platform. The base can be used to apply shear flow (or oscillatory flow).

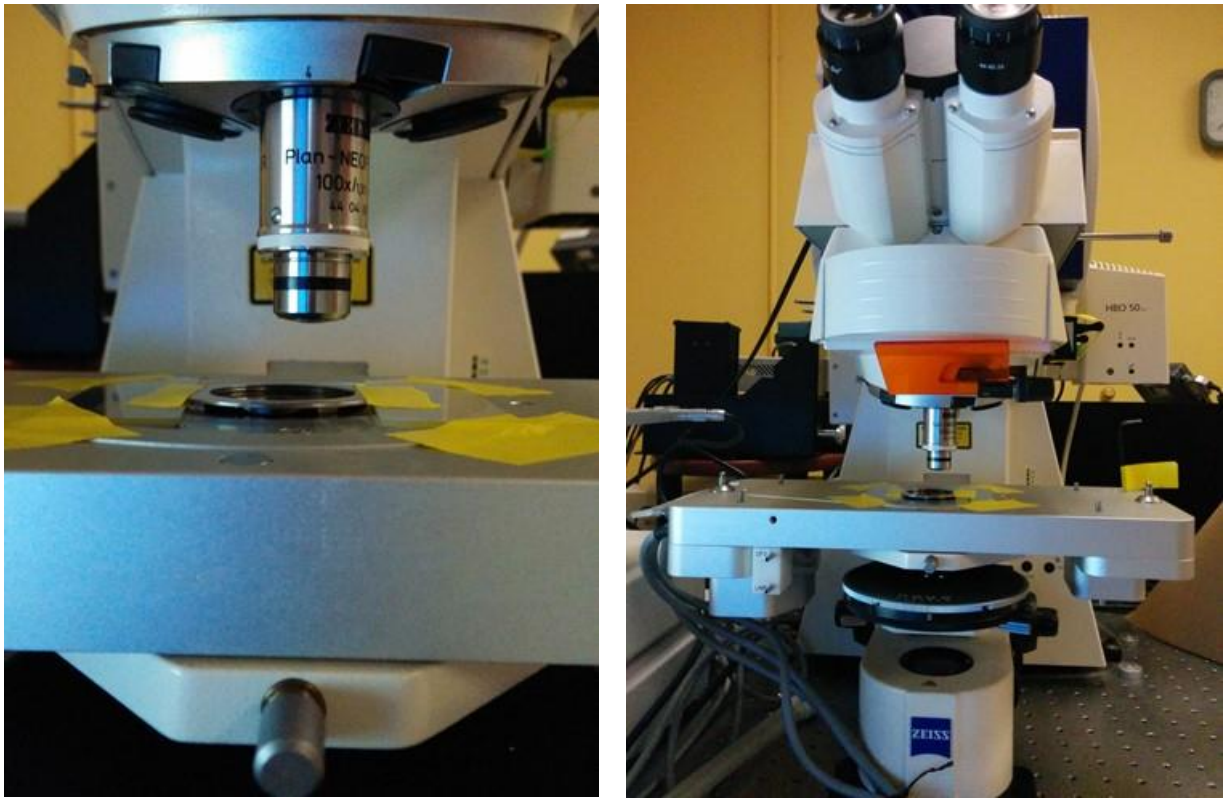

Figure 8.1 Confocal microscope coupled with the base of a Linkam platform.

The lid of the Linkam platform was substituted with a home-made lid since the quartz in the top plate was too thick to use the low distance immersion lenses available. A close up of the lid and how it is set on the Linkam base is reported in Figure 8.2.

The lid screen was obtained by gently cutting a 48x60 mm microscope slide with a diamond glass cutter. The home-made lid was then positioned on two microscope slide and held in position by tape.

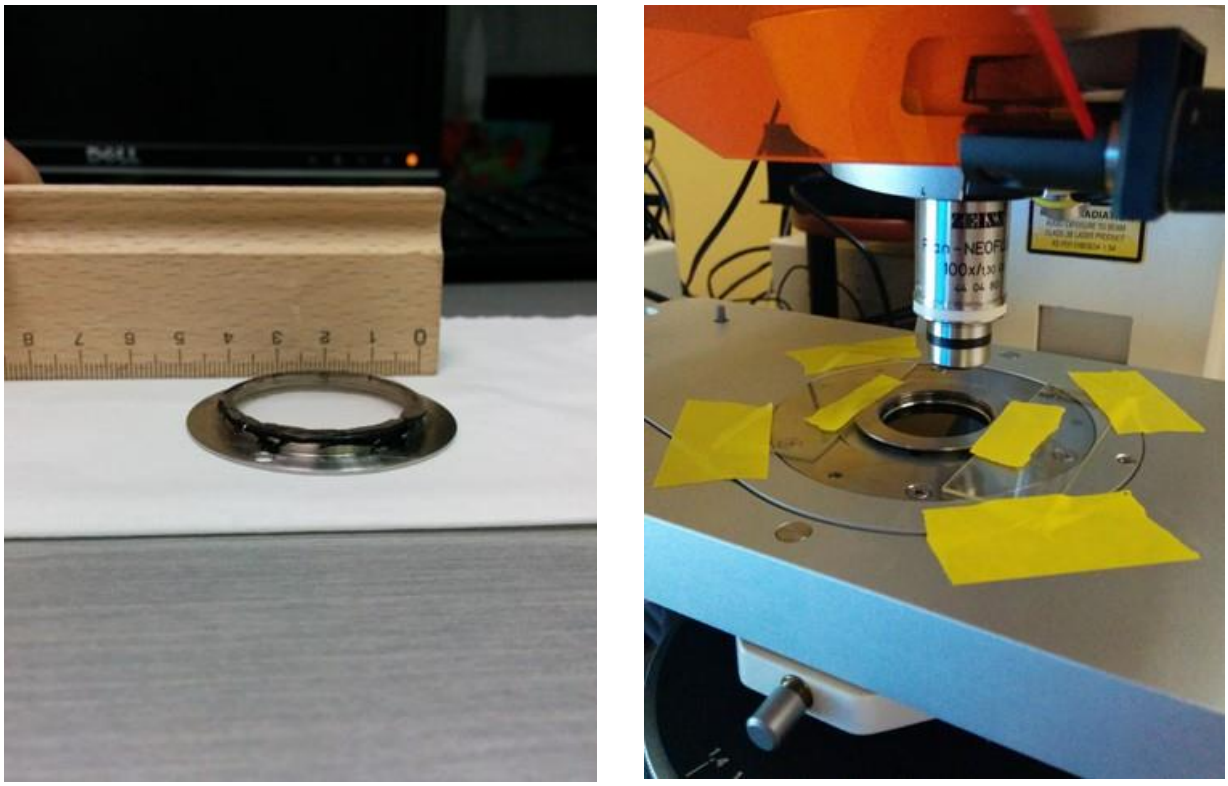

Figure 8.2 Home-made lid for the Linkam platform and close up of the position on the Linkam base.

The objective used was a Plan-Neofluor 100x with numerical aperture of 1.3. During shear, only low shear rates or few micrometers squared section of the sample can be scanned because of the high resolution required to have some information on the nanoparticles. A compromise between the scan time and the deformation induced by the applied shear flow needs to be found. Furthermore, extended application of the laser causes local heating provoking undesired local deformations. Unfortunately, this simple set up is not sufficient to obtain neat shear flows.

Problems related to breakage of the delicate microscope slide during positioning and flow and not perfect alignments of the plates were often encountered making difficult to obtain interesting data. A more refined top plate alternative should be designed in order to solve these issues.

An example of the achievable results at rest is reported in Figure 8.3

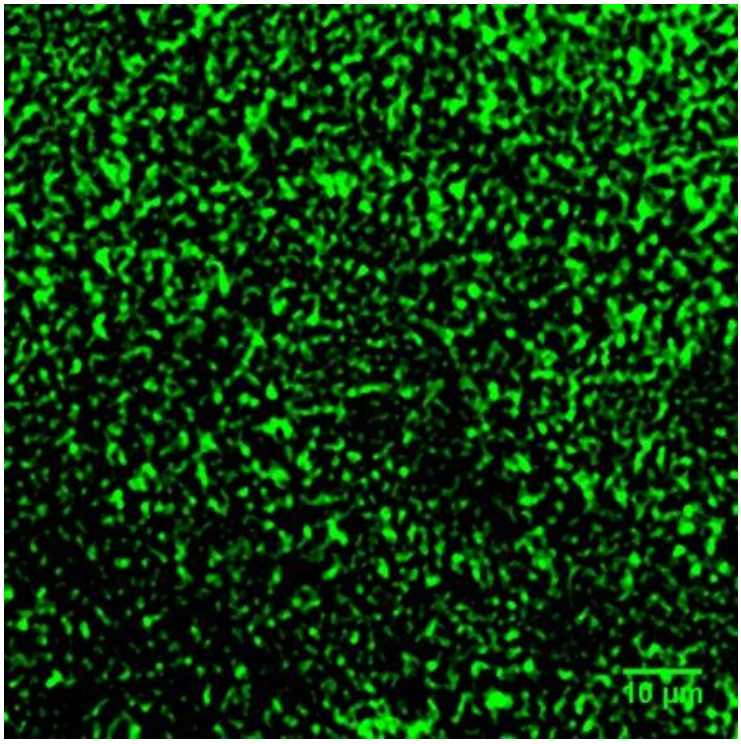

Figure 8.3 1 wt. % MWCNTs (green) in epoxy (black). The scale bar is 10 μm.

MWCNTs appear in green while the matrix is in black. Individual particles show bent conformations but overall orientation state is difficult to define because of the non-sufficient resolution. The system is overall homogenous and large aggregates are practically absent.